Modeling Antennas and Scatterers of Arbitrary Shape Embedded in Layered Dielectric Media

Krzysztof A. Michalski
Dalian Zheng

DTIC
ELECTE
DEC 0 5 1989
D
D cb

November 30, 1989

Electromagnetics & Microwave Laboratory
Department of Electrical Engineering
Texas A&M University

Modeling Antennas and Scatterers of Arbitrary Shape Embedded in Layered Dielectric Media

Krzysztof A. Michalski
Dalian Zheng

Accesion For

NTIS CRA&I	✓
DTIC TAB	☐
Unannounced	☐
Justification	

By

Distribution /

Availability Codes

| Dist | Avail and / or Special |

A-1

November 30, 1989

Electromagnetics & Microwave Laboratory
Department of Electrical Engineering
Texas A&M University

Abstract

A general approach is developed for the rigorous analysis of radiation, scattering, and guidance of electromagnetic fields by conducting objects of arbitrary shape embedded in layered dielectric media. This approach is based on the mixed-potential form of the electric field integral equation, which is amenable to the existing, well-established numerical solution procedures, originally developed for objects in homogeneous space. Numerical results are presented for surfaces and wires that penetrate an interface between dissimilar media and for open microstrip transmission lines of finite thickness. Computed and measured data are also given for coax-fed rectangular and triangular microstrip patch antennas.

Contents

List of Figures

List of Tables

Chapter 1

Introduction

Simple and efficient method of moments (MOM) [1] procedures have recently been developed for the solution of the electromagnetic scattering and radiation problems involving objects of arbitrary shape [2, 3, 4, 5, 6, 7]. These procedures are based on the mixed-potential form of the electric field integral equation (EFIE) – so named, because it involves both the vector and scalar potentials, the former expressed in terms of the induced current, and the latter in terms of the induced charge. In the case of perfectly electrically conducting (PEC) objects, the EFIE is more general than the magnetic field integral equation (MFIE) [8], since it is applicable to both closed and open surfaces [9]. The mixed-potential EFIE (MPIE, for short) is preferable to several other possible variants of the EFIE, because it only requires potential forms of the Green's functions, which are less singular than their derivatives encountered in other forms of the EFIE [4]. In the MOM technique originally developed by Rao *et al.* [5], the surface of the PEC object is modeled in terms of triangular patches and specially designed basis functions defined on pairs of adjacent triangles are used, which yield a surface current representation free of line or point charges at subdomain boundaries. This technique also employs a testing scheme in which the derivatives of the scalar potential are in effect replaced by finite differences. More recently, Schaubert *et al.* [10] extended this procedure to volume integral equations for penetrable bodies, which they modeled in terms of tetrahedral elements.

The procedures described above were originally developed for antennas and scatterers residing in a homogeneous space. Although this restriction is not severe in some aerospace applications where the effect of the environment can be neglected, it does exclude many problems of practical interest in which the proximity of the earth must be taken into account. Indeed, often the influence of the ground or the ocean, which in many cases can be adequately represented by a model consisting of one or more planar, dielectric layers, is the dominant

effect in the problem. Microwave and millimeterwave integrated circuits also consist of conductors embedded in layered dielectric media.

In this report we develop MPIE formulations for arbitrarily shaped objects in layered media that are amenable to the well–established MOM procedures, such as those implemented in the triangle-patch code [5, 7, 11] and its thin-wire counterpart, MININEC [12, 13]. Since a great amount of effort went into the development of these codes – which can presently only handle objects in free space or over PEC ground – it is desirable to have a formulation that would allow one to easily extend them to the case of bodies in stratified media. Although, for simplicity, we limit attention to PEC objects and surface integral equations, our formulation can easily be extended to dielectric bodies in conjunction with either volume [10] or surface [6] integral equations. Unlike in free space, or even in some complex environments with PEC boundaries, it is not a trivial task to formulate an MPIE for objects of arbitrary shape in layered media, because in such environments the vector and scalar potentials are not unique [14] and the scalar potentials of point charges associated with horizontal and vertical dipoles are not, in general, identical [15]. Additional complications arise when the objects penetrate one or more of the interfaces between dielectric layers.

The advantages of the MPIE over the other forms of the EFIE are even more pronounced in a layered medium than in free space, because the Green's functions for layered media comprise Sommerfeld-type integrals [16], which are extremely laborious to evaluate. Since the MPIE involves potential forms of the Green's functions, the Sommerfeld integrals it requires converge faster than those present in any other form of the EFIE [4]. These advantages were previously recognized by several researchers. Mosig and Gardiol [17, 18] have applied the MPIE in conjunction with the Glisson and Wilton's [4] MOM procedure to a rectangular microstrip antenna. Johnson [19] has used a similar approach to solve the problem of a vertical cylinder penetrating the interface between contiguous half-spaces. Wilton and Singh [20] have applied an MPIE to analyze a periodic array of slots in a conducting screen backed with a layered dielectric. Michalski et al. [21, 22] have used an MPIE to solve the problem of a horizontal two-element wire array above and on opposite sides of the interface between two media. As was pointed out in [23, 24, 25], the success of these efforts can be attributed to the fact that the structures considered could only support either vertical or horizontal components of the current. To our knowledge, an MPIE for arbitrarily shaped objects in a layered medium was first published in [24]. However, it was assumed in that paper that the antenna or scatterer was confined to a single layer. In a two-dimensional case, an MPIE has been derived by Xu [26].

2

Numerous papers have been published on the subject of antennas and scatterers in layered media, but – with the exception of the geophysics literature – most of them only deal with planar geometries, such as microstrip antennas, transmission lines, *etc.* Since the emphasis here is on objects of *arbitrary* shape, we do not review papers in this category, to conserve space. The problem of arbitrarily shaped thin wires which are near to or penetrate an interface between contiguous half-spaces has been solved by Burke and Miller [27]. However, their approach, which is implemented in the powerful Numerical Electromagnetics Code (NEC) [28], is not easily extendable to arbitrary surfaces. From the many works devoted to electromagnetic modeling of buried inhomogeneities in the context of geophysical prospecting, we only mention the recent representative papers by Hohmann [29] and by Wannamaker *et al.* [30]. These authors use the volume integral equation technique in conjunction with a rather crude – but entirely adequate in the quasi-static regime – MOM procedure employing piece-wise constant current expansion and point-matching [1]. To overcome the problems associated with the singular behavior of the electric Green's function, Hohmann [29] employed a mixed-potential formulation, but only to the primary (or whole-space) component of the kernel; the part comprising the Sommerfeld integrals was left in the slowly convergent field form. Mention should also be made of the work by Karlsson and Kristensson [31], who employed the extended boundary condition integral equation in conjunction with the T-matrix approach to compute the field scattered by obstacles buried in a stratified ground. This method, however, is only applicable to closed, smooth bodies and is only practical for simple shapes.

The outline of this report is as follows. Chapter 2 contains the statement of the problem and a general discussion of various forms of the EFIE in a layered medium. In Chapter 3, alternative forms of the vector potential Green's function are derived for the layered medium. These Green's functions are utilized in Chapter 4, where three alternative mixed-potential formulations, referred to as Formulations A, B and C, are developed for arbitrarily shaped PEC objects. Formulation C, which is found to be particularly well suited for the application of the moment method, is specialized in Appendix A to two particularly important situations, where the object resides in contiguous half-spaces or is partially embedded in a grounded dielectric slab. In Chapter 5, the MOM procedures introduced in [4, 5, 7] are adapted to solve the MPIE based on Formulation C of Chapter 4. For surfaces of arbitrary shape, the triangle-patch model [5] is employed, while thin-wire structures are modeled by straight tubular segments [7]. The wire-to-patch junction model developed by Hwu *et al.* [7] has been adopted for the analysis of coax–fed microstrip patch antennas. Formulation C is also

3

specialized in Chapter 5 to the case of an open transmission line consisting of an infinite conductor of arbitrary cross-section partially embedded in a grounded dielectric slab. In the numerical procedure, the conductor's cross-section profile is modeled by straight line segments [4]. In Chapter 6, the numerical procedures used to evaluate the Sommerfeld integrals are discussed. In Chapter 7, sample numerical results are presented for several cases of interest involving PEC plates, cylinders, thin-wire antennas, coax–fed microstrip patch antennas, and open microstrip lines. Where possible, comparisons are made with measured data or with computed results obtained by other researchers. Finally, in Chapter 8, we draw conclusions and make recommendations for future work.

Chapter 2

Preliminaries

2.1   Statement of the Problem

Consider a medium consisting of $n + 1$ dielectric layers separated by n planar interfaces parallel to the xy–plane of a Cartesian coordinate system and located at $z = z_l$, $l = 1,2,\ldots,n$, as illustrated in Fig. 2.1. The medium of the ith layer is characterized by permeability μ_i and permittivity ϵ_i, which may be complex if the medium is lossy. Let the PEC object (or collection of objects) in Fig. 2.1 occupy p layers with indices $l_1, l_2, \ldots, l_p$, where $1 \leq p \leq n+1$. For later convenience, define the ordered set of indices $L = \{l_1, l_2, \ldots, l_p\}$, in which $l_k < l_{k+1}$. Let S_i denote the surface of the object(s) in the ith layer and let $\hat{n}_i$ be a unit vector normal to S_i. The quantity of interest is the surface current density $J(r)$ excited on the object(s) by a given time-harmonic incident electric field E^{inc}. The $e^{j\omega t}$ time variation is assumed and suppressed.

2.2   Electric Field Integral Equation (EFIE)

The EFIE for the current density J on the surface S of the PEC object(s) embedded in a layered medium is obtained by enforcing the boundary condition [32]

$$-\hat{n}_m \times E^s_m(r) = \hat{n}_m \times E^{inc}_m(r), \quad r \text{ on } S_m, \quad m \in L \tag{2.1}$$

where r is the position vector defined with respect to a global coordinate origin, E^{inc}_m is the "incident" electric field (i.e., the field in the absence of the object) in the mth layer, and E^s_m is the scattered field in the mth layer. For the structure of Fig. 2.1, E^s_m and the scattered magnetic field H^s_m can be expressed as

$$-E^s_m(r) = \sum_{i \in L} \left[j\omega A^{mi}(r) + \nabla \phi^{mi}(r) \right] \tag{2.2}$$

5
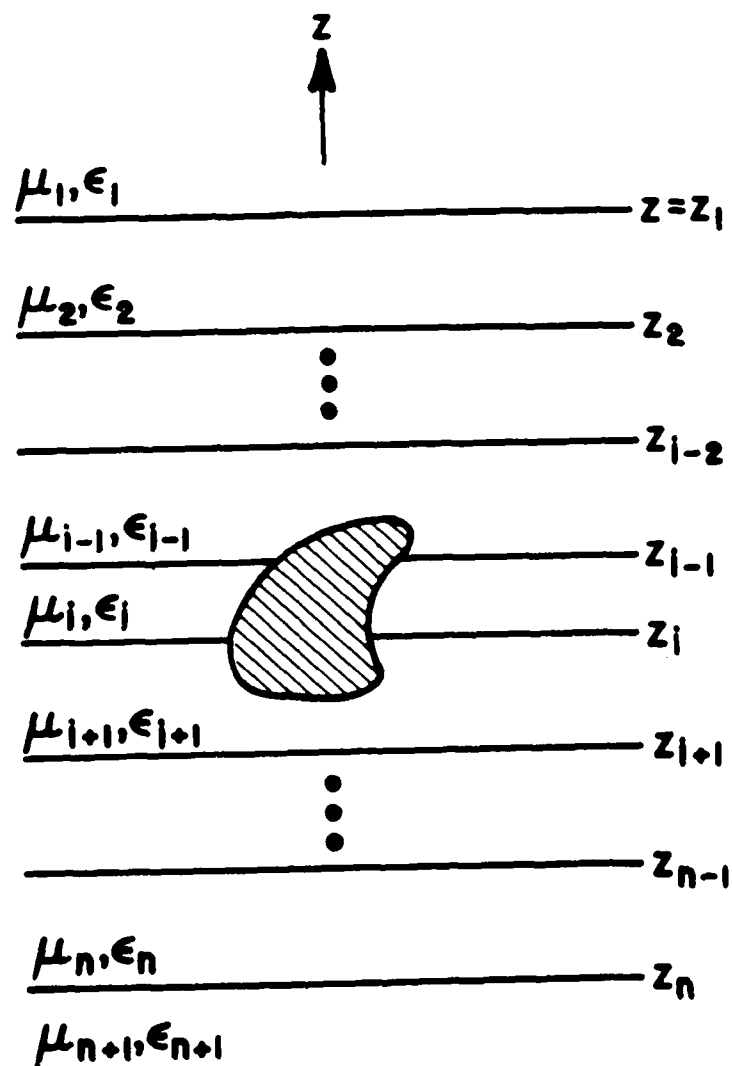
Figure 2.1: Scatterer of arbitrary shape embedded in a layered dielectric medium.

$$H_m^s(r) = \frac{1}{\mu_m} \nabla \times \sum_{i \in L} A^{mi}(r) \tag{2.3}$$

where A^{mi} is the magnetic vector potential in the mth layer due to the current density J in the ith layer, and is given as

$$A^{mi}(r) = \int_{S_i} G_A^{mi}(r \mid r') \cdot J(r') \, dS' \tag{2.4}$$

and $\phi^{mi}(r)$ is the corresponding scalar potential which is related to $A^{mi}(r)$ through the Lorentz condition

$$\phi^{mi}(r) = \frac{j\omega}{k_m^2} \nabla \cdot A^{mi}(r) \tag{2.5}$$

where $k_m^2 = \omega^2 \epsilon_m \mu_m$. In (2.4), G_A^{mi} is the dyadic Green's function which represents the magnetic vector potential in region m due to a unit-strength, arbitrarily oriented current dipole in region i. $\underline{\underline{G}}_A^{mi}$ can be found by solving the inhomogeneous Helmholtz equation

$$(\nabla^2 + k_m^2) \underline{\underline{G}}_A^{mi}(r \mid r') = -\mu_m \underline{\underline{I}} \delta(r - r') \tag{2.6}$$

where $\underline{\underline{I}}$ is the idemfactor, subject to the condition that the tangential component of E_m^s and H_m^s be continuous across the interfaces between dielectric layers. As is well known [16], for a horizontal, say, x-directed dipole, two components of the vector potential are required to satisfy the boundary conditions at the interfaces. Traditionally [33], the z component has been selected in addition to the x component. The Green's function in this case takes the form [24]

$$\underline{\underline{G}}_A^{mi} = (\hat{x}\,\hat{x} + \hat{y}\,\hat{y}) G_{xx}^{mi} + \hat{z}\,\hat{x}\, G_{zx}^{mi} + \hat{z}\,\hat{y}\, G_{zy}^{mi} + \hat{z}\,\hat{z}\, G_{zz}^{mi}. \tag{2.7}$$

However, one may as well postulate the y component of the vector potential to accompany the primary x component [14]. This strategy leads to an alternative form of the Green's function,

$$\underline{\underline{G}}_A^{mi} = \hat{x}\,\hat{x}\, G_{xx}^{mi} + \hat{y}\,\hat{y}\, G_{yy}^{mi} + (\hat{x}\,\hat{y} + \hat{y}\,\hat{x}) G_{xy}^{mi} + \hat{z}\,\hat{z} G_{zz}^{mi}. \tag{2.8}$$

In (2.7) and (2.8) G_{xx}^{mi} denotes the x-component of A^{mi} due to an x-directed, unit-strength electric dipole, G_{xy}^{mi} the x-component of A^{mi} due to a similar, y-directed dipole, etc. We note that, except for G_{zz}^{mi}, the corresponding components in (2.7) and (2.8) are different, even though the same notation is used. The entries of the dyadics in (2.7) and (2.8) are developed

7

in the next chapter, and are shown to comprise improper integrals of the Sommerfeld [16] type.

Still other Green's functions, in addition to those in (2.7) and (2.8) are possible. For example, one can obtain another form of $\underline{\underline{G}}_A^{mi}$ by postulating that the y and z components of the vector potential, instead of the x and z or x and y components, accompany an x-directed dipole. However, this and other forms of $\underline{\underline{G}}_A^{mi}$ are less attractive for our purpose than (2.7) and (2.8), and are not considered here.

Substitution of (2.2) into (2.1) yields

$$\hat{n}_m \times \sum_{i \in L} \left[j\omega A^{mi}(r) + \nabla \phi^{mi}(r) \right] = \hat{n}_m \times E_m^{inc}(r), \quad r \text{ on } S_m, \quad m \in L \tag{2.9}$$

which, by invoking (2.4) and (2.5), can be further transformed to

$$\frac{j\omega}{k_m^2} \hat{n}_m \times (\nabla \nabla \cdot + k_m^2) \sum_{i \in L} \int_{S_i} \underline{\underline{G}}_A^{mi}(r \mid r') \cdot J(r') \, dS'$$

$$= \hat{n}_m \times E_m^{inc}(r), \quad r \text{ on } S_m, \quad m \in L. \tag{2.10}$$

This equation is referred to as vector-potential EFIE [34], since it only involves the magnetic vector potential. Although (2.10) has often been used in MOM analyses of straight wire antennas or planar scatterers, the presence of the mixed tangential derivatives makes it less suitable for objects of arbitrary shape. By introducing the differential operator under the integral sign in (2.10), we may obtain another form of the EFIE, in which the dyadic kernel is the Green's function for the electric field. However, this EFIE is not attractive because the kernel is highly singular, which makes the evaluation of the integrals required by the MOM procedure difficult when the observation point is within the integration interval [35]. Also, the required differentiation of the Sommerfeld-type integrals adversely affects their convergence. These difficulties can be avoided if only *one* of the operators nabla is introduced inside the integral in (2.10) and then transferred, by a series of transformations, to act on the current. The result is the mixed-potential EFIE discussed below.

2.3   Mixed-Potential EFIE (MPIE)

We note that (2.9) would be in the desired mixed-potential form if the scalar potential were expressed in terms of the surface charge density $q(r)$. With this goal in mind, we substitute (2.4) into (2.5) and introduce the operator nabla under the integral sign (this step can be justified [36, 37]) to obtain

8

$$\phi^{mi}(\boldsymbol{r}) = \frac{j\omega}{k_m^2} \int\limits_{S_i} \left[\boldsymbol{\nabla} \cdot \underline{\underline{\boldsymbol{G}}}_A^{mi}(\boldsymbol{r} \,|\, \boldsymbol{r}') \right] \cdot \boldsymbol{J}(\boldsymbol{r}') \, dS'. \tag{2.11}$$

Obviously, our objective would be achieved if we transferred the divergence operator to act on the current, in view of the equation of continuity, $\boldsymbol{\nabla} \cdot \boldsymbol{J} = -j\omega q$. It is shown below that this can only be accomplished if a scalar function G_ϕ^{mi} can be found, such that

$$\frac{j\omega}{k_m^2} \boldsymbol{\nabla} \cdot \underline{\underline{\boldsymbol{G}}}_A^{mi}(\boldsymbol{r} \,|\, \boldsymbol{r}') = \frac{1}{j\omega} \boldsymbol{\nabla}' G_\phi^{mi}(\boldsymbol{r} \,|\, \boldsymbol{r}'). \tag{2.12}$$

In a homogeneous medium, where G_ϕ^{mi} may be interpreted as the Green's function for the scalar potential, this is a quite trivial task. If the medium is stratified, however, G_ϕ^{mi} satisfying (2.12) does not in general exist [24], which can be attributed to the fact that the scalar potentials of point charges associated with horizontal and vertical current dipoles in a layered medium are in general different [15]. Hence, in order to achieve our goal, we follow the procedure proposed in [23, 24], and introduce a scalar function K_ϕ^{mi} and a vector function $\boldsymbol{P}^{mi}$ according to

$$\frac{j\omega}{k_m^2} \boldsymbol{\nabla} \cdot \boldsymbol{G}_A^{mi}(\boldsymbol{r} \,|\, \boldsymbol{r}') = \frac{1}{j\omega} \boldsymbol{\nabla}' K_\phi^{mi}(\boldsymbol{r} \,|\, \boldsymbol{r}') + j\omega \boldsymbol{P}^{mi}(\boldsymbol{r} \,|\, \boldsymbol{r}'). \tag{2.13}$$

One should note that in the above the choice of K_ϕ^{mi} and $\boldsymbol{P}^{mi}$ is not unique.

Upon substituting (2.13) into (2.11) and using a vector identity (p. 487, [38]) and the Gauss theorem [38, p. 503], we can express the scalar potential as

$$\phi^{mi}(\boldsymbol{r}) = \int\limits_{S_i} K_\phi^{mi}(\boldsymbol{r} \,|\, \boldsymbol{r}') \, q(\boldsymbol{r}') \, dS' + j\omega \int\limits_{S_i} \boldsymbol{P}^{mi}(\boldsymbol{r} \,|\, \boldsymbol{r}') \cdot \boldsymbol{J}(\boldsymbol{r}') \, dS'$$
$$+ \frac{1}{j\omega} \left[\oint\limits_{C_i} K_\phi^{mi}(\boldsymbol{r} \,|\, \boldsymbol{r}') \, \boldsymbol{J}(\boldsymbol{r}') \cdot \hat{\boldsymbol{u}}_i \, dC' - \oint\limits_{C_{i-1}} K_\phi^{mi}(\boldsymbol{r} \,|\, \boldsymbol{r}') \, \boldsymbol{J}(\boldsymbol{r}') \cdot \hat{\boldsymbol{u}}_{i-1} \, dC' \right] \tag{2.14}$$

where C_i and C_{i-1} are the contours formed by the intersection of the surface S_i with the interfaces at $z = z_i$ and $z = z_{i-1}$, respectively, and $\hat{\boldsymbol{u}}_i$ and $\hat{\boldsymbol{u}}_{i-1}$ are the unit vectors perpendicular at $\boldsymbol{r}'$ to C_i and C_{i-1}, respectively, in the planes tangent to S_i (Fig. 2.2). Substituting (2.14) into (2.9), we finally obtain

$$\hat{\boldsymbol{n}}_m \times \sum_{i \in L} \left\{ j\omega \int\limits_{S_i} \boldsymbol{K}_A^{mi}(\boldsymbol{r} \,|\, \boldsymbol{r}') \cdot \boldsymbol{J}(\boldsymbol{r}') \, dS' + \boldsymbol{\nabla} \int\limits_{S_i} K_\phi^{mi}(\boldsymbol{r} \,|\, \boldsymbol{r}') q(\boldsymbol{r}') \, dS' \right.$$
$$\left. + \frac{\boldsymbol{\nabla}}{j\omega} \left[\oint\limits_{C_i} K_\phi^{mi}(\boldsymbol{r} \,|\, \boldsymbol{r}') \boldsymbol{J}(\boldsymbol{r}') \cdot \hat{\boldsymbol{u}}_i \, dC' - \oint\limits_{C_{i-1}} K_\phi^{mi}(\boldsymbol{r} \,|\, \boldsymbol{r}') \boldsymbol{J}(\boldsymbol{r}') \cdot \hat{\boldsymbol{u}}_{i-1} \, dC' \right] \right\}$$
$$= \hat{\boldsymbol{n}}_m \times \boldsymbol{E}_m^{inc}(\boldsymbol{r}), \quad \boldsymbol{r} \text{ on } S_m, \quad m \in L \tag{2.15}$$

9
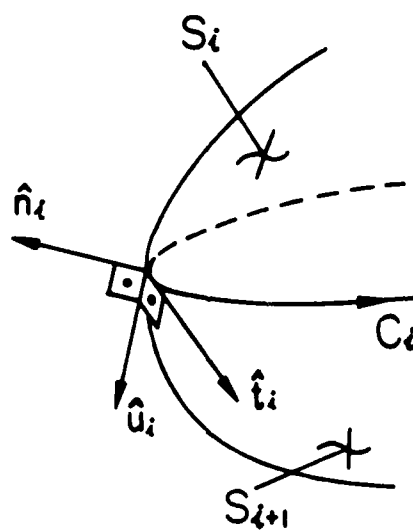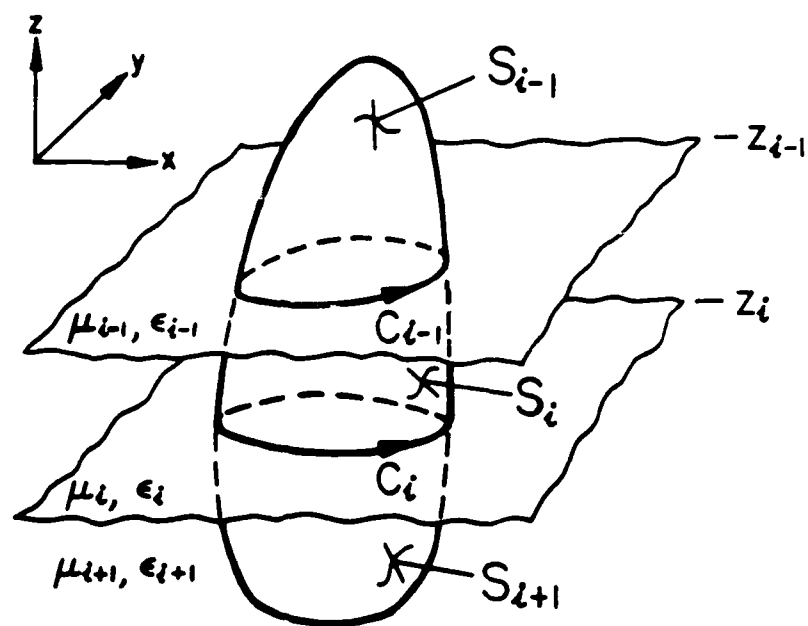
Figure 2.2: Arbitrarily shaped surface penetrating two adjacent interfaces.

where we have introduced the dyadic kernel

$$\underline{\underline{K}}_A^{mi}(r \mid r') = G_A^{mi}(r \mid r') + \nabla P^{mi}(r \mid r').$$ (2.16)

We note that (2.15) would be in the desired mixed-potential form [4, 5] if it were not for the presence of the term contributed by the contour integrals, which occur when the object penetrates one or more of the interfaces. In Chapter 4 we show that with a proper choice of $\underline{\underline{G}}_A^{mi}$ and K_ϕ^{mi} in (2.13) the contour integrals cancel out. We note, however, that even if a formulation is chosen in which the contour integrals persist, the MOM procedures developed in [4, 5] can be extended to accommodate these terms. As a matter of fact, the "correction term" ∇P^{mi} could also be handled in this manner, instead of being incorporated into the vector potential kernel via (2.16).

Chapter 3

Derivation of Green's Functions for the Magnetic Vector Potential

The dyadic Green's function $\underline{\underline{G}}_A^{mi}(r\,|\,r')$ in (2.4) is the vector potential in region m due to a unit-strength, arbitrarily-oriented Hertzian dipole in the ith layer. The direct solution of (2.6) for $\underline{\underline{G}}_A^{mi}$ is extremely tedious, since various components of this dyadic couple in the boundary conditions at the interfaces between dielectric layers. Therefore, in this chapter, we derive the Green's function by means of the Fourier transformation, which in effect reduces the original problem to that of solving an equivalent transmission-line network along the z coordinate.

3.1 Reduction of Maxwell's Equations to Transmission Line Equations for Sources in Layered Media

For the geometry of Fig. 3.1a, we are interested in the electromagnetic field (E, H) everywhere in the medium due to prescribed distributions of time-harmonic electric and magnetic currents J and M, respectively. Since the structure is infinite along the x and y coordinates, we can simplify the analysis by utilizing the "shifted" Fourier transform pair

$$\mathcal{F}\{f(x - x', y - y')\} \equiv \tilde{f}(k_x, k_y)$$
$$= \int\limits_{-\infty}^{\infty} \int\limits_{-\infty}^{\infty} f(x - x', y - y')e^{j[k_x(x-x')+k_y(y-y')]}\,dx\,dy \tag{3.1}$$

$$\mathcal{F}^{-1}\{\tilde{f}(k_x, k_y)\} \equiv f(x - x', y - y')$$
$$= \frac{1}{(2\pi)^2} \int\limits_{-\infty}^{\infty} \int\limits_{-\infty}^{\infty} \tilde{f}(k_x, k_y)e^{-j[k_x(x-x')+k_y(y-y')]}\,dk_x\,dk_y \tag{3.2}$$

12
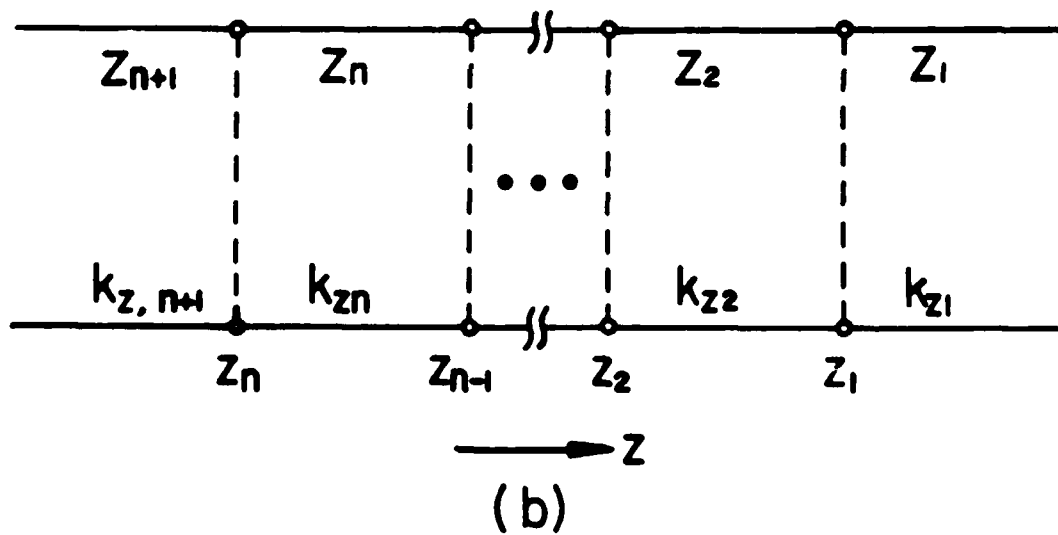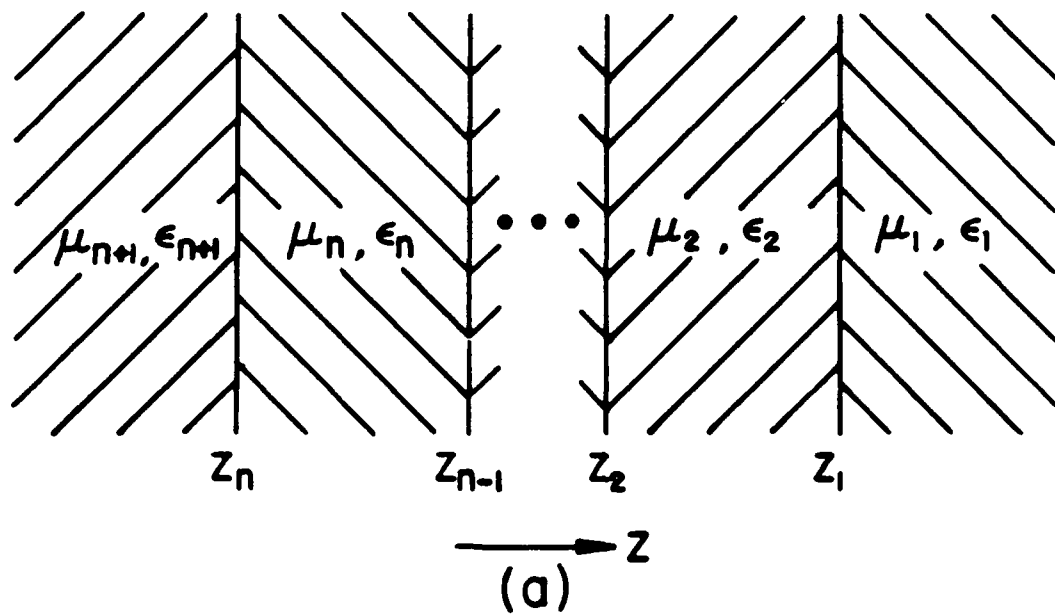
Figure 3.1: (a) Plane-stratified dielectric medium and (b) its transmission-line network representation.

13

where (x', y') locates the projection of the source point on the xy–plane (Fig. 3.2). The inverse Fourier integrals (3.2) can be conveniently expressed in terms of the Sommerfeld integrals [16] of the form

$$S_n \left[\tilde{f}(k_\rho) \right] = \int_0^\infty \tilde{f}(k_\rho) \, J_n(k_\rho \xi) \, k_\rho^{n+1} \, dk_\rho \qquad (3.3)$$

by changing to polar coordinates in both the transform and space domains according to

$$x - x' = \xi \cos \zeta, \quad y - y' = \xi \sin \zeta \qquad (3.4)$$

$$k_x = k_\rho \cos \alpha, \quad k_y = k_\rho \sin \alpha \qquad (3.5)$$

where (Fig. 3.2)

$$\xi = \sqrt{(x - x')^2 + (y - y')^2}, \quad \zeta = \arctan\left(\frac{y - y'}{x - x'}\right) \qquad (3.6)$$

$$k_\rho = \sqrt{k_x^2 + k_y^2}, \quad \alpha = \arctan\left(\frac{k_y}{k_x}\right) \qquad (3.7)$$

and where J_n is the Bessel function of order n. Hence, using (3.3), we can express (3.2) as

$$\mathcal{F}^{-1}\left\{\tilde{f}(k_\rho)\right\} = \frac{1}{2\pi} S_0 \left[\tilde{f}(k_\rho)\right]. \qquad (3.8)$$

We also find that

$$\mathcal{F}^{-1}\left\{jk_x \tilde{f}(k_\rho)\right\} = \frac{\cos \zeta}{2\pi} S_1[\tilde{f}(k_\rho)] \qquad (3.9)$$

$$\mathcal{F}^{-1}\{jk_y \tilde{f}(k_\rho)\} = \frac{\sin \zeta}{2\pi} S_1[\tilde{f}(k_\rho)] \qquad (3.10)$$

$$\mathcal{F}^{-1}\{k_x^2 \tilde{f}(k_\rho)\} = -\frac{1}{4\pi} \left\{\cos 2\zeta \, S_2[\tilde{f}(k_\rho)] - S_0[k_\rho^2 \tilde{f}(k_\rho)]\right\} \qquad (3.11)$$

$$\mathcal{F}^{-1}\{k_y^2 \tilde{f}(k_\rho)\} = \frac{1}{4\pi} \left\{\cos 2\zeta \, S_2[\tilde{f}(k_\rho)] + S_0[k_\rho^2 \tilde{f}(k_\rho)]\right\} \qquad (3.12)$$

$$\mathcal{F}^{-1}\{k_x k_y \tilde{g}(k_\rho)\} = -\frac{1}{4\pi} \sin 2\zeta \, S_2[\tilde{g}(k_\rho)]. \qquad (3.13)$$

14
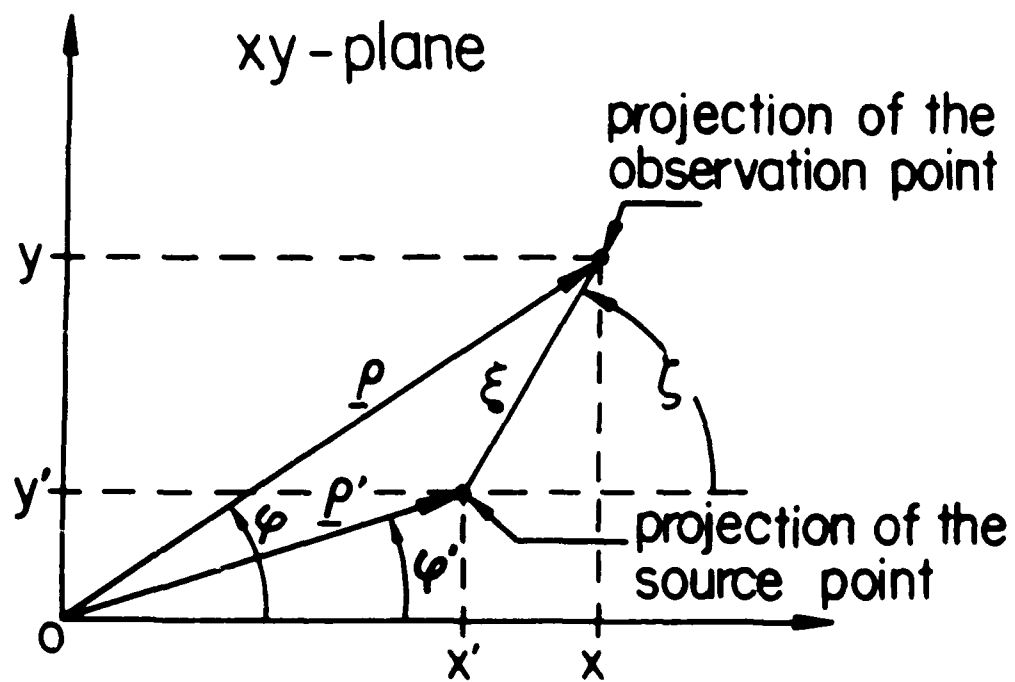
Figure 3.2: Definition of the distance ξ and angle ζ.

These relationships will be used in the formulation of vector potential Green's functions. We list them here for later convenience.

Since the structure of Fig. 3.1a can be regarded as a uniform cylindrical waveguide (of infinite cross-section) with z as the longitudinal (axial) coordinate, it is fruitful to decompose the field and source vectors into their transverse and longitudinal parts, $i.e.$, we can write $E = E_t + \hat{z}E_z$, $H = H_t + \hat{z}H_z$, $etc.$ The solution of the field equations for E and H is facilitated by eliminating the dependent longitudinal components from the Maxwell's equations [39, 40]. Hence, by eliminating E_z and H_z and invoking the Fourier transformation (3.1), we arrive at

$$-\frac{d}{dz}\widetilde{E}_t = j\omega\mu\left(\underline{\underline{I}} + \frac{\widetilde{\nabla}_t\widetilde{\nabla}_t}{k^2}\right)\cdot\left(\widetilde{H}_t \times \hat{z}\right) + \widetilde{M}_{te} \times \hat{z} \tag{3.14}$$

$$-\frac{d}{dz}\widetilde{H}_t = j\omega\epsilon\left(\underline{\underline{I}} + \frac{\widetilde{\nabla}_t\widetilde{\nabla}_t}{k^2}\right)\cdot\left(\hat{z} \times \widetilde{E}_t\right) + \hat{z} \times \widetilde{J}_{te} \tag{3.15}$$

where the equivalent transverse electric and magnetic current distributions are given, respectively, as

$$\widetilde{J}_{te} = \widetilde{J}_t - \hat{z} \times \frac{\widetilde{\nabla}_t\widetilde{M}_z}{j\omega\mu} \tag{3.16}$$

and

$$\widetilde{M}_{te} = \widetilde{M}_t + \hat{z} \times \frac{\widetilde{\nabla}_t\widetilde{J}_z}{j\omega\epsilon}, \tag{3.17}$$

$\underline{\underline{I}}$ is a unit dyadic, and $\widetilde{\nabla}_t = -jk_x\hat{x} - jk_y\hat{y}$ is the transform domain counterpart of the transverse operator nabla. The longitudinal field components are derivable from the transverse components as [40]

$$\widetilde{E}_z = \frac{1}{j\omega\epsilon}\left\{\widetilde{\nabla}_t \cdot \left(\widetilde{H}_t \times \hat{z}\right) - \widetilde{J}_z\right\} \tag{3.18}$$

$$\widetilde{H}_z = \frac{1}{j\omega\mu}\left\{\widetilde{\nabla}_t \cdot \left(\hat{z} \times \widetilde{E}_t\right) - \widetilde{M}_z\right\} \tag{3.19}$$

Equations (3.14)-(3.19) hold for each layer of the stratified medium (Fig. 3.1a). The layer subscript has been suppressed in these equations for simplicity.

Since any vector can be represented as a sum of two parts, one of which is solenoidal and the other irrotational, we may express the vectors $\widetilde{E}_t$ and $\widetilde{H}_t \times \hat{z}$ as [40]

$$\widetilde{E}_t = -\widetilde{\nabla}_t V^e - \widetilde{\nabla}_t V^h \times \hat{z} \tag{3.20}$$

16

$$\widetilde{\boldsymbol{H}}_t \times \hat{\boldsymbol{z}} = -\widetilde{\boldsymbol{\nabla}}_t I^e - \widetilde{\boldsymbol{\nabla}}_t I^h \times \hat{\boldsymbol{z}}. \tag{3.21}$$

Using these equations in (3.18) and (3.19), we can express the longitudinal field components as

$$\tilde{E}_z = \frac{1}{j\omega\epsilon} \left(k_\rho{}^2 I^e - \tilde{J}_z \right) \tag{3.22}$$

$$\widetilde{H}_z = \frac{1}{j\omega\mu} \left(k_\rho{}^2 V^h - \widetilde{M}_z \right) \tag{3.23}$$

where $k_\rho{}^2 = k_x^2 + k_y^2$. Equations (3.20)-(3.23) indicate that in source-free regions, (V^e, I^e) and (V^h, I^h) generate, respectively, field transverse magnetic (TM) and transverse electric (TE) to z. To determine the scalar functions V^e, I^e, V^h, and I^h, we use (3.20) and (3.21) to eliminate $\widetilde{\boldsymbol{E}}_t$ and $\widetilde{\boldsymbol{H}}_t$ from (3.14) and (3.15). As a result, we obtain the equations [40]

$$-\frac{dV^q}{dz} = jk_z Z^q I^q + v^q \tag{3.24}$$

$$-\frac{dI^q}{dz} = jk_z Y^q V^q + i^q \tag{3.25}$$

where the superscript "q" stands for either "e" or "h" and where $k_z^2 = k^2 - k_\rho{}^2$. The modal impedances Z^q (admittances Y^q) are defined as

$$Z^e = \frac{1}{Y^e} = \frac{k_z}{\omega\epsilon} \tag{3.26}$$

$$Z^h = \frac{1}{Y^h} = \frac{\omega\mu}{k_z} \tag{3.27}$$

and the source functions v^q and i^q are given by [40]

$$v^e = -\frac{\tilde{J}_z}{j\omega\epsilon} + \frac{1}{k_\rho{}^2} \left(\hat{\boldsymbol{z}} \times \widetilde{\boldsymbol{\nabla}}_t \right) \cdot \widetilde{\boldsymbol{M}}_t \tag{3.28}$$

$$i^e = \frac{1}{k_\rho{}^2} \widetilde{\boldsymbol{\nabla}}_t \cdot \tilde{\boldsymbol{J}}_t \tag{3.29}$$

$$v^h = \frac{1}{k_\rho{}^2} \widetilde{\boldsymbol{\nabla}}_t \cdot \widetilde{\boldsymbol{M}}_t \tag{3.30}$$

$$i^h = -\frac{\widetilde{M}_z}{j\omega\mu} - \frac{1}{k_\rho{}^2} \left(\hat{\boldsymbol{z}} \times \widetilde{\boldsymbol{\nabla}}_t \right) \cdot \tilde{\boldsymbol{J}}_t. \tag{3.31}$$

17

Equations (3.24) and (3.25) have the form of transmission-line equations for the voltage V^q and current I^q. To the lth layer of the stratified medium (Fig. 3.1a) there corresponds a transmission line section with characteristic impedance Z_l^q and propagation constant k_{z_l}. Hence, the layered medium of Fig. 3.1a may be represented by two transmission-line networks, which may be referred to as the TM and TE networks, each of the form shown in Fig. 3.1b. The TM network has characteristic impedances Z_l^e and sources (v^e, i^e), while the TE network has characteristic impedances Z_l^h and is driven by (v^h, i^h). Depending on the sources (cf. (3.28)–(3.31)), the TM, TE, or both networks may be excited. These network problems must be solved subject to the condition that the voltages and currents be continuous across the interfaces between contiguous line sections. These conditions are the consequence of the continuity of the transverse components of the electric and magnetic fields across the interfaces between adjacent dielectric layers (Fig. 3.1a).

The solution of the transmission-line equations (3.24) and (3.25) is facilitated if one appeals to the principle of superposition and considers the effect of the voltage and current sources separately. Hence, with only voltage sources present $(i^q = 0)$, (3.24) and (3.25) reduce to

$$\left(\frac{d}{dz^2} + k_z^2\right) I^q = jk_z Y^q v^q \tag{3.32}$$

$$V^q = -\frac{Z^q}{jk_z}\frac{d}{dz}I^q. \tag{3.33}$$

From these equations, the impedances seen looking to the left and to the right at a point z on the transmission line can be expressed, respectively, as

$$\overleftarrow{Z}^q(z) = -\frac{V^q(z)}{I^q(z)} = \frac{Z^q}{jk_z}\frac{d}{dz}\ln I^q(z) \tag{3.34}$$

and

$$\overrightarrow{Z}^q(z) = \frac{V^q(z)}{I^q(z)} = -\frac{Z^q}{jk_z}\frac{d}{dz}\ln I^q(z). \tag{3.35}$$

Similarly, with only current sources present $(v^q = 0)$, (3.24) and (3.25) reduce to

$$\left(\frac{d}{dz^2} + k_z^2\right) V^q = jk_z Z^q i^q \tag{3.36}$$

$$I^q = -\frac{Y^q}{jk_z}\frac{d}{dz}V^q. \tag{3.37}$$

18

The admittances seen looking to the left and to the right at a point z on the transmission line can be in this case expressed, respectively, as

$$\overleftarrow{Y}^q(z) = -\frac{I^q(z)}{V^q(z)} = \frac{Y^q}{jk_z}\frac{d}{dz}\ln V^q(z) \tag{3.38}$$

and

$$\overrightarrow{Y}^q(z) = \frac{I^q(z)}{V^q(z)} = -\frac{Y^q}{jk_z}\frac{d}{dz}\ln V^q(z). \tag{3.39}$$

Once the transmission-line equations (3.32), (3.33), (3.36) and (3.37) are solved for (V^e, I^e) and (V^h, I^h), we determine $(\widetilde{\boldsymbol{E}}, \widetilde{\boldsymbol{H}})$ from (3.20)–(3.23). Finally, the inverse Fourier transformation (3.2) is employed to recover $(\boldsymbol{E}, \boldsymbol{H})$. The solution of (3.32), (3.33), (3.36) and (3.37) for the stratified medium of Fig. 3.1a is discussed in the next section.

3.2   Solution of Transmission-Line Equations

It was shown in the last section that the layered medium of Fig. 3.1a can be represented by the transmission-line network of Fig. 3.1b. The voltage and the current in each transmission-line section are governed by (3.24) and (3.25), or equivalently, by (3.32), (3.33), (3.36), and (3.37). In solving these equations, it is helpful to define for each interface the impedances and voltage reflection coefficients, as illustrated in Fig. 3.3. (For notational simplicity, we suppress the superscripts "q".) The solution of (3.32), (3.33), (3.36), and (3.37) is simplified by first considering point-source excitations and then obtaining the total response by use of the superposition theorem [40]. Without loss of generality, we assume that the sources are located in the ith section of the transmission line (which corresponds to the ith layer in Fig. 3.1a) and that the impedances $\overleftarrow{Z}_i(z_i) \equiv \overleftarrow{Z}_i$ and $\overrightarrow{Z}_i(z_{i-1}) \equiv \overrightarrow{Z}_{i-1}$ (or their inverses $\overleftarrow{Y}_i$ and $\overrightarrow{Y}_{i-1}$) are specified. Hence, if we denote the current I in the ith line section due to a point voltage $v = -\delta(z - z')$ in the same section as $\widetilde{G}_{ii}^I$, we obtain from (3.32)

$$\left(\frac{d^2}{dz^2} + k_{zi}^2\right) \widetilde{G}_{ii}^I(z, z') = -jk_{zi}Y_i\delta(z - z'). \tag{3.40}$$

This equation must be solved subject to the boundary conditions (cf. (3.34) and (3.35))

$$\overleftarrow{Z}_i = \frac{Z_i}{jk_{zi}}\frac{d}{dz}\ln \widetilde{G}_{ii}^I(z, z'), \quad z = z_i \tag{3.41}$$

$$\overrightarrow{Z}_{i-1} = -\frac{Z_i}{jk_{zi}}\frac{d}{dz}\ln \widetilde{G}_{ii}^I(z, z'), \quad z = z_{i-1}. \tag{3.42}$$

19
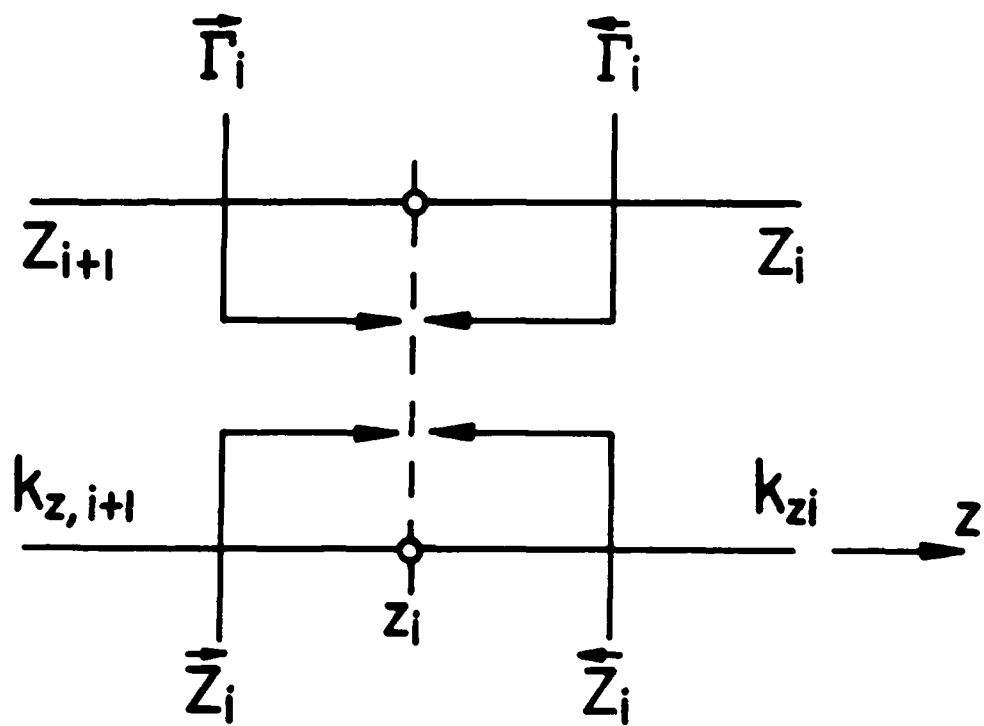
Figure 3.3: Reflection coefficients and impedances associated with the ith interface.
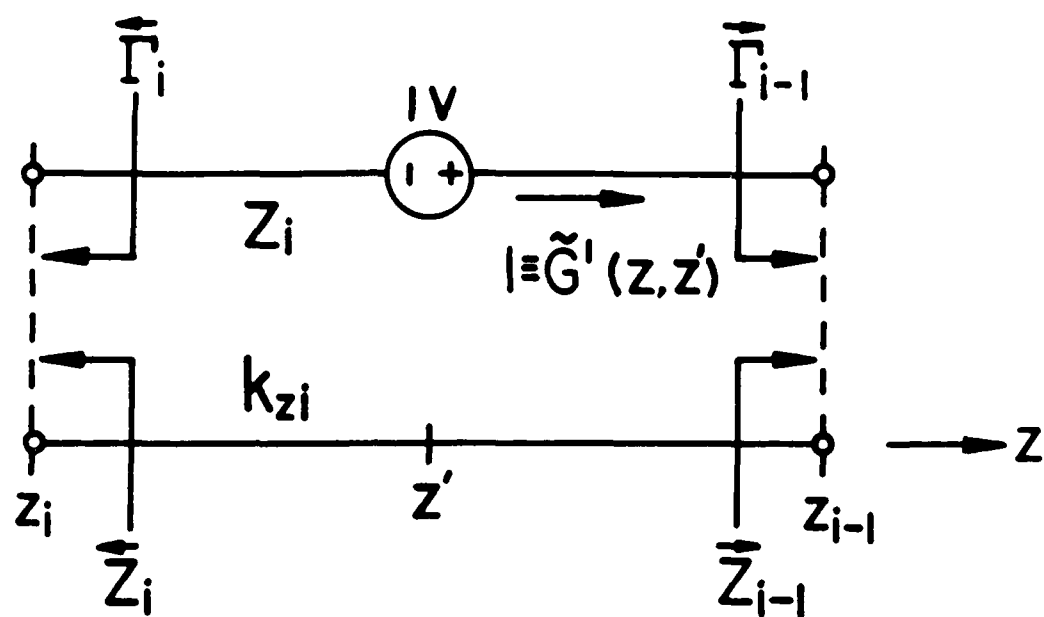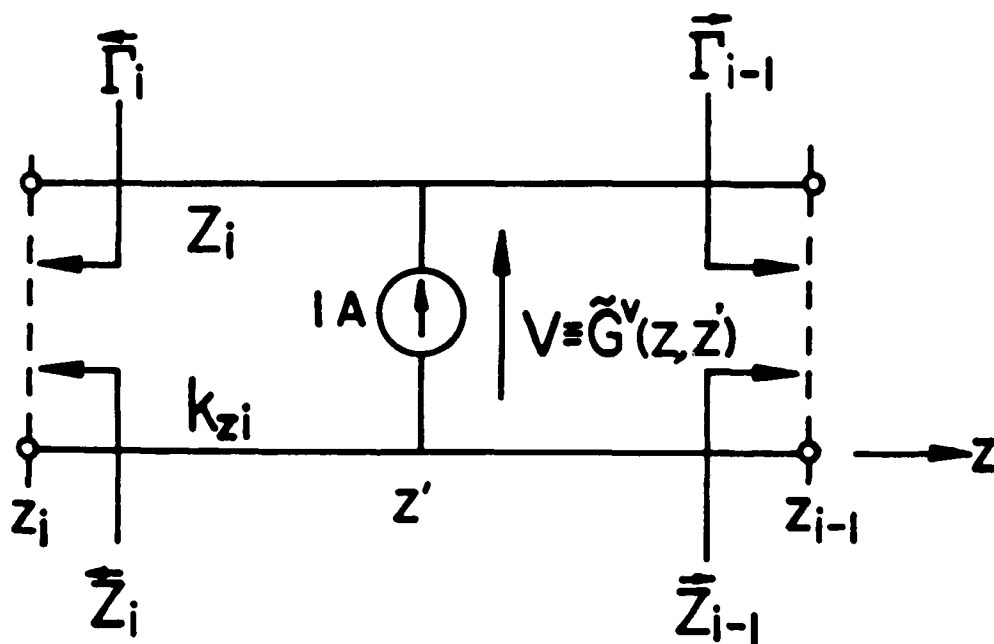
Figure 3.4: (a) Voltage source and (b) current source in the ith transmission-line section.

Equations (3.40)–(3.42) can be represented by the network shown in Fig. 3.4a.

In a like manner, if we denote the voltage V in the ith line section due to the point current $i = -\delta(z - z')$ in the same section as $\widetilde{G}_{ii}^V$, we obtain from (3.36)

$$\left(\frac{d^2}{dz^2} + k_{zi}^2\right)\widetilde{G}_{ii}^V(z, z') = -jk_{zi}Z_i\delta(z - z').$$

(3.43)

The boundary conditions in this case are (cf. (3.38) and (3.39))

$$\overleftarrow{Y}_i = \frac{Y_i}{jk_{zi}}\frac{d}{dz}\ln\widetilde{G}_{ii}^I(z, z'), \quad z = z_i$$

(3.44)

$$\overrightarrow{Y}_{i-1} = -\frac{Y_i}{jk_{zi}}\frac{d}{dz}\ln\widetilde{G}_{ii}^I(z, z'), \quad z = z_{i-1}.$$

(3.45)

Equations (3.43)–(3.45) have the network representation shown in Fig. 3.4b.

We first turn attention to (3.43); the solution of (3.40) will follow by duality. Hence, solving (3.43) subject to the boundary conditions in (3.44) and (3.45), we obtain

$$\widetilde{G}_{ii}^V(z, z') = \frac{Z_i}{2}\left[e^{-jk_{zi}|z-z'|} + \widetilde{Q}_i^V(z, z')\right]$$

(3.46)

with

$$\widetilde{Q}_i^V(z, z') = \frac{1}{D_i}\left\{\overleftarrow{\Gamma}_i e^{-jk_{zi}[(z+z')-2z_i]} + \overrightarrow{\Gamma}_{i-1}e^{-jk_{zi}[2z_{i-1}-(z+z')]}\right.$$

$$\left. +2\overleftarrow{\Gamma}_i\overrightarrow{\Gamma}_{i-1}e^{-j2\psi_i}\cos\left[k_{zi}(z - z')\right]\right\}$$

(3.47)

$$D_i = 1 - \overleftarrow{\Gamma}_i\overrightarrow{\Gamma}_{i-1}e^{-j2\psi_i}$$

(3.48)

where $\psi_i = k_{zi}d_i$, $d_i = z_{i-1} - z_i$. The reflection coefficients $\overrightarrow{\Gamma}_k$ and $\overleftarrow{\Gamma}_k$ (see Fig. 3.3) are given by, respectively,

$$\overrightarrow{\Gamma}_k = \frac{\overrightarrow{Z}_k - Z_{k+1}}{\overrightarrow{Z}_k + Z_{k+1}}, \quad k = 1, 2, \cdots, n$$

(3.49)

and

$$\overleftarrow{\Gamma}_k = \frac{\overleftarrow{Z}_k - Z_k}{\overleftarrow{Z}_k + Z_k}, \quad k = 1, 2, \cdots, n$$

(3.50)

where $\overrightarrow{\Gamma}_0 \equiv 0 \equiv \overleftarrow{\Gamma}_{n+1}$.

The yet unspecified impedances $\overrightarrow{Z}_k$ and $\overleftarrow{Z}_k$ can be obtained from the analysis of the transmission-line network of Fig. 3.1b. It can be shown that these impedances are given by the recursion formulas

$$\overrightarrow{Z}_k = Z_k \frac{\overrightarrow{Z}_{k-1} + jZ_k t_k}{Z_k + j\overrightarrow{Z}_{k-1} t_k}, \quad k = 2, 3, \cdots, n \tag{3.51}$$

and

$$\overleftarrow{Z}_k = Z_{k+1} \frac{\overleftarrow{Z}_{k+1} + jZ_{k+1} t_{k+1}}{Z_{k+1} + j\overleftarrow{Z}_{k+1} t_{k+1}}, \quad k = n-1, n-2, \cdots, 1 \tag{3.52}$$

where $\overrightarrow{Z}_1 \equiv Z_1$, $\overleftarrow{Z}_n \equiv Z_{n+1}$, and $t_k = \tan \psi_k$.

From (3.46), one can compute the voltage anywhere in the ith line section, including the terminals, due to a unit current source in the same section (*cf.* Fig. 3.4b). The voltage in any other, say mth section due to this source can be easily determined from the analysis of the transmission-line network of Fig. 3.1b as

$$\tilde{G}^V_{mi}(z, z') = \begin{cases} \tilde{G}^V_{ii}(z_{i-1}, z') \overrightarrow{T}^V_{mi}(z), & i-1 \geq m \geq 1 \\[2ex] \tilde{G}^V_{ii}(z_i, z') \overleftarrow{T}^V_{mi}(z), & n+1 \geq m \geq i+1 \end{cases} \tag{3.53}$$

where the voltage transfer functions $\overrightarrow{T}^V_{mi}$ and $\overleftarrow{T}^V_{mi}$ are given, respectively, as

$$\overrightarrow{T}^V_{mi}(z) = \frac{e^{-jk_{zm}(z-z_m)}}{1 + \overrightarrow{\Gamma}_{m-1} e^{-j2\psi_m}} \left\{ 1 + \overrightarrow{\Gamma}_{m-1} e^{-j2k_{zm}(z_{m-1}-z)} \right\} \cdot \prod_{k=m}^{i-2} \frac{\left(1 + \overrightarrow{\Gamma}_k\right) e^{-j\psi_{k+1}}}{1 + \overrightarrow{\Gamma}_k e^{-j2\psi_{k+1}}} \tag{3.54}$$

and

$$\overleftarrow{T}^V_{mi}(z) = \frac{e^{-jk_{zm}(z_{m-1}-z)}}{1 + \overleftarrow{\Gamma}_m e^{j2\psi_m}} \left\{ 1 + \overleftarrow{\Gamma}_m e^{-j2k_{zm}(z-z_m)} \right\} \cdot \prod_{k=i+1}^{m-1} \frac{\left(1 + \overleftarrow{\Gamma}_k\right) e^{-j\psi_k}}{1 + \overleftarrow{\Gamma}_k e^{-j2\psi_k}}. \tag{3.55}$$

This completes the solution of (3.43). Equation (3.40) can be solved by a dual procedure. However, this is not necessary: we can obtain $\tilde{G}^I_{mi}$ from $\tilde{G}^V_{mi}$ by replacing in the latter all impedances Z_i by their reciprocals Y_i (as a result of this operation, all reflection coefficients change signs, as is evident from (3.49)–(3.50)). The functions $\tilde{G}^I_{mi}$ and $\tilde{G}^V_{mi}$ will be referred to, respectively, as the current and voltage transmission-line Green's functions.

3.3 Derivation of Dyadic Green's Functions for the Magnetic Vector Potential in a Plane-Stratified Medium

The magnetic vector potential $\boldsymbol{A}^{mi}$ in the mth layer of the stratified medium (Fig. 3.1a) due to a current distribution $\boldsymbol{J}$ occupying a volume V_i in the ith layer can be obtained from

$$A^{mi}(r) = \int_{V_i} \underline{\underline{G}}_A^{mi}(r \mid r') \cdot J(r') \, dV' \tag{3.56}$$

where $\underline{\underline{G}}_A^{mi}$ is the dyadic Green's function for the magnetic vector potential, which can be expressed either in the traditional form (2.7), or the alternative form (2.8). To determine the elements of the dyadic in (3.56), we appeal to the transmission-line analogy and make use of the transmission-line Green's functions developed in Sections 3.1 and 3.2. Hence, from (3.29) and (3.31) we determine that an x-directed dipole with $\tilde{J} \equiv \tilde{J}_t = \hat{x}\delta(z - z')$ gives rise to transmission-line sources i^e and i^h given, respectively, as

$$i^e(z) = -\frac{jk_x}{k_\rho^2}\delta(z - z') \tag{3.57}$$

and

$$i^h(z) = -\frac{jk_y}{k_\rho^2}\delta(z - z') \tag{3.58}$$

where we assume that the sources are in the ith layer, *i.e.*, $z_i < z' < z_{i-1}$. Obviously, both the TM and TE transmission-line networks are excited in this case. The current generators given by (3.57) and (3.58) excite, respectively, the voltages V_{mi}^e and V_{mi}^h in the mth sections of the transmission-line network. From Section 3.2, we find

$$V_{mi}^e(z) = \frac{jk_x}{k_\rho^2}\tilde{G}_{mi}^{V_e}(z, z') \tag{3.59}$$

and

$$V_{mi}^h(z) = \frac{jk_y}{k_\rho^2}\tilde{G}_{mi}^{V_h}(z, z'). \tag{3.60}$$

For a y-directed dipole with $\tilde{J} \equiv \tilde{J}_t = \hat{y}\delta(z - z')$, (3.29) and (3.31) yield

$$i^e(z) = -\frac{jk_y}{k_\rho^2}\delta(z - z') \tag{3.61}$$

$$i^h(z) = +\frac{jk_x}{k_\rho^2}\delta(z - z'). \tag{3.62}$$

These sources excite the voltages (*cf.* Section 3.2)

$$V_{mi}^e(z) = \frac{jk_y}{k_\rho^2}\tilde{G}_{mi}^{V_e}(z, z') \tag{3.63}$$

and

24

$$V_{mi}^h(z) = -\frac{jk_x}{k_\rho{}^2}\tilde{G}_{mi}^{V_h}(z, z') \tag{3.64}$$

respectively.

Finally, for a vertical dipole with $\tilde{\boldsymbol{J}} \equiv \hat{\boldsymbol{z}}\tilde{J}_z = \hat{\boldsymbol{z}}\delta(z - z')$, we obtain from (3.28)

$$v^e(z) = -\frac{1}{j\omega\epsilon_i}\delta(z - z'). \tag{3.65}$$

Hence, only the TM transmission-line network is excited in this case. The current I_{mi}^e in the mth section due to the voltage source give in (3.65) is easily found as ($cf.$ Section 3.2)

$$I_{mi}^e(z) = \frac{1}{j\omega\epsilon_i}\tilde{G}_{mi}^{I_e}(z, z'). \tag{3.66}$$

We now must relate these transmission-line voltages and currents to the components of the magnetic vector potential. First, we turn our attention to a vertical dipole source, which gives rise to only the z-component of the vector potential. Outside the source ($z \neq z'$), the z-component of the electric field can be expressed in terms of $\tilde{A}_z^{mi}$ as

$$\tilde{E}_z^{mi} = -\frac{j\omega}{k_m^2}(\frac{d^2}{dz^2} + k_m^2)\tilde{A}_z^{mi} = -\frac{j\omega}{k_m^2}k_\rho{}^2\tilde{A}_z^{mi}. \tag{3.67}$$

On the other hand, from (3.22) we have

$$\tilde{E}_z^{mi} = \frac{1}{j\omega\epsilon_m}k_\rho{}^2 I_m^e. \tag{3.68}$$

Eliminating $\tilde{E}_z^{mi}$ between (3.67) and (3.68), we obtain

$$\tilde{A}_z^{mi} = \mu_m I_{mi}^e. \tag{3.69}$$

It can be shown that this solution also holds in the source region ($z = z'$). If the current I_{mi}^e in (3.69) is that generated by a z-directed dipole, then $\tilde{A}_z^{mi} = \tilde{G}_{zz}^{mi}$. Hence, substituting from (3.66) into (3.69), we obtain

$$\hat{G}_{zz}^{mi} = \frac{1}{j\omega}\frac{\mu_m}{\epsilon_i}\tilde{G}_{mi}^{I_e}. \tag{3.70}$$

The horizontal (x- or y- directed) dipole source may give rise to all components of $\widetilde{\boldsymbol{A}}^{mi}$, $i.e.$, $\widetilde{\boldsymbol{A}}^{mi} = \hat{\boldsymbol{x}}\tilde{A}_x^{mi} + \hat{\boldsymbol{y}}\tilde{A}_y^{mi} + \hat{\boldsymbol{z}}\tilde{A}_z^{mi}$. The transverse electric field components can be expressed as

$$\tilde{E}_x^{mi} = -\frac{j\omega}{k_m^2}\left[(k_m^2 - k_x^2)\tilde{A}_x^{mi} - k_x k_y \tilde{A}_y^{mi} - jk_x\frac{\partial}{\partial z}\tilde{A}_z^{mi}\right] \tag{3.71}$$

25

$$\tilde{E}_y^{mi} = -\frac{j\omega}{k_m^2}\left[-k_x k_y \tilde{A}_x^{mi} + (k_m^2 - k_y^2)\tilde{A}_y^{mi} - jk_y\frac{\partial}{\partial z}\tilde{A}_z^{mi}\right].$$ (3.72)

On the other hand, from (3.20) we find

$$\tilde{E}_x^{mi} = jk_x V_{mi}^e + jk_y V_{mi}^h$$ (3.73)

$$\tilde{E}_y^{mi} = jk_y V_{mi}^e - jk_x V_{mi}^h.$$ (3.74)

Eliminating $\tilde{E}_x^{mi}$ and $\tilde{E}_y^{mi}$ from (3.71)–(3.74), we have two independent equations and three unknown components of $\overline{\tilde{A}}^{mi}$. Therefore, the solution of these equations is not unique, and one of the components of the vector potential can be set to zero.

3.3.1 Traditional Form of the Green's Function

In the traditional approach [16], it is postulated that an x-directed current dipole generates the x and z components of the vector potential. Hence, eliminating $\tilde{E}_x^{mi}$ and $\tilde{E}_y^{mi}$ from (3.71)–(3.74), and letting $\tilde{A}_y^{mi} = 0$, we obtain

$$\tilde{A}_x^{mi} = -\frac{k_\rho^2}{\omega k_y}V_{mi}^h$$ (3.75)

$$\frac{\partial}{\partial z}\tilde{A}_z^{mi} = \frac{1}{j\omega}\left[k_m^2 V_{mi}^e - \frac{k_x}{k_y}k_{zm}^2 V_{mi}^h\right].$$ (3.76)

Substituting (3.59) and (3.60) into (3.75) and (3.76), we have

$$\tilde{G}_{xx}^{mi} = \frac{1}{j\omega}\tilde{G}_{mi}^{V_h}$$ (3.77)

and

$$\frac{\partial}{\partial z}\tilde{G}_{zx}^{mi} = \frac{k_x}{\omega k_\rho^2}\left[k_m^2 \tilde{G}_{mi}^{V_e} - k_{zm}^2 \tilde{G}_{mi}^{V_h}\right],$$ (3.78)

from which we obtain

$$\tilde{G}_{zx}^{mi} = -\frac{k_x}{\omega k_\rho^2}\left[\frac{k_m^2}{k_{zm}^2}\frac{\partial}{\partial z}\tilde{G}_{mi}^{V_e} - \frac{\partial}{\partial z}\tilde{G}_{mi}^{V_h}\right].$$ (3.79)

Similarly, we assume that the y-directed current dipole generates the y and z components of the vector potential. Changing x to y and k_x to k_y in (3.77) and (3.79), we obtain

$$\tilde{G}_{yy}^{mi} = \tilde{G}_{xx}^{mi} = \frac{1}{j\omega}\tilde{G}_{mi}^{V_h}$$ (3.80)

26

$$\tilde{G}_{zy}^{mi} = -\frac{k_y}{\omega k_\rho^2}\left[\frac{k_m^2}{k_{zm}^2}\frac{\partial}{\partial z}\tilde{G}_{mi}^{V_e} - \frac{\partial}{\partial z}\tilde{G}_{mi}^{V_h}\right].\tag{3.81}$$

Thus, the elements of the dyadic (2.7) have been obtained in the Fourier transform domain. By using the relationships given in (3.8)–(3.13), one can express the space domain counterparts of (3.70) and (3.77)–(3.81) as

$$G_{xx}^{mi} = G_{yy}^{mi} = \frac{1}{2\pi j\omega}S_0\left[\tilde{G}_{mi}^{V_h}\right]\tag{3.82}$$

$$G_{zx}^{mi} = -\frac{1}{2\pi j\omega}\cos\zeta\, S_1\left[\frac{1}{k_\rho^2}\left(\frac{k_m^2}{k_{zm}^2}\frac{\partial}{\partial z}\tilde{G}_{mi}^{V_e} - \frac{\partial}{\partial z}\tilde{G}_{mi}^{V_h}\right)\right]\tag{3.83}$$

$$G_{zy}^{mi} = \tan\zeta\, G_{zx}^{mi}\tag{3.84}$$

and

$$G_{zz}^{mi} = \frac{1}{2\pi j\omega}\frac{\mu_m}{\epsilon_i}S_0\left[\tilde{G}_{mi}^{I_e}\right].\tag{3.85}$$

3.3.2 Alternative Form of the Green's Function

Taking an alternative approach [15], we suppose that a horizontal (x- or y- directed) dipole source gives rise to x and y components of $\widetilde{\boldsymbol{A}}^{mi}$. Eliminating $\tilde{E}_x^{mi}$ and $\tilde{E}_y^{mi}$ from (3.71)–(3.74), and letting $\tilde{A}_z^{mi} = 0$, we obtain

$$\tilde{A}_x^{mi} = -\frac{1}{j\omega}\left(\frac{k_m^2}{k_{zm}^2}jk_x V_{mi}^e - jk_y V_{mi}^h\right)\tag{3.86}$$

$$\tilde{A}_y^{mi} = -\frac{1}{j\omega}\left(\frac{k_m^2}{k_{zm}^2}jk_y V_{mi}^e - jk_x V_{mi}^h\right).\tag{3.87}$$

If the voltages V_{mi}^e and V_{mi}^h in (3.73) and (3.74) are those generated by an x-directed dipole, then $\tilde{A}_x^{mi} \equiv \tilde{G}_{xx}^{mi}$ and $\tilde{A}_y^{mi} \equiv \tilde{G}_{yx}^{mi}$. Hence, substituting from (3.59) and (3.60) into (3.86) and (3.87), we obtain

$$\tilde{G}_{xx}^{mi} = \frac{1}{j\omega}\left(\frac{k_m^2 k_x^2}{k_{zm}^2 k_\rho^2}\tilde{G}_{mi}^{V_e} + \frac{k_y^2}{k_\rho^2}\tilde{G}_{mi}^{V_h}\right)\tag{3.88}$$

$$\tilde{G}_{yx}^{mi} = \frac{k_x k_y}{j\omega k_\rho^2}\left(\frac{k_m^2}{k_{zm}^2}\tilde{G}_{mi}^{V_e} - \tilde{G}_{mi}^{V_h}\right).\tag{3.89}$$

Similarly, substituting from (3.63) and (3.64) into (3.86) and (3.87), we obtain

27

$$\tilde{G}^{mi}_{xy} \equiv \tilde{G}^{mi}_{yx} \tag{3.90}$$

and

$$\tilde{G}^{mi}_{yy} = \frac{1}{j\omega} \left(\frac{k_m^2 k_y^2}{k_{zm}^2 k_\rho^2} \tilde{G}^{V_e}_{mi} + \frac{k_x^2}{k_\rho^2} \tilde{G}^{V_h}_{mi} \right). \tag{3.91}$$

That $\tilde{G}^{mi}_{xy} = \tilde{G}^{mi}_{yx}$ was already anticipated in (2.8).

Thus, we have obtained the elements of (2.8) in the Fourier transform domain. Upon using (3.79)–(3.13), they can be expressed in the space domain as

$$G^{mi}_{xx} = \frac{1}{4\pi j\omega} \left\{ S_0 \left[\frac{k_m^2}{k_{zm}^2} \tilde{G}^{V_e}_{mi} + \tilde{G}^{V_h}_{mi} \right] - \cos\zeta\, S_2 \left[\frac{1}{k_\rho^2} \left(\frac{k_m^2}{k_{zm}^2} \tilde{G}^{V_e}_{mi} - \tilde{G}^{V_h}_{mi} \right) \right] \right\} \tag{3.92}$$

$$G^{mi}_{yy} = \frac{1}{4\pi j\omega} \left\{ S_0 \left[\frac{k_m^2}{k_{zm}^2} \tilde{G}^{V_e}_{mi} + \tilde{G}^{V_h}_{mi} \right] + \cos\zeta\, S_2 \left[\frac{1}{k_\rho^2} \left(\frac{k_m^2}{k_{zm}^2} \tilde{G}^{V_e}_{mi} - \tilde{G}^{V_h}_{mi} \right) \right] \right\} \tag{3.93}$$

$$G^{mi}_{xy} = G^{mi}_{yx} = -\frac{1}{4\pi j\omega} \sin 2\zeta\, S_2 \left[\frac{1}{k_\rho^2} \left(\frac{k_m^2}{k_{zm}^2} \tilde{G}^{V_e}_{mi} - \tilde{G}^{V_h}_{mi} \right) \right] \tag{3.94}$$

with G^{mi}_{zz} given by (3.85).

3.4 Electric Field in the Layered Medium due to a Plane Wave Incident in Region 1

Consider an incident plane wave in region 1, given as

$$\boldsymbol{E}^i(\boldsymbol{r}) = \left(E_\theta\, \hat{\boldsymbol{\theta}}_1 + E_\varphi\, \hat{\boldsymbol{\varphi}}_1 \right) e^{j\boldsymbol{k}_1 \cdot \boldsymbol{r}} \tag{3.95}$$

where the propagation vector $\boldsymbol{k}_1$ is

$$\boldsymbol{k}_1 = k_1 \left(\sin\theta_1 \cos\varphi_1\, \hat{\boldsymbol{x}} + \sin\theta_1 \sin\varphi_1\, \hat{\boldsymbol{y}} + \cos\theta_1\, \hat{\boldsymbol{z}} \right) \tag{3.96}$$

and $(\hat{\boldsymbol{\theta}}_1, \hat{\boldsymbol{\varphi}}_1)$ define the angle of arrival of the plane wave in terms of the usual spherical coordinate convention. We can utilize the analysis in Sections 3.1–3.3 to obtain the total "incident" electric field in the mth layer due to the plane wave given in (3.95). We easily find that the incident field in the top layer ($m = 1$) is given as

$$\boldsymbol{E}^{inc}_1(\boldsymbol{r}) = \left\{ \hat{\boldsymbol{x}} \left[-E_\varphi \sin\varphi_1 \left(1 + \overleftarrow{\Gamma}^h_1 e^{-j2k_1 \cos\theta_1 (z-z_1)} \right) \right.\right.$$
$$\left.\left. + E_\theta \cos\varphi_1 \cos\theta_1 \left(1 + \overleftarrow{\Gamma}^e_1 e^{-j2k_1 \cos\theta_1 (z-z_1)} \right) \right] \right.$$

$$+\hat{\boldsymbol{y}}\left[E_\varphi \cos\varphi_1 \left(1 + \overleftarrow{\Gamma}_1^h e^{-j2k_1\cos\theta_1(z-z_1)}\right)\right.$$

$$\left.+E_\theta \sin\varphi_1 \cos\theta_1 \left(1 + \overleftarrow{\Gamma}_1^e e^{-j2k_1\cos\theta_1(z-z_1)}\right)\right]$$

$$-\hat{\boldsymbol{z}}E_\theta \sin\theta_1 \left(1 - \overleftarrow{\Gamma}_1^e e^{-j2k_1\cos\theta_1(z-z_1)}\right)\Bigg\} e^{jk_1[\sin\theta_1(\cos\varphi_1 x + \sin\varphi_1 y) + \cos\theta_1 z]} \quad (3.97)$$

and the field in other layers $(m \neq 1)$ as

$$\boldsymbol{E}_m^{inc}(\boldsymbol{r}) = \left\{ \hat{\boldsymbol{x}}\left[-E_\varphi \sin\varphi_1 \left(1 + \overleftarrow{\Gamma}_1^h\right) \overleftarrow{T}_{m1}^{V_h}(z)\right.\right.$$

$$\left.+E_\theta \cos\varphi_1 \frac{1}{\eta_1}\overleftarrow{Z}_1^e \left(1 - \overleftarrow{\Gamma}_1^e\right) \overleftarrow{T}_{m1}^{V_e}(z)\right]$$

$$+\hat{\boldsymbol{y}}\left[E_\varphi \cos\varphi_1 \left(1 + \overleftarrow{\Gamma}_1^h\right) \overleftarrow{T}_{m1}^{V_h}(z) + E_\theta \sin\varphi_1 \frac{1}{\eta_1}\overleftarrow{Z}_1^e \left(1 - \overleftarrow{\Gamma}_1^e\right) \overleftarrow{T}_{m1}^{V_e}(z)\right]$$

$$-\hat{\boldsymbol{z}}E_\theta \frac{\eta_m}{\eta_1} \sin\theta_m \left(1 - \overleftarrow{\Gamma}_1^e\right) \overleftarrow{T}_{m1}^{I_e}(z)\right\} e^{jk_m(\cos\varphi_1\sin\theta_m x + \sin\varphi_1\sin\theta_m y + \cos\theta_m z)} \quad (3.98)$$

where $\overleftarrow{Z}_1^e$, $\overleftarrow{\Gamma}_1$, and $\overleftarrow{T}_{m1}$ are given in Section 3.2, with $k_{zm} = k_m \cos\theta_m$, where θ_m can be obtained from the Snell's law, $k_1 \sin\theta_1 = k_m \sin\theta_m$. In (3.98), $\eta_m = \sqrt{\mu_m/\epsilon_m}$ is the intrinsic impedance of the dielectric of region m.

Chapter 4

Formulation of the Mixed-Potential Electric Field Integral Equation

As mentioned in Chapter 2, the decomposition embodied in (2.13) is non-unique, which means that an infinite number of different MPIEs is possible. We observe, however, by referring to (2.16), that the presence of the "correction" function $\boldsymbol{P}^{mi}$ has the undesirable effect of introducing new elements in the dyadic kernel $\underline{\underline{K}}_A^{mi}$, in addition to those already present in $\underline{\underline{G}}_A^{mi}$. Ideally, of course, $\boldsymbol{P}^{mi}$ should be zero, which – unfortunately – is only possible in a few special cases [15]. Hence, the best one can do is to develop MPIEs for which one or two of the components of $\boldsymbol{P}^{mi}$ are zero. It is shown below that for the vector potential Green's functions (2.7) and (2.8) the x and y components of $\boldsymbol{P}^{mi}$ are not independent, thus leaving us, for each $\underline{\underline{G}}_A^{mi}$, with only two degrees of freedom: either $P_x^{mi} = P_y^{mi} = 0$ and $P_z^{mi} \neq 0$, or $P_x^{mi} \neq 0$, $P_y^{mi} \neq 0$, and $P_z^{mi} = 0$. Of the four possible "minimal" formulations, only three lead to distinct MPIEs. These three are discussed in detail below, where they are referred to as Formulations A, B, and C. Most of our derivations are done in the Fourier transform domain defined in (3.1) and (3.2), which greatly simplifies the algebra.

4.1 Formulation A

In this formulation, we employ the alternative form of $\underline{\underline{G}}_A^{mi}$ given in (2.8). In the Fourier transform domain, the x, y, and z components of (2.13) become

$$\frac{j\omega}{k_m^2}\left(-jk_x\widetilde{G}_{xx}^{mi} - jk_y\widetilde{G}_{xy}^{mi}\right) = \frac{1}{j\omega}jk_x\widetilde{K}_\phi^{mi} + j\omega\widetilde{P}_x^{mi} \tag{4.1}$$

$$\frac{j\omega}{k_m^2}\left(-jk_x\widetilde{G}_{xy}^{mi} - jk_y\widetilde{G}_{yy}^{mi}\right) = \frac{1}{j\omega}jk_y\widetilde{K}_\phi^{mi} + j\omega\widetilde{P}_y^{mi} \tag{4.2}$$

$$\frac{j\omega}{k_m^2}\frac{\partial}{\partial z}\tilde{G}_{zz}^{mi} = \frac{1}{j\omega}\frac{\partial}{\partial z'}\widetilde{K}_\phi^{mi} + j\omega\tilde{P}_z^{mi}. \tag{4.3}$$

Using (3.88) through (3.91) in (4.1) and (4.2), one finds that $\tilde{P}_x^{mi}$ and $\tilde{P}_y^{mi}$ are related by

$$\tilde{P}_y^{mi} = \frac{k_y}{k_x}\tilde{P}_x^{mi}. \tag{4.4}$$

In Formulation A, we choose $\tilde{P}_x^{mi} = P_y^{ni} = 0$, in which case K_ϕ^{mi} can be interpreted as the scalar potential of a point charge associated with a horizontal dipole [15]. Solving (4.1) or (4.2) for $\widetilde{K}_\phi^{mi}$, one obtains

$$\widetilde{K}_\phi^{mi} = -j\omega\frac{\tilde{G}_{mi}^{V_e}}{k_{zm}^2} \tag{4.5}$$

which can be substituted into (4.3) to yield

$$\hat{P}_z^{mi} = \frac{\mu_i\epsilon_i - \mu_m\epsilon_m}{\epsilon_i k_{zm}^2}\tilde{I}_{mi}^{V_e} \tag{4.6}$$

where we have introduced for later convenience

$$\tilde{I}_{mi}^{V_q} = \begin{cases} \overrightarrow{Z}_{i-1}^q\tilde{G}_{ii}^{I_q}(z_{i-1}, z')\overrightarrow{T}_{mi}^{V_q}(z), & i-1 \geq m \geq 1 \\[2ex] -\overleftarrow{Z}_i^q\tilde{G}_{ii}^{I_q}(z_i, z')\overleftarrow{T}_{mi}^{V_q}(z), & n+1 \geq m > i+1 \end{cases} \tag{4.7}$$

in which the superscript "q" stands for "e" or "h." Observe that $\tilde{P}_z^{mi} \equiv 0$ when $m = i$, i.e., when the source and observation points are within the same layer.

Substituting (3.70), (3.88)–(3.91) and (4.6) into the Fourier domain counterpart of (2.16), and using the relations given in (3.8)–(3.13), one obtains the dyadic kernel

$$\underline{\underline{K}}_A^{mi}(r\,|\,r') = \hat{x}\,\hat{x}K_{xx}^{mi} + \hat{y}\,\hat{y}K_{yy}^{mi} + \hat{z}\,\hat{z}K_{zz}^{mi}$$
$$+(\hat{x}\,\hat{y} + \hat{y}\,\hat{x})K_{xy}^{mi} + \hat{x}\,\hat{z}K_{xz}^{mi} + \hat{y}\,\hat{z}K_{yz}^{mi} \tag{4.8}$$

with the elements given by

$$K_{xx}^{mi} = G_{xx}^{mi} = \frac{1}{4\pi j\omega}\left\{k_m^2 S_0\left(\frac{1}{k_{zm}^2}\tilde{G}_{mi}^{V_e}\right) + S_0\left(\tilde{G}_{mi}^{V_h}\right)\right.$$
$$\left. + \cos 2\zeta\, S_2\left[\frac{1}{k_\rho^2}\left(\tilde{G}_{mi}^{V_h} - \frac{k_m^2}{k_{zm}^2}\tilde{G}_{mi}^{V_e}\right)\right]\right\} \tag{4.9}$$

$$K_{yy}^{mi} = G_{yy}^{mi} = \frac{1}{4\pi j\omega}\left\{k_m^2 S_0\left(\frac{1}{k_{zm}^2}\tilde{G}_{mi}^{V_e}\right) + S_0\left(\tilde{G}_{mi}^{V_h}\right)\right.$$
$$\left. - \cos 2\zeta\, S_2\left[\frac{1}{k_\rho^2}\left(\tilde{G}_{mi}^{V_h} - \frac{k_m^2}{k_{zm}^2}\tilde{G}_{mi}^{V_e}\right)\right]\right\} \tag{4.10}$$

31

$$K_{xy}^{mi} = G_{xy}^{mi} = \frac{1}{4\pi j\omega} \sin 2\zeta \, S_2 \left[\frac{1}{k_\rho^{\,2}} \left(\widetilde{G}_{mi}^{V_h} - \frac{k_m^2}{k_{zm}^2} \widetilde{G}_{mi}^{V_e} \right) \right] \tag{4.11}$$

$$K_{xz}^{mi} = \frac{\partial}{\partial x} P_z^{mi} = -\frac{\cos \zeta}{2\pi} S_1 \left(\widetilde{P}_z^{mi} \right) \tag{4.12}$$

$$K_{yz}^{mi} = \frac{\partial}{\partial y} P_z^{mi} = -\frac{\sin \zeta}{2\pi} S_1 \left(\widetilde{P}_z^{mi} \right) \tag{4.13}$$

$$K_{zz}^{mi} = G_{zz}^{mi} + \frac{\partial}{\partial z} P_z^{mi} = \frac{\mu_i}{2\pi j\omega\epsilon_m} S_0 \left(\widetilde{G}_{mi}^{I_e} \right) . \tag{4.14}$$

Finally, the Fourier inversion of $\widetilde{K}_\phi^{mi}$ in (4.5) yields the scalar potential kernel

$$K_\phi^{mi} = -\frac{j\omega}{2\pi} S_0 \left(\frac{\widetilde{G}_{mi}^{V_e}}{k_{zm}^2} \right) . \tag{4.15}$$

We observe from (4.9) through (4.15) that in this formulation, when $m \neq i$, the effect of $\boldsymbol{\nabla} \boldsymbol{P}^{mi}$ in (2.16) is to introduce two new entries, K_{xz}^{mi} and K_{yz}^{mi}, and to modify G_{zz}^{mi}. However, when the object is confined to a single layer ($m = i$), we simply have $\underline{\underline{K}}_A^{mi} = \underline{\underline{G}}_A^{mi}$, so no modification of the Green's function is required.

A useful property of Formulation A is the cancellation of the contour integrals in (2.15), which is the result of the continuity with respect to the z' coordinate of the scalar potential kernel at the ith interface: $K_\phi^{mi}(z' = z_i + 0) = K_\phi^{m,i+1}(z' = z_i - 0)$. We note, however, that a continuity with respect to the z coordinate does not hold, i.e., $K_\phi^{mi}(z = z_m + 0) \neq K_\phi^{m+1,i}(z = z_m - 0)$.

4.2 Formulation B

In this formulation, as in Formulation A, we employ the alternative form (2.8) of $\underline{\underline{G}}_A^{mi}$. However, rather than choosing $\widetilde{P}_x^{mi} = \widetilde{P}_y^{mi} = 0$, we select $\widetilde{P}_z^{mi} = 0$ in (4.1) through (4.3). In this case K_ϕ^{mi} can be interpreted as the scalar potential of a point charge associated with a vertical dipole [15]. From (4.3) and (3.70), we find

$$\widetilde{K}_\phi^{mi} = -j\omega \frac{\widetilde{G}_{mi}^{V_e}}{k_{zi}^2} \tag{4.16}$$

which can be substituted into (4.1) to yield

$$\widetilde{P}_x^{mi} = \omega k_x \frac{\mu_m \epsilon_m - \mu_i \epsilon_i}{k_{zi}^2 k_{zm}^2} \widetilde{G}_{mi}^{V_e} \tag{4.17}$$

32

which, in view of (4.4), also specifies $\tilde{P}_y^{mi}$.

Referring to (2.16) and proceeding as in Formulation A, we obtain the dyadic kernel

$$
\begin{aligned}
\underline{\underline{K}}_A^{mi}(\boldsymbol{r} \mid \boldsymbol{r}') &= \hat{\boldsymbol{x}}\,\hat{\boldsymbol{x}} K_{xx}^{mi} + \hat{\boldsymbol{y}}\,\hat{\boldsymbol{y}} K_{yy}^{mi} + \hat{\boldsymbol{z}}\,\hat{\boldsymbol{z}} K_{zz}^{mi} \\
&\quad + (\hat{\boldsymbol{x}}\,\hat{\boldsymbol{y}} + \hat{\boldsymbol{y}}\,\hat{\boldsymbol{x}})\, K_{xy}^{mi} + \hat{\boldsymbol{z}}\,\hat{\boldsymbol{x}} K_{zx}^{mi} + \hat{\boldsymbol{z}}\,\hat{\boldsymbol{y}} K_{zy}^{mi}
\end{aligned}
\tag{4.18}
$$

with the elements given by

$$
\begin{aligned}
K_{xx}^{mi} = G_{xx}^{mi} + \frac{\partial}{\partial x} P_x^{mi} &= \frac{1}{4\pi j\omega}\left\{ k_i^2 S_0\left(\frac{1}{k_{zi}^2}\tilde{G}_{mi}^{V_e}\right) + S_0\left(\breve{G}_{mi}^{V_h}\right) \right. \\
&\quad \left. + \cos 2\zeta\, S_2\left[\frac{1}{k_\rho^{\,2}}\left(\tilde{G}_{mi}^{V_h} - \frac{k_i^2}{k_{zi}^2}\tilde{G}_{mi}^{V_e}\right)\right]\right\}
\end{aligned}
\tag{4.19}
$$

$$
\begin{aligned}
K_{yy}^{mi} = G_{yy}^{mi} + \frac{\partial}{\partial y} P_y^{mi} &= \frac{1}{4\pi j\omega}\left\{ k_i^2 S_0\left(\frac{1}{k_{zi}^2}\tilde{G}_{mi}^{V_e}\right) + S_0\left(\breve{G}_{mi}^{V_h}\right) \right. \\
&\quad \left. - \cos 2\zeta\, S_2\left[\frac{1}{k_\rho^{\,2}}\left(\tilde{G}_{mi}^{V_h} - \frac{k_i^2}{k_{zi}^2}\tilde{G}_{mi}^{V_e}\right)\right]\right\}
\end{aligned}
\tag{4.20}
$$

$$
K_{xy}^{mi} = G_{xy}^{mi} + \frac{\partial}{\partial x} P_y^{mi} = \frac{1}{4\pi j\omega}\sin 2\zeta\, S_2\left[\frac{1}{k_\rho^{\,2}}\left(\tilde{G}_{mi}^{V_h} - \frac{k_i^2}{k_{zi}^2}\tilde{G}_{mi}^{V_e}\right)\right]
\tag{4.21}
$$

$$
K_{zx}^{mi} = \frac{\partial}{\partial z} P_x^{mi} = \frac{\cos \zeta}{2\pi} S_1\left(\tilde{R}^{mi}\right)
\tag{4.22}
$$

$$
K_{zy}^{mi} = \frac{\partial}{\partial z} P_y^{mi} = \frac{\sin \zeta}{2\pi} S_1\left(\tilde{R}^{mi}\right)
\tag{4.23}
$$

$$
K_{zz}^{mi} = G_{zz}^{mi} = \frac{\mu_m}{2\pi j\omega\epsilon_i} S_0\left(\tilde{G}_{mi}^{I_e}\right)
\tag{4.24}
$$

where $\tilde{R}^{mi}$ is nonzero only for $m \neq i$ and is given by

$$
\tilde{R}^{mi} = \frac{\mu_i\epsilon_i - \mu_m\epsilon_m}{\epsilon_m k_{zi}^2}\tilde{I}_{mi}^{I_e}
\tag{4.25}
$$

in which $\tilde{I}_{mi}^{I_e}$ can be obtained from $\tilde{I}_{mi}^{V_e}$ given in (4.7) by replacing in the latter the characteristic impedances Z_i^e by their reciprocals.

Finally, the Fourier inversion of $\widetilde{K}_\phi^{mi}$ in (4.16) gives the scalar potential kernel

$$
K_\phi^{mi} = -\frac{j\omega}{2\pi} S_0\left(\frac{\tilde{G}_{mi}^{V_e}}{k_{zi}^2}\right).
\tag{4.26}
$$

We note that in Formulation B two new entries (K_{zx}^{mi} and K_{zy}^{mi}), not present in $\underline{\underline{G}}_A^{mi}$, are introduced to the dyadic kernel $\underline{\underline{K}}_A^{mi}$. Also, extra terms are added to G_{xx}^{mi}, G_{yy}^{mi}, and G_{xy}^{mi}. In the case where the object is confined to a single layer ($m = i$), $\underline{\underline{K}}_A^{mi} = \underline{\underline{G}}_A^{mi}$, and Formulation B becomes identical to Formulation A.

The continuity properties of the scalar potential kernel in Formulation B are complementary to those in Formulation A; that is, in the present case $K_\phi^{mi}(z' = z_i + 0) \neq K_\phi^{m,i+1}(z' = z_i - 0)$ and $K_\phi^{mi}(z = z_m + 0) = K_\phi^{m+1,i}(z = z_m - 0)$. As a result, the contour integrals in (2.15) do exist when the object penetrates one or more of the interfaces.

4.3   Formulation C

The point of departure in this formulation is the traditional form of $\underline{\underline{G}}_A^{mi}$ given in (2.7). Using it in (2.13), we obtain in the Fourier transform domain

$$\frac{j\omega}{k_m^2}\left(-jk_x\widetilde{G}_{xx}^{mi} + \frac{\partial}{\partial z}\widetilde{G}_{zx}^{mi}\right) = \frac{1}{j\omega}jk_x\widetilde{K}_\phi^{mi} + j\omega\widetilde{P}_x^{mi} \tag{4.27}$$

$$\frac{j\omega}{k_m^2}\left(-jk_y\widetilde{G}_{xx}^{mi} + \frac{\partial}{\partial z}\widetilde{G}_{zy}^{mi}\right) = \frac{1}{j\omega}jk_y\widetilde{K}_\phi^{mi} + j\omega\widetilde{P}_y^{mi} \tag{4.28}$$

$$\frac{j\omega}{k_m^2}\frac{\partial}{\partial z}\widetilde{G}_{zz}^{mi} = \frac{1}{j\omega}\frac{\partial}{\partial z'}\widetilde{K}_\phi^{mi} + j\omega\widetilde{P}_z^{mi}. \tag{4.29}$$

From (4.27) and (4.29), and referring to (3.79) through (3.81), we find that (4.4) still holds. Since G_{zz}^{mi} in the present case is the same as that in the "alternative" Green's function (2.8), specifying $\widetilde{P}_z^{mi} = 0$ results in an MPIE identical to that in Formulation B. We therefore set $\widetilde{P}_x^{mi} = \widetilde{P}_y^{mi} = 0$ in (4.27) and (4.28), which yields the scalar potential kernel

$$\widetilde{K}_\phi^{mi} = \frac{j\omega}{k_\rho^2}\left(\widetilde{G}_{mi}^{V_e} - \widetilde{G}_{mi}^{V_h}\right). \tag{4.30}$$

From the above and (4.29), there results

$$\widetilde{P}_z^{mi} = \frac{1}{j\omega}\left[\frac{\mu_m}{k_m^2\epsilon_i}\frac{\partial}{\partial z}\widetilde{G}_{mi}^{I_e} + \frac{1}{k_\rho^2}\frac{\partial}{\partial z'}\left(\widetilde{G}_{mi}^{V_h} - \widetilde{G}_{mi}^{V_e}\right)\right]. \tag{4.31}$$

Substituting (3.70), (3.79) through (3.81) and (4.31) into the Fourier domain counterpart of (2.16), and using the relations given in (3.8)–(3.13), we obtain the dyadic kernel

$$\begin{aligned}\underline{\underline{K}}_A^{mi}(\mathbf{r}\,|\,\mathbf{r}') = (\hat{\mathbf{x}}\,\hat{\mathbf{x}} + \hat{\mathbf{y}}\,\hat{\mathbf{y}})\,K_{xx}^{mi} + \hat{\mathbf{x}}\,\hat{\mathbf{z}}K_{xz}^{mi} + \hat{\mathbf{y}}\,\hat{\mathbf{z}}K_{yz}^{mi}\\
+\hat{\mathbf{z}}\,\hat{\mathbf{x}}K_{zx}^{mi} + \hat{\mathbf{z}}\,\hat{\mathbf{y}}K_{zy}^{mi} + \hat{\mathbf{z}}\,\hat{\mathbf{z}}K_{zz}^{mi}\end{aligned} \tag{4.32}$$

with the elements given by

$$K_{xx}^{mi} = G_{xx}^{mi} = \frac{1}{2\pi j\omega} S_0 \left(\widetilde{G}_{mi}^{V_h} \right) \tag{4.33}$$

$$K_{xz}^{mi} = \frac{\partial}{\partial x} P_z^{mi} = -\frac{\mu_i}{2\pi j\omega\epsilon_m} \cos\zeta\, S_1 \left[\frac{1}{k_\rho^2} \left(\widetilde{W}_{mi}^{V_e} - \frac{k_m^2}{k_{zm}^2} \widetilde{W}_{mi}^{V_h} \right) \right] \tag{4.34}$$

$$K_{yz}^{mi} = \frac{\partial}{\partial y} P_z^{mi} = -\frac{\mu_i}{2\pi j\omega\epsilon_m} \sin\zeta\, S_1 \left[\frac{1}{k_\rho^2} \left(\widetilde{W}_{mi}^{V_e} - \frac{k_m^2}{k_{zm}^2} \widetilde{W}_{mi}^{V_h} \right) \right] \tag{4.35}$$

$$K_{zx}^{mi} = G_{zx}^{mi} = -\frac{1}{2\pi j\omega} \cos\zeta\, S_1 \left[\frac{1}{k_\rho^2} \left(\frac{k_m^2}{k_{zm}^2} \widetilde{W}_{mi}^{I_e} - \widetilde{W}_{mi}^{I_h} \right) \right] \tag{4.36}$$

$$K_{zy}^{mi} = G_{zy}^{mi} = -\frac{1}{2\pi j\omega} \sin\zeta\, S_1 \left[\frac{1}{k_\rho^2} \left(\frac{k_m^2}{k_{zm}^2} \widetilde{W}_{mi}^{I_e} - \widetilde{W}_{mi}^{I_h} \right) \right] \tag{4.37}$$

$$K_{zz}^{mi} = G_{zz}^{mi} + \frac{\partial}{\partial z} P_z^{mi} = \frac{\mu_m}{2\pi j\omega\epsilon_i} S_0 \left[\widetilde{G}_{mi}^{I_e} - \frac{k_i^2}{k_\rho^2} \left(\frac{k_{zm}^2}{k_m^2} \widetilde{G}_{mi}^{I_e} - \widetilde{G}_{mi}^{I_h} \right) \right] \tag{4.38}$$

where we have introduced

$$\widetilde{W}_{ii}^{V} = \frac{jk_{zi}}{2Z_iD_i} \left\{ \overleftarrow{\Gamma}_i e^{-jk_{zi}[(z+z')-2z_i]} - \overrightarrow{\Gamma}_{i-1} e^{-jk_{zi}[2z_{i-1}-(z+z')]} \right.$$
$$\left. + 2j\overleftarrow{\Gamma}_i \overrightarrow{\Gamma}_{i-1} e^{-j2\psi_i} \sin\left[k_{zi}(z-z')\right] \right\}, \quad m = i \tag{4.39}$$

$$\widetilde{W}_{mi}^{V} = -\frac{jk_{zm}}{Z_m} \widetilde{I}_{mi}^{V}, \quad m \neq i \tag{4.40}$$

with $\widetilde{I}_{mi}^{V}$ given in (4.7). For notational simplicity, we have suppressed in (4.39) and (4.40) the superscripts "e" or "h". We note that one can obtain $\widetilde{W}_{mi}^{I}$ from $\widetilde{W}_{mi}^{V}$ by replacing in the latter the characteristic impedances Z_i by their reciprocals.

Finally, the Fourier inversion of (4.30) gives

$$K_\phi^{mi} = \frac{j\omega}{2\pi} S_0 \left[\frac{1}{k_\rho^2} \left(\widetilde{G}_{mi}^{V_e} - \widetilde{G}_{mi}^{V_h} \right) \right]. \tag{4.41}$$

As in Formulation A, this K_ϕ^{mi} may be interpreted as the scalar potential of a point charge associated with a horizontal dipole [15]. However, these two potentials are not identical, since each corresponds to a different form of the vector potential Green's function.

We observe from (4.33) through (4.38) that Formulation C introduces two new entries (K_{xz}^{mi} and K_{yz}^{mi}), not present in $\underline{\underline{G}}_A^{mi}$, to the dyadic kernel. Also, extra terms are added to G_{zz}^{mi}. In contrast to Formulations A and B, these modifications occur even if the object is confined to a single layer. As in Formulation A, the scalar potential kernel in the present case has the continuity property that $K_\phi^{mi}(z' = z_i + 0) = K_\phi^{m,i+1}(z' = z_i - 0)$, which causes the contour integrals in (2.15) to cancel. Formulation C also shares with Formulation B the useful property that $K_\phi^{mi}(z = z_m + 0) = K_\phi^{m+1,i}(z = z_m - 0)$.

35

4.4 Discussion

The properties of three MPIEs are summarized for easy reference in Table 4.1. Each of the three formulations, called A, B or C, can be derived from either the alternative or the traditional form of the dyadic Green's function for the vector potential. These two dyadics are shown in matrix form in the first column of Table 4.1. We note that Formulation A is derived from the alternative forms of $\underline{\underline{G}}_A^{mi}$, Formulation C from the traditional form, and Formulation B from either of the two (this is due to the fact that both forms of $\underline{\underline{G}}_A^{mi}$ share the same G_{zz}^{mi}). The distinguishing feature of each of the three formulations is the choice of the scalar potential kernel K_ϕ^{mi}, which also specifies the "correction" vector $\boldsymbol{P}^{mi}$ according to (2.13). Although, as the second column of Table 4.1 indicates, the scalar potential kernels in Formulations A and C are both associated with a horizontal dipole, they are different, because they correspond to different vector potential Green's functions. In Formulation B, K_ϕ^{mi} is that associated with a vertical dipole. Actually, by properly choosing K_ϕ^{mi}, one can also derive Formulation A from the traditional form of $\underline{\underline{G}}_A^{mi}$, and Formulation C from the alternative form.

The forms of the dyadic vector potential kernel are shown for each of the three formulations in the third column of Table 4.1. Comparing this column with column one, we observe that in all three formulations two new entries, in addition to those already present in $\underline{\underline{G}}_A^{mi}$, appear in $\underline{\underline{K}}_A^{mi}$, which is of course undesirable. We note, however (as indicated in the fourth column of Table 4.1), that in Formulations A and B the number of the entries in $\underline{\underline{K}}_A^{mi}$ is not increased over that in $\underline{\underline{G}}_A^{mi}$, when the object is confined to a single layer ($m = i$). We should also point out that the correspondence between the number of entries in $\underline{\underline{K}}_A^{mi}$ and the number of distinct Sommerfeld integrals that need be evaluated is not one-to-one. In fact, we can show by referring to Sections 4.1–4.3 that in the general case only four distinct Sommerfeld integrals are required in all three formulations. When $m = i$, the number of distinct integrals in Formulations A and B reduces to three.

As mentioned at the end of Chapter 2, one may leave the $\boldsymbol{P}^{mi}$ term as a part of the scalar potential (*cf.* (2.15)), thus avoiding the modification of the vector potential kernel as in (2.16). However, since this would constitute a departure from the standard form of the MPIE [4, 5], we prefer to proceed according to (2.16). Although in our formulations some of the terms introduced to $\underline{\underline{K}}_A^{mi}$ by $\nabla \boldsymbol{P}^{mi}$ in (2.16) become singular when $\boldsymbol{r}$ and $\boldsymbol{r}'$ coincide on an interface, they are no more singular than the terms already present in $\underline{\underline{G}}_A^{mi}$, and can be handled in a similar way as the latter.

Table 4.1: Summary of the properties of three mixed-potential formulations

Formulation and authors	Contour integrals	Continuity of K_ϕ^{mi} at the interfaces	Properties of $\underline{\underline{K}}_A^{mi}$ for $m = i$	Form of $\underline{\underline{K}}_A^{mi}$	Choice of K_ϕ^{mi}	Form of $\underline{\underline{G}}_A^{mi}$
A Johnson [19] (vertical tube); Michalski & Smith [22] (horizontal wires)	No	$K_\phi^{mi}(z' = z_i^+) = K_\phi^{m,i+1}(z' = z_i^-)$ $K_\phi^{mi}(z = z_m^+) \neq K_\phi^{m+1,i}(z = z_m^-)$	$\underline{\underline{K}}_A^{mi} = \underline{\underline{G}}_A^{mi}$	$\begin{bmatrix} K_{xx}^{mi} & K_{xy}^{mi} & K_{xz}^{mi} \\ K_{xy}^{mi} & K_{yy}^{mi} & K_{yz}^{mi} \\ 0 & 0 & K_{zz}^{mi} \end{bmatrix}$	K_ϕ^{mi} associated with horizontal dipole: $P_x^{mi} = P_y^{mi} = 0$ $P_z^{mi} \neq 0$	Alternative: $\begin{bmatrix} G_{xx}^{mi} & G_{xy}^{mi} & 0 \\ G_{xy}^{mi} & G_{yy}^{mi} & 0 \\ 0 & 0 & G_{zz}^{mi} \end{bmatrix}$
B Michalski & Zheng [25] (thin wire)	Yes	$K_\phi^{mi}(z' = z_i^+) \neq K_\phi^{m,i+1}(z' = z_i^-)$ $K_\phi^{mi}(z = z_m^+) = K_\phi^{m+1,i}(z = z_m^-)$	$\underline{\underline{K}}_A^{mi} = \underline{\underline{G}}_A^{mi}$ $K_{zz}^{mi} = K_{xy}^{mi} = 0$	$\begin{bmatrix} K_{xx}^{mi} & K_{xy}^{mi} & 0 \\ K_{xy}^{mi} & K_{yy}^{mi} & 0 \\ K_{xz}^{mi} & K_{xy}^{mi} & K_{zz}^{mi} \end{bmatrix}$	K_ϕ^{mi} associated with vertical dipole: $P_x^{mi} \neq 0, P_y^{mi} \neq 0$ $P_z^{mi} = 0$	
C Mosig & Gardiol [17] (planar patch); Michalski [23,24] (single layer); Michalski, et al. [21] (horizontal wires); Wilton & Singh [20] (periodic planar slots)	No	$K_\phi^{mi}(z' = z_i^+) = K_\phi^{m,i+1}(z' = z_i^-)$ $K_\phi^{mi}(z = z_m^+) = K_\phi^{m+1,i}(z = z_m^-)$		$\begin{bmatrix} K_{xx}^{mi} & 0 & K_{xz}^{mi} \\ 0 & K_{xx}^{mi} & K_{yz}^{mi} \\ K_{xz}^{mi} & K_{xy}^{mi} & K_{zz}^{mi} \end{bmatrix}$	K_ϕ^{mi} associated with horizontal dipole: $P_x^{mi} = P_y^{mi} = 0$ $P_z^{mi} \neq 0$	Traditional: $\begin{bmatrix} G_{xx}^{mi} & 0 & 0 \\ 0 & G_{xx}^{mi} & 0 \\ G_{xz}^{mi} & G_{xy}^{mi} & G_{zz}^{mi} \end{bmatrix}$

37

The continuity properties of the scalar potential kernels across the interfaces are summarized in the fifth column of Table 4.1. In Formulations A and C, K_ϕ^{mi} is continuous with respect to z', which results in the cancellation of the undesirable contour integrals in (2.15) (*cf.*the sixth column). In Formulations B and C, K_ϕ^{mi} is continuous with respect to z, which results in considerable simplifications in the numerical procedure when the object penetrates one or more interfaces. This last point can be fully appreciated only after we have discussed the details of the MOM procedure in the next chapter.

We conclude from the above summary that when the object is confined to a single layer, Formulations A and B become identical and are preferable to Formulation C, because they have fewer terms in $\underline{\underline{K}}_A^{mi}$. In the general case, Formulation C enjoys a clear advantage over Formulations A and B, because it does not have contour integrals and because its scalar potential kernel is continuous at the interfaces with respect to z, which results in the simplifications mentioned above. If we had to choose between Formulations A and B, we would prefer the latter, because the advantages of having the scalar potential kernel continuous with respect to z more than compensate for the complications caused by the presence of the contour integrals. This point is further elaborated upon in the next chapter.

The previous works related to the mixed-potential EFIE and reviewed in Chapter 1 can be classified as shown in the last column of Table 4.1.

Chapter 5

Numerical Method

In the previous chapter, three alternative MPIE formulations – referred to as Formulations A, B and C – have been derived for PEC antennas or scatterers residing in plane-stratified dielectric media with an arbitrary number of layers. Formulation C has been found to be particularly well suited for the application of the MOM procedures originated by Wilton and his co-workers [4, 5, 7]. This formulation is adopted here in conjunction with those procedures to analyze the radiation and scattering by a PEC object of arbitrary shape residing in layered media. For simplicity, but without loss of generality, we describe this method in the context of the two-media problem illustrated in Fig. 5.1. Also, for simplicity, the interface between the two media is taken to be the xy–plane of a Cartesian coordinate system. The upper ($z > 0$) half-space, which is characterized by ϵ_1 and μ_1, will be referred to as region 1, and the lower ($z < 0$) half space in Fig. 5.1a, or the slab ($-d < z < 0$) in Fig. 5.1b, both characterized by ϵ_2 and μ_2, as region 2. The parts of the surface S of the object which are in regions 1 and 2 are denoted as S_1 and S_2, respectively.

As was already mentioned, based on the analysis of Section 4.4, Formulation C has been selected for the problems of Fig. 5.1. Hence, upon specializing the MPIE of (2.15) to the present case, one obtains

$$\hat{n}_m \times \sum_{i=1}^{2} \left[j\omega A^{mi}(r) + \nabla \phi^{mi}(r) \right] = \hat{n}_m \times E_m^{inc}(r), \quad r \text{ on } S_m, \quad m = 1, 2 \tag{5.1}$$

where, for notational simplicity, we have introduced

$$A^{mi}(r) = \int_{S_i} \underline{\underline{K}}_A^{mi}(r \mid r') \cdot J(r') \, dS' \tag{5.2}$$

$$\phi^{mi}(r) = \int_{S_i} K_\phi^{mi}(r \mid r') \, q(r') \, dS' \tag{5.3}$$
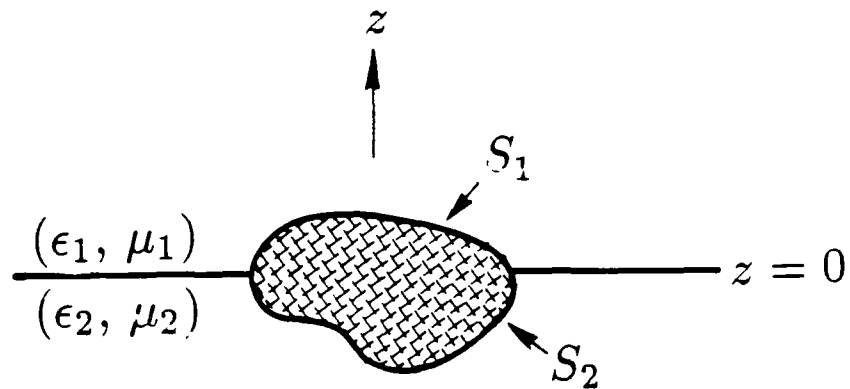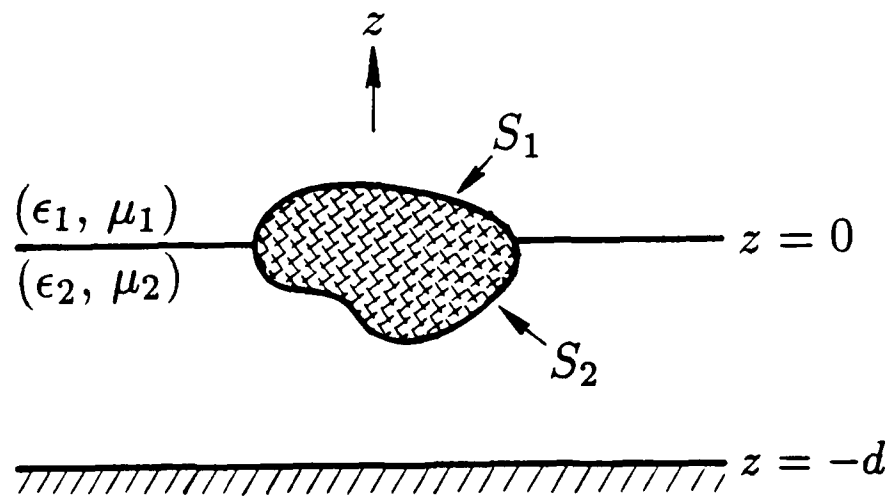
Figure 5.1: PEC object of arbitrary shape embedded in (a) contiguous half-spaces, and (b) in a grounded slab.

in which the kernel elements are given in Appendix A. The integrals (5.2) and (5.3) represent the modified potentials, and should not be confused with the original potentials given in (2.4) and (2.5).

We note that the contour integrals encountered in (2.15) are absent in (5.1), which is characteristic of Formulation C. The quantity of interest for the scattering and radiation problems is the surface current distribution on S, from which other characteristics, such as the far field pattern or radar cross-section, can readily be computed. For the transmission line problem, there is no excitation and (5.1) becomes a non-standard eigenvalue problem, with the propagation constants as eigenvalues and the modal current distributions as eigenfunctions.

In solving the integral equations, the MOM schemes developed in [3, 4, 5, 7] are employed. These procedures are modified to account for the dyadic character of the vector potential kernel, to ensure the current continuity across the interface, and to allow for the charge discontinuity there [19]. In the MOM, basis functions are chosen to represent the unknown currents, testing functions are chosen to enforce the integral equation, and these are used to derive an impedance matrix approximant to the integral equation.

5.1 Surface of Arbitrary Shape

Following the procedure described by Rao *et al.* [5], the surface S of the obۍ ۍt is modeled in terms of triangular patches in a manner suggested in Fig. 5.2. The surface current density on S is approximated as

$$J(r) = \sum_{n=1}^{N} I_n \Lambda_n(r) \tag{5.4}$$

where N is the number of interior (nonboundary) edges and Λ_n is the vector basis function defined on the adjacent triangles associated with the nth edge, and is given as

$$\Lambda_n(r) = \begin{cases} \dfrac{\rho_n^+}{h_n^+}, & r \text{ in } S_n^+ \\[2mm] \dfrac{\rho_n^-}{h_n^-}, & r \text{ in } S_n^- \\[2mm] 0, & \text{otherwise} \end{cases} \tag{5.5}$$

in which $h_n^\pm$ is the height of triangle $S_n^\pm$ relative to the nth edge of length l_n, and $\pm\rho_n^\pm$ is the vector from the free vertex of $S_n^\pm$ to an arbitrary point on patch $S_n^\pm$, as shown in Fig. 5.3. The
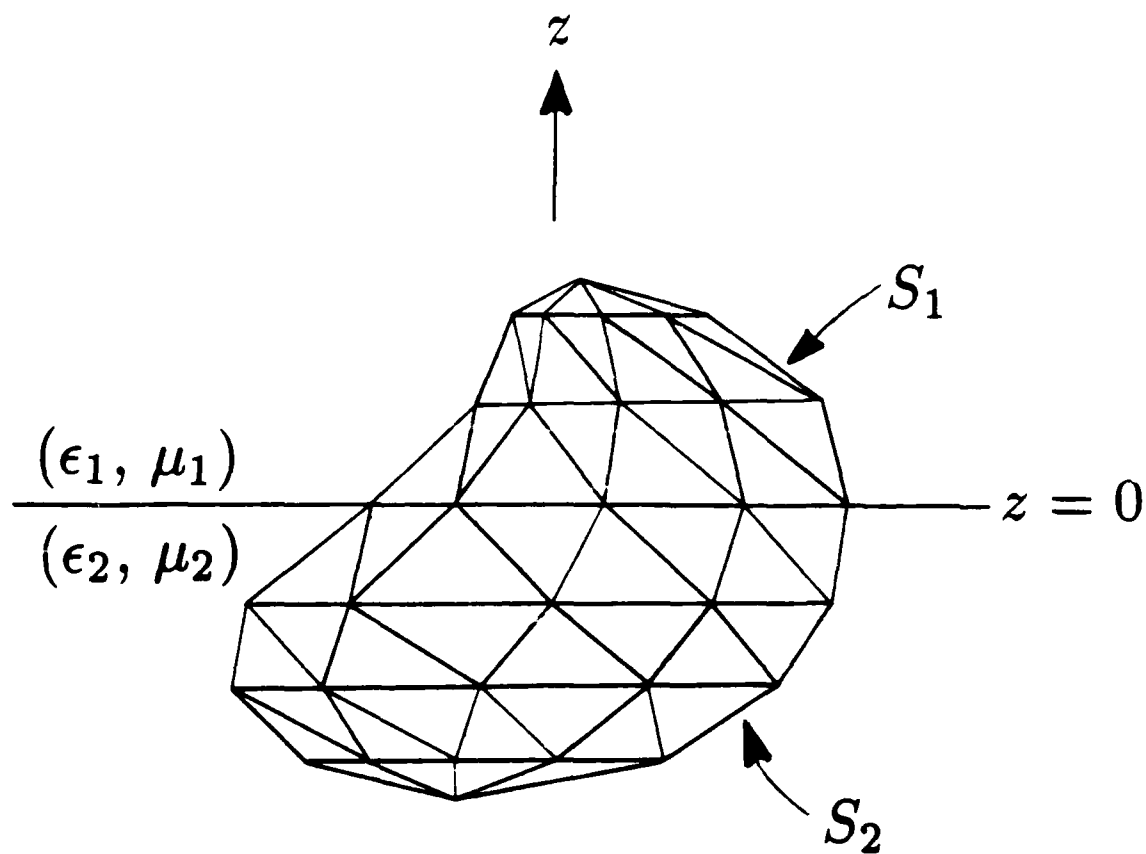
41

Figure 5.2: Triangle-patch model of an arbitrary surface penetrating the interface between dissimilar media.
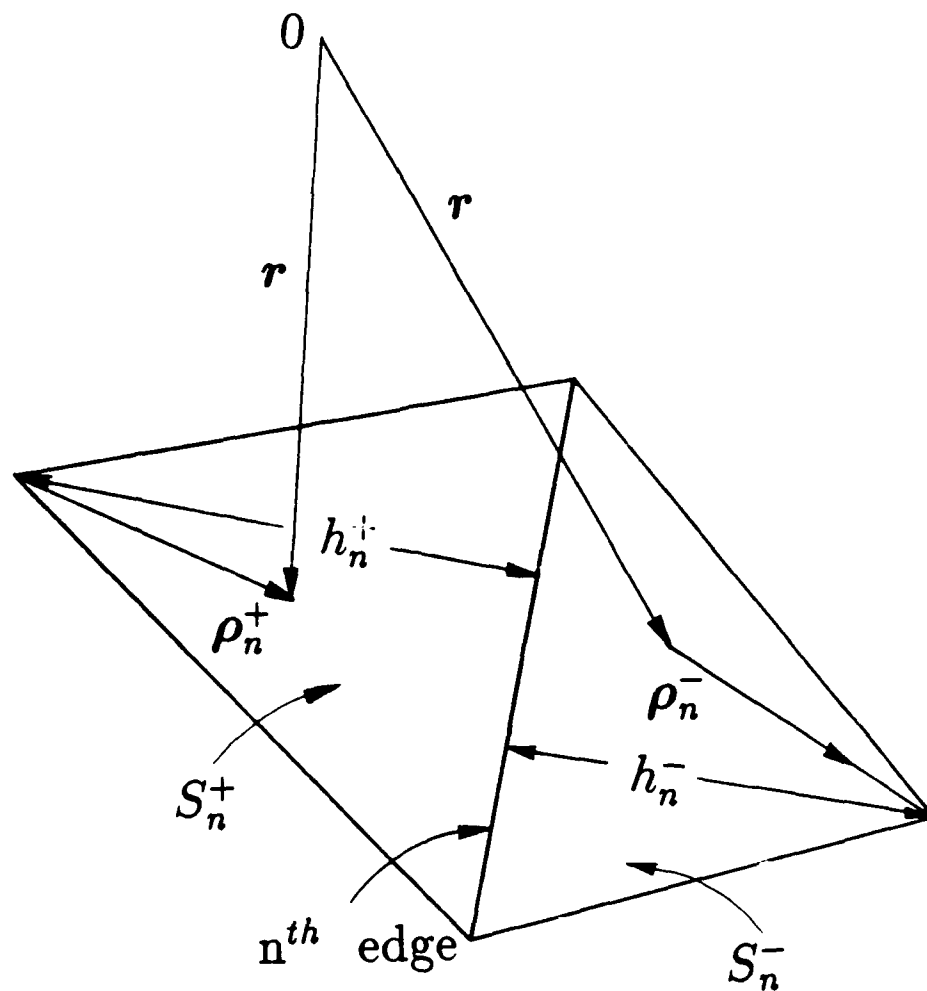
Figure 5.3: Local coordinates associated with an edge.

expansion for the surface charge density q, which is obtained by using (5.4) in the equation of continuity, calls for the surface divergence of Λ_n, which is found as

$$\nabla_s \cdot \Lambda_n(r) = \begin{cases} \dfrac{2}{h_n^+}, & r \text{ in } S_n^+ \\[2ex] -\dfrac{2}{h_n^-}, & r \text{ in } S_n^- \\[2ex] 0, & \text{otherwise} . \end{cases} \tag{5.6}$$

When the expansions for J and q are used in (5.1) and the resulting equations tested by integration along the path from the centroid of S_p^+ to the middle of the edge l_p and then to the centroid of S_p^-, an $N \times N$ system of linear equations is obtained, which may be written in matrix form as

$$[Z_{pn}][I_n] = [V_p] \tag{5.7}$$

where the elements of Z_{pn} and V_p are given as

$$Z_{pn} = \frac{j\omega}{2} \left(A_{pn}^- + A_{pn}^+ \right) - \frac{1}{j\omega} \left(\Phi_{pn}^- - \Phi_{pn}^+ \right) \tag{5.8}$$

$$V_p = \frac{1}{2} \left(E_p^- + E_p^+ \right) \tag{5.9}$$

where $p, n = 1, 2, \ldots, N$, and

$$A_{pn}^\pm = \int_{S_,} \rho_p^{c\pm} \cdot \underline{\underline{K}}_A^{mi} \left(r_p^{c\pm} \,|\, r' \right) \cdot \Lambda_n \left(r' \right) dS' \tag{5.10}$$

$$\Phi_{pn}^\pm = \int_{S_,} K_\phi^{mi} \left(r_p^{c\pm} \,|\, r' \right) \nabla_s' \cdot \Lambda_n \left(r' \right) dS' \tag{5.11}$$

$$E_p^\pm = \rho_p^{c\pm} \cdot E_m^{inc} \left(r_p^{c\pm} \right) . \tag{5.12}$$

In the above, $\rho_p^{c\pm}$ is the vector between the free vertex and the centroid of $S_p^\pm$, with ρ_p^{c-} directed toward and ρ_p^{c+} directed away from the vertex, and $r_p^{c\pm}$ is the vector from the coordinate origin to the centroid of $S_p^\pm$.

It is worthwhile to elaborate on one aspect of the above procedure, which is peculiar to the layered medium case. As suggested in Fig. 5.2, the triangle-patch model of S must take into account the position of the interface, since no triangular patch is allowed to cross it. This arrangement ensures the continuity of the current on S across the interface and allows for the discontinuity of the charge there (cf. (5.5), (5.6)). A typical triangle pair associated

44

(ϵ_1, μ_1)
(ϵ_2, μ_2)
$z = 0$
S_p^-
l_p
S_F^+

(a)

$\hat{u}_p^+$
$\hat{u}_p^-$
(ϵ_1, μ_1)
(ϵ_2, μ_2)
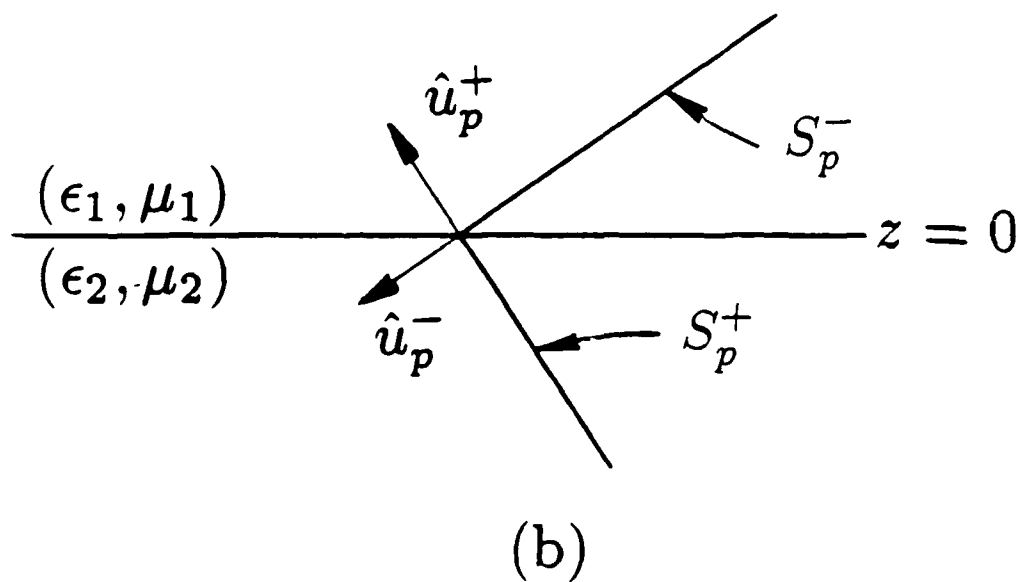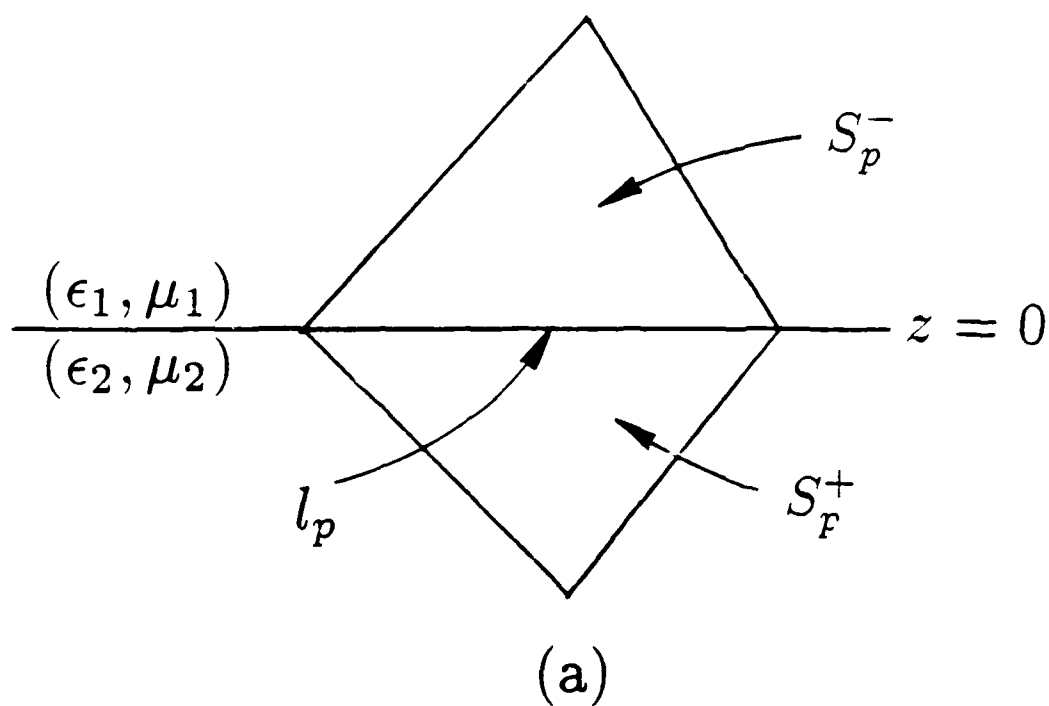$z = 0$
S_p^-
S_p^+

(b)

Figure 5.4: (a) Side view and (b) cross-sectional view of a triangle pair straddling the interface between two media.

with edge p on the interface is illustrated in Fig. 5.4. In testing (5.1) with Λ_p, one should bear in mind that S_p^- and S_p^+ are in different layers. For example, testing $\nabla \phi^{mi}$ in (5.1) with Λ_p yields

$$\int\limits_{S_p^+} \nabla \phi^{2i} \cdot \Lambda_p \, dS + \int\limits_{S_p^-} \nabla \phi^{1i} \cdot \Lambda_p \, dS = - \int\limits_{S_p^+} \phi^{2i} \nabla \cdot \Lambda_p \, dS - \int\limits_{S_p^-} \phi^{1i} \nabla \cdot \Lambda_p \, dS$$

$$+ \int\limits_{l_p} \left(\phi^{2i} \Lambda_p^+ \cdot \hat{u}_p^+ + \phi^{1i} \Lambda_p^- \cdot \hat{u}_p^- \right) dl \qquad (5.13)$$

where use has been made of the Gauss' theorem [38, p. 503] and where Λ_p^+ and Λ_p^- signify, respectively, Λ_p evaluated at the top and bottom sides of the interface. We observe the undesirable line integral in (5.13), which does not occur for objects in homogeneous space. Even in the present case, however, this integral disappears for Formulations B and C (see Chapter 4) in view of the continuity of the scalar potential kernels as z crosses an interface and the fact that $\hat{u}_p^+ \cdot \Lambda_p^+ = -\hat{u}_p^- \cdot \Lambda_p^-$ on l_p, which follows from (5.5). In Formulation A, the line integrals contribute a contour integral at the intersection of S with the interface, quite similar to that in (2.14), which is present in Formulation B. However, due to the approximations made in the testing procedure [5], the latter is actually easier to handle than the former–hence our statement in Chapter 4 regarding the superiority of Formulation B over A. Formulation C is, of course, free of either of these contour integrals.

It is worth noting that, apart from the presence of the Sommerfeld integrals, the only difference between (5.8)–(5.12) and their free space counterparts [5] is the dyadic character of the vector potential kernel in (5.10). The surface integrals in (5.10)–(5.11) can be efficiently evaluated in normalized area coordinates and reused for different matrix elements, as described in [5].

As in the free space problem, the integrands of $A^{mi}(r)$ and $\Phi^{mi}(r)$ are singular at $r = r'$, i.e., when the observation point coincides with the source point. As mentioned in Appendix A, this singularity arises from the closed form part of the Green's function. Thus, when the observation point is close to the source point, extraction of the inverse-$|r - r'|$ behavior is necessary before numerical integration is performed. The technique developed in [41] may be used for the treatment of such singularities.

5.2 Thin Wire of Arbitrary Shape

We next consider a thin-wire structure of arbitrary shape with radius a, which may penetrate the interface between two dissimilar dielectric layers, as shown in Fig. 5.5. The parts of the
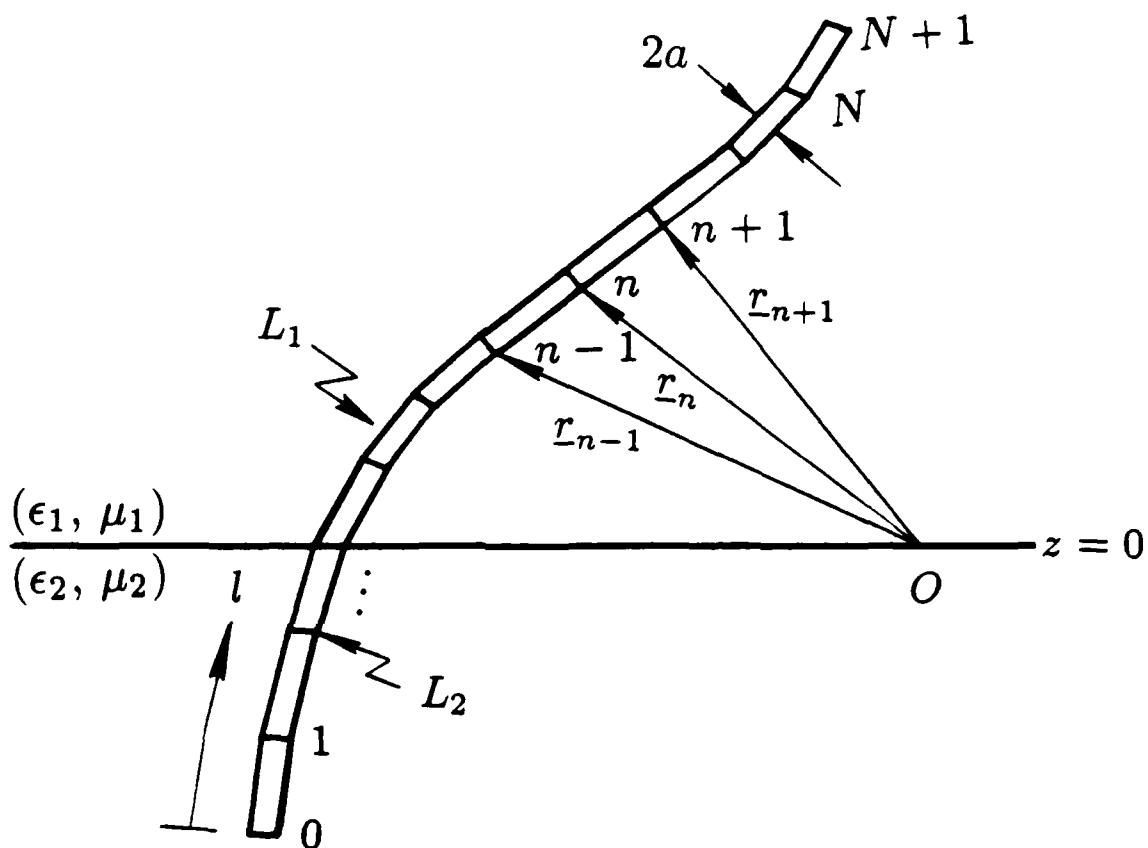
Figure 5.5: Straight-segment model of a thin-wire of arbitrary shape which penetrates the interface between dissimilar media.

wire which are in regions 1 and 2 are denoted as L_1 and L_2, respectively. The wire is modeled in terms of $N + 1$ straight tubular segments and the vectors $\boldsymbol{r}_n$, $n = 0, 1, \ldots, N + 1$, defined with respect to the global coordinate origin O, locate the end points of the linear segments, as illustrated in Fig. 5.5. The same points are designated by l_n with respect to the local arc-length coordinate l along the axis of the wire. By making use of the thin wire approximation [3], we may express the potentials (5.2) and (5.3) as

$$\boldsymbol{A}^{mi}(l) = \int_{L_i} \underline{\underline{\boldsymbol{K}}}_A^{mi}(l \,|\, l') \cdot \boldsymbol{I}(l') \, dl' \tag{5.14}$$

$$\Phi^{mi}(l) = \int_{L_i} K_\phi^{mi}(l \,|\, l') \, Q(l') \, dl' \tag{5.15}$$

where we have introduced the total current $\boldsymbol{I}(l) = 2\pi a \, \boldsymbol{J}(l)$ and the linear charge density $Q(l) = 2\pi a q(l)$. Since on the wire $\boldsymbol{r}$ is determined by l, we have, for simplicity, replaced the former by the latter in (5.14) and (5.15). Similar remarks apply to $\boldsymbol{r}'$ and l'. Following the MOM developed in [7], the current density along the wire is approximated as

$$\boldsymbol{I}(l) = \sum_{n=1}^{N} I_n \Lambda_n(l) \tag{5.16}$$

where $\Lambda_n(l)$ is the vector expansion function given by

$$\Lambda_n(l) = \begin{cases} \dfrac{\boldsymbol{\rho}_n^+}{h_n^+}, & l \text{ in } S_n^+ \\[2mm] \dfrac{\boldsymbol{\rho}_n^-}{h_n^-}, & l \text{ in } S_n^- \\[2mm] 0, & \text{otherwise} . \end{cases} \tag{5.17}$$

in which $h_n^\pm$ is the length of the segment $S_n^\pm$ relative to the nth node and $\pm \boldsymbol{\rho}_n^\pm$ is the vector from the free node of $S_n^\pm$ to an arbitrary point on the $S_n^\pm$ segment, as shown in Fig. 5.6. The divergence of $\Lambda_n(l)$, which is proportional to the linear charge density associated with this basis function, is

$$\nabla \cdot \Lambda_n(l) = \begin{cases} \dfrac{1}{h_n^+}, & l \text{ in } S_n^+ \\[2mm] -\dfrac{1}{h_n^-}, & l \text{ in } S_n^- \\[2mm] 0, & \text{otherwise} . \end{cases} \tag{5.18}$$
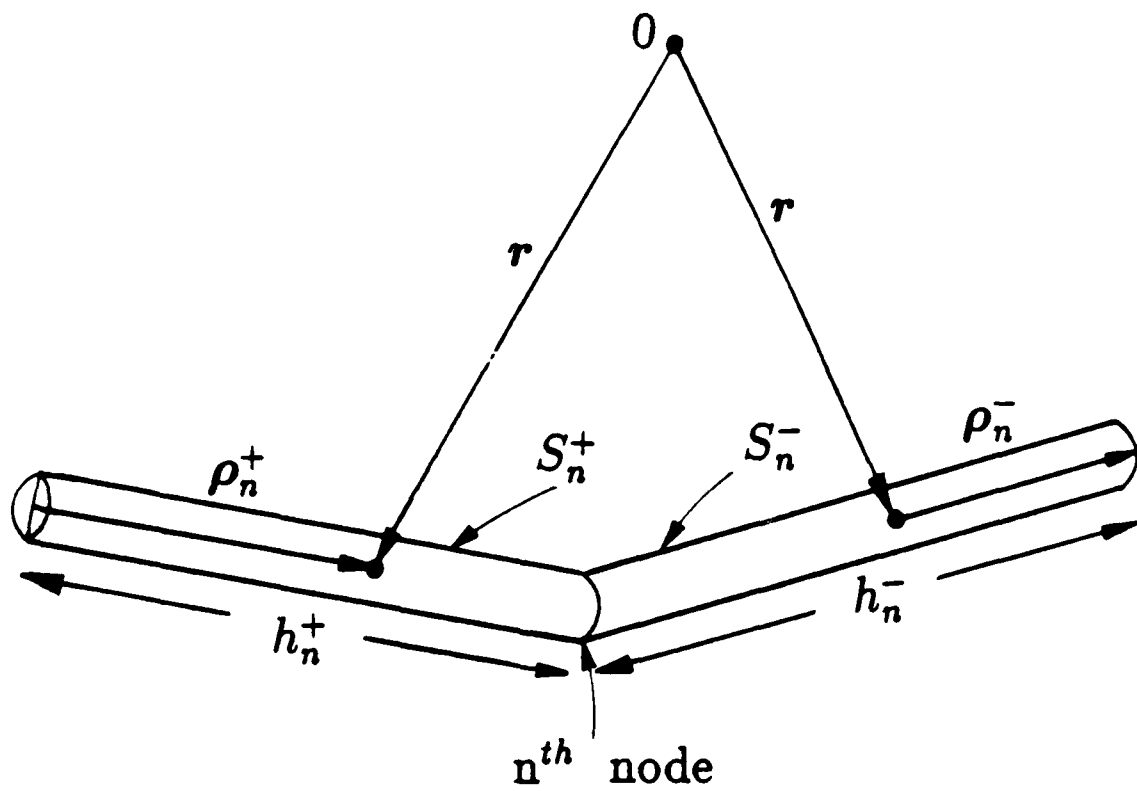
Figure 5.6: Local coordinates associated with the nth node of a wire.

When the expansions for I and Q are used in (5.1) and the resulting equations tested with $\Lambda_n(l)$, an $N \times N$ system of linear equations is obtained, which may be written in matrix form as

$$[Z_{pn}][I_n] = [V_p] \tag{5.19}$$

where

$$Z_{pn} = j\omega \left(A_{pn}^+ + A_{pn}^- \right) - \frac{1}{j\omega} \left(\Phi_{pn}^- - \Phi_{pn}^+ \right) \tag{5.20}$$

$$V_p = \boldsymbol{\rho}_p^{c+} \cdot \boldsymbol{E}_m^{inc}(l_p^{c+}) + \boldsymbol{\rho}_p^{c-} \cdot \boldsymbol{E}_m^{inc}(l_p^{c-}) \tag{5.21}$$

in which

$$A_{pn}^{\pm} = \int\limits_{L_i} \boldsymbol{\rho}_p^{c\pm} \cdot \underline{\underline{\boldsymbol{K}}}_A^{mi}(l_p^{c\pm} \,|\, l') \cdot \boldsymbol{\Lambda}_n(l') \, dl' \tag{5.22}$$

$$\Phi_{pn}^{\pm} = \int\limits_{L_i} K_\phi^{mi}(l_p^{c\pm} \,|\, l') \, \nabla' \cdot \boldsymbol{\Lambda}_n(l') \, dl' \tag{5.23}$$

and

$$l_p^{c\mp} = \frac{l_p + l_{p\pm1}}{2}. \tag{5.24}$$

In (5.22) and (5.23), we employ the exact kernel on the source segment and the reduced kernel otherwise.

It is observed that the integrand of (5.22) consists of seven terms contributed by the non-zero elements of the dyadic kernel $\underline{\underline{\boldsymbol{K}}}_A^{mi}$. For example, the contribution of K_{zz}^{mi} to A_{pn}^+ is

$$\int\limits_{L_i} \boldsymbol{\rho}_p^{c+} \cdot \hat{\boldsymbol{x}} K_{zz}^{mi}(l_p^{c+} \,|\, l') \, \hat{\boldsymbol{z}} \cdot \boldsymbol{\Lambda}_n(l') \, dl'$$

$$= \boldsymbol{\rho}_p^{c+} \cdot \hat{\boldsymbol{x}} \left[\int\limits_{l_{n-1}}^{l_n} K_{zz}^{mi}(l_p^{c+} \,|\, l') \frac{\boldsymbol{\rho}_n'^+}{h_n^+} \cdot \hat{\boldsymbol{z}} \, dl' + \int\limits_{l_n}^{l_{n+1}} K_{zz}^{mi}(l_p^{c+} \,|\, l') \frac{\boldsymbol{\rho}_n'^-}{h_n^-} \cdot \hat{\boldsymbol{z}} \, dl' \right]. \tag{5.25}$$

The integrals in (5.25) may be further transformed as

$$\int\limits_{l_{n-1}}^{l_n} K_{zz}^{mi}(l_p^{c+} \,|\, l') \frac{\boldsymbol{\rho}_n'^+}{h_n^+} \, dl'$$

$$= \frac{1}{2} \int\limits_{-\Delta^+}^{\Delta^+} K_{zz}^{mi}(l_p^{c+} \,|\, s' + l_n^{c+}) \, ds' + \frac{1}{h_n^+} \int\limits_{-\Delta^+}^{\Delta^+} K_{zz}^{mi}(l_p^{c+} \,|\, s' + l_n^{c+}) s' \, ds' \tag{5.26}$$

and

$$\int\limits_{l_n}^{l_{n+1}} K_{xz}^{mi}(l_p^{c+} \mid l') \frac{\rho_n'^-}{h_n^-} \, dl'$$

$$= \frac{1}{2} \int\limits_{-\Delta^-}^{\Delta^-} K_{xz}^{mi}(l_p^{c+} \mid s' + l_n^{c-}) \, ds' - \frac{1}{h_n^-} \int\limits_{-\Delta^-}^{\Delta^-} K_{xz}^{mi}(l_p^{c+} \mid s' + l_n^{c-}) s' \, ds' \tag{5.27}$$

where $\Delta^{\pm} = h_n^{\pm}/2$.

An examination of (5.20) and of the above expressions reveals that the right-hand integrals in (5.26) can be used in the matrix elements $Z_{p-1,n-1}$, $Z_{p,n-1}$, $Z_{p-1,n}$, and Z_{pn}, resulting in considerable savings in matrix fill time.

As suggested in Fig. 5.5, no straight segment is allowed to cross the interface, where the charge is discontinuous. Also, by using the same arguments as given in Section 5.1, one can prove that no extra terms need to be added to (5.20) to account for the interface, if Formulation C is used.

5.3 Microstrip Patch Antenna of Arbitrary Shape

The structure considered in this section is a microstrip patch antenna of arbitrary shape driven by a coaxial transmission line, as illustrated in Fig. 5.7. The dielectric slab and the PEC ground plane are assumed to be of infinite extent. The shape of the patch (also assumed to be PEC) is arbitrary and is modeled by triangular elements. The probe-to-patch junction can be located anywhere on the patch, including edges and corners, but it must coincide with a node of the triangle—element mesh.

Following the procedure developed by Hwu and Wilton [7], the surface current density on the patch S_P and the total axial current on the wire S_W are approximated as, respectively,

$$\boldsymbol{J}(\boldsymbol{r}) \approx \sum_{n=1}^{N_P} I_n^P \boldsymbol{\Lambda}^P(\boldsymbol{r}) + I^J \boldsymbol{\Lambda}^J(\boldsymbol{r}), \quad \boldsymbol{r} \text{ on } S_P \tag{5.28}$$

and

$$I(\boldsymbol{r}) \, \hat{\boldsymbol{\ell}} \approx \sum_{n=1}^{N_W} I_n^W \boldsymbol{\Lambda}^W(\boldsymbol{r}) + I^J \boldsymbol{\Lambda}^J(\boldsymbol{r}), \quad \boldsymbol{r} \text{ on } S_W \tag{5.29}$$

where $\boldsymbol{\Lambda}^P(\boldsymbol{r})$ and $\boldsymbol{\Lambda}^W(\boldsymbol{r})$ are the basis functions previously defined in (5.5) and (5.17), respectively (the superscripts "P" and "W" have been introduced to distinguish between functions associated with the patch and the wire). The basis function associated with the wire–to–patch junction is given as [7, 42]

51

microstrip patch

ϵ_1, μ_1

ϵ_2, μ_2

N_W

d

1

2b

coaxial feed probe

2a

(a)
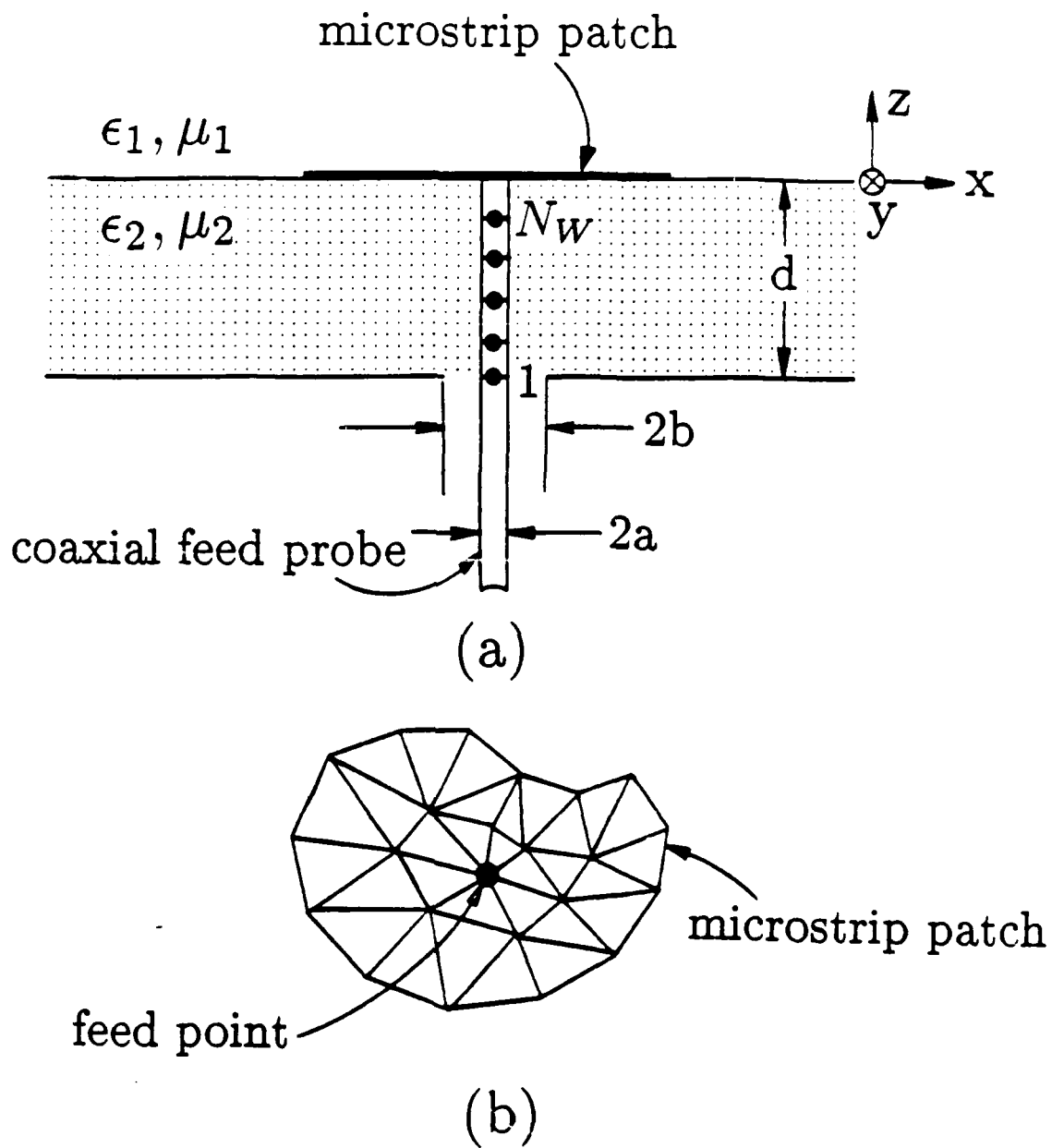
microstrip patch

feed point

(b)

Figure 5.7: Coax–fed microstrip patch antenna. (a) Cross-sectional view. (b) Top view showing a triangle-element model of an arbitrarily shaped patch.

$$
\Lambda^J(\boldsymbol{r}) =
\begin{cases}
K_l \left[1 - \dfrac{(h_l^{J-})^2}{(\boldsymbol{\rho}_l^{J-} \cdot \hat{\boldsymbol{h}}_l^{J-})^2} \right] \Lambda_l^P(\boldsymbol{r}), & \boldsymbol{r} \text{ in } S_l^{J-} \\[3ex]
\Lambda_J^W(\boldsymbol{r}), & \boldsymbol{r} \text{ in } S^{J+} \\[3ex]
0, & \text{otherwise}
\end{cases}
\tag{5.30}
$$

where the index l refers to the lth triangle, S_l^{J-}, at the junction (*cf.* Fig. 5.8), $\Lambda_l^P(\boldsymbol{r})$ and $\hat{\boldsymbol{h}}_l^{J-}$ are the patch basis function and the vector height, respectively, associated with the edge opposite the junction vertex in S_l^{J-}, $\Lambda_J^W(\boldsymbol{r})$ is the wire basis function associated with the junction node $N_W + 1$, and K_l is the normalization constant given as

$$
K_l = \frac{\alpha_l}{\ell_l \displaystyle\sum_{l=1}^{N_J} \alpha_l} = \frac{\alpha_l}{\ell_l \alpha^t}
\tag{5.31}
$$

where α_l is the angle between the two edges of S_l^{J-} common to the junction vertex, l_l is the length of the edge opposite the junction in S_l^{J-}, N_J is the number of triangular elements attached to the junction, and α^t is the sum of the N_J junction vertex angles. The divergence of $\Lambda^J(\boldsymbol{r})$, which is proportional to the surface charge density near the junction, is given as

$$
\nabla_s \cdot \Lambda^J(\boldsymbol{r}) =
\begin{cases}
-\dfrac{2K_l}{h_l^{J-}}, & \boldsymbol{r} \text{ in } S_l^{J-} \\[3ex]
\dfrac{1}{h^{J+}}, & \boldsymbol{r} \text{ in } S^{J+} \\[3ex]
0, & \text{otherwise.}
\end{cases}
\tag{5.32}
$$

The basis function (5.30) enforces the current continuity at the junction and it correctly models the near–singular behavior of the patch current near the feed probe. Unlike some other "attachment modes" described in the literature [18, 43, 44, 45, 46], it is applicable even in cases where the microstrip patch antenna is driven at an edge or a vertex.

The testing procedures for S_P and S_W are identical to those described in Sections 5.1 and 5.2, respectively. In testing the equations associated with the junction, we first integrate along the wire axis from the center of the attached wire segment to the junction, and then along the paths from the junction to the centroid of each triangle element associated with the junction. The resulting equations are subsequently combined into a single equation for the junction, by weighting each with the associated triangle vertex angle and summing the results for each junction triangle element. Substituting the current expansions (5.28–5.29)
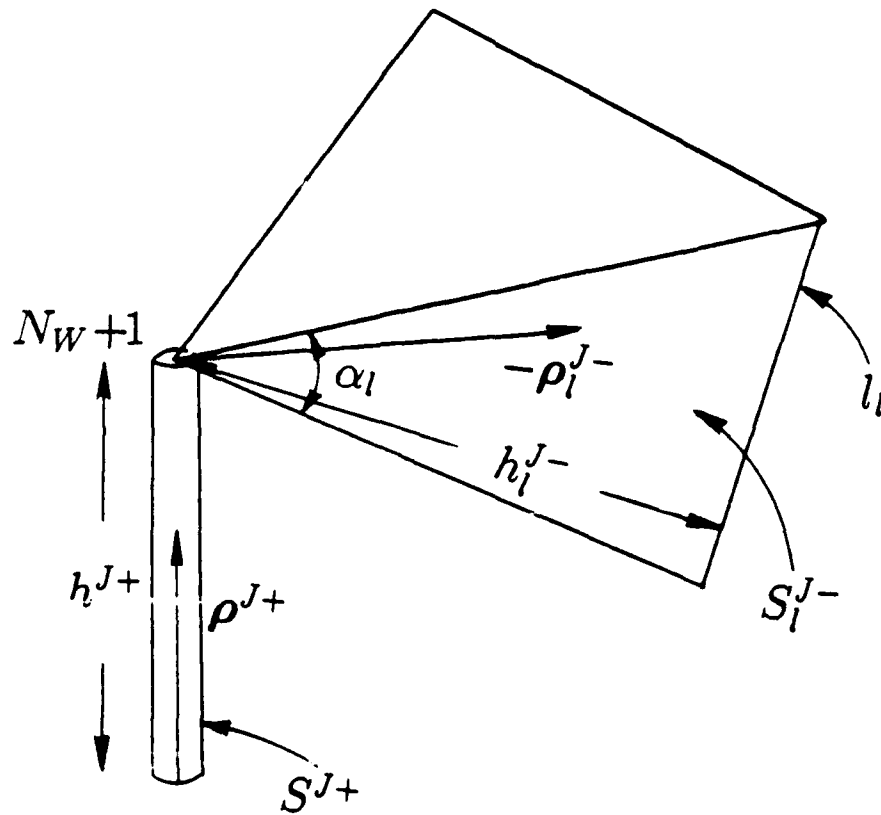
53

Figure 5.8: Geometrical parameters associated with the wire-to-surface junction.

into (5.1) and testing the resulting equations by the method described above, we obtain an $N \times N$ system of linear algebraic equations, where $N = N_P + N_W + 1$, which may be written in matrix form as

$$
\begin{bmatrix}
\begin{bmatrix} Z^{PP} \end{bmatrix} & \begin{bmatrix} Z^{PW} \end{bmatrix} & \begin{bmatrix} Z^{PJ} \end{bmatrix} \\[2mm]
\begin{bmatrix} Z^{WP} \end{bmatrix} & \begin{bmatrix} Z^{WW} \end{bmatrix} & \begin{bmatrix} Z^{WJ} \end{bmatrix} \\[2mm]
\begin{bmatrix} Z^{JP} \end{bmatrix} & \begin{bmatrix} Z^{JW} \end{bmatrix} & Z^{JJ}
\end{bmatrix}
\begin{bmatrix}
\begin{bmatrix} I^P \end{bmatrix} \\[2mm]
\begin{bmatrix} I^W \end{bmatrix} \\[2mm]
I^J
\end{bmatrix}
=
\begin{bmatrix}
\begin{bmatrix} V^P \end{bmatrix} \\[2mm]
\begin{bmatrix} V^W \end{bmatrix} \\[2mm]
V^J
\end{bmatrix}
\tag{5.33}
$$

where the elements of the submatrices $\begin{bmatrix} Z^{PP} \end{bmatrix}$, $\begin{bmatrix} Z^{WW} \end{bmatrix}$, $\begin{bmatrix} V^P \end{bmatrix}$, and $\begin{bmatrix} V^W \end{bmatrix}$ are defined in previous sections, and the elements of the other submatrices are given as

$$
Z_{pn}^{P\gamma} = \frac{j\omega}{2} \left(A_{pn}^{P\gamma-} + A_{pn}^{P\gamma+} \right) - \frac{1}{j\omega} \left(\Phi_{pn}^{P\gamma-} - \Phi_{pn}^{P\gamma+} \right), \quad \gamma = W \text{ or } J
\tag{5.34}
$$

$$
Z_{pn}^{W\gamma} = j\omega \left(A_{pn}^{W\gamma+} + A_{pn}^{W\gamma-} \right) - \frac{1}{j\omega} \left(\Phi_{pn}^{W\gamma-} - \Phi_{pn}^{W\gamma+} \right), \quad \gamma = P \text{ or } J
\tag{5.35}
$$

$$
Z_n^{J\gamma} = \frac{1}{\alpha^t} \sum_{l=1}^{N_J} \alpha_l \left(j\omega A_{ln}^{J\gamma-} - \frac{1}{j\omega} \Phi_{ln}^{J\gamma-} \right) + j\omega A_n^{J\gamma+} + \frac{1}{j\omega} \Phi_n^{J\gamma+}, \quad \gamma = P, W \text{ or } J
\tag{5.36}
$$

$$
V^J = \frac{1}{2\alpha^t} \sum_{l=1}^{N_J} \alpha_l \, \boldsymbol{\rho}_l^{c-} \cdot \boldsymbol{E}^{inc}(\boldsymbol{r}_l^{c-}) + \boldsymbol{\rho}_{N_W+1}^{c+} \cdot \boldsymbol{E}^{inc}(l_{N_W+1}^{c+})
\tag{5.37}
$$

in which

$$
A_{pn}^{P\gamma\pm} = \int_S \boldsymbol{\rho}_p^{c\pm} \cdot \underline{\underline{\boldsymbol{K}}}_A^{22}(\boldsymbol{r}_p^{c\pm} \,|\, \boldsymbol{r}') \cdot \boldsymbol{\Lambda}_n^{\gamma}(\boldsymbol{r}') \, ds', \quad \gamma = W \text{ or } J
\tag{5.38}
$$

$$
A_{pn}^{W\gamma\pm} = \int_S \boldsymbol{\rho}_p^{c\pm} \cdot \underline{\underline{\boldsymbol{K}}}_A^{22}(l_p^{c\pm} \,|\, \boldsymbol{r}') \cdot \boldsymbol{\Lambda}_n^{\gamma}(\boldsymbol{r}') \, ds', \quad \gamma = P \text{ or } J
\tag{5.39}
$$

$$
A_{ln}^{J\gamma-} = -A_{ln}^{P\gamma-}, \quad A_n^{J\gamma+} = A_{N_W+1,n}^{W\gamma+}
\tag{5.40}
$$

$$
\Phi_{pn}^{P\gamma\pm} = \int_S K_\phi^{22}(\boldsymbol{r}_p^{c\pm} \,|\, \boldsymbol{r}') \, \boldsymbol{\nabla}' \cdot \boldsymbol{\Lambda}_n^{\gamma}(\boldsymbol{r}') \, ds', \quad \gamma = W \text{ or } J
\tag{5.41}
$$

$$
\Phi_{pn}^{W\gamma\pm} = \int_S K_\phi^{22}(l_p^{c\pm} \,|\, \boldsymbol{r}') \, \boldsymbol{\nabla}' \cdot \boldsymbol{\Lambda}_n^{\gamma}(\boldsymbol{r}') \, ds', \quad \gamma = P \text{ or } J
\tag{5.42}
$$

$$
\Phi_{ln}^{J\gamma-} = \Phi_{ln}^{P\gamma-}, \quad \Phi_n^{J\gamma+} = \Phi_{N_W+1,n}^{W\gamma+}
\tag{5.43}
$$

The antenna is excited by a coaxial cable from below the ground plane (cf.Fig. 5.7). The magnetic current frill model [47] is used to model the junction between the coaxial transmission line and the dielectric substrate. It is assumed that the field distribution in the coax aperture is that of the TEM mode with a known voltage V_{in}. The magnetic current radiating in the grounded slab environment provides the "incident fields" [48, 49]

$$E_z^{inc}(\rho, z) = \frac{V_{in}}{\ln\left(\dfrac{b}{a}\right)} S_0 \left\{ \frac{-jk_{z1}\epsilon_2 + k_{z2}\epsilon_1 \cot(k_{z2}z)}{D^e k_{z2}} \right.$$

$$\left. \cdot \frac{\sin(k_{z2}z)}{\cos(k_{z2}d)} \left[J_0(ak_\rho) - J_0(bk_\rho) \right] \right\}_{\xi=|\boldsymbol{\rho}-\boldsymbol{\rho}_c|} \tag{5.44}$$

$$E_\rho^{inc}(\rho, z) = \frac{V_{in}}{\ln\left(\dfrac{b}{a}\right)} S_1 \left\{ \frac{jk_{z1}\epsilon_2 + k_{z2}\epsilon_1 \tan(k_{z2}z)}{D^e k_\rho^2} \right.$$

$$\left. \cdot \frac{\cos(k_{z2}z)}{\cos(k_{z2}d)} \left[J_0(ak_\rho) - J_0(bk_\rho) \right] \right\}_{\xi=|\boldsymbol{\rho}-\boldsymbol{\rho}_c|} \tag{5.45}$$

where D^e and D^h are definded in Appendix A.2, and ξ is the horizontal distance between the field point and the center of the coax inner conductor at $\boldsymbol{\rho}_c$. Once the system (5.33) is solved, the input impedance of the microstrip patch antenna is found as

$$Z_{in} = \frac{V_{in}}{I_{in}} \tag{5.46}$$

where I_{in} is the current at the base of the coaxial probe.

The computation of the matrix elements in (5.33) is extremely time consuming, due mainly to the presence of Sommerfeld–type integrals, which must be repeatedly evaluated for different source and field points. For the structure shown in Fig. 5.7, the integrals encountered in $\left[Z^{PP}\right]$ depend only on the distance ξ, while those in $\left[Z^{PW}\right]$ and $\left[Z^{WP}\right]$ depend, respectively, on (ξ, z') and (ξ, z). This suggests a time saving scheme, in which the Sommerfeld integrals for a given geometry and frequency are pre-computed for a grid of points (using the methods of Chapter 6), and these values are used in the solution phase to interpolate the values of the Sommerfeld intergals for all required combinations of source and field points [50, 17, 18]. We have implemented this method using one-dimensional quadratic Lagrange interpolation for the Z^{PP} terms, and two-dimensional cubic Lagrange interpolation for the Z^{WP} and Z^{PW} terms.

In cases where the substrate is electrically thin, a simplified feed model may be employed to analyze the antenna of Fig. 5.7, without appreciable loss of accuracy. In this model,

the coax probe is replaced by a vertical filament of constant current I_{in}, which enters the microstrip patch and spreads radially away from the junction point. The excitation current on the patch can be approximated by $I_{in}\Lambda^{J-}(r)$, where Λ^J is defined in (5.30). This current is now considered to be the source of the "incident field," and the current distribution on the microstrip patch is the only unknown. Otherwise, the solution procedure is similar to that described above, and it leads to a matrix equation

$$[Z^{PP}][I^P] = [V^P] \tag{5.47}$$

where Z_{pn}^{PP} are given in (5.8), and V^P is very similar in form to Z_p^{PJ}, given in (5.34). Once (5.47) is solved for the patch current, the antenna's input impedance is calculated as

$$Z_{in} = -\int_{-a}^{0} \boldsymbol{E}^P \cdot \hat{z}\, dz' + Z_{coax} \tag{5.48}$$

where $\boldsymbol{E}^P$ is the field due to the total current on the microstrip patch evaluated at the location of the probe, and Z_{coax} is the correction term required to account for the "probe self-impedance." Several different expressions for Z_{coax} have been used in the literature [51, 52, 53], with the most elaborate form recently given by Mosig and Hall [54, p. 434]:

$$Z_{coax} = \frac{\eta_0 k_0 d}{2\pi}\left\{ k_0 d\sqrt{\epsilon_r} + j\left[\operatorname{arsinh}\left(\frac{2d}{a}\right) + \frac{a - \sqrt{a^2 + 4d^2}}{2d}\right]\right\} \tag{5.49}$$

where it is assumed that the upper medium is free space with the intrinsic impedance η_0, and ϵ_r is the relative dielectric constant of the substrate.

The simplified and rigorous coax–feed models will be referred to as the 1st– and 2nd–order models, respectively.

5.4 Transmission Line of Arbitrary Cross-Section

The structure under consideration is shown in a cross-sectional view in Fig. 5.9. The ground plane at $z = -d$ is assumed to be perfectly conducting. The arbitrarily shaped PEC cylinder may be open (for example, infinitely thin strip) or closed (finite-thickness strip), and is of infinite extent and invariant along the y coordinate. As illustrated in Fig. 5.9, the contour of the cylinder cross-section is approximated in terms of straight line segments. The definitions of the ends of the segments and the local arc–length coordinate parallel to the segments are the same as those in Section 5.2, except that in this case l and r depend only on the transverse coordinates x and z. We assume that all field components depend on the longitudinal coordinate y according to $e^{-jk_y y}$, where $k_y = \beta - j\alpha$ represents the propagation
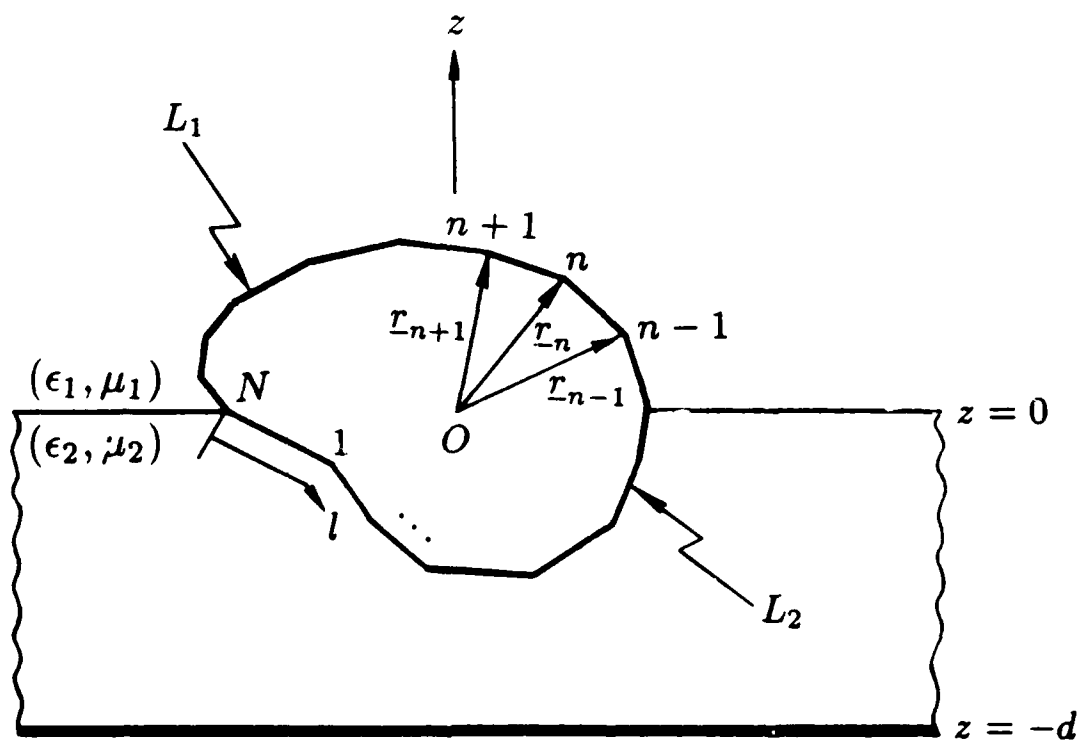
57

Figure 5.9: Straight line segment model of a cylinder of arbitrary cross-section embedded in a grounded slab.

constant of the mode. For this two-dimensional problem, the surface current density on the cylinder can be decomposed as

$$\boldsymbol{J}(\boldsymbol{r}) = \boldsymbol{J}_t(\boldsymbol{r}) + \hat{\boldsymbol{y}}\, J_y(\boldsymbol{r}) \tag{5.50}$$

where $\boldsymbol{J}_t(\boldsymbol{r})$ and $J_y(\boldsymbol{r})$ are the transverse and longitudinal surface current densities, respectively, and can be expressed as

$$\boldsymbol{J}_t(\boldsymbol{r}) = \boldsymbol{J}_t(l)e^{-jk_y y} \tag{5.51}$$

$$J_y(\boldsymbol{r}) = J_y(l)e^{-jk_y y} \tag{5.52}$$

where l is the local arc-length coordinate along the circumference of the conductor and is a function of the transverse position only (*cf.* Fig. 5.9). Thus, for the transmission line structure, (5.1) may be expressed as

$$\hat{\boldsymbol{n}}_m \times \sum_{i=1}^{2} \left[j\omega \boldsymbol{A}^{mi}(l) + (\boldsymbol{\nabla}_t - \hat{\boldsymbol{y}}jk_y)\, \Phi^{mi}(l) \right] = 0, \quad m = 1, 2 \tag{5.53}$$

where

$$\boldsymbol{\nabla}_t = \hat{\boldsymbol{x}}\, \frac{\partial}{\partial x} + \hat{\boldsymbol{z}}\, \frac{\partial}{\partial z} \tag{5.54}$$

$$\boldsymbol{A}^{mi}(l) = \int_{L_i} \underline{\underline{\boldsymbol{K}}}_A^{mi}(l\,|\,l') \cdot \boldsymbol{J}(l')\, dl' \tag{5.55}$$

$$\Phi^{mi}(l) = \int_{L_i} K_\phi^{mi}(l\,|\,l')\, q(l')\, dl'. \tag{5.56}$$

The charge density $q(l)$ in (5.56) can be obtained by using the equation of continuity,

$$q(l) = \frac{1}{-j\omega}\, (\boldsymbol{\nabla}_t - \hat{\boldsymbol{y}}jk_y) \cdot \boldsymbol{J}(l). \tag{5.57}$$

The elements of $\underline{\underline{\boldsymbol{K}}}_A^{mi}$ and K_φ^{mi} can be obtained from (A.18)–(A.37) by making the following changes:

$$S_0[\tilde{g}(k_\rho)] \longrightarrow S_0[\tilde{g}(k_x)] = \int_{-\infty}^{\infty} \tilde{g}(k_x)e^{-jk_x(x-x')}\, dk_x \tag{5.58}$$

$$\cos\zeta\, S_1[\tilde{g}(k_\rho)] \longrightarrow S_0[jk_x\tilde{g}(k_x)] \tag{5.59}$$

$$\sin\zeta\, S_1[\tilde{g}(k_\rho)] \longrightarrow jk_y S_0[\tilde{g}(k_x)] \tag{5.60}$$

59

$$g_i(r) = \frac{e^{-jk_ir}}{r} \longrightarrow \frac{\pi}{j} H_0^{(2)}(\rho\sqrt{k_i^2 - k_y^2}) \tag{5.61}$$

where $\rho = \sqrt{(x - x')^2 + (z - z')^2}$. Following the MOM procedure developed in [4] for objects in free space, the surface current densities may be approximated as

$$\boldsymbol{J}_t = \sum_{n=1}^{N^t} I_n^t \, \boldsymbol{\Lambda}_n(l) \tag{5.62}$$

$$J_y = \sum_{n=1}^{N^y} I_n^y \, \Pi_n(l) \tag{5.63}$$

where $\boldsymbol{\Lambda}_n(l)$ is given in (5.17) and

$$\Pi_n(l) = \begin{cases} 1, & l_{n-1} < l < l_n \\ \\ 0, & \text{otherwise} . \end{cases} \tag{5.64}$$

Substituting (5.55) and (5.56), and using (5.62) and (5.63) in (5.53), and testing the resulting equation with $\boldsymbol{\Lambda}_n$ and with $\hat{\boldsymbol{y}}\,\Pi_n$, one obtains the matrix equation

$$\left[\begin{array}{cc} \left[Z_{pn}^{tt}\right] & \left[Z_{pn}^{ty}\right] \\ \left[Z_{pn}^{yt}\right] & \left[Z_{pn}^{yy}\right] \end{array} \right] \left[\begin{array}{c} [I_n^t] \\ {}[I_n^y] \end{array} \right] = \left[\begin{array}{c} 0 \\ 0 \end{array} \right] \tag{5.65}$$

where the elements of Z_{pn} are given as

$$Z_{pn}^{tt} = j\omega \left[\frac{h_p^+}{4} \left(A_{pn}^{tt++} + A_{pn}^{tt+-} \right) + \frac{h_p^-}{4} \left(A_{pn}^{tt-+} + A_{pn}^{tt--} \right) \right] \\ - \frac{1}{j\omega} \left[\frac{1}{h_n^+} \left(\Phi_{pn}^{-+} - \Phi_{pn}^{++} \right) - \frac{1}{h_n^-} \left(\Phi_{pn}^{--} - \Phi_{pn}^{+-} \right) \right] \tag{5.66}$$

$$Z_{pn}^{ty} = j\omega \left(\frac{h_p^+}{2} A_{pn}^{ty++} + \frac{h_p^-}{2} A_{pn}^{ty-+} \right) + \frac{k_y}{\omega} \left(\Phi_{pn}^{-+} - \Phi_{pn}^{++} \right) \tag{5.67}$$

$$Z_{pn}^{yt} = j\omega \frac{h_p^+}{2} \left(A_{pn}^{yt++} + A_{pn}^{yt+-} \right) + \frac{k_y}{\omega} h_p^+ \left(\frac{1}{h_n^+} \Phi_{pn}^{++} - \frac{1}{h_n^-} \Phi_{pn}^{+-} \right) \tag{5.68}$$

$$Z_{pn}^{yy} = j\omega h_p^+ \left(A_{pn}^{yy++} - \frac{k_y^2}{\omega^2} \Phi_{pn}^{++} \right) \tag{5.69}$$

in which

$$A_{pn}^{\tau\eta\pm\pm} = \pm \int_{l_{n\mp1}}^{l_n} \hat{\boldsymbol{\tau}}_p^\pm \cdot \underline{\underline{\boldsymbol{K}}}_A^{mi}(l_p^{c\pm} \,|\, l') \cdot \hat{\boldsymbol{\eta}}_n^\pm \, dl', \quad (\tau,\eta) = (t,y) \tag{5.70}$$

60

$$\Phi_{pn}^{\pm\pm} = \pm \int\limits_{l_{n\mp1}}^{l_n} K_\phi^{mi}(l_p^{c\pm} \mid l') \, dl'. \tag{5.71}$$

where $\pm$ in front of the integrals (5.70) and (5.71) corresponds to the segment $S_n^\pm$. In the above equations, the first and second superscripts $\pm$ correspond, respectively, to segments $S_p^\pm$ and $S_n^\pm$.

The evaluation of the matrix elements ($cf.$(5.70)–(5.71)) involves double integrations in the space and spectrum domains. One notes that the order of the integrations may be changed and the integration in space domain can be done in closed form. Here, we only give the expressions for the matrix elements for the practically most important case of a strip confined to the cover medium (region 1):

$$\int\limits_{l_{n\mp1}}^{l_n} K_{xx}^{11}(l_p^{c\pm} \mid l') \, dl' = \frac{\mu_1}{4\pi} \left\{ I_{pn}^{\pm\pm} - S_{pn}^{\pm\pm} \left[\frac{\mu_1 k_{z2} \cot(k_{z2}d) - j\mu_2 k_{z1}}{D^h j k_{z1}} \right] \right\} \tag{5.72}$$

$$\int\limits_{l_{n\mp1}}^{l_n} K_{xz}^{11}(l_p^{c\pm} \mid l') \, dl' = -\frac{\mu_1}{2\pi} (\mu_1\epsilon_1 - \mu_2\epsilon_2) S_{pn}^{\pm\pm} \left[\frac{j k_x}{D^e D^h} \right] \tag{5.73}$$

$$\int\limits_{l_{n\mp1}}^{l_n} K_{yz}^{11}(l_p^{c\pm} \mid l') \, dl' = -\frac{\mu_1}{2\pi} (\mu_1\epsilon_1 - \mu_2\epsilon_2) S_{pn}^{\pm\pm} \left[\frac{j k_y}{D^e D^h} \right] \tag{5.74}$$

$$\int\limits_{l_{n\pm1}}^{l_n} K_{zx}^{11}(l_p^{c\pm} \mid l') \, dl' = - \int\limits_{l_{n\pm1}}^{l_n} K_{xz}^{11}(l_p^{c\pm} \mid l') \, dl' \tag{5.75}$$

$$\int\limits_{l_{n\pm1}}^{l_n} K_{zy}^{11}(l_p^{c\pm} \mid l') \, dl' = - \int\limits_{l_{n\pm1}}^{l_n} K_{yz}^{11}(l_p^{c\pm} \mid l') \, dl' \tag{5.76}$$

$$\int\limits_{l_{n\mp1}}^{l_n} K_{zz}^{11}(l_p^{c\pm} \mid l') \, dl' = \frac{\mu_1}{4\pi} \left\{ I_{pn}^{\pm\pm} + S_{pn}^{\pm\pm} \left[\frac{\epsilon_1 k_{z2} \tan(k_{z2}d) + j\epsilon_2 k_{z1}}{D^e j k_{z1}} \right] \right.$$
$$\left. + 2(\mu_2\epsilon_2 - \mu_1\epsilon_1) S_{pn}^{\pm\pm} \left[\frac{j k_{z1}}{D^e D^h} \right] \right\} \tag{5.77}$$

$$\int\limits_{l_{n\mp1}}^{l_n} K_\phi^{11}(l_p^{c\pm} \mid l') \, dl' = \frac{1}{4\pi\epsilon_1} \left\{ I_{pn}^{\pm\pm} - S_{pn}^{\pm\pm} \left[\frac{\mu_1 k_{z2} \cot(k_{z2}d) - j\mu_2 k_{z1}}{D^h j k_{z1}} \right] \right.$$
$$\left. + 2(\mu_2\epsilon_2 - \mu_1\epsilon_1) S_{pn}^{\pm\pm} \left[\frac{j k_{z1}}{D^e D^h} \right] \right\} \tag{5.78}$$

where we have introduced the notations

$$I_{pn}^{\pm\pm} = \pm\frac{\pi}{j} \int\limits_{-\Delta^\pm}^{\Delta^\pm} H_0^{(2)}(\rho_{pn}^{\pm\pm}\sqrt{k_1^2 - k_y^2})\, ds', \tag{5.79}$$

$$S_{pn}^{\pm\pm}[\tilde{f}(k_x)] = \pm 2 \int\limits_{-\infty}^{\infty} \tilde{f}(k_x) e^{-jk_{z1}(z_p^\pm + z_n^\pm)} e^{-jk_x(x_p^\pm - x_n^\pm)}$$
$$\cdot \frac{\sin\left[(k_{z1}D_n^{z\pm} - k_x D_n^{x\pm})\Delta^\pm\right]}{k_{z1}D_n^{z\pm} - k_x D_n^{x\pm}}\, dk_x \tag{5.80}$$

where

$$\rho_{pn}^{\pm\pm} = \left[(x_p^\pm - x_n^\pm - D_n^{x\pm}s')^2 + (z_p^\pm - z_n^\pm - D_n^{z\pm}s')^2\right]^{\frac{1}{2}} \tag{5.81}$$

$$D_n^{x\pm} = \hat{\rho}_n^\pm \cdot \hat{x}, \quad D_n^{z\pm} = \hat{\rho}_n^\pm \cdot \hat{z} \tag{5.82}$$

with $\Delta^\pm = h_n^\pm/2$, and where the $\pm$ in front of integrals (5.79) and (5.80) corresponds to the segment $S_n^\pm$. Substituting (5.72) through (5.77) into (5.70), and (5.78) into (5.71), one obtains the matrix elements for the case of a strip confined to the cover region. In a manner similar to that mentioned in Section 5.2, the integrals in (5.70) and (5.71) may be reused for different matrix elements.

The homogeneous system (5.65) has non-trivial solutions for those values of k_y, which render its determinant vanish. Hence, to obtain the propagation constants of the various modes of the microstrip, a search is performed for the zeroes of the determinant in the complex k_y-plane. For each propagation constant, the homogeneous system (5.65) is solved for the corresponding modal current distribution.

Chapter 6

Numerical Evaluation of Sommerfeld Integrals

The dyadic and scalar kernels of the MPIE comprise Sommerfeld integrals $S_n(\tilde{f})$ of the form (3.3). When the MPIE is solved by the MOM, as discussed in the previous chapter, these integrals must be numerically evaluated for wide ranges of variation in media parameters, frequency, and spatial variables. Several numerical algorithms for the computation of those integrals are developed in this chapter, based on the deformation of the integration path off the real axis into the complex k_ρ-plane. Section 6.1 contains a detailed discussion of the integrals associated with the half-space problem. One of the techniques developed therein is also employed to evaluate the improper integrals that arise in the grounded slab geometry pertinent to microstrip patch antennas. Section 6.2 is devoted to the evaluation of spectral integrals associated with the microstrip transmission line problem.

6.1 Sommerfeld Integrals for the Half-Space Problem

The Sommerfeld integrals encountered in this work can be expressed as ($cf.$ (3.3))

$$S_n[\tilde{f}(k_\rho)] = \int_0^\infty \tilde{f}(k_\rho)\, J_n(\xi\, k_\rho) k_\rho^{\,n+1}\, dk_\rho. \tag{6.1}$$

For the half-space problem, the integrand in (6.1) is given as

$$\tilde{f}(k_\rho) = \frac{N(k_1, k_2; k_\rho)}{D(k_1, k_2; k_\rho)} \begin{cases} e^{-jk_{z1}|z+z'|}, & m = i \\ e^{-j(k_{zm}|z|+k_{zi}|z'|)}, & m \neq i \end{cases} \tag{6.2}$$

where the functions N and D can assume different forms ($cf.$ Appendix A.1), and where

$$k_{zi} = \sqrt{k_i^2 - k_\rho^{\,2}}, \quad i = 1, 2. \tag{6.3}$$

The function k_{zi} has branch points at $k_\rho = \pm k_i$. For analytical convenience, we will assume that the media are lossy; that is, $k_i = k_i' - jk_i''$, where both k_i' and k_i'' are positive numbers. A lossless medium will be considered to be the limit of a lossy medium as the dissipation goes to zero ($k_i'' \to 0$). We also assume that $k_2' > k_1'$ and $k_2'' > k_1''$, which hold in most practical situations. To specify k_{zi} uniquely, we may view the complex k_ρ-plane, where $k_\rho = \zeta' + j\zeta''$, as a two-sheeted Riemann surface with the sheets connected along the branch cuts. On this surface, k_{zi} is a single-valued analytic function of k_ρ. The choice of the branch cuts in the complex k_ρ-plane is rather arbitrary, although a particular choice may be convenient for a specific problem. In this work, we exclusively use the branch cuts specified by the requiremert that $\mathrm{Im}(k_{zi}) < 0$ everywhere on one sheet, referred to as the top or proper sheet. The other sheet, on which $\mathrm{Im}(k_{zi}) > 0$, is then referred to as the bottom, or improper sheet. This definition implies that the two sheets are joined together by the curve defined by $\mathrm{Im}(k_{zi}) = 0$, which therefore locates the desired branch cut. Let us first write [55]

$$k_{zi}^2 = |k_{zi}|^2 e^{j\theta} = k_i^2 - k_\rho^2, \quad -2\pi < \theta < 2\pi \tag{6.4}$$

whence

$$k_{zi} = |k_{zi}| e^{j\theta/2}. \tag{6.5}$$

It is clear that if $\mathrm{Im}(k_{zi}) < 0$, $-\pi < \theta/2 < 0$, and if $\mathrm{Im}(k_{zi}) > 0$, $0 < \theta/2 < \pi$. This suggests that we define a two-sheeted k_{zi}^2-plane, where $-2\pi < \theta < 0$ on the top sheet and $0 < \theta < 2\pi$ on the bottom sheet, as shown in Fig. 6.1. These sheets are joined along the positive real axis, where

$$\mathrm{Im}(k_{zi}^2) = 0 \quad \text{and} \quad \mathrm{Re}(k_{zi}^2) \geq 0. \tag{6.6}$$

For later reference, we also show in Fig. 6.1 the regions where $\mathrm{Re}(k_{zi}) > 0$ and $\mathrm{Re}(k_{zi}) < 0$ in the entire two-sheeted k_{zi}^2-plane. We now map the two-sheeted k_{zi}^2-plane into a two-sheeted k_ρ^2-plane by means of (6.4). The result is shown in Fig. 6.2, where we have introduced the notation

$$k_i^2 = (k_i'^2 - k_i''^2) - j2k_i'k_i'' \equiv \tau + j\Omega. \tag{6.7}$$

It follows from (6.4) and (6.7) that the branch cuts in the k_ρ^2-plane are defined by

$$\mathrm{Re}(k_\rho^2) \leq \tau \quad \text{and} \quad \mathrm{Im}(k_\rho^2) = \Omega. \tag{6.8}$$

64

Figure 6.1: Two sheets of the k_{zi}^2-plane. (a) Top sheet ($\operatorname{Im} k_{zi} < 0$) and (b) bottom sheet ($\operatorname{Im} k_{zi} > 0$).
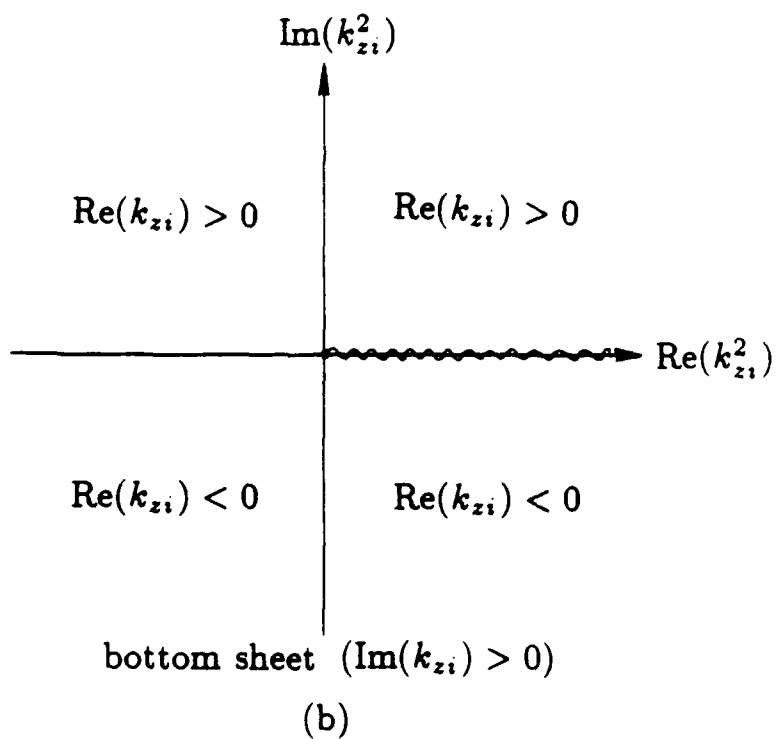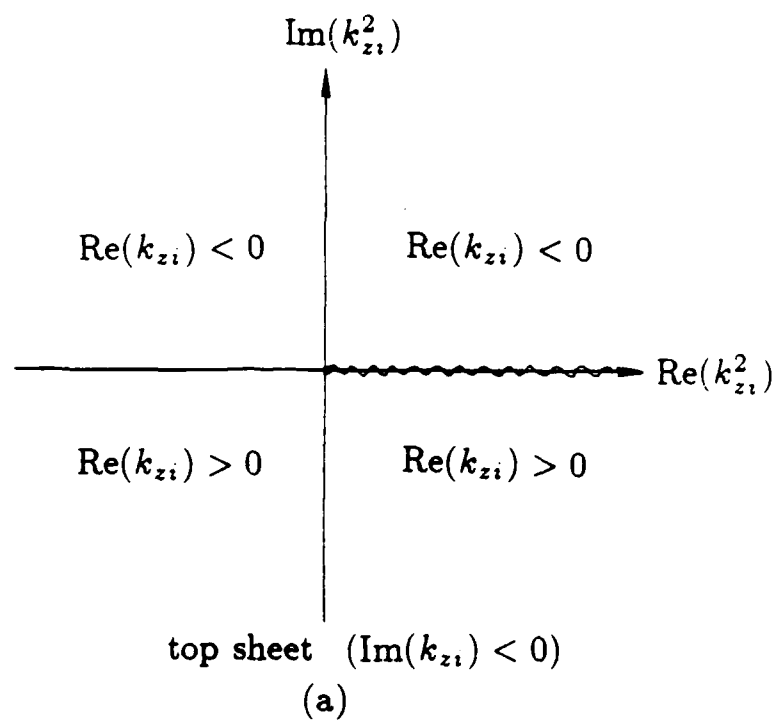
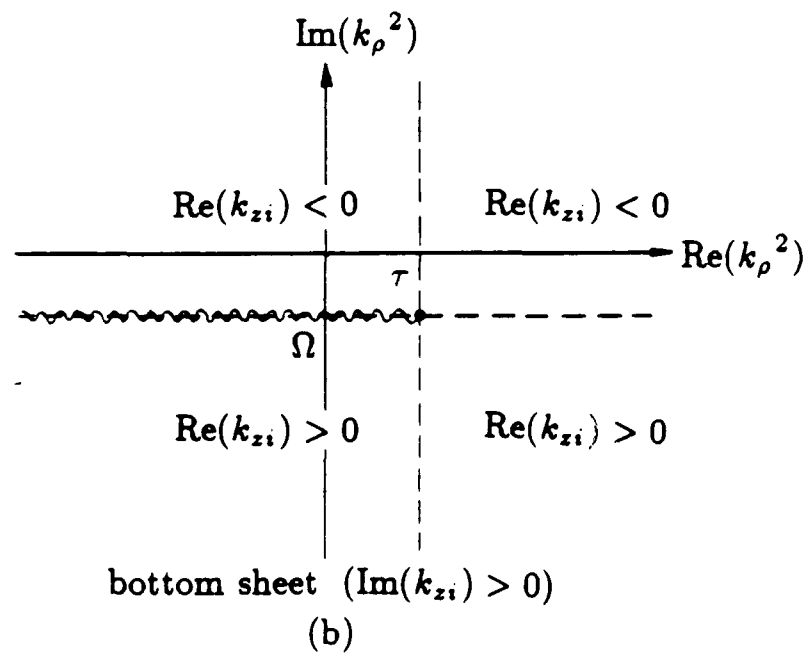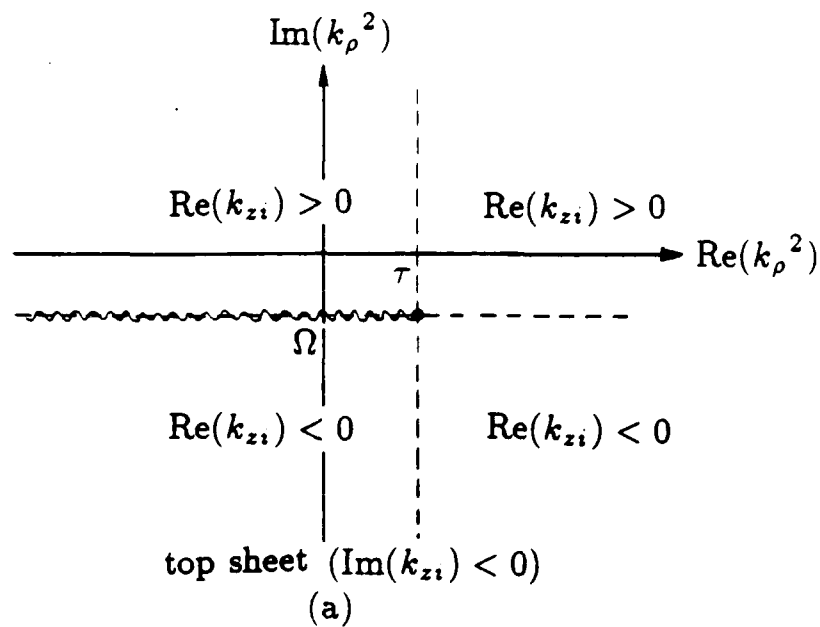Figure 6.2: Two sheets of the k_ρ^2-plane. (a) Top sheet ($\text{Im} k_{zi} < 0$) and (b) bottom sheet ($\text{Im} k_{zi} > 0$).

Finally, the two-sheeted complex $k_\rho{}^2$-plane is mapped into a two-sheeted k_ρ-plane. Noting that $k_\rho{}^2 = \zeta'^2 - \zeta''^2 + j2\zeta'\zeta''$, we conclude from (6.8) that the branch cuts in the k_ρ-plane are specifed by

$$\zeta'^2 - \zeta''^2 < \tau, \text{ and } 2\zeta'\zeta'' = \Omega. \tag{6.9}$$

This mapping is illustrated in Fig. 6.3.

So far, we have only considered a single square root function k_{zi}. However, the integrand of (6.1) depends on both k_{z1} and k_{z2}. Therefore, to make it single-valued, we must introduce two pairs of branch cuts in the k_ρ-plane, defined by $\text{Im}(k_{z1}) = 0$ and $\text{Im}(k_{z2}) = 0$, respectively (Fig. 6.4a). We may now view the k_ρ-plane as a four-sheeted Riemann surface, as illustrated schematically in Fig. 6.4b [33]. Observe that everywhere on Sheet I, $\text{Im}(k_{z1}) < 0$ and $\text{Im}(k_{z2}) < 0$.

In addition to the branch point discussed above, the integrand of (6.1) may exhibit a pair of first order poles at the zeroes of the denominator function

$$D(k_1, k_2; k_\rho) = \epsilon_1 k_{z2} + \epsilon_2 k_{z1} \tag{6.10}$$

which are given by

$$k_{\rho p} = \pm \sqrt{\frac{k_1^2 k_2^2}{k_1^2 + k_2^2}}. \tag{6.11}$$

These poles only exist on Sheets I and IV. Their location is indicated in Fig. 6.4a, which represents Sheet I of the Riemann surface.

In view of the above discussion it should be clear that to ensure the convergence of the integral (6.1), the integration path should be selected on Sheet I, as illustrated in Fig. 6.4a.

Numerical evaluation of the Sommerfeld integrals (6.1) is difficult because of the oscillatory behavior of the integrand and its rapid variation near the singularitites (branch points and poles). Various numerical integration techniques have been developed to carry out these integrals. The real-axis path has been used in related problems by Siegel and King [56], Kuo and Mei [57], Lin and Mei [58], Katehi and Alexopoulous [59], Johnson and Dudley [60], and Mosig and Gardiol [17, 61]. The techniques of deforming the integration path to a contour off the real axis to avoid the singularities and to accelerate convergence of the integrals have been developed by Miller *et al.* [62], Sarkar [63], Burke *et al.* [50], Michalski [24] and Michalski and Butler [64]. The method of deforming the integration path from the real axis to vertical branch cuts has been used by Fuller and Wait [65], and Kong *et al.* [66]. Several approximate approaches have been used by Hansen [67], and by Mosig and Gardiol [61].
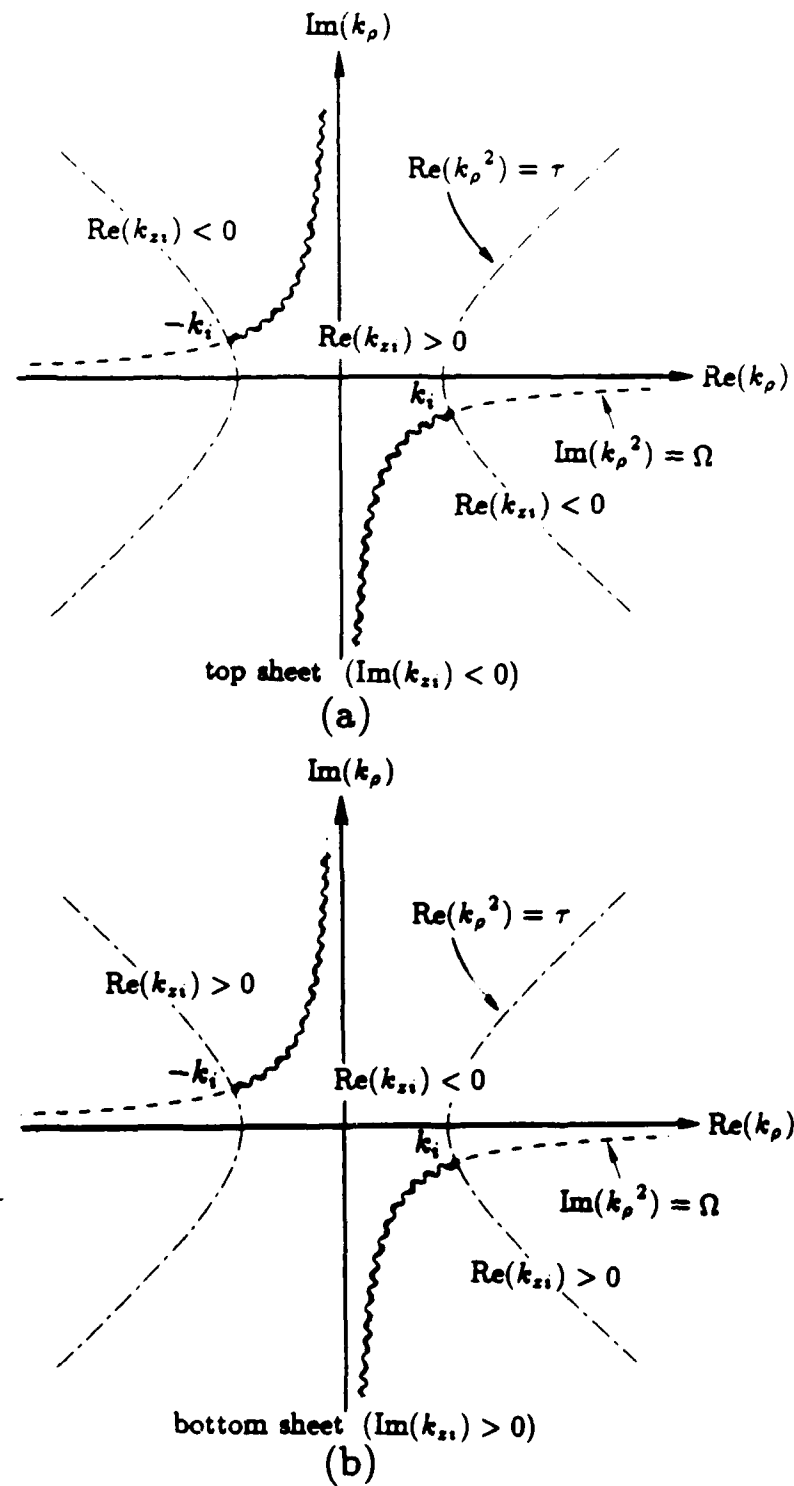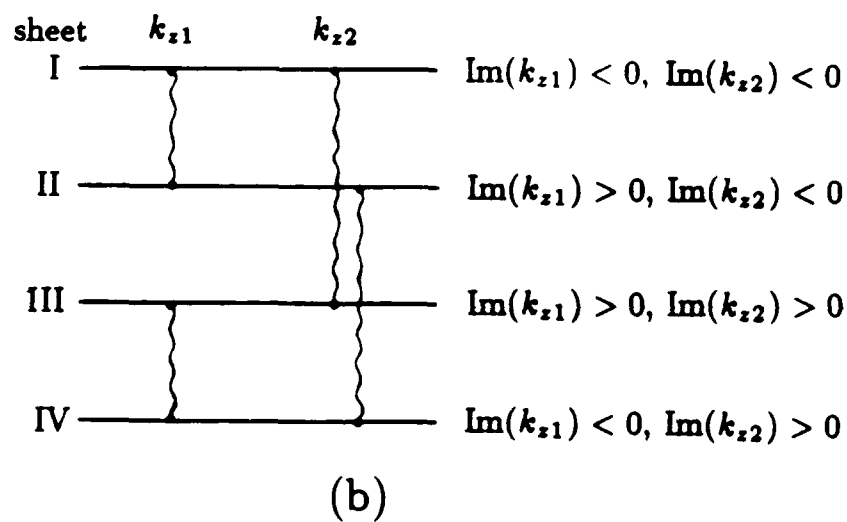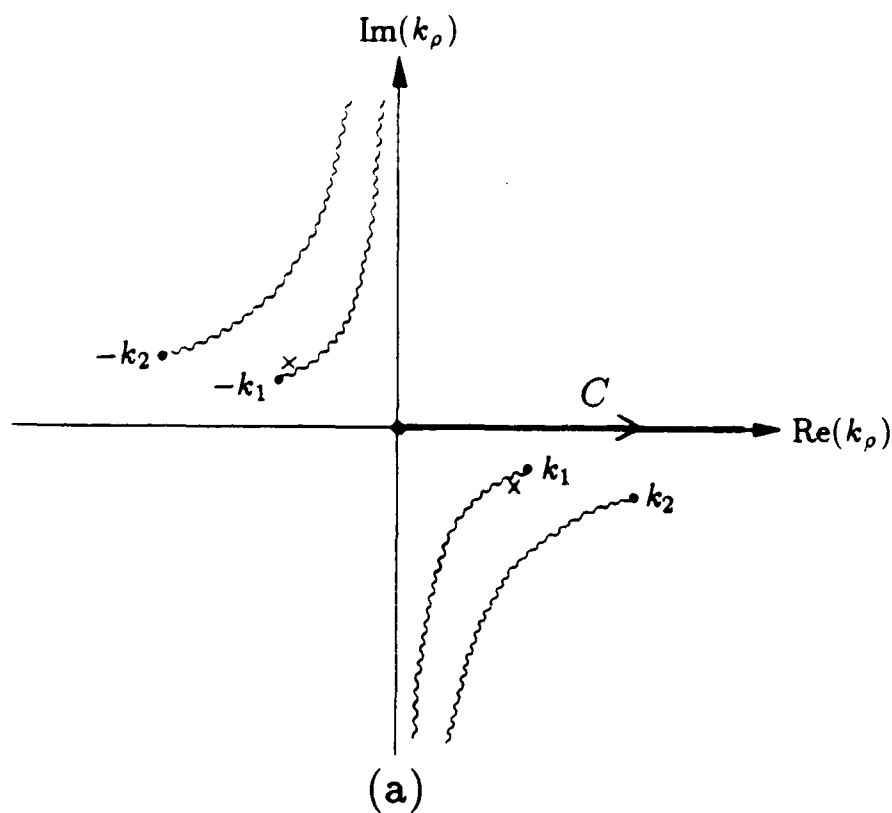
Figure 6.3: Two sheeted k_ρ-plane. (a) Top sheet ($\mathrm{Im}\, k_{zi} < 0$) and (b) bottom sheet ($\mathrm{Im}\, k_{zi} > 0$).

Figure 6.4: (a) The k_ρ-plane showing the branch cuts for k_{z1} and k_{z2}. (b) The Riemann surface of four sheets in the k_ρ-plane.

The steepest descent path (SDP) is probably the most efficient one to use [24]. However, since a closed form expression for the SDP is not available when r and r' are in different layers, we employ in this work, as a compromise, four suboptimal paths, which are chosen depending on the relative values of $\xi = |\rho - \rho'|$ and $h = |z| + |z'|$, and on the parameters of the media. The necessity to evaluate Bessel functions of complex arguments on these paths does not significantly affect the efficiency of our approach, because it has been demonstrated by Grun and Rahmat-Samii [68] that the simple polynomial approximations of Bessel functions given in [69] can be analytically continued into the complex plane. Since all the paths employed, or similar, have been previously described in the literature, we only summarize them below.

Path I

The integration path developed by Michalski and Butler [64] is illustrated in Fig. 6.5a. This path avoids the real-axis singularities and is the SDP for the exponential function part of the integrand (but not for the whole integrand). Hence, on this path the exponential function decreases monotonically, because the imaginary part of the exponent is by definition constant on the SDP. When the source and observation points are in the same layer i for $i = 1, 2$, one can use the transformation

$$k_\rho = sk_0\sqrt{2jn_i + s^2}, \ 0 \le s < \infty \tag{6.12}$$

where s is a real variable, $n_i = \sqrt{\epsilon_i}$ and $\mathrm{Re}\sqrt{\ } > 0$. If $i \ne m$, i.e., the source and field points are in different layers, we choose

$$k_\rho = k_0\sqrt{\frac{-2C}{B + \sqrt{B^2 - 4AC}}}, \ 0 \le s < \infty \tag{6.13}$$

in which the $\mathrm{Re}\sqrt{\ } > 0$ and $\mathrm{Im}\sqrt{\ } < 0$ branches should be selected for the external and internal roots, respectively. The parameters in (6.13) are given as
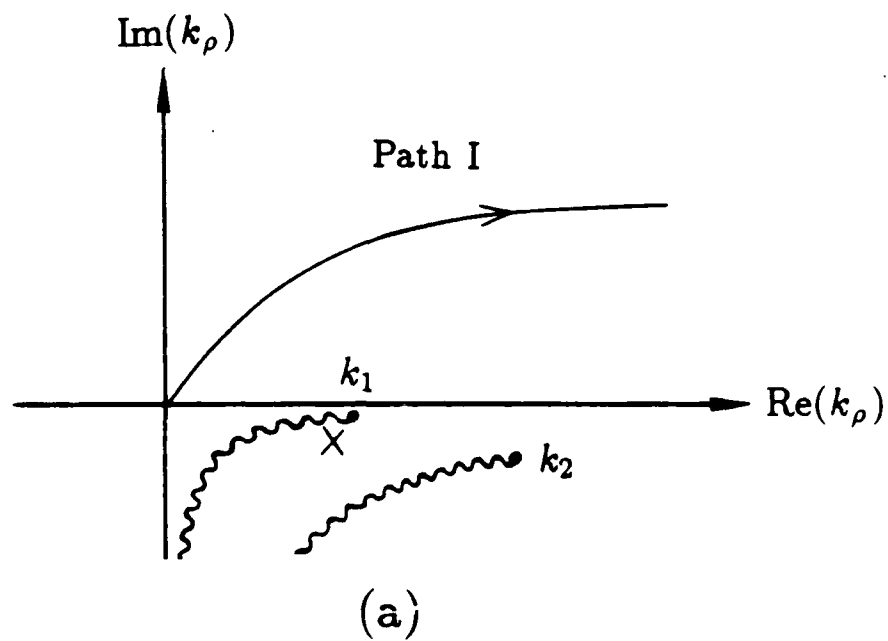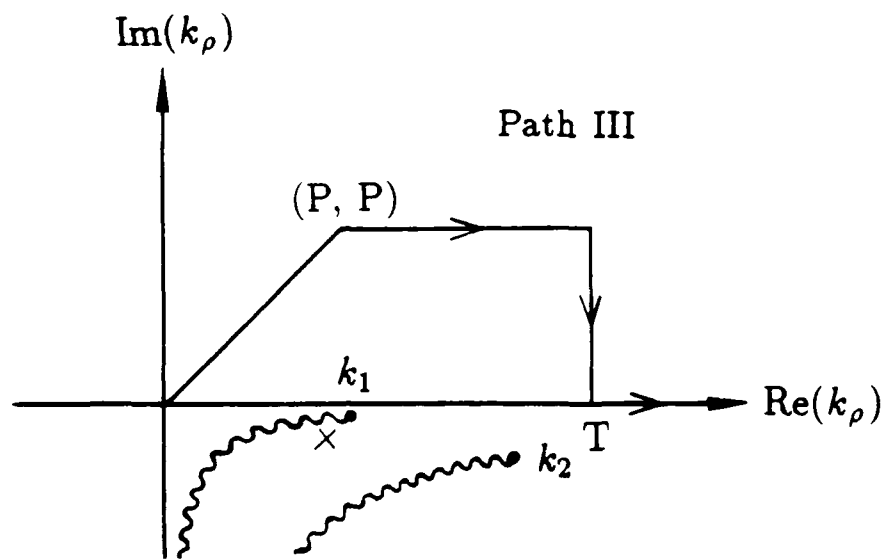
$$A = (z'^2 - z^2)^2 \tag{6.14}$$

$$B = 4|z'z|de - 2s(z'^2 + z^2) \tag{6.15}$$

$$C = s^2 - 4sn_in_m|z'z| \tag{6.16}$$

with

$$d = n_i|z'| + n_m|z| \tag{6.17}$$

70

Im(k_ρ)

Path I

k_1

Re(k_ρ)

k_2

(a)

Im(k_ρ)

Path II

(P, P)

k_1

Re(k_ρ)

k_2

(b)

71
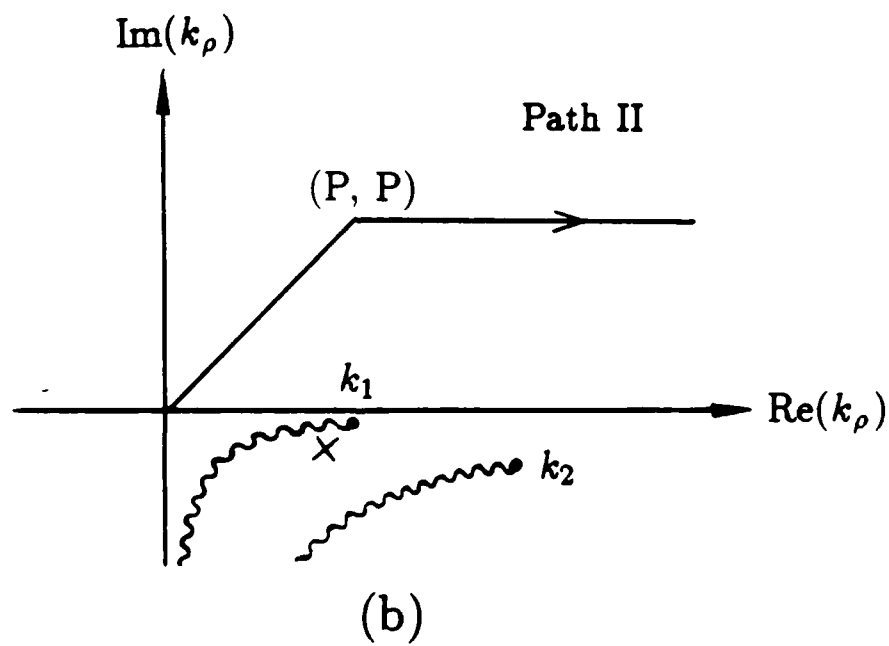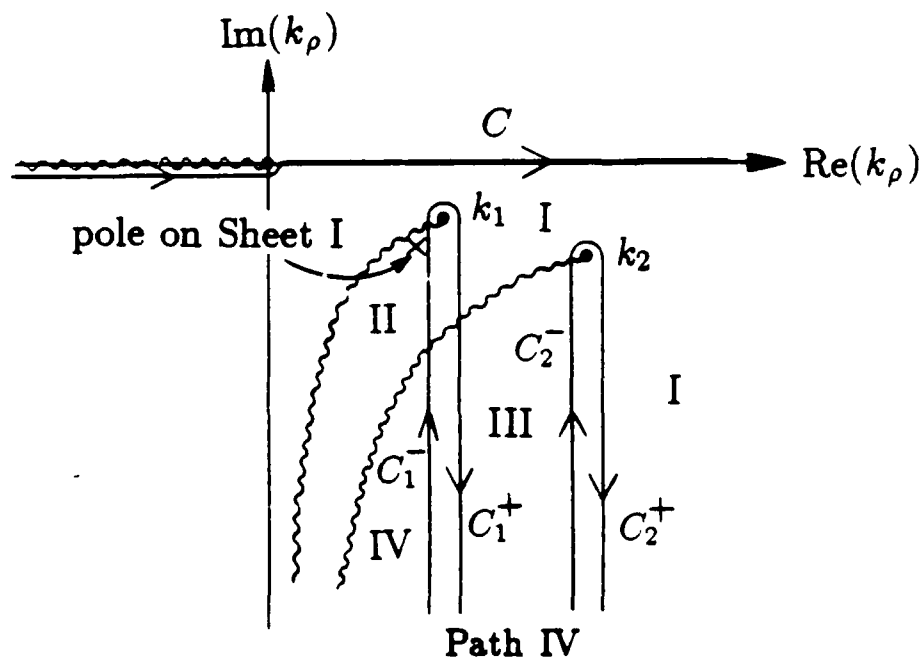
Figure 6.5: Various integration paths in the complex k_ρ-plane.

$$c = n_i |z| + n_m |z'|. \tag{6.18}$$

Since the oscillations due to the Bessel function are still present, this path selection is most efficient when $h = |z'| + |z| > \xi$. Also, the exponential growth of the Bessel function away from the real axis limits how far the path can veer off into the complex plane, which restricts the applicability of this method. In the case $m = i$, this method is applicable provided ξ is electrically small in the mediumi, *i.e.*,

$$k_0 \xi < \frac{1}{n_i'}. \tag{6.19}$$

When $m \neq i$, this restriction becomes

$$k_0 \xi < \frac{|z'| + |z|}{n_i' |z'| + n_m' |z|}. \tag{6.20}$$

To numerically evaluate the integral (6.1) along this path, a low-order Gauss-Legrandre quadrature is repeatedly employed between consecutive "break points," which are derived from the real-axis zeroes of the Bessel function. When each of three consecutive intervals contributes less than 10^{-4} of the accumulated sum, the semi-infinite integration is terminated and is said to converge.

Path II

An alternate path [50], which initially strays from the real axis to avoid the branch points at k_1 and k_2, then continues parallel to the real axis, as shown in Fig. 6.5b, has been used to overcome the limitations (6.19) and (6.20) in using Path I. The parameter P is chosen according to

$$P = \min\left(\frac{1}{\xi}, \frac{1}{h}\right). \tag{6.21}$$

which restricts the contour to small values of $\xi \, \mathrm{Im}(k_\rho)$, to limit the growth of the Bessel function. This compromise path accelerates the convergence of the exponential function (even though it is not the SDP), while avoiding the overflow in the evaluation of the Bessel function. On this path we employ the same numerical integration technique as that used on Path I

Path III

When $\xi \gg h$, especially when $h = 0$, Paths I and II are not efficient, because there may be many oscillations of the Bessel function before convergence is achieved. Therefore, we introduce Path III, which initially strays from the real axis to avoid the singularities, then returns at $k_\rho = T$ to the real axis. The point T is arbitrarily chosen as $T = k_0(n_2 + 1)$

(recall that we assume $k_2' > k_1'$). On the first part we employ the same numerical integration technique as that used on Path I. On the real axis ($k_\rho > T$) we employ the method of averages [17, 61, 70], which is summarized below.

Let us consider the integral

$$I = \int_T^\infty f(k_\rho) \, J_n(\xi k_\rho) \, k_\rho^{n+1} \, dk_\rho \qquad (6.22)$$

where $f(k_\rho)$ is a continuous function, and $J_n(\xi k_\rho)$ has successive zeroes, k_{ρ_m}, superior to the integration boundary T. It follows from the method of averages [17, 61] that

$$I \approx I_1^M = 2^{1-M} \sum_{m=1}^M \binom{M-1}{m-1} I_m^1 \qquad (6.23)$$

where

$$I_m^1 = \int_T^{k_{\rho_m}} f(k_\rho) \, J_n(\xi k_\rho) k_\rho^{n+1} \, dk_\rho, \quad m = 1, 2, \ldots, M. \qquad (6.24)$$

The choice of M in (6.23) depends on the requirement of the accuracy in the problem. In this work, we choose $M = 5$. The method of averages is especially suitable when the observation and source points are on the interface. We find that one still can obtain the accurate result of Sommerfeld integrals by using this method when the observation and source points are off the interface, provided that $\xi \gg h$.

Path IV

Integration along Path III becomes inefficient when ξ becomes large, because there may be many oscillations of the Bessel function between 0 and T. In this case, it is useful to deform the integration path to two vertical paths, as shown in Fig. 6.5d. For this purpose, by using the relation

$$2J_n(x) = H_n^{(2)}(x) + (-1)^{n+1} H_n^{(2)}(-x) \qquad (6.25)$$

where $H_n^{(2)}$ is the Hankel function of the second kind and order n, one can express (6.1) as

$$S_n(\tilde{f}) = \frac{1}{2} \int_{-\infty}^\infty \tilde{f}(k_{z1}, k_{z2}; k_\rho) \, Q_n(\xi k_\rho) \, k_\rho^{n+1} e^{-J\xi k_\rho} \, dk_\rho \qquad (6.26)$$

where we have introduced

$$Q_n(\xi k_\rho) = H_n^{(2)}(\xi k_\rho) e^{J\xi k_\rho} \qquad (6.27)$$

74

which has the asymptotic form [69]

$$Q_n(\xi k_\rho) \sim \sqrt{2/(\pi \xi k_\rho)}\, e^{j(\frac{1}{2}n+\frac{1}{4})\pi}. \tag{6.28}$$

It is noted the transformation (6.25) introduces a branch point singularity at $k_\rho = 0$ and the associated branch cut on the negative real axis (Fig. 6.5d). Hence, the integral (6.26) should be taken in the Cauchy principal value sense for $n \geq 1$. As a result, (6.26) becomes

$$S_n(\tilde{f}) = \int_C g(k_\rho)\, dk_\rho - j\pi \mathrm{Res}\{g(0)\} \tag{6.29}$$

where

$$g(k_\rho) = \frac{1}{2}\tilde{f}(k_\rho)\, Q_n(\xi k_\rho) k_\rho{}^{n+1} e^{-j\xi k_\rho} \tag{6.30}$$

and Res $\{g(0)\}$ is the residue of the integrand at $k_\rho = 0$. The integration path C is that illustrated in Fig. 6.5d. In the following analysis, we will refer to this path as the "original" path of integration.

We observe that when $\mathrm{Im}(k_\rho)$ becomes negative, the integrand in (6.26) decays exponentially. It is clear that, for large values of ξ, one should deform the integration path into the vertical paths [65, 66] as illustrated in Fig. 6.5d. The integral (6.26) can be written in this case as

$$S_n = S_n^{(1)} + S_n^{(2)} \tag{6.31}$$

where $S_n^{(1)}$ and $S_n^{(2)}$ are the integrals along the two vertical paths emanating from k_1 and k_2, respectively, as shown in Fig. 6.5d. Referring to Figs. 6.3 and 6.4, we observe that the integration path C_1 starts on Sheet IV, where $\mathrm{Re}(k_{z1}, k_{z2}) \geq 0$, and proceeds upward along the vertical; it leaves Sheet IV when it crosses the k_{z2} branch cut, and enters a region of Sheet II, where $\mathrm{Re}(k_{z1}, k_{z2}) \geq 0$; it then reaches Sheet I, where $\mathrm{Re}(k_{z1}) \leq 0$ and $\mathrm{Re}(k_{z2}) \geq 0$, when it crosses the k_{z1} branch cut; it turns around the branch point at k_1 and goes down along the vertical; finally, it leaves Sheet I when it crosses the k_{z2} branch cut, and enters a region of Sheet III, where $\mathrm{Re}(k_{z1}) \leq 0$ and $\mathrm{Re}(k_{z2}) \geq 0$. Similar analysis indicates that the path C_2 starts on Sheet III, proceeds upward along the vertical from Sheet III to Sheet I, and reaches the branch point at k_2. On this part of C_2, $\mathrm{Re}(k_{z1}) \leq 0$ and $\mathrm{Re}(k_{z2}) \geq 0$. The integration path C_2 finally emanates from k_2 and proceeds down along the vertical on Sheet I, where $\mathrm{Re}(k_{z1}, k_{z2}) \leq 0$. From the above considerations, one can determine the branches of the square root functions k_{z1} and k_{z2} along the vertical paths as follows:

75

$$\begin{aligned}
&\text{Re}(k_{z1}, k_{z2}) > 0, && \text{on } C_1^- \\
&\text{Re}(k_{z1}) < 0, \ \text{Re}(k_{z2}) > 0, && \text{on } C_1^+ \text{ and } C_2^- \\
&\text{Re}(k_{z1}, k_{z2}) < 0, && \text{on } C_2^+.
\end{aligned} \tag{6.32}$$

Introducing the variable transformations

$$k_\rho = k_1 - jk_0 s^2, \ \ 0 \le s < \infty, \ \ \text{on } C_1 \tag{6.33}$$

$$k_\rho = k_2 - jk_0 s^2, \ \ 0 \le s < \infty, \ \ \text{on } C_2 \tag{6.34}$$

we obtain the following integrals by invoking (6.32):

$$S_n^{(1)} = \frac{e^{-jk_1\xi}}{2} \int_0^\infty \left[\tilde{f}(-k_{z1}, k_{z2}; k_\rho) - \tilde{f}(k_{z1}, k_{z2}; k_\rho) \right]$$

$$\left. \cdot Q_n(\xi k_\rho) \, k_\rho^{n+1} \right|_{k_\rho = k_0(n_1 - js^2)} (-2jk_0 s)e^{-k_0\xi s^2} \, ds \tag{6.35}$$

and

$$S_n^{(2)} = \frac{e^{-jk_2\xi}}{2} \int_0^\infty \left[\tilde{f}(-k_{z1}, -k_{z2}; k_\rho) - \tilde{f}(-k_{z1}, k_{z2}; k_\rho) \right]$$

$$\left. \cdot Q_n(\xi k_\rho) \, k_\rho^{n+1} \right|_{k_\rho = k_0(n_2 - js^2)} (-2jk_0 s)e^{-k_0\xi s^2} \, ds \tag{6.36}$$

where it is assumed that $\text{Re}(k_{z1}, k_{z2}) \ge 0$. The proximity of the pole at $k_{\rho p}$ (cf. (6.11)) on Sheet I to the integration path C_1 makes the integrand vary rapidly near $s = 0$. To remedy this difficulty, a pole subtraction technique is employed [71], which transforms the integral (6.35) as

$$S_n^{(1)} = \frac{e^{-jk_1\xi}}{2} \left\{ \left(\int_0^\infty \left[\tilde{f}(-k_{z1}, k_{z2}; k_\rho) - \tilde{f}(k_{z1}, k_{z2}; k_\rho) \right] \right. \right.$$

$$\left. \left. \cdot Q_n(\xi k_\rho) \, k_\rho^{n+1} \right|_{k_\rho = k_0(n_1 - js^2)} \left((-2jk_0 s) - \frac{2R_p s_p}{s^2 - s_p^2} \right) e^{-k_0\xi s^2} \, ds + j\pi R_p W\left(\sqrt{k_0\xi}\, s_p\right) \right\} \tag{6.37}$$

where R_p is the Residue of $\{ \tilde{f}(k_{z1}, k_{z2}; k_\rho) Q_n(\xi k_\rho) k_\rho^{n+1} \}$ at $k_\rho = k_{\rho p}$, s_p is the pole location in the s-plane, and $W(z) = e^{-z^2} \text{erfc}(-jz)$ is the Error function [69].

Based on the considerations above and on our computational experience, a set of guidelines has been developed for determining the "best" path of integration. The guide chart is given in Fig. 6.6.
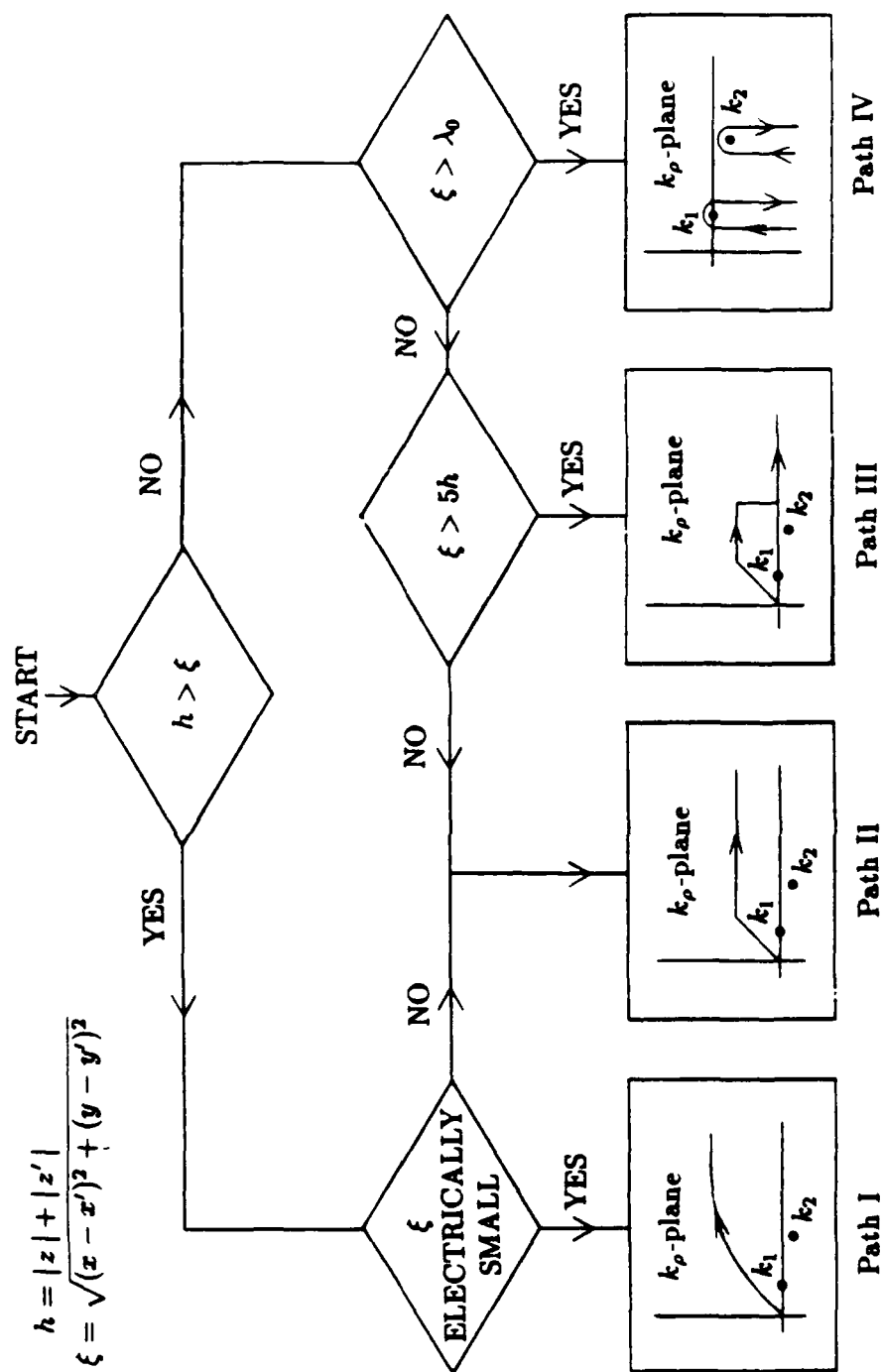
Figure 6.6: Diagram illustrating the selection of integration paths.

The integrals that arise for the grounded slab geometry pertinent to microstrip patch antennas are similar to those considered above. Their integrand functions have similar behavior to those of the half–space problem, except that they do not have branch points associated with the slab region, but have surface wave poles, which are located betwen k_1 and k_2 in the k_ρ-plane. To evaluate those integrals, we have employed Path III shown in Fig. 6.5c, in conjunction with the interpolation scheme described in Section 5.3.

6.2 Sommerfeld Integrals for the Transmission Line Problem

In this section, to simplify the discussion, we only consider the case where the infinite conductor is confined to the cover medium (region 1). A typical integral that arises in this context is given in (5.80). This integral can be expressed in terms of the integrals of the form

$$I = \int_0^\infty \frac{N(k_{z1}, k_{z2}, k_x)}{D^e D^h} e^{-jk_{z1}(z+z')} \left\{ \begin{array}{c} \cos[k_x(x - x')] \\ \sin[k_x(x - x')] \end{array} \right\} dk_x \qquad (6.38)$$

where the cosine or sine functions arise depending on whether the numerator functions N are even or odd in k_x. The denominator functions D^e and D^h are given in (A.38) and (A.39), respectively, and

$$k_{zi} = \sqrt{k_i^2 - k_x^2 - k_y^2}, \quad i = 1, 2. \qquad (6.39)$$

The propagation constant will be expressed as

$$k_y = \beta - j\alpha \qquad (6.40)$$

where β is the phase constant and α is the attenuation constant. It will be assumed that $\alpha \geq 0$ and $\beta > 0$.

It can be shown that the integrand of (6.38) is an even function of k_{z2}. Therefore, unlike in the half-space problem, only one pair of branch points, associated with k_{z1}, arise in the present case. These branch points and the associated branch cuts, selected by the criteria given in Section 6.1, define a k_x-plane as a two-sheeted Riemann surface. As before, $\text{Im}(k_{z1}) < 0$ on the top sheet and the opposite holds on the bottom sheet. Since the value of k_y will be specified on each iteration of the search procedure, we express k_{z1} as

$$k_{z1} = \sqrt{\kappa^2 - k_x^2} \qquad (6.41)$$

78

where we have defined

$$\kappa^2 = k_1^2 - k_y^2 = (k_1^2 - \beta^2 + \alpha^2) + j2\alpha\beta$$
$$= \tau + j\Omega. \tag{6.42}$$

We assume, for simplicity, that the media are lossless. Consequently, k_1 in (6.42) is real.

With the notation introduced above, we can directly use the analysis which led to Fig. 6.2, provided that $k_\rho{}^2$-plane is replaced by k_x^2-plane. Therefore, referring to Fig. 6.2, we define the branch cut in the k_x^2-plane by

$$\text{Re}(k_x^2) < \tau \quad \text{and} \quad \text{Im}(k_x^2) = \Omega. \tag{6.43}$$

These relations define a pair of branch cuts in the k_x-plane, whose shape depends on the values of k_1 (and thus frequency) and k_y (or α and β). In addition to the branch points, there will also be a finite number of poles in the top sheet of the k_x-plane, contributed by the zeroes of the denominator functions D^e and D^h. These poles are easily determined in the k_ρ-plane (recall that $k_\rho{}^2 = k_x^2 + k_y^2$), where they are located on the real axis between k_1 and k_2, and also between $-k_2$ and $-k_1$ [32]. Their locations in the k_x-plane will depend on the value of k_y. In the following analysis, we assume for simplicity that only one pair of poles, $\pm k_s$, associated with the TM_0 mode of the slab, occurs. This is the case most frequently encountered in practice.

As mentioned above, the shape and location of the branch-cuts in the k_x-plane depends on the value of k_y. Following the analyses of [72, 73, 74], we divide the range of k_y into three subregions, according to

$$\begin{array}{ll} (i) & k_s^2 < \beta^2 < k_2^2, \;\; \alpha = 0 \\ (ii) & k_1^2 < \beta^2 - \alpha^2 < k_s^2 \\ (iii) & -\infty < \beta^2 - \alpha^2 < k_1^2 \end{array} \tag{6.44}$$

where $\beta^2 - \alpha^2 = \text{Re}(k_y^2)$. In region i, k_y is real and the stripline mode is bound, *i.e.*, it propagates unattenuated. The fields of bound modes are concentrated in the region of the strip and decay exponentially in transverse directions away from it. In regions ii and iii, k_y is complex ($\alpha > 0$), and the mode is said to be leaky [72, 73, 74]. In this regime, the mode is attenuated as it propagates, due to the leakage of energy into the environment. In region ii, there is only leakage into a surface wave of the slab, which propagates away from the strip. It can be shown [72] that the field of such mode decays exponentially in the z direction, but increases exponentially away from the strip in $\pm x$ directions. For k_y in region iii, the

79

leakage is both into the surface wave and into the space wave. The field amplitude increases exponentially in the directions perpendicular to the strip [72, 75].

Let us first consider the bound modes, for which k_y is in region i ($cf.(6.44)$). With $\tau < 0$ and $\Omega = 0$ in (6.42), the two-sheeted complex k_x^2-plane is mapped into a two-sheeted k_x-plane as illustrated in Fig. 6.7a. The poles are in this case located in the $(-i\sqrt{k_y^2 - k_1^2}, j\sqrt{k_y^2 - k_1^2})$ interval of the imaginary k_x-axis, as shown in Fig. 6.7a. The integration path in (6.38) is chosen along the real axis on the top sheet (Fig. 6.7a).

When k_y passes from region i to region ii, k_y acquires the imaginary part, so that $\tau < 0$ and $\Omega > 0$. In this process the pole on the negative imaginary axis in the k_x-plane moves to the origin, then enters the first quadrant, as illustrated in Fig. 6.7b. In a like manner, the pole on the positive imaginary axis moves to the third quadrant. The integration path must be deformed so that the pole in the first quadrant lies below the path, as illustrated in Fig. 6.7b. The first quadrant pole contributes an exponentially increasing surface wave, in agreement with the discussion above.

When k_y moves from region ii to region iii, the value of τ changes sign, hence in region iii $\tau > 0$ and $\Omega > 0$ ($cf.$ (6.42) and (6.44)). At the transition point $\tau = 0$, the branch points in the first and third quadrants switch positions along the diagonal line in the k_x-plane. Therefore, the integration path must go above the branch point κ in the first quadrant, as illustrated in Fig. 6.7c. One can prove that this, in turn, leads to a modal field which grows exponentially in the z direction [75]. The dashed line on the integration path in Fig. 6.7c signifies that the path is on the bottom sheet.

As the above analysis indicates, different integration paths must be employed depending on which mode is being computed. The various paths are suggested in Fig. 6.7. In the computer implementation, to accelerate the convergence of the integral and to avoid the singularities, slightly modified paths, shown in Fig. 6.8, have been employed. For bound modes, we use the paths shown in Fig. 6.8a, where the value of P is arbitrarily chosen as $P = k_1$. For k_y in region ii, the paths in Fig. 6.8b are employed, where P is the same as that in Fig. 6.8a and the value of T is chosen as $T = |\operatorname{Re}(k_2^2 - k_y^2)^{\frac{1}{2}}| + k_1$, to ensure that the pole is located to the left of this point. The integration around the pole is carried out by the method of residues. For k_y in region iii, we employ the paths shown in Fig. 6.8c, where T is the same as that in Fig. 6.8b and the value of P is chosen as $P = |\operatorname{Im}(k_1^2 - k_y^2)^{\frac{1}{2}}| + k_1$, to ensure that the branch point in the first quadrant lies below the paths. In all three cases, when $z = z' = 0$ (this is always the case for an infinitely thin strip), we use path C_1 in Fig. 6.8. When the path is on the real axis, the method of averages [17] discussed in the
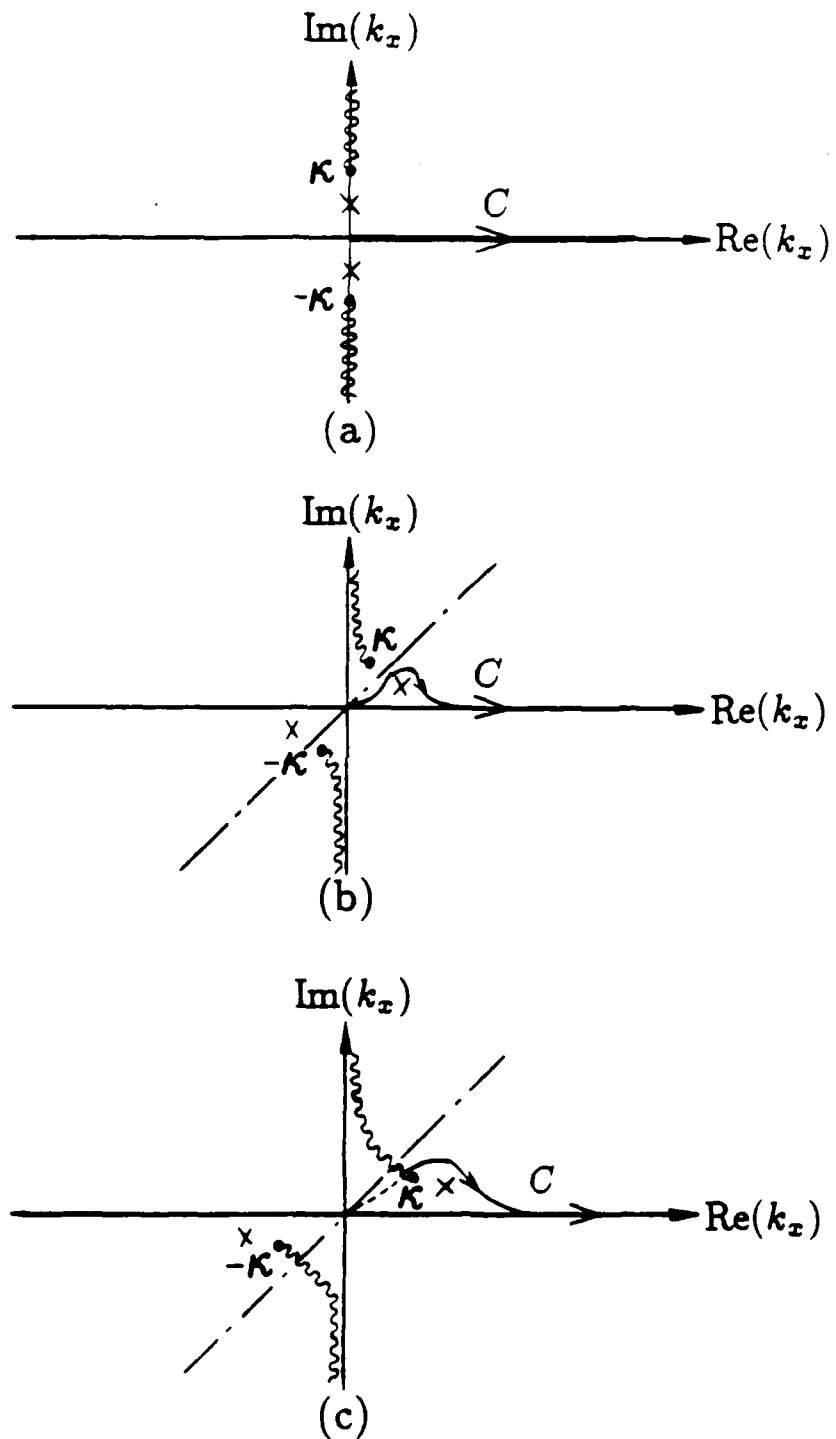
Figure 6.7: The k_x-plane showing the branch cuts, the poles, and the integration paths for (a) bound modes, region i, (b) leaky modes, region ii, and (c) leaky modes, region iii.
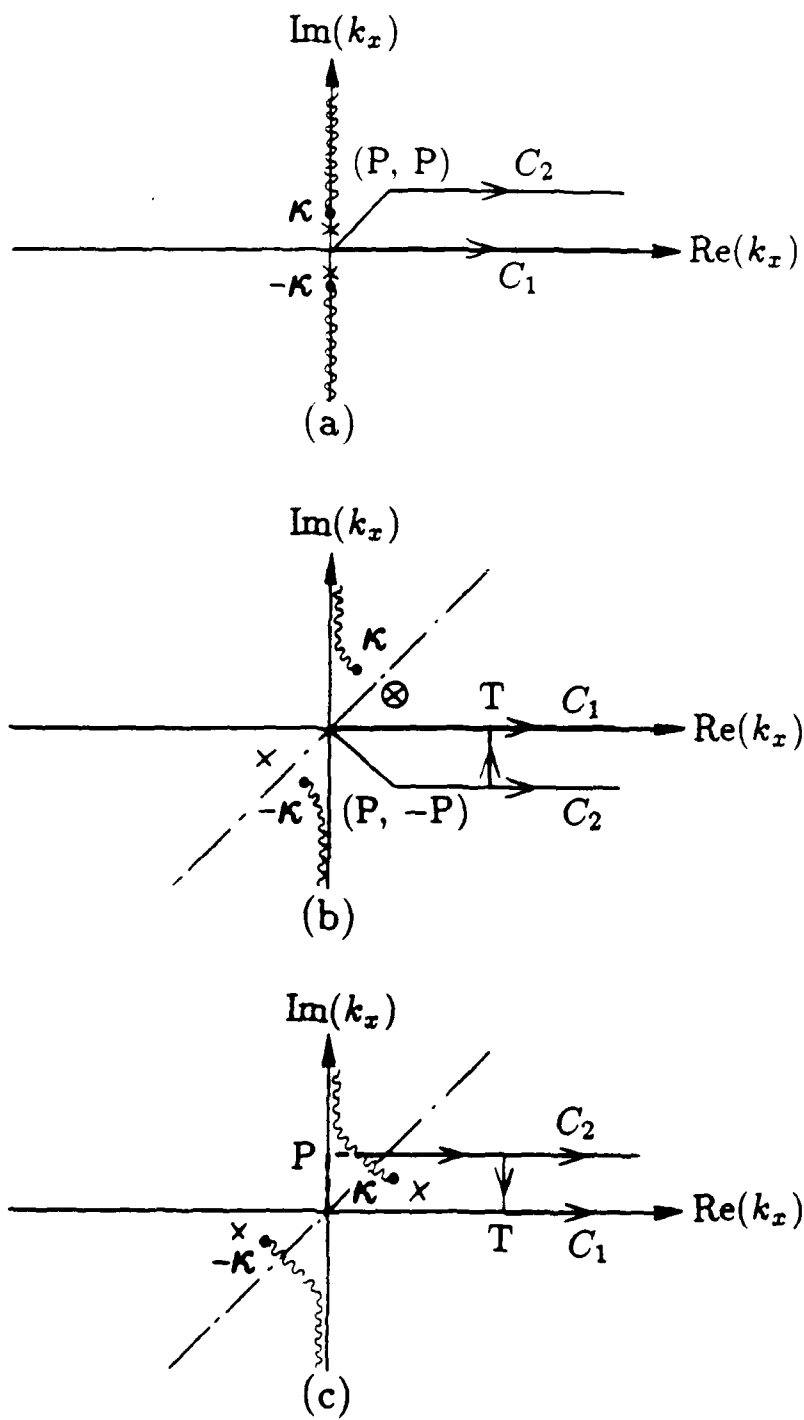
Figure 6.8: Various integration paths actually implemented for (a) bound modes, region i, (b) leaky modes, region ii, and (c) leaky modes, region iii.

previous section is employed to accelerate the rate of convergence. When $h = |z| + |z'| > 0$, path C_2 is used to benefit the convergence from the exponential function associated with h.

Chapter 7

Numerical Results

In this chapter, we present sample numerical results for antennas and scatterers partially buried in earth or water, for coax–fed microstrip patch antennas, and for open microstrip lines. In all cases, the medium of region 1 is free space with parameters $\epsilon_1 = \epsilon_0$ and $\mu_1 = \mu_0$. The medium of region 2 is characterized by ϵ_2 and $\mu_2 = \mu_0$, and it may be lossy or lossless. In the former case, its permittivity is complex and is given as $\epsilon_2 = \epsilon_0 \epsilon_r - j\sigma/\omega$, where ϵ_r and σ are the relative dielectric constant and the conductivity of the medium, respectively, and $\omega = 2\pi f$. The loss tangent, $\tan \delta = \sigma/(\omega\epsilon)$, is also used to characterize the losses of the medium.

In Sections 7.1 and 7.2, to facilitate the interpretation of the results, we take in all cases $f = 300\,\text{MHz}$, which corresponds to free space wavelength $\lambda_0 = 1\,\text{m}$. The results for driven antennas assume unit-strength δ-gap generators, and the results for scatterers assume illumination by plane waves incident normally on the interface.

7.1   Surfaces

We first consider a straight, inclined, thin-wire antenna with radius a, partially buried in dry earth, as illustrated in Fig. 7.1a. In the numerical procedure, the wire was approximated by a flat, narrow strip of equivalent width $4a$ [76], which was modeled by 60 triangular patches, as shown in Fig. 7.1b. In Fig. 7.2, the computed current distributions on the wire are compared with the data from the NEC [27]. A good agreement is observed for the inclination angle $\alpha = 45°$ (Fig. 7.2a), while for $\alpha = 80°$ (Fig. 7.2b) the agreement is less favorable. A possible explanation of this slight disagreement is the fact that in the NEC formulation a charge discontinuity condition at the interface is enforced, which is strictly valid only for the vertical antenna [27]. Obviously, this condition would affect the solution

84
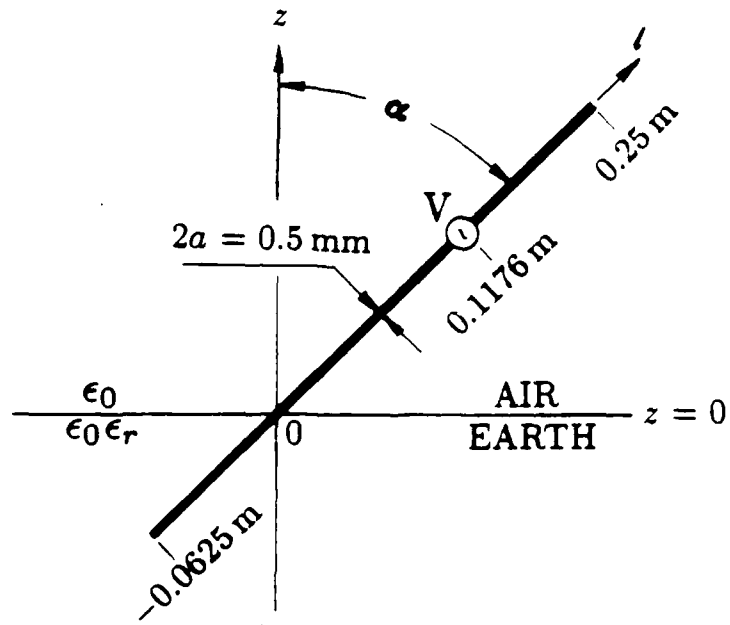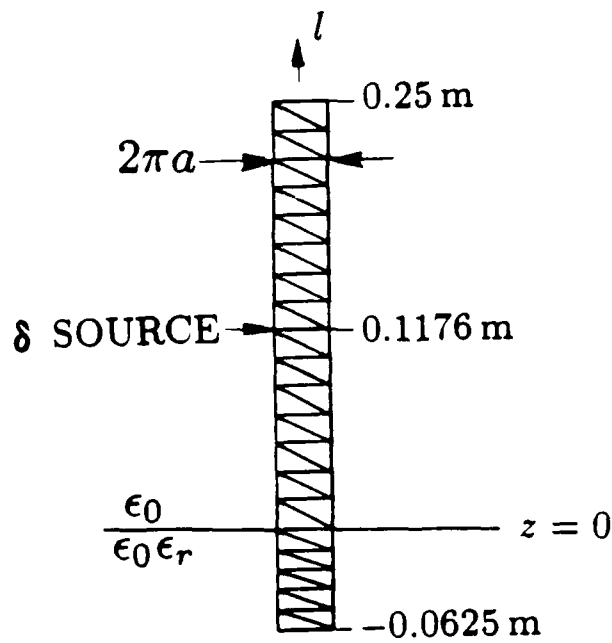
Figure 7.1: (a) Inclined thin-wire antenna partially buried in earth and (b) its strip model.
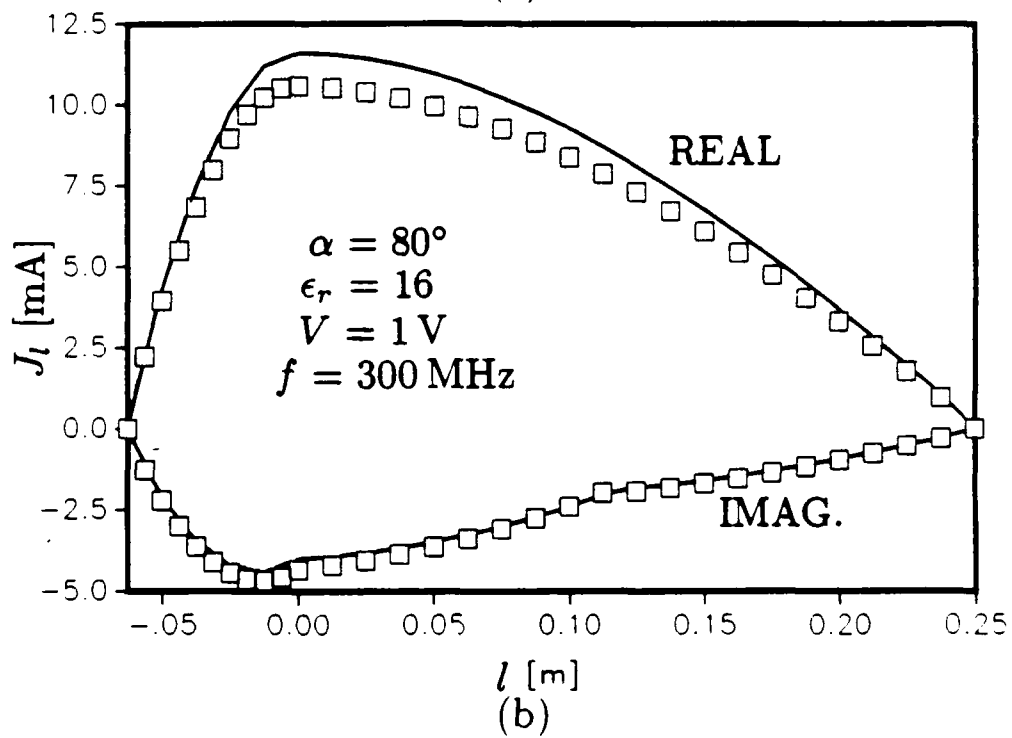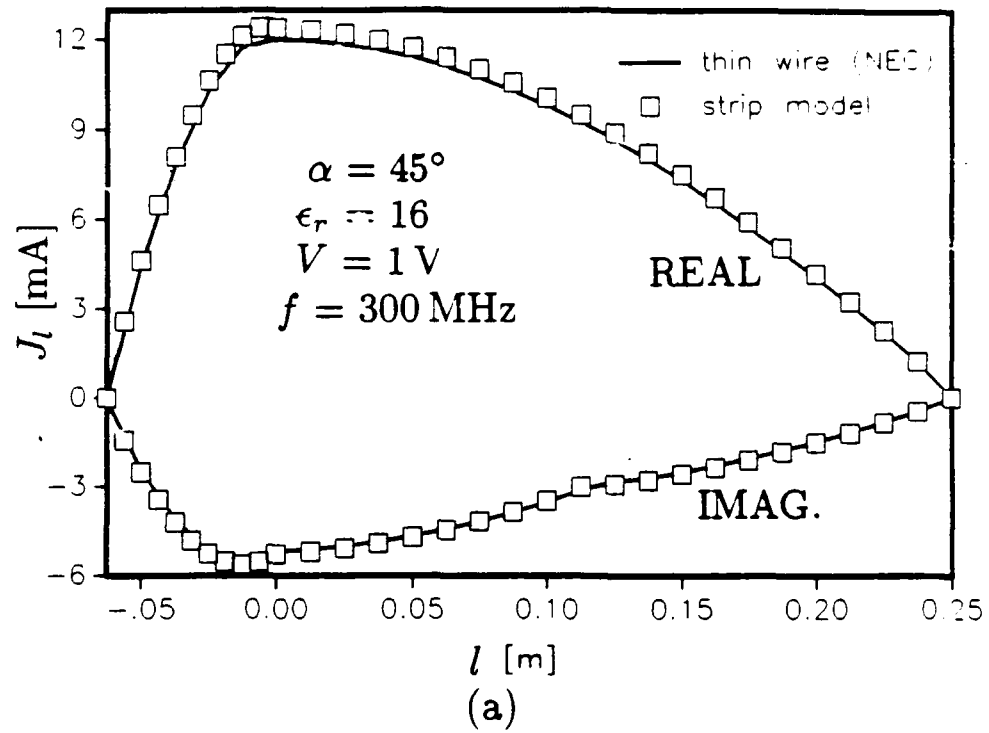
Figure 7.2: Current distribution on the strip model of Fig. 7.1 for (a) $\alpha = 45°$ and (b) $\alpha = 80°$.

more for $\alpha = 80°$ than for $\alpha = 45°$.

In Fig. 7.3 is shown a relatively thick, vertical, cylindrical antenna, which penetrates the interface between two media. This so-called ground stake antenna was previously analyzed by Butler and Michalski [77]. In the numerical procedure, the circular cylinder was approximated by a square cylinder with the same circumference, and was modeled by 112 triangular patches. We show the axial current distribution on the antenna for the cases where the lower medium is dry earth (Fig. 7.4a) and salt water (Fig. 7.4b). Our results are seen to perfectly agree with the data obtained in [77]. Since our code can handle surfaces of arbitrary shape, it was a simple matter to examine the effect of putting the end caps on the hollow cylinder. The resulting current distributions are also displayed in Fig. 7.4. One observes that, as expected, the caps only affect the current near the ends of the cylindrical surface.

The results in Fig. 7.5 are for a finite, hollow, horizontal cylinder, which is partially buried in a dielectric medium (see the inset). The corresponding two-dimensional problem has been solved by Xu [26], who employed the magnetic field integral equation formulation. One observes that both the magnitude (Fig. 7.5a) and phase (Fig. 7.5b) of the normalized current distribution along the circumference and in the middle of the finite tube agree favorably with the corresponding results for the infinite cylinder. In the triangle-patch model of the cylinder, 288 patches were employed.

In Figs. 7.6–7.9, we present results for a flat, rectangular plate partially buried in dry earth (see the inset in Fig. 7.6a). The magnitudes of the dominant and transverse components of the current distribution on the plate are shown in Fig. 7.7a and Fig. 7.7b for the inclination angle $\alpha = 30°$, and in Fig. 7.9a and Fig. 7.9b for $\alpha = 60°$. In the triangle-patch model of the plate, 252 patches were employed.

The slight nonsymmetry with respect to the center line of the plate observed in the transverse component of the current is due to the fact that the symmetry of the plate was not preserved in its triangle-patch model. In Figs. 7.6 ($\alpha = 30°$) and 7.8 ($\alpha = 60°$) we compare the dominant component of the current distribution along the center line of the plate with the corresponding result for an infinite strip [26]. One observes a reasonably good agreement between the two results, both in magnitude (Fig. 7.6a) and phase (Fig. 7.6b) for $\alpha = 30°$, and a less favorable agreement for $\alpha = 60°$. This discrepancy can perhaps be attributed to the fact that an infinite strip is not a very good model for the relatively short plate.

87
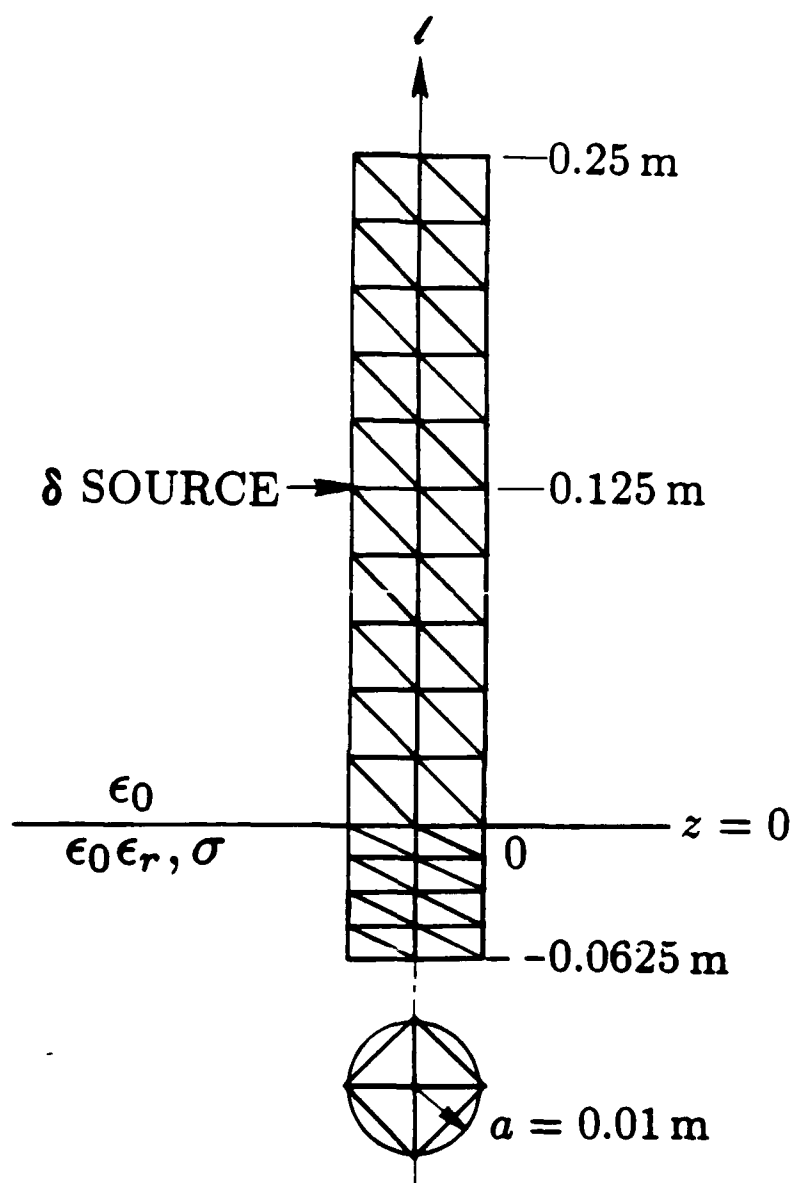
Figure 7.3: Triangle-patch approximation of a vertical, cylindrical antenna that penetrates the interface between two media.
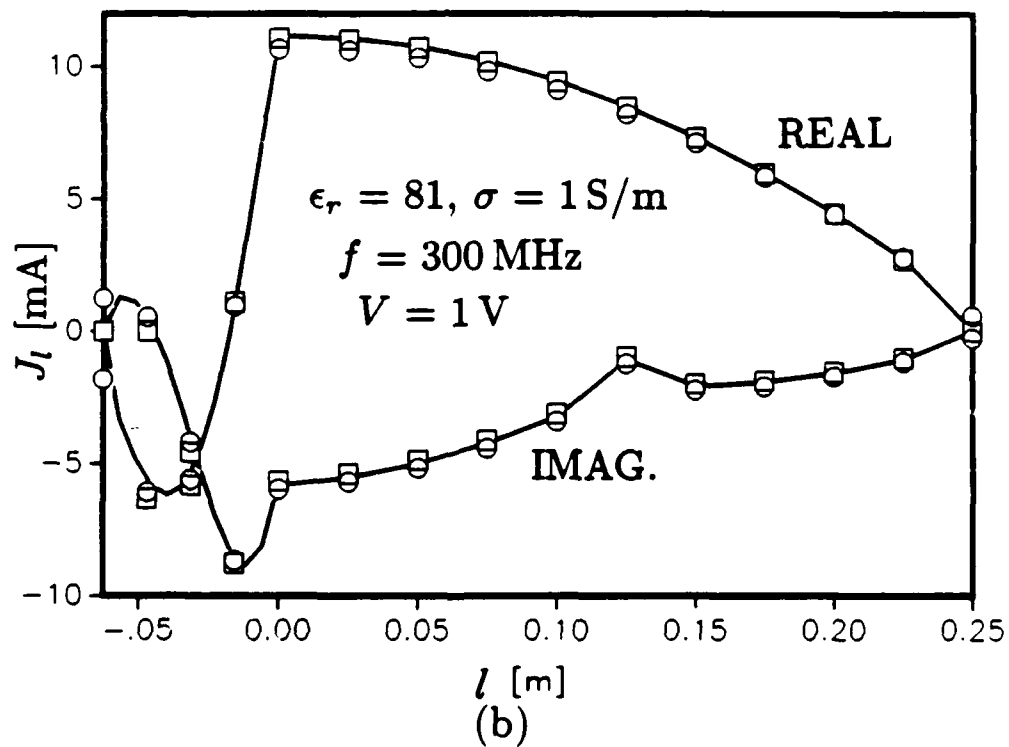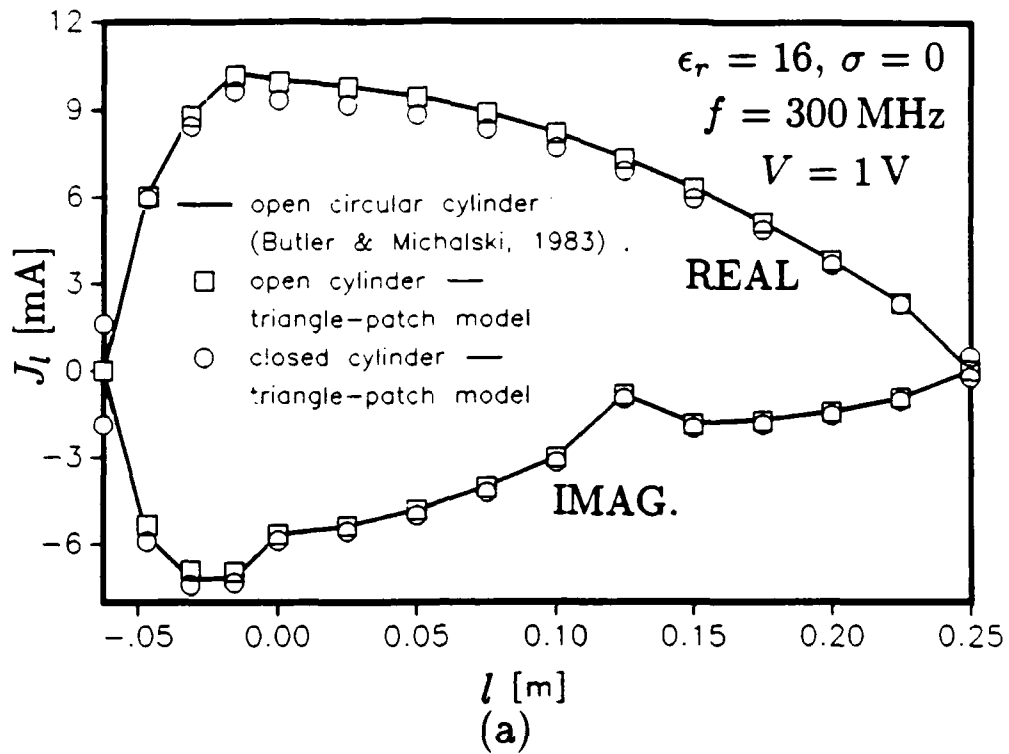
Figure 7.4: Current distribution on an open-ended and closed tubular antenna of Fig. 7.3 partially buried in (a) dry earth and (b) salt water.
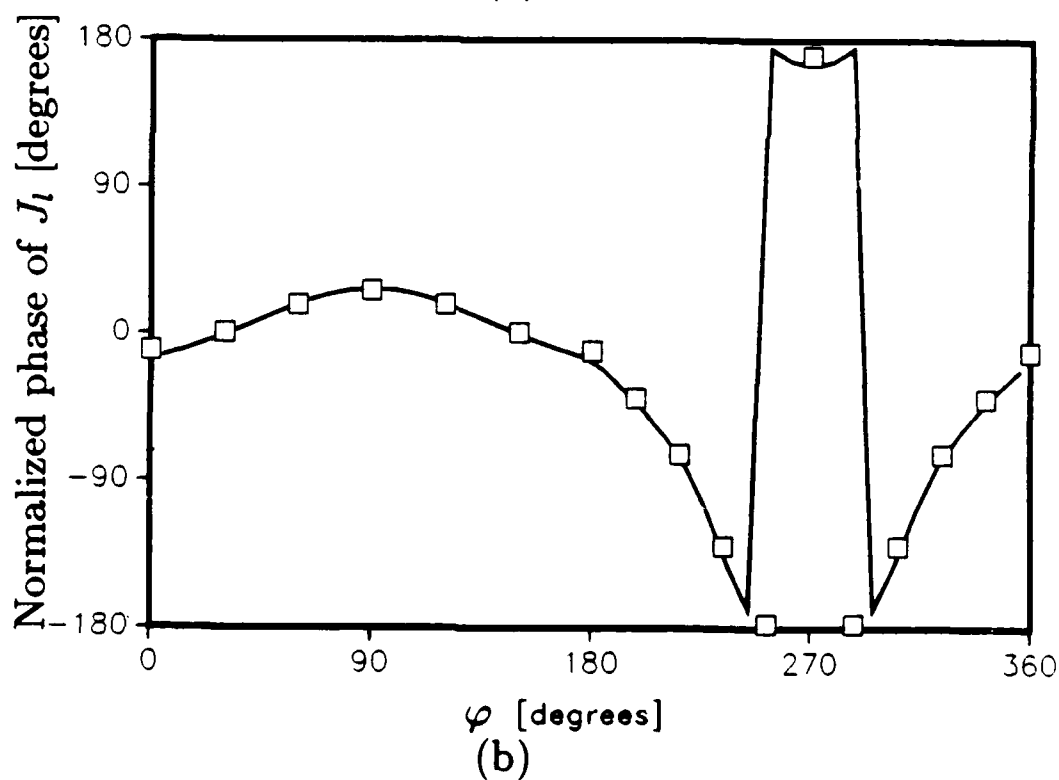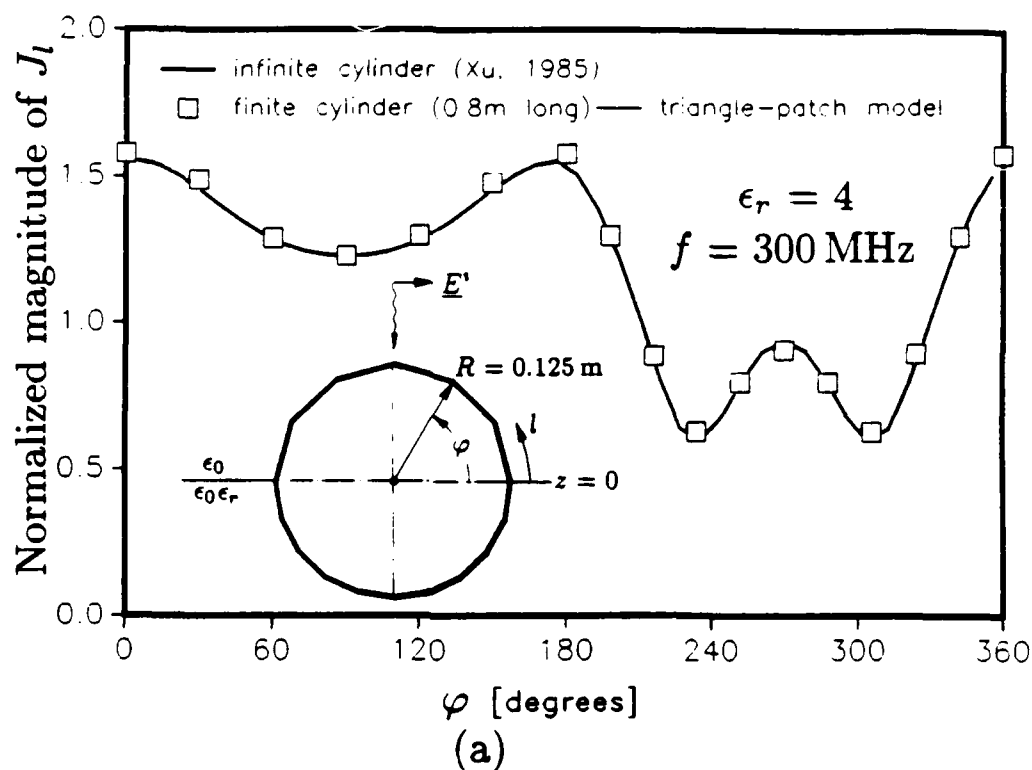
Figure 7.5: (a) Magnitude and (b) phase of the current J_ℓ on a horizontal tube partially buried in a dielectric medium. The current is normalized to the incident magnetic field at $\phi = 90°$ on the surface of the tube.
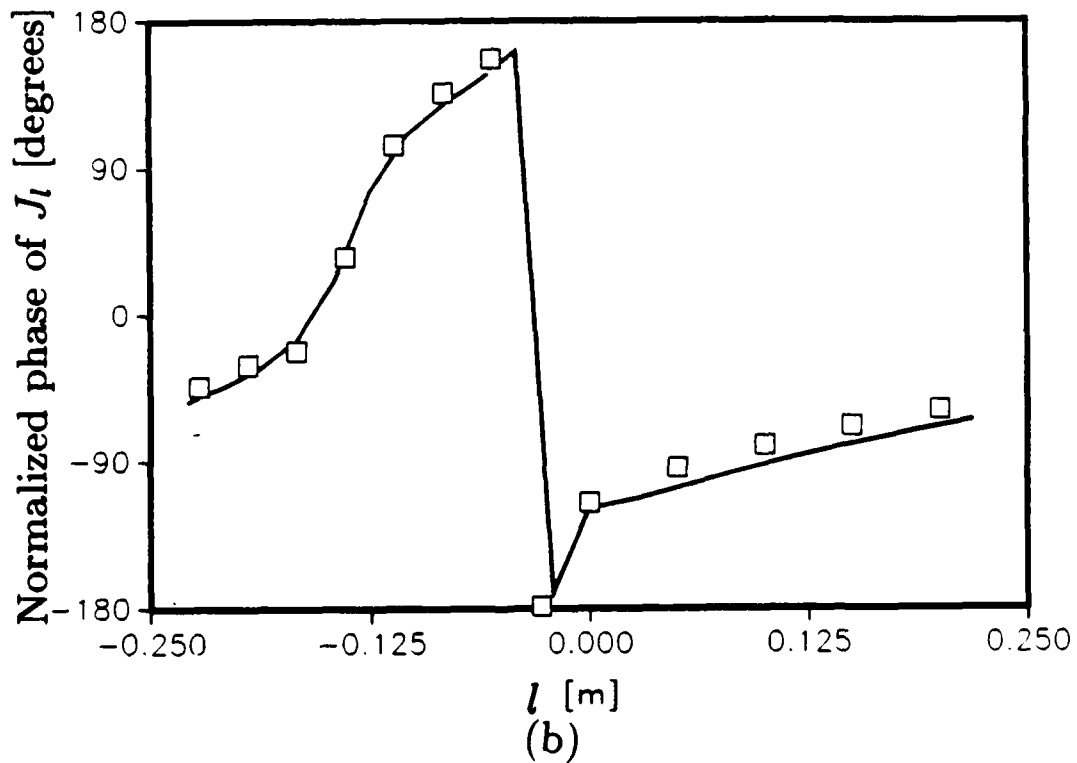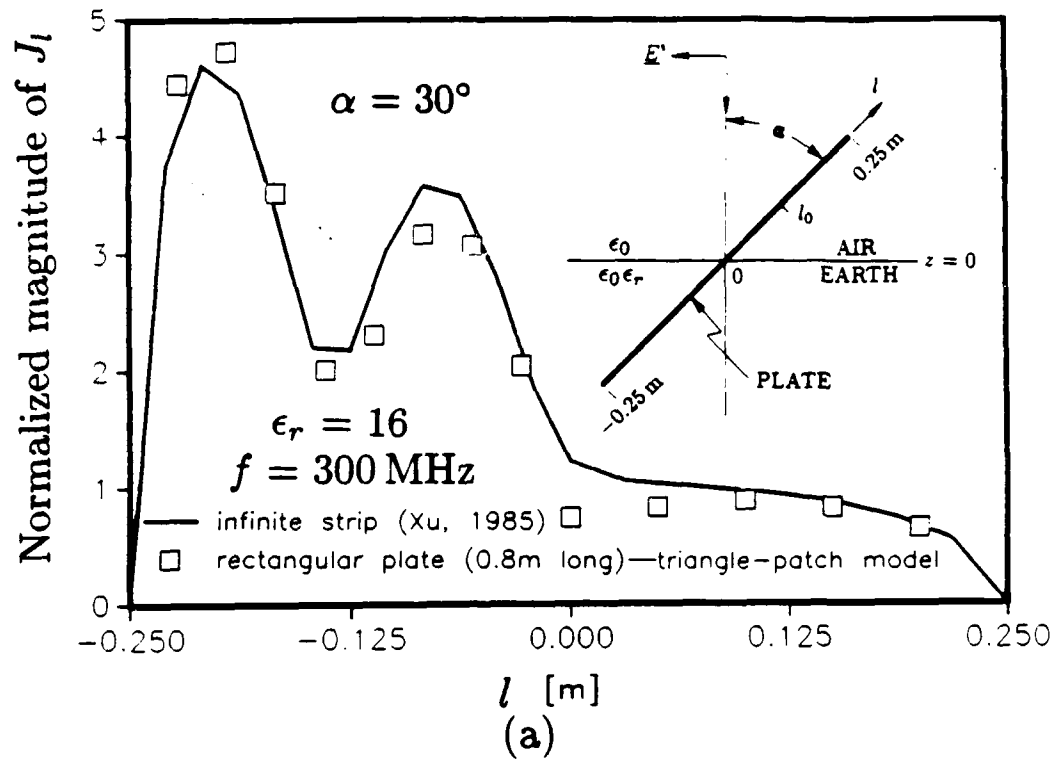
90

Figure 7.6: (a) Magnitude and (b) phase of the current J_ℓ along the center line of a rectangular plate partially buried in dry earth, for the inclination angle $\alpha = 30°$. The current is normalized to the incident magnetic field at $\ell_0 = 0.125\,\text{m}$.

91
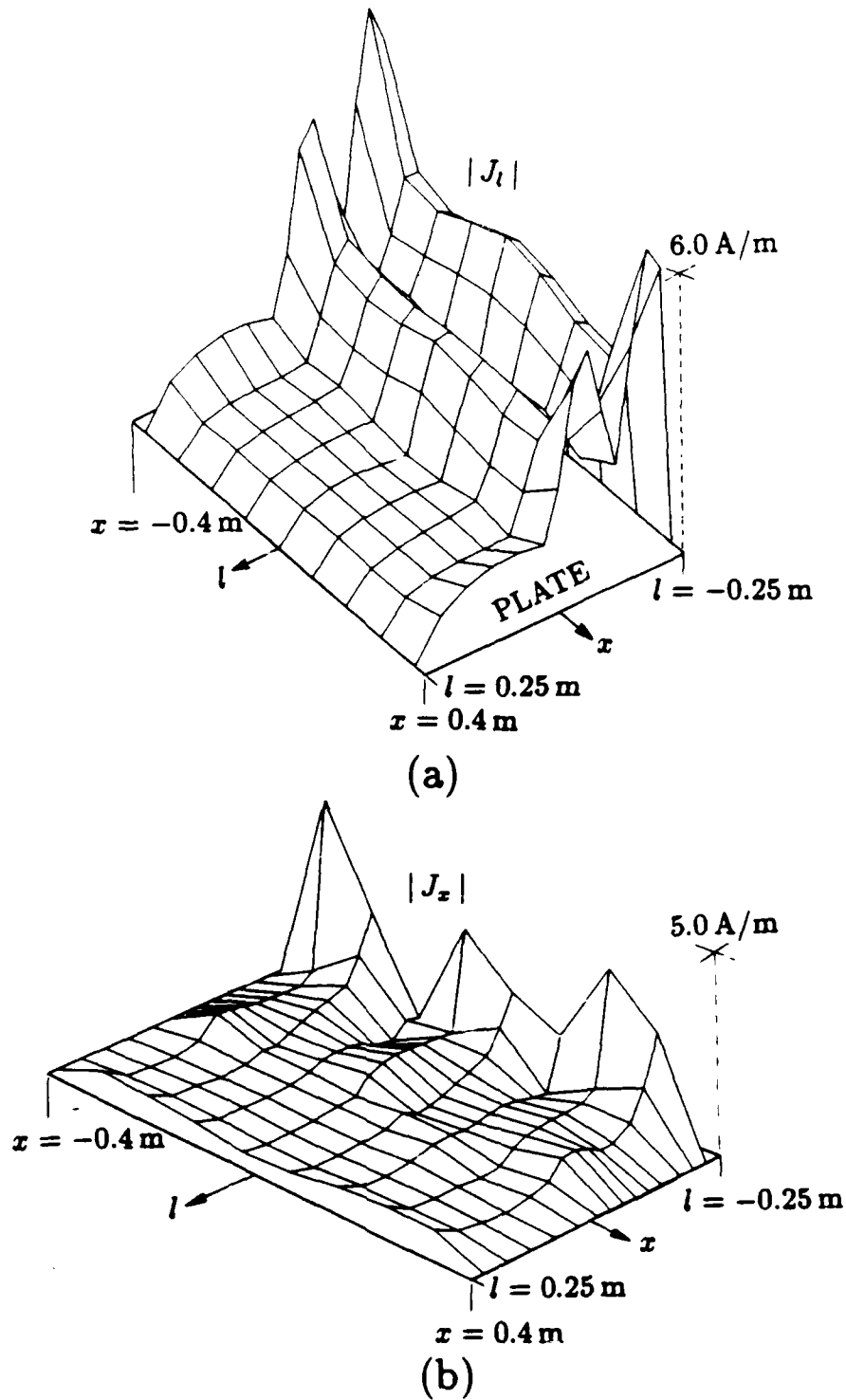
Figure 7.7: Magnitude of (a) the longitudinal and (b) transverse component of the current induced on the rectangular plate of Fig. 7.6 for $\alpha = 30°$, by a normally-incident plane wave with $H_x^i = 1$ A/m.
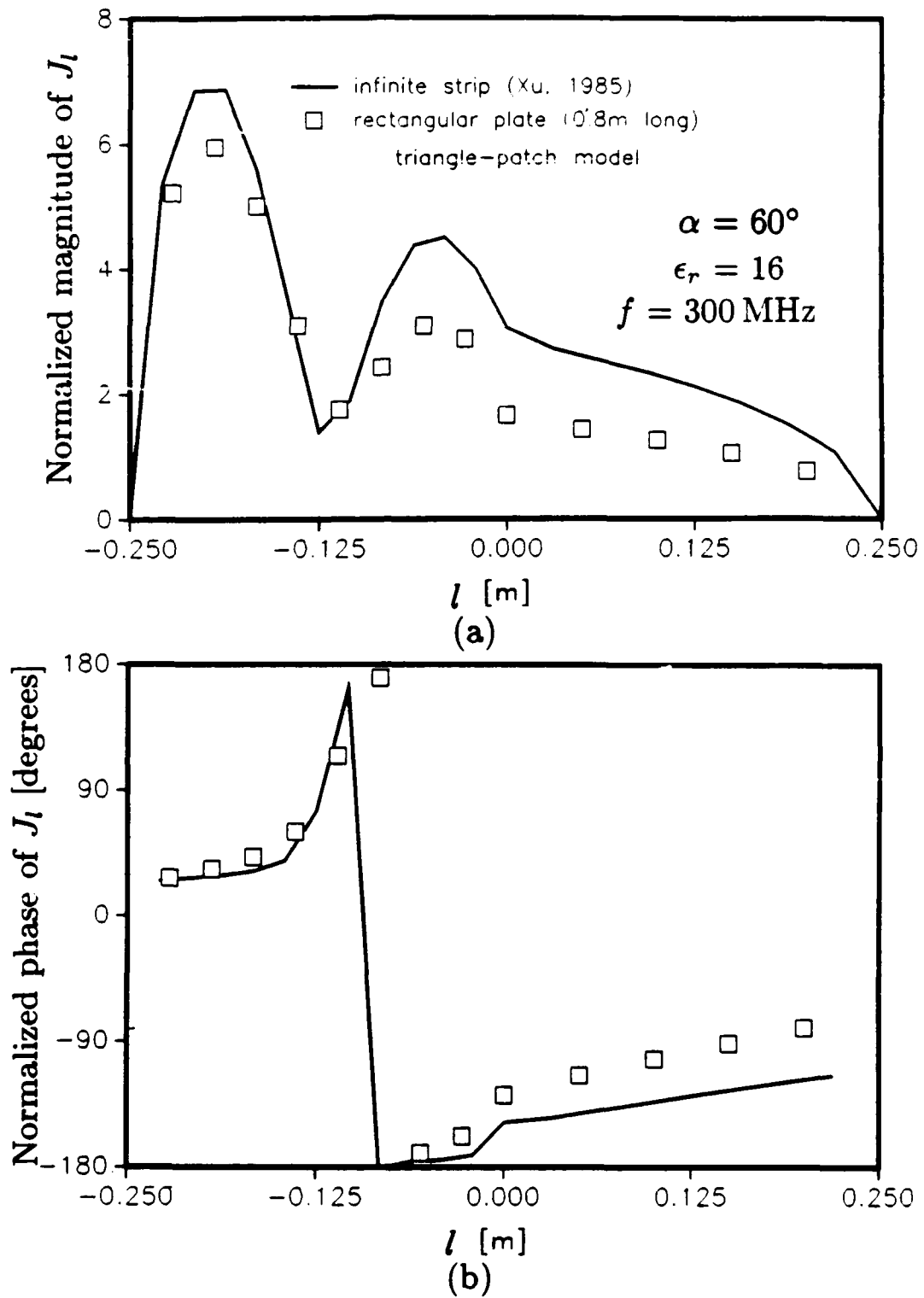
Figure 7.8: (a) Magnitude and (b) phase of the current J_ℓ along the center line of a rectangular plate of Fig. 7.6 for $\alpha = 60°$. The current is normalized to the incident magnetic field at $\ell_0 = 0.125\,\mathrm{m}$.

93
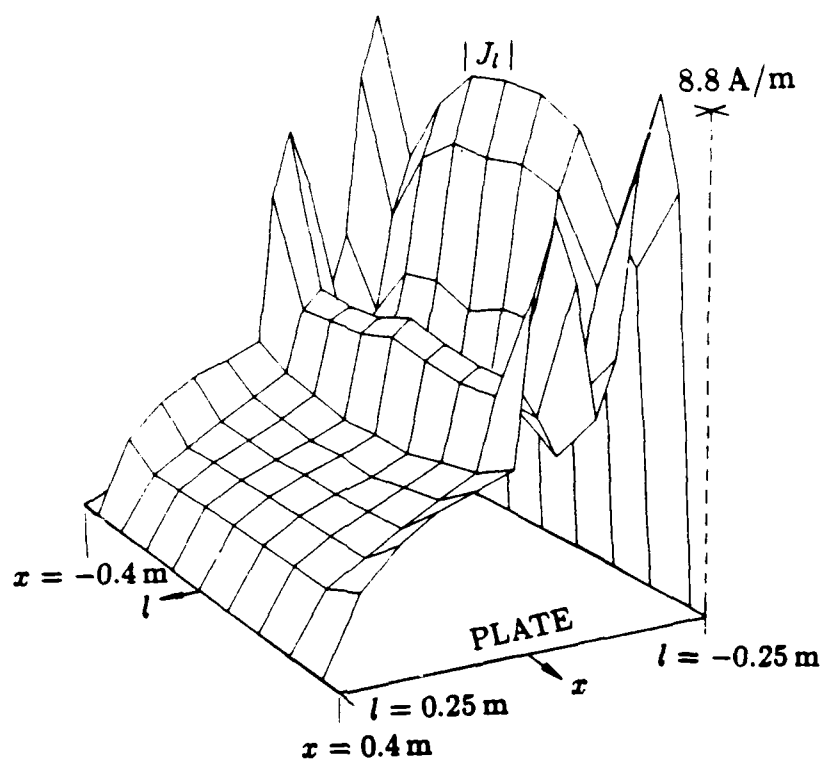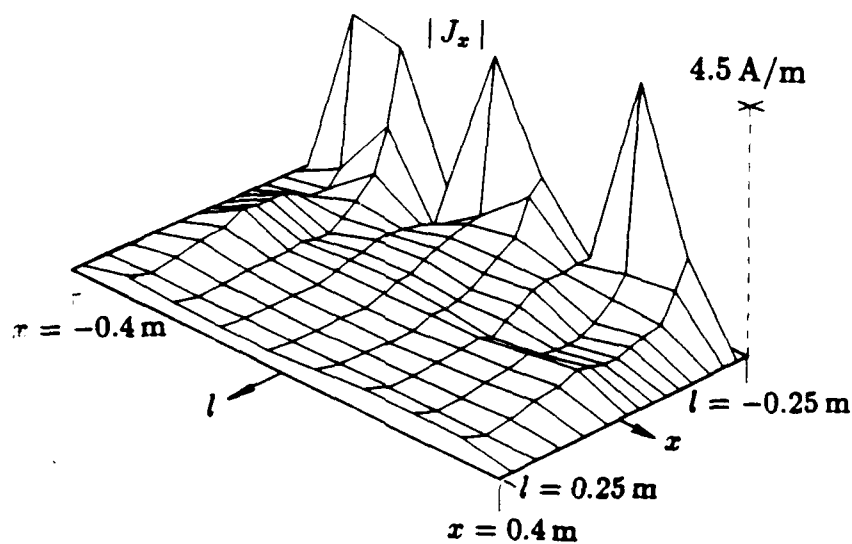
Figure 7.9: Magnitude of (a) the longitudinal and (b) transverse component of the current induced on the rectangular plate of Fig. 7.6 for $\alpha = 60°$, by a normally–incident plane wave with $H_x^i = 1$ A/m.

7.2 Thin Wires

The next problem considered is that of a straight, inclined, thin-wire antenna which is partially buried in moist earth, as shown in Fig. 7.10. The computed current distributions on the antenna for $\alpha = 45°$ and $\alpha = 80°$ are compared in Figs. 7.11a and 7.11b, respectively, with the NEC [27]. The agreement is seen to be excellent in the first case, but it is poor in the last case. A possible explanation of this discrepancy of the results for $\alpha = 80°$ has been given in the previous section.

Next, we consider the case of a vertical, rectangular, loop antenna partially immersed in water, as illustrated in Fig. 7.12, for which measured data are available [78]. The current distributions on the lower arm of the loop are presented in Fig. 7.13 ($\epsilon_r = 81$, $\sigma = 0$) for tap water, and in Figs. 7.14 ($\epsilon_r = 79$, $\sigma = 1\,\mathrm{S/m}$) and 7.15 ($\epsilon_r = 76$, $\sigma = 1.75\,\mathrm{S/m}$) for salt water. One observes a good agreement of the computed and measured results, both in magnitude and phase.

7.3 Coax–Fed Microstrip Patch Antennas

In this section, we present sample computed and measured input impedance data (normalized to $50\,\Omega$) for triangular, rectangular, and square coaxially fed microstrip patch antennas, as illustrated in Fig. 5.7. In all cases, the substrate parameters are: $\epsilon_r = 2.484$ and $\tan\delta = 6 \times 10^{-4}$, and the dimensions of the probe are: $a = 0.635\,\mathrm{mm}$ and $b = 2.095\,\mathrm{mm}$.

The results in Fig. 7.16 are for a triangular patch antenna previously analyzed by Pichon et al. [43] using a simple, zero–order coax feed model. In the numerical method, the conducting patch was modeled by 121 triangular elements. Computed results are presented for both the 1st– and 2nd–order models of the coax feed (cf. Section 5.3). As expected, the 2nd–order model data are closer to the measured results than the simplified model data. In Fig. 7.17 are shown results for the same triangular patch antenna, but driven at a vertex. This case illustrates the flexibility of the rigorous coax–feed model presented in Section 5.3. In Figs. 7.18 and 7.19, we present results for a rectangular patch antenna with two different substrate thicknesses. This antenna was previously analyzed by Hall and Mosig [46], who used a rectangular element model of the patch. In the present case, the antenna was approximated by 160 triangular elements. The results indicate that, as expected, the 1st–order feed model breaks down for thick substrates.

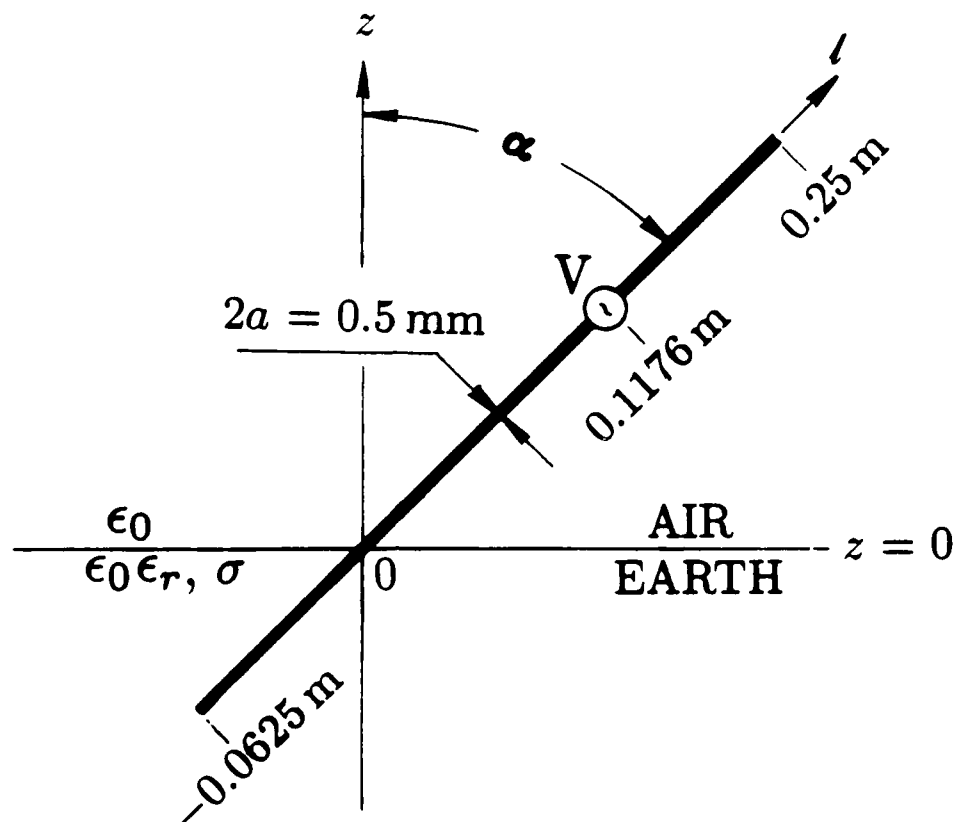Finally, in Fig. 7.20, we show results for a square patch antenna fed by a coaxial probe

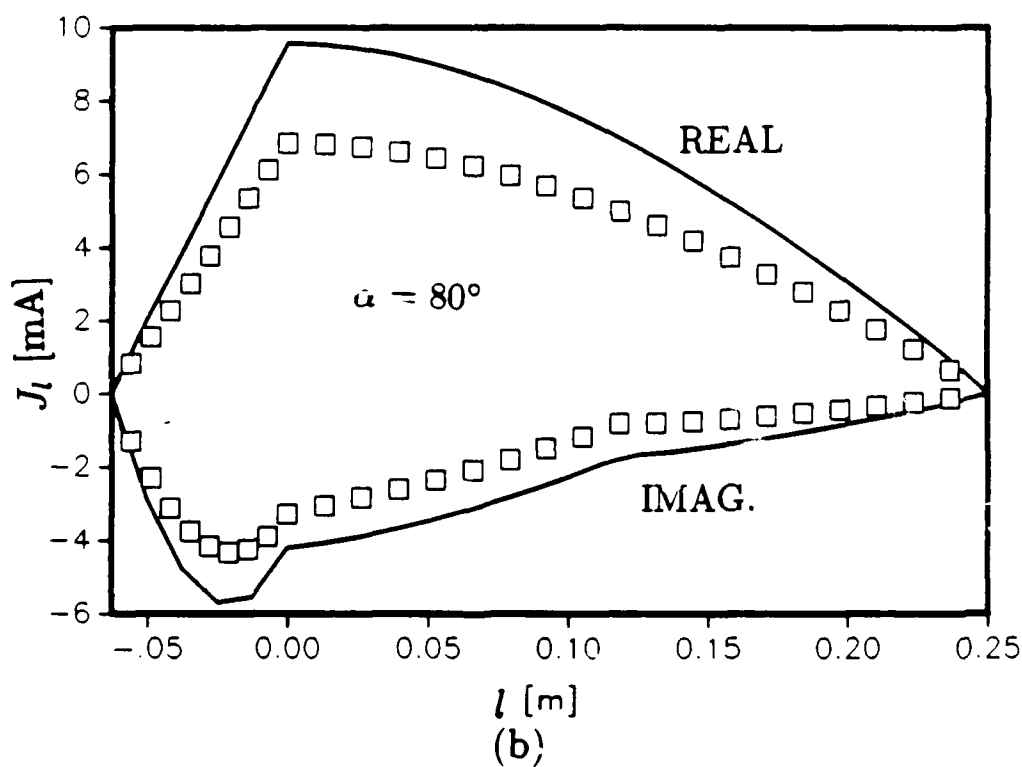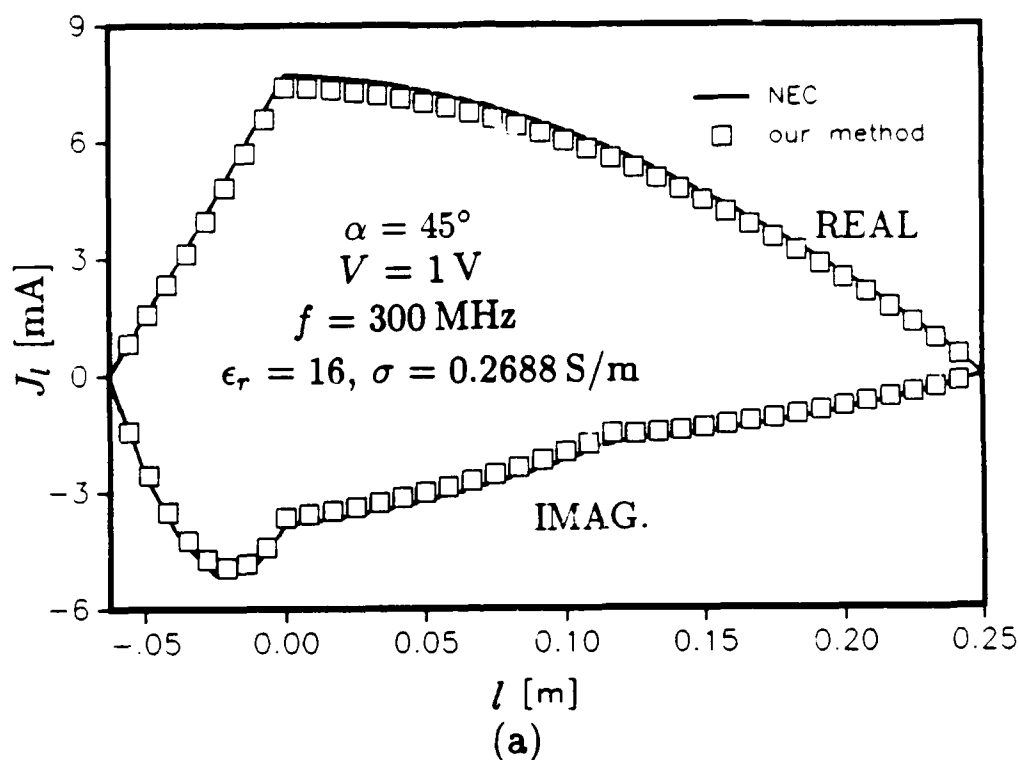Figure 7.10: Inclined thin-wire antenna partially buried in moist earth.

Figure 7.11: Current distribution on the thin-wire antenna of Fig. 7.10 for (a) $\alpha = 45°$ and (b) $\alpha = 80°$.
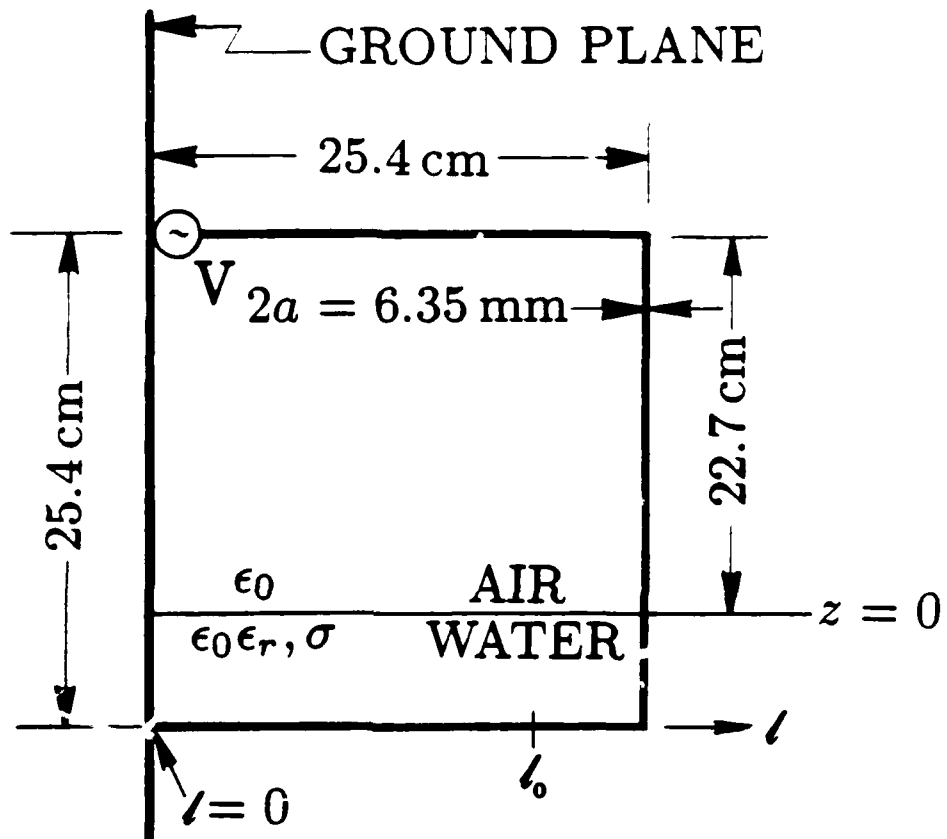
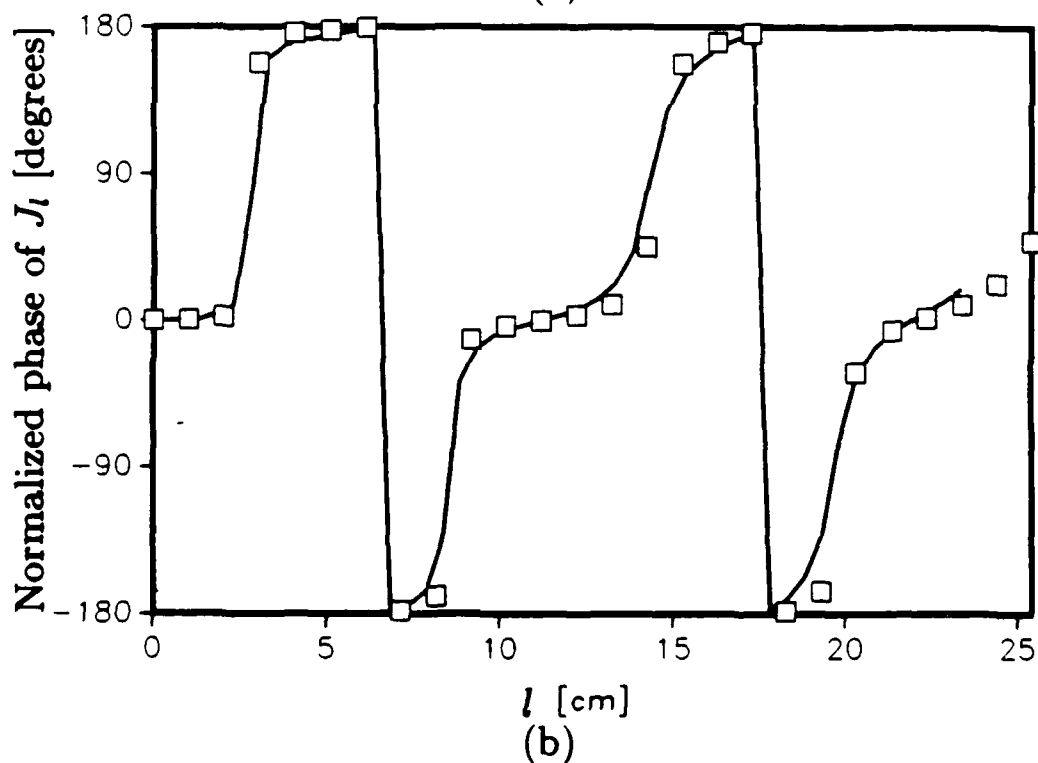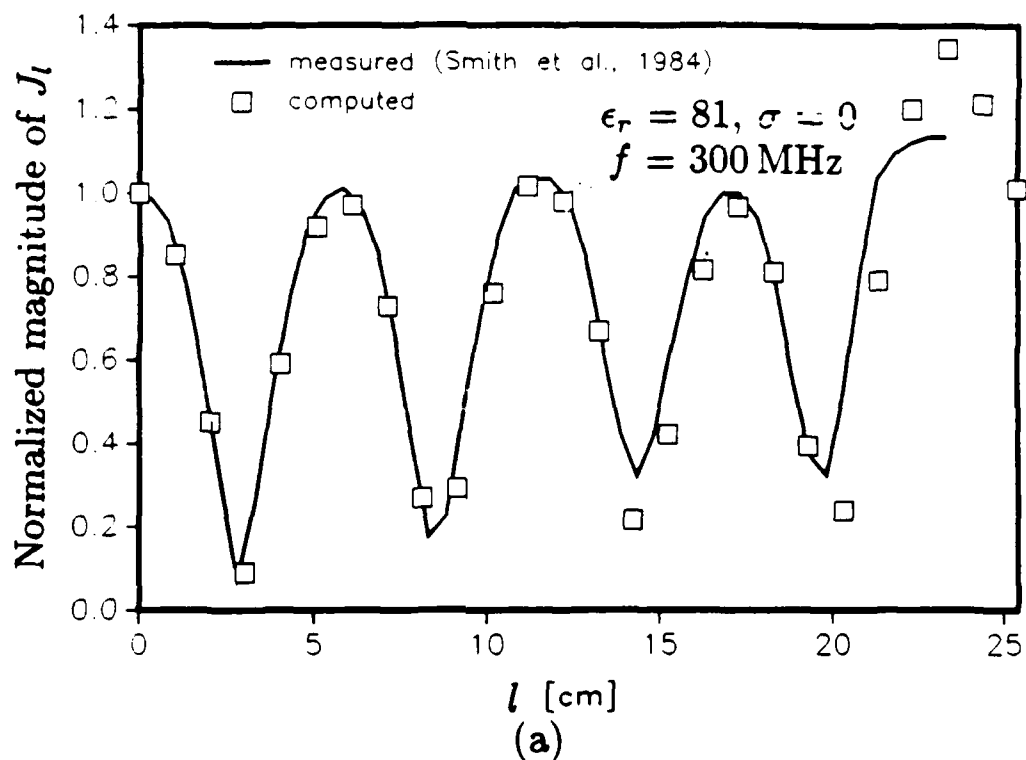Figure 7.12: Vertical rectangular–loop antenna partially immersed in water.

Figure 7.13: (a) Magnitude and (b) phase of the current J_ℓ on the lower arm of the rectangular-loop antenna of Fig. 7.12 ($\epsilon_r = 81$, $\sigma = 0$). The current is normalized to its value at the point $\ell_0 = 0$.
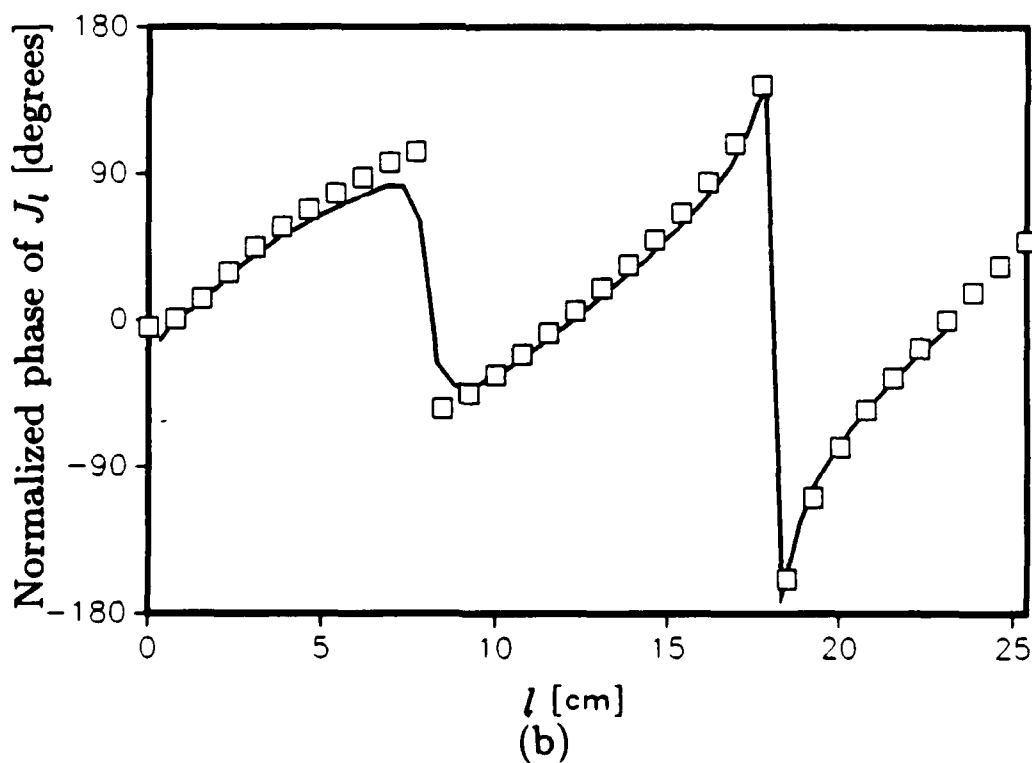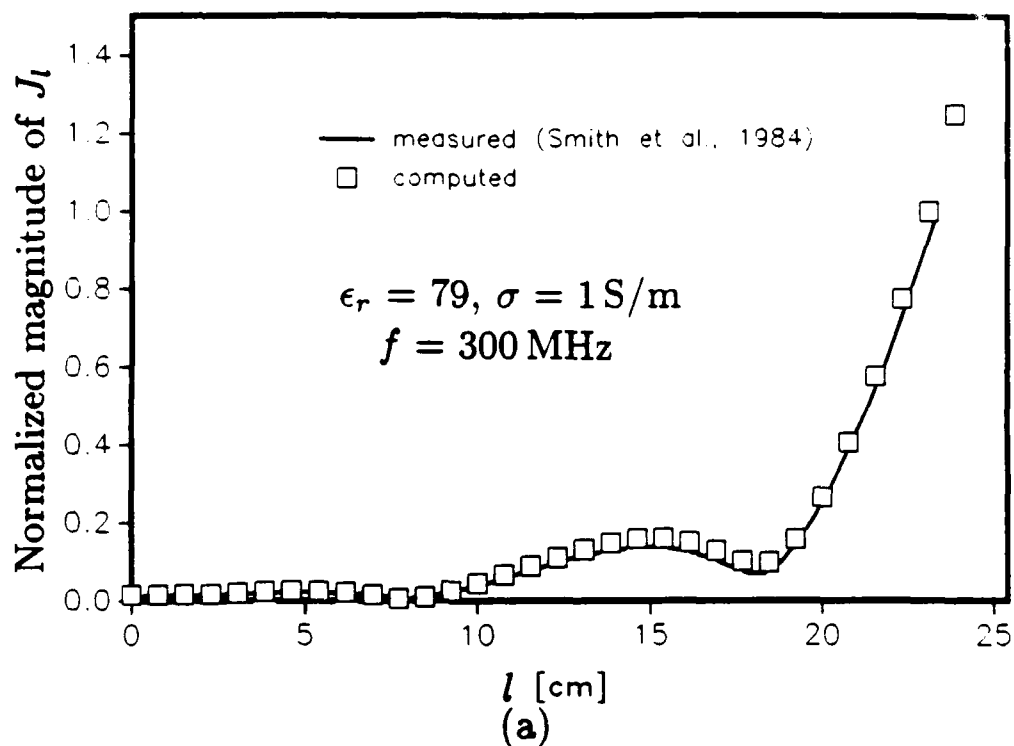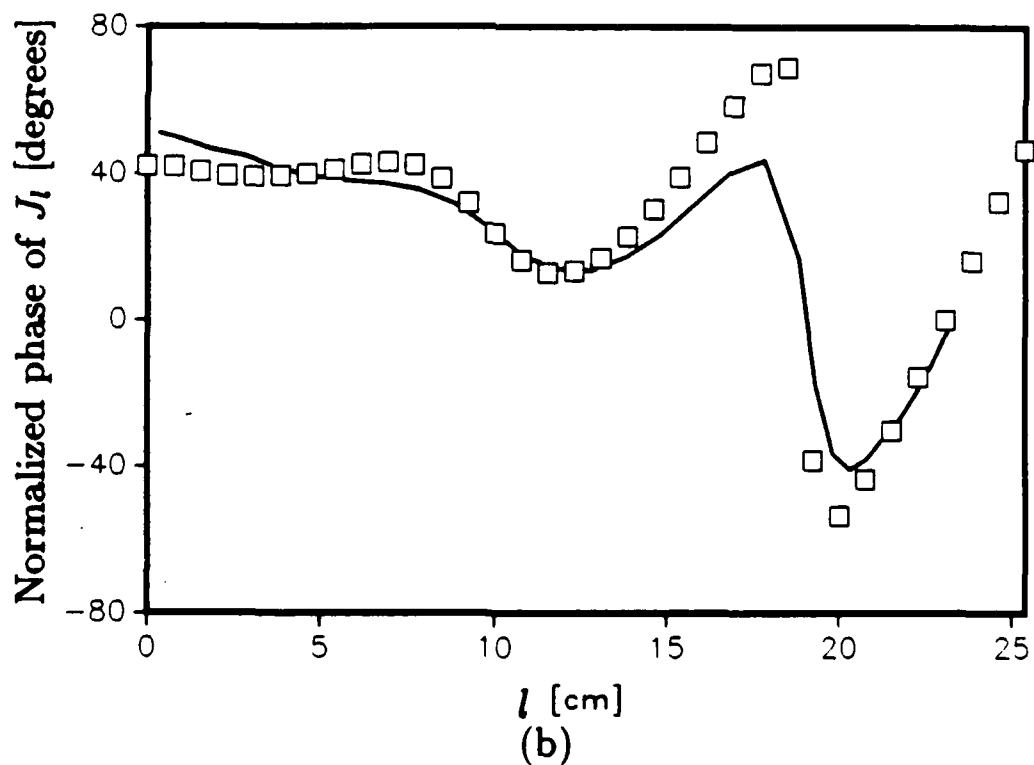
Figure 7.14: (a) Magnitude and (b) phase of the current J_ℓ on the lower arm of the rectangular-loop antenna of Fig. 7.12 ($\epsilon_r = 79$, $\sigma = 1\,\text{S/m}$). The current is normalized to its value at the point $\ell_0 = 23.3\,\text{cm}$.
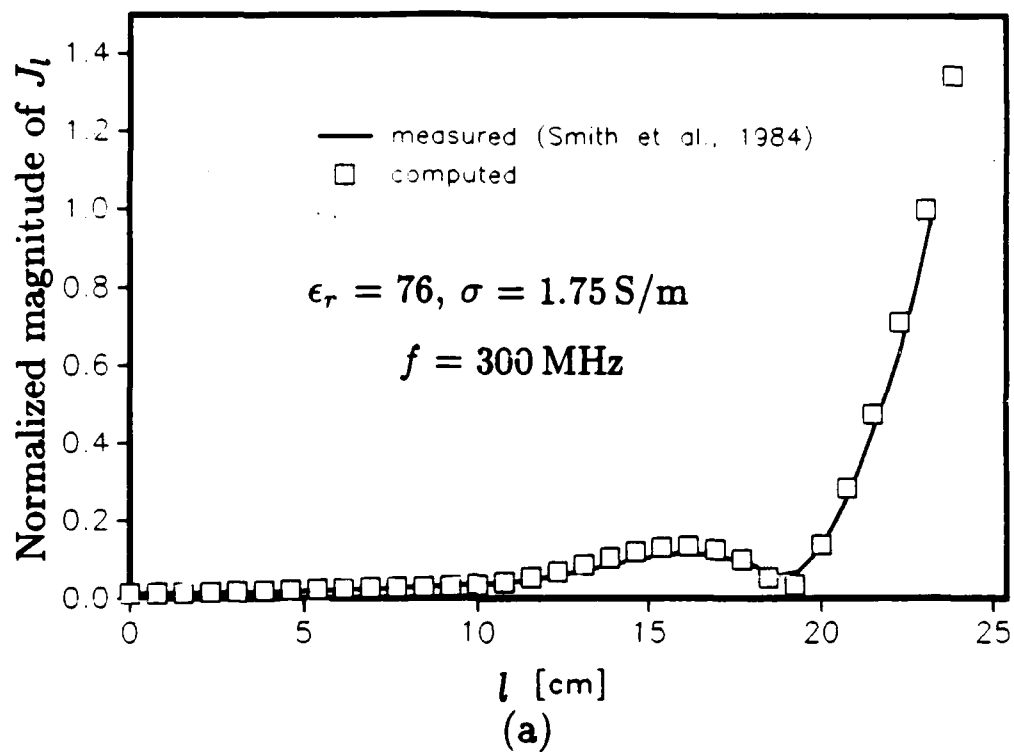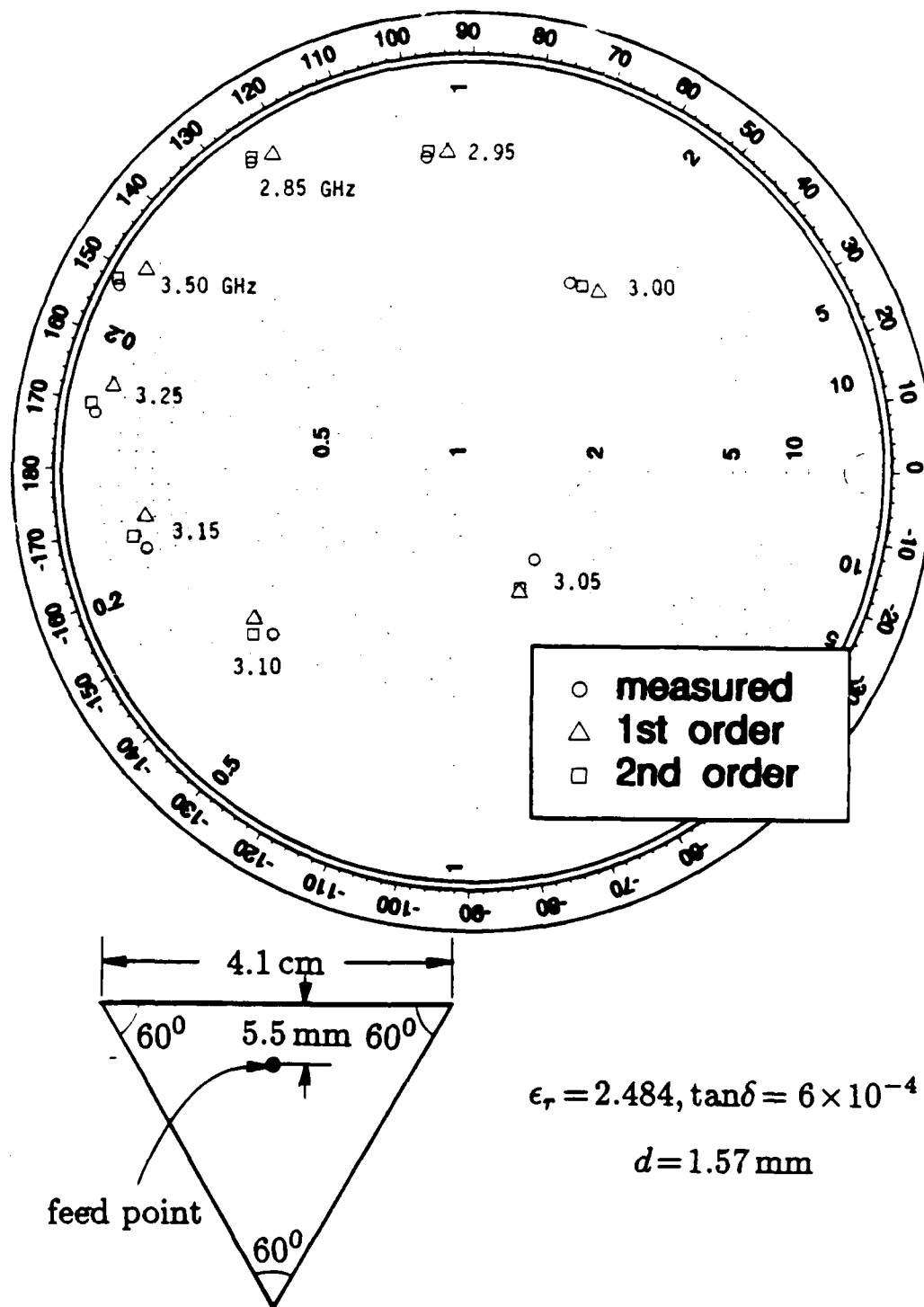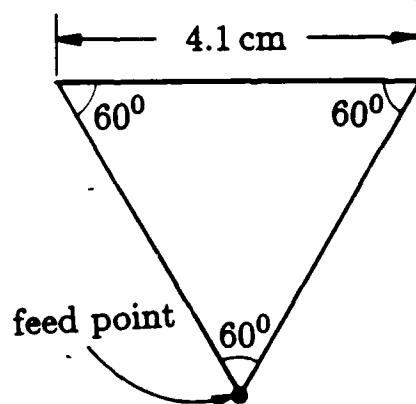
100

Figure 7.15: (a) Magnitude and (b) phase of the current J_ℓ on the lower arm of the rectangular–loop antenna of Fig. 7.12 ($\epsilon_r = 76$, $\sigma = 1.75\,\mathrm{S/m}$). The current is normalized to its value at the point $\ell_0 = 23.3\,\mathrm{cm}$.
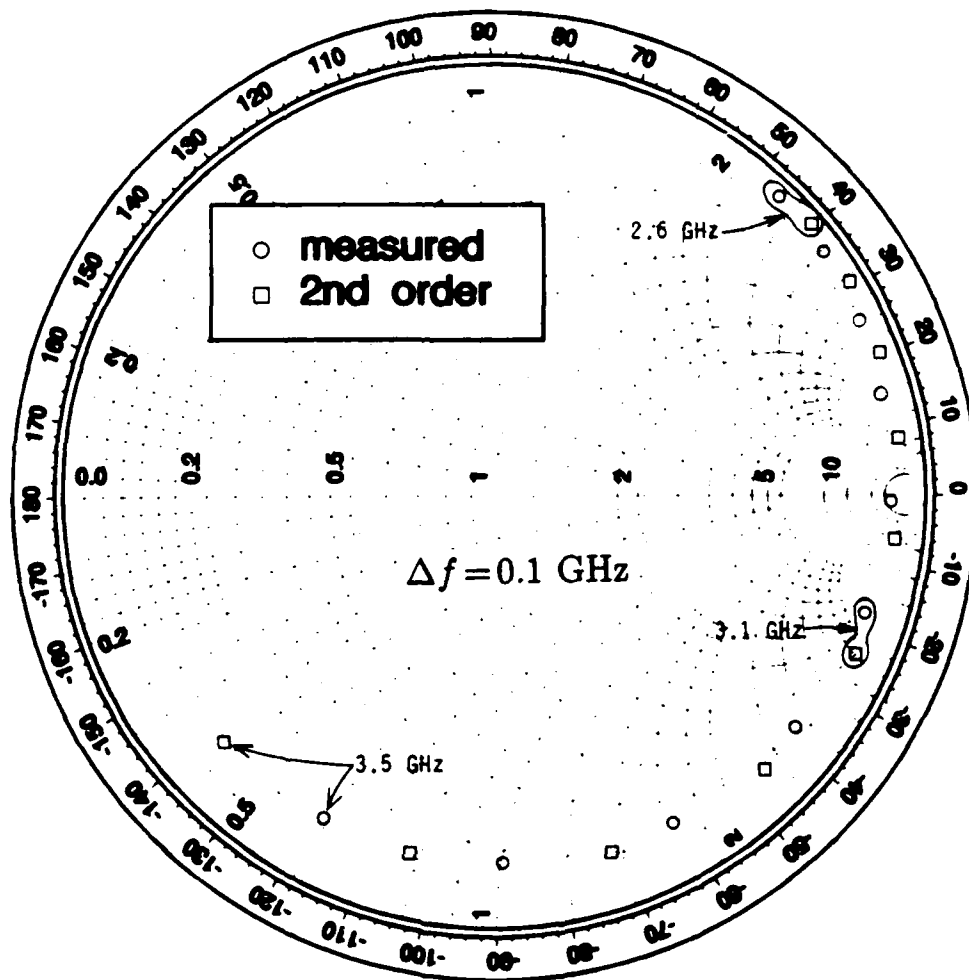
101

Figure 7.16: Input impedance of a coax-fed triangular patch microstrip antenna.

Figure 7.17: Input impedance of a triangular patch antenna coax–fed at a vertex.
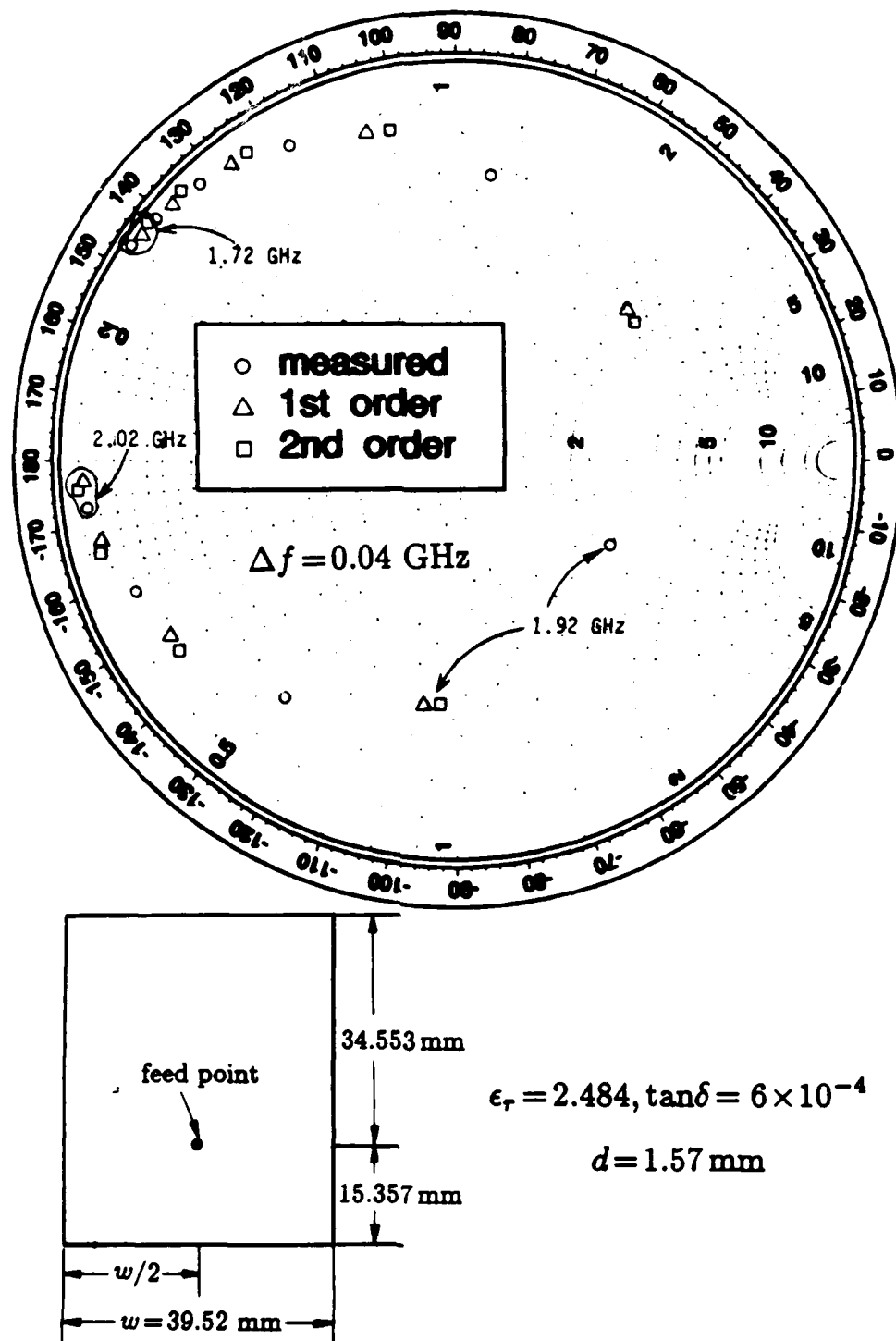
Figure 7.18: Input impedance of a coax–fed rectangular patch microstrip antenna with moderately thick substrate.
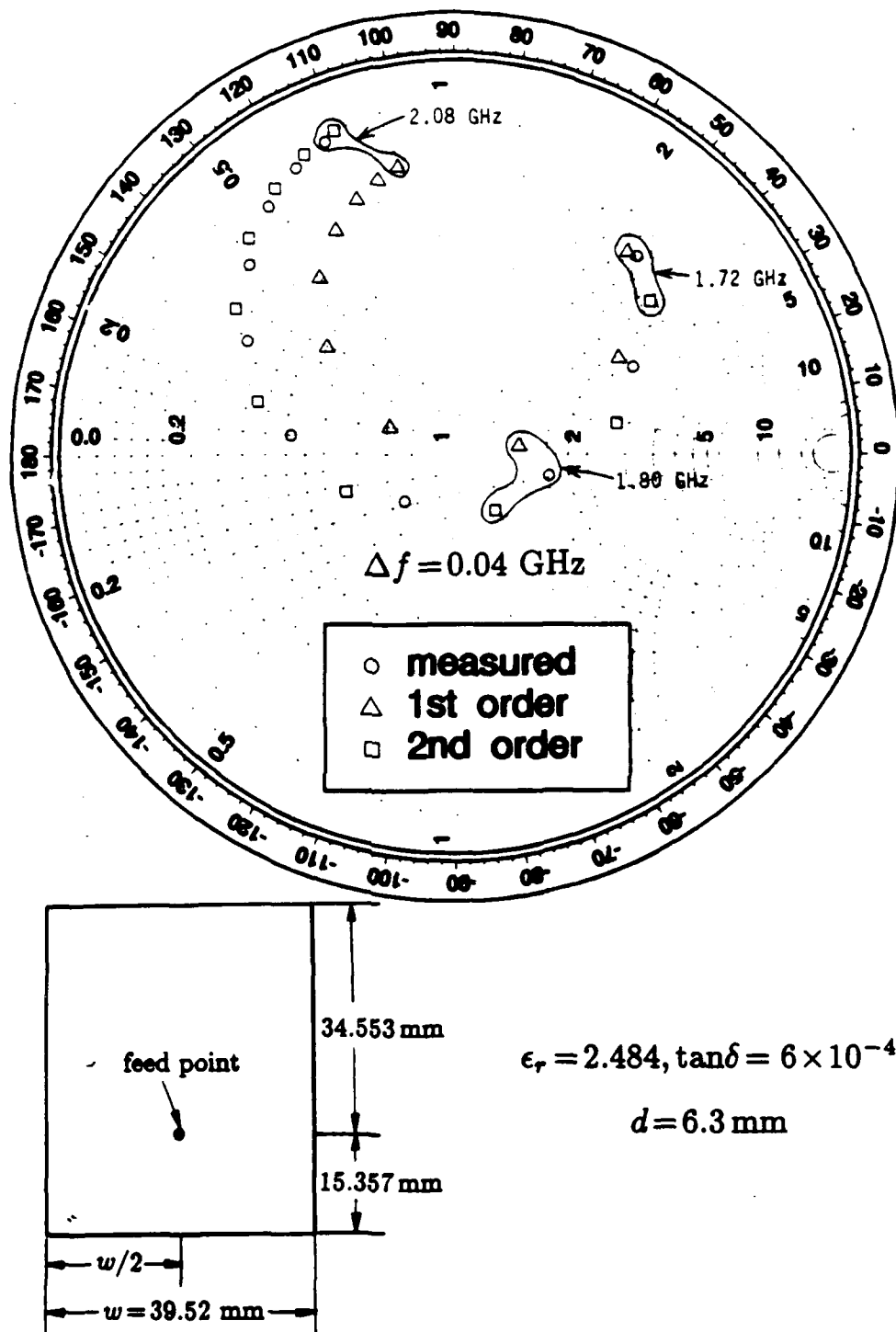
Figure 7.19: Input impedance of a coax-fed rectangular patch microstrip antenna with thick substrate.

at an edge. The patch was approximated by 128 triangular elements. As in the other cases' presented above, we observe a good agreement between the measured data and the results computed using the 2nd–order coax–feed model, except for a small phase shift, which we attribute, in part, to measurement inaccuracies and to discrepancies between the catalog and actual values of ϵ_r.

7.4 Open Microstrip Transmission Lines

In this section we present results for open microstrip lines of the form shown in Fig. 5.9, except that the conductor is confined to the upper medium. The current distributions included here are normalized to have a maximum value of one for the longitudinal current density.

The first set of results is for an essentially planar microstrip line, illustrated in Fig. 7.21. The PEC strip is of width w and it may be infinitely thin, or it may have finite thickness t. In Fig. 7.22, we present the dispersion curves for the lowest mode (EH_0) and the first higher mode (EH_1) for an infinitely thin microstrip line and for a line with finite thickness ($t/w = 0.1$). The dimensions are $w = 15\,mm$, $d = 0.794\,mm$, $\epsilon_r = 2.32$. In this figure, Oliner and Lee's results [73, 79] for $t = 0$ are also plotted for comparison. Oliner and Lee's analysis is based on the transverse-resonance method in conjunction with the Wiener-Hopf approach developed in [80]. Our result for the phase constant of the EH_1 mode, shown in Fig. 7.22a, is seen to agree completely with Oliner and Lee's work (within the error in reading from their curves) both in the bound and leaky regimes, except at the low end of the frequency range. The agreement of the attenuation constants, plotted in Fig. 7.22b, appears to be slightly less favorable. Note that in [73] and in [79], data for α are only given for, respectively, $f > 5\,GHz$ and $f > 6\,GHz$. In Figs. 7.18 and 7.19, we show the current distributions of the EH_0 and EH_1 modes on an infinitely thin strip at $f = 5\,GHz$ and $f = 10\,GHz$, respectively. The longitudinal currents (J_y) are plotted in Figs. 7.23a and 7.24a, and the transverse currents (J_x) in Figs. 7.23b and 7.24b. The symbols correspond to the locations where the current values are actually computed. Observe that nonuniform-width basis functions were used to better capture the singular behavior of the longitudinal current near the edges of the strip. It is noted in Figs. 7.23 and 7.24 that there is very little change in the longitudinal current distribution as the mode passes from the bound regime to the leaky regime. However, there is a noticeable change in the transverse current distribution.

In Figs. 7.25 and 7.26, we show the current distributions of the EH_0 and EH_1 modes for
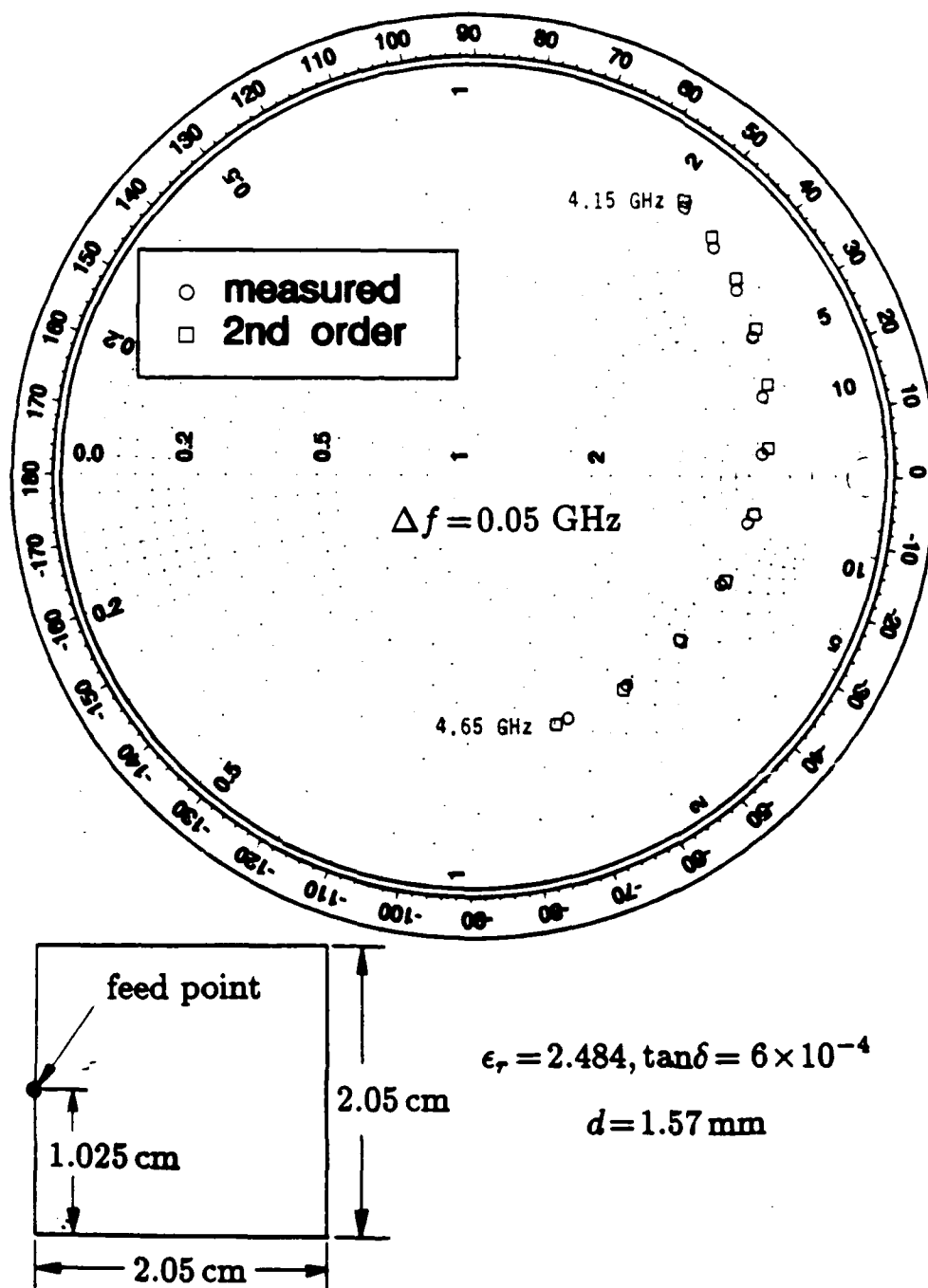
Figure 7.20: Input impedance of a square patch microstrip antenna coax-fed at an edge.
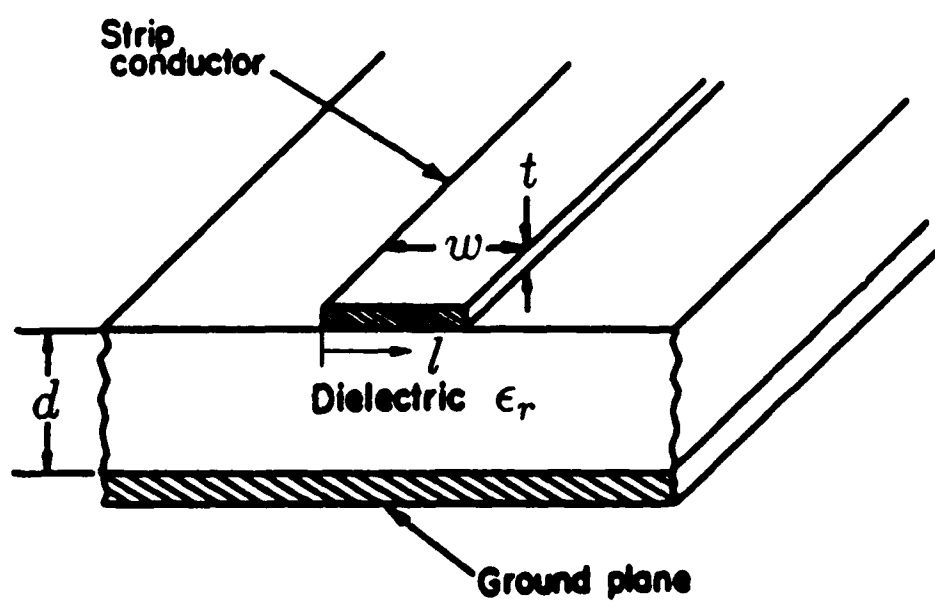
Figure 7.21: Open microstrip line.
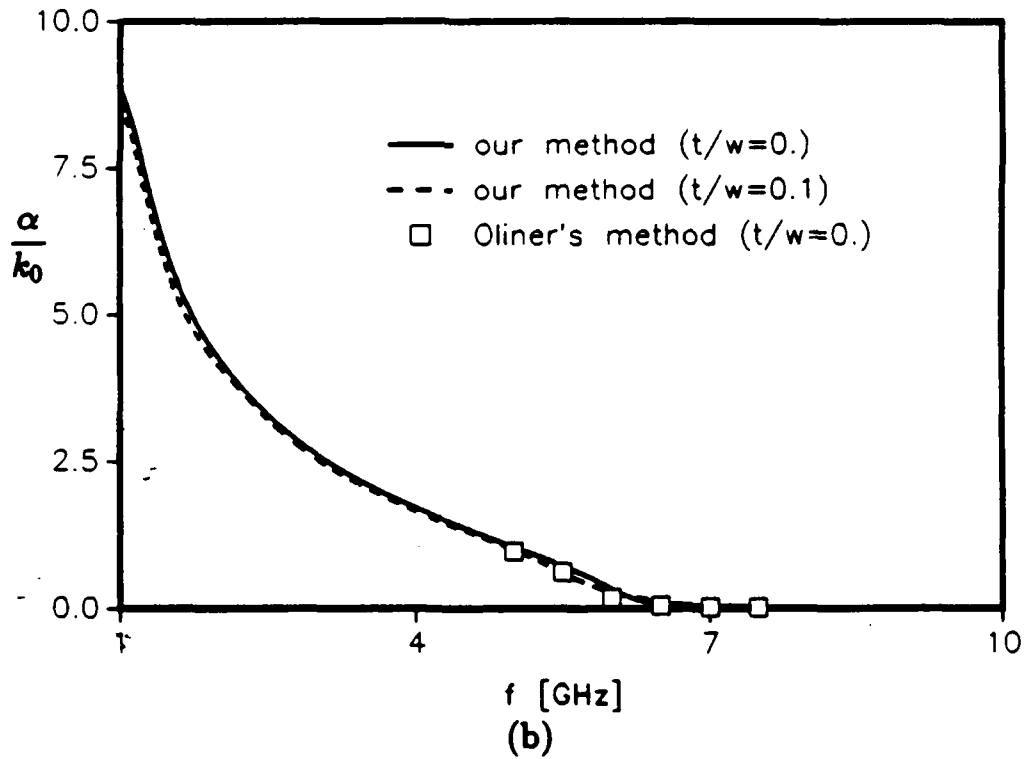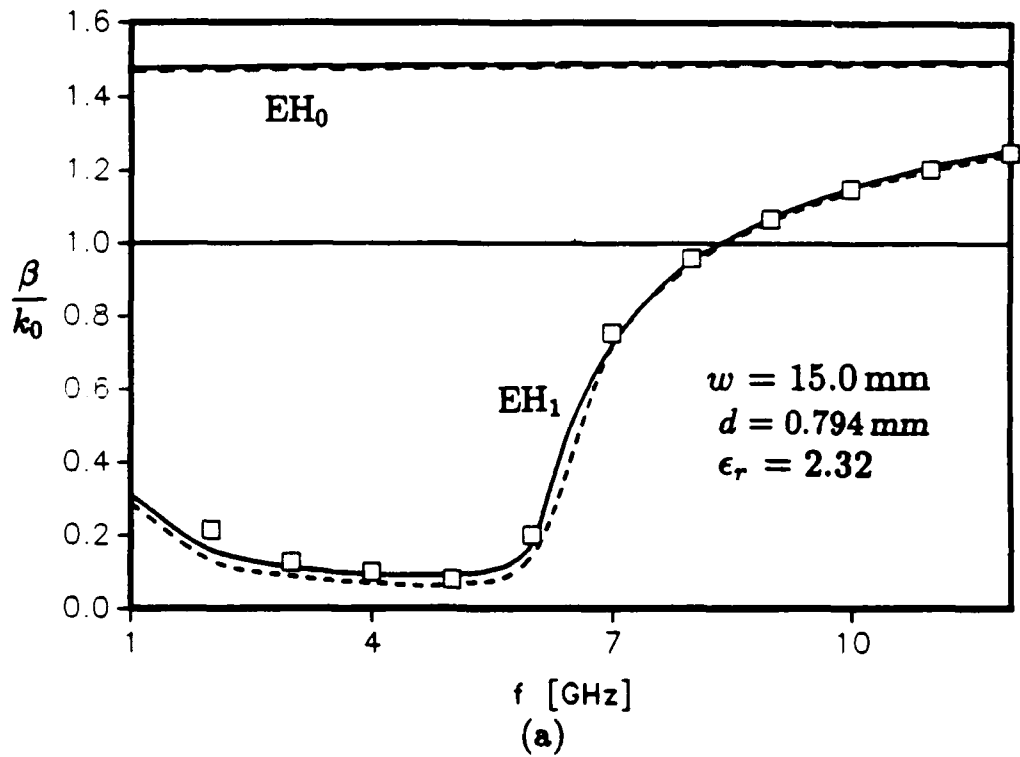
Figure 7.22: Variation with frequency (a) of the normalized phase constant for the lowest mode (EH_0) and the first higher mode (EH_1), and (b) of the normalized attenuation constant for the EH_1 mode.

Figure 7.23: (a) Longitudinal and (b) transverse current distributions of the EH_0 mode at $f = 5\,\mathrm{GHz}$ and $f = 10\,\mathrm{GHz}$ for an infinitely thin microstrip.

110

Figure 7.24: (a) Longitudinal and (b) transverse current distributions of the EH_1 mode at $f = 5\,\mathrm{GHz}$ (leaky regime *iii*) and $f = 10\,\mathrm{GHz}$ (bound regime *i*) for an infinitely thin microstrip line.

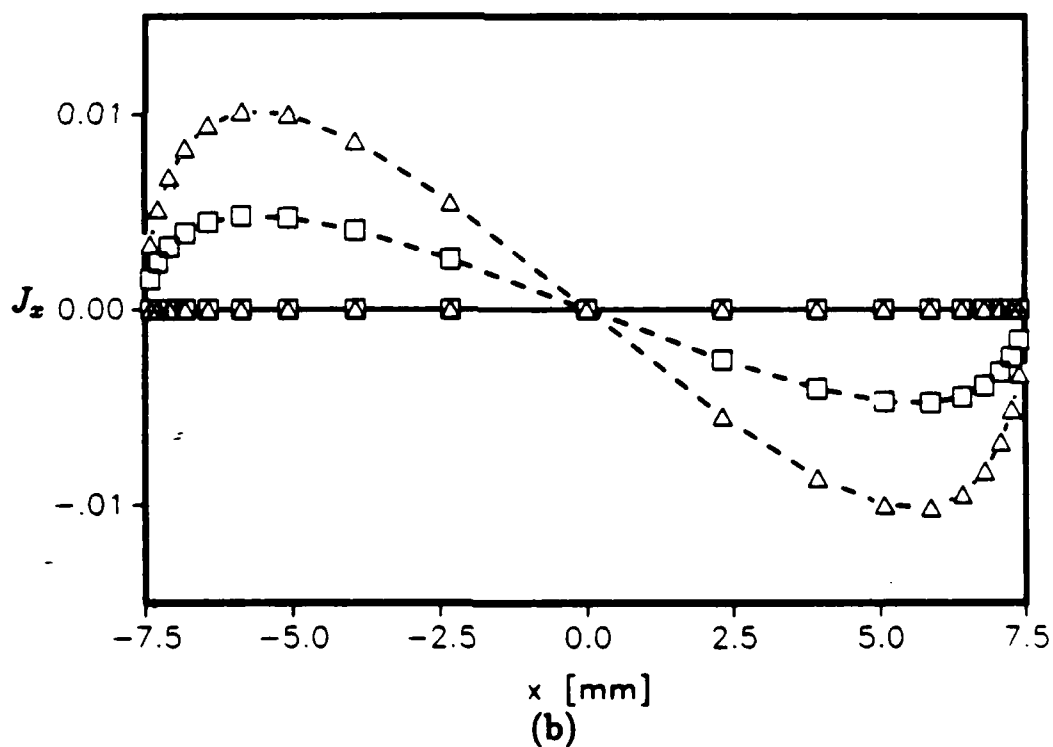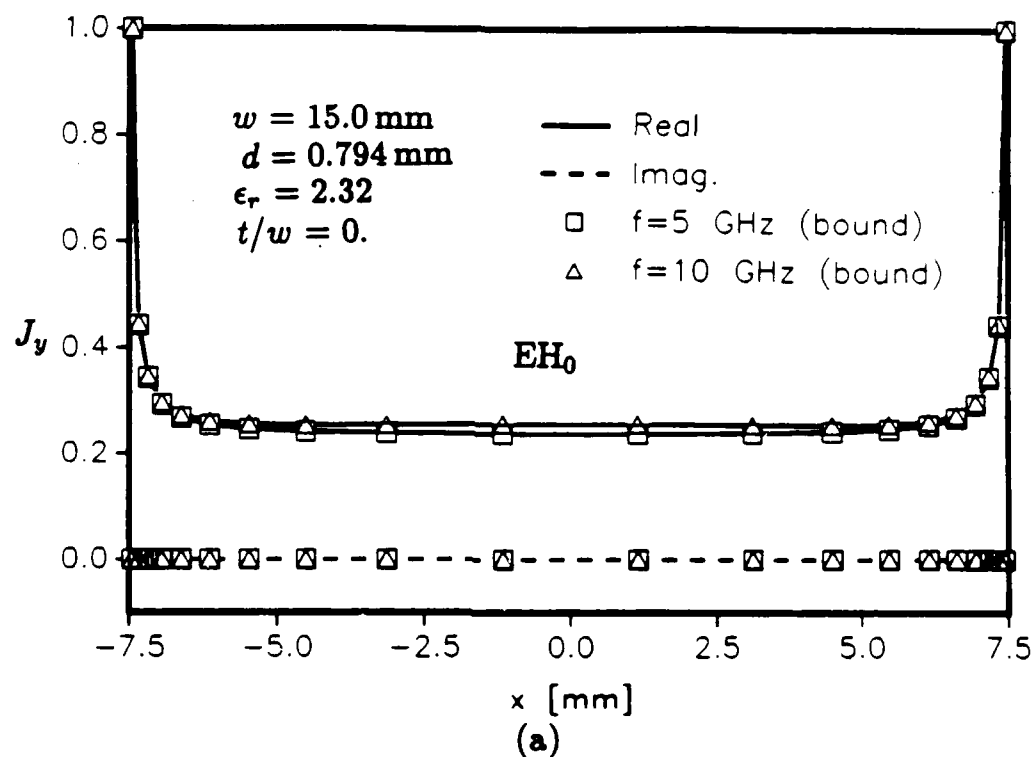Figure 7.25: (a) Longitudinal and (b) transverse current distributions of the EH_0 mode at $f = 5\,\mathrm{GHz}$ and $f = 10\,\mathrm{GHz}$ for a microstrip line of finite thickness.

112

a strip with finite thickness ($t/w = 0.1$) at $f = 5\,\text{GHz}$ and $f = 10\,\text{GHz}$, respectively. It is noted that the current is concentrated on the lower face of the strip, as expected.

In Fig. 7.27, we present the dispersion curves for the lowest mode (EH_0) and the first three higher modes (EH_1, EH_2, and EH_3) for an infinitely thin microstrip line with $w = 3\,\text{mm}$, $d = 0.635\,\text{mm}$, and $\epsilon_r = 9.8$. One should keep in mind that the actual boundary corresponding to the leaky mode region iii for each mode is $(1 + (\alpha/k_0)^2)^{\frac{1}{2}}$, which obviously depends on the attenuation constant of the mode ($cf.$ (6.44)). As is evident in Fig. 7.27, the phase constants for the higher modes increase again after reaching a minimum and continue to increase as the frequency is lowered further. It is noted that k_y stays in region iii as the frequency decreases. In Fig. 7.28, we show the normalized phase constant for the EH_1 mode and the region iii boundary corresponding to this mode. In Fig. 7.29, we present the current distribution for the EH_2 mode at $f = 25\,\text{GHz}$ (leaky regime iii) and $f = 35\,\text{GHz}$ (bound regime). In Fig. 7.30, we show the current distribution for the EH_3 mode at $f = 35\,\text{GHz}$ (leaky regime iii) and at $f = 50\,\text{GHz}$ (leaky regime ii).

In Fig. 7.31, we plot the effective dielectric constant, defined as $\epsilon_\text{eff} = (\beta/k_0)^2$, as a function of d/λ_0, for various widths and thicknesses of the strip. One observes that the effective dielectric constant decreases with the thickness of the strip. This effect is more pronounced at low frequencies.

We should mention that, at this writing, the results for an open microstrip line with finite thickness by a rigorous approach are not available. We only can compare our results with those for a shielded microstrip with finite thickness. The result in Fig. 7.31 has been found to agree favorably with that given in [81] (which is not shown in the figure) for a shielded strip line with a large size of the outer shield.

The last set of results is for a circular-wire transmission line backed by a grounded dielectric slab, for which a limited amount of data are available in the literature [82]. In Fig. 7.32, we present the fundamental mode effective dielectric constant as a function of d/λ_0. The corresponding data taken from [82] are also plotted for comparison and are seen to agree well with our results. In Fig. 7.33, we present dispersion curves of the fundamental mode (EH_0) and the first higher mode (EH_1) for a circular-wire transmission line with $h/d=0.25$. It is observed that in the chosen frequency range the EH_1 mode is leaky troughout. Finally, in Fig. 7.34 we show the longitudinal and transverse modal current distributions for both modes at $d/\lambda_0=0.3$.
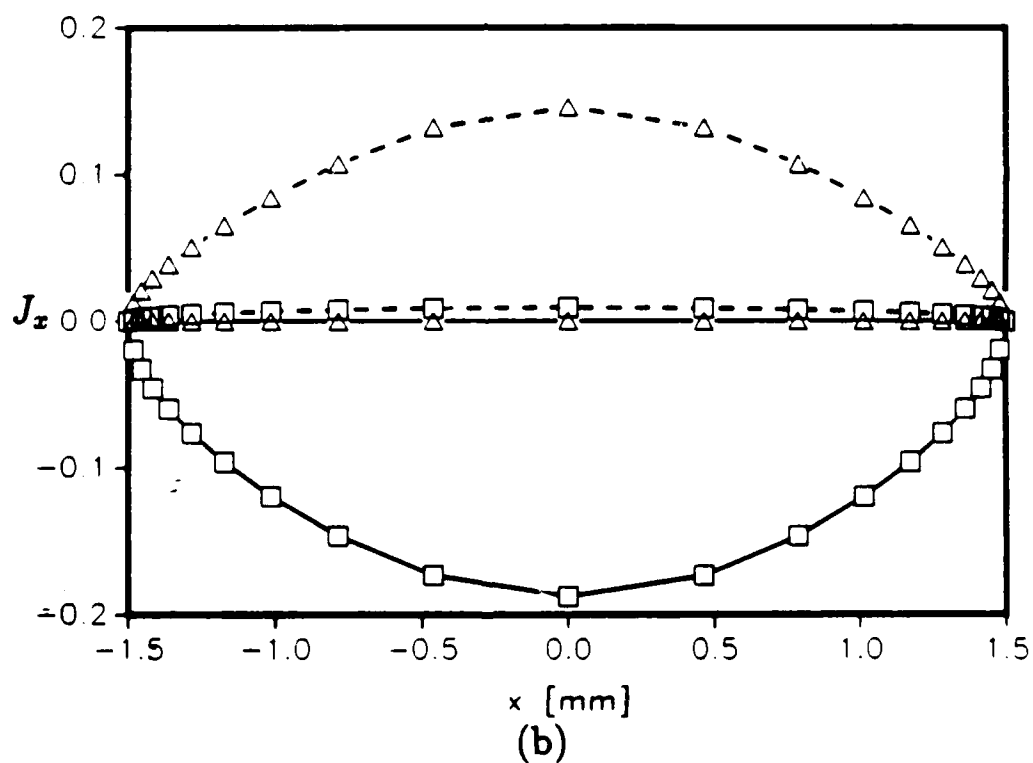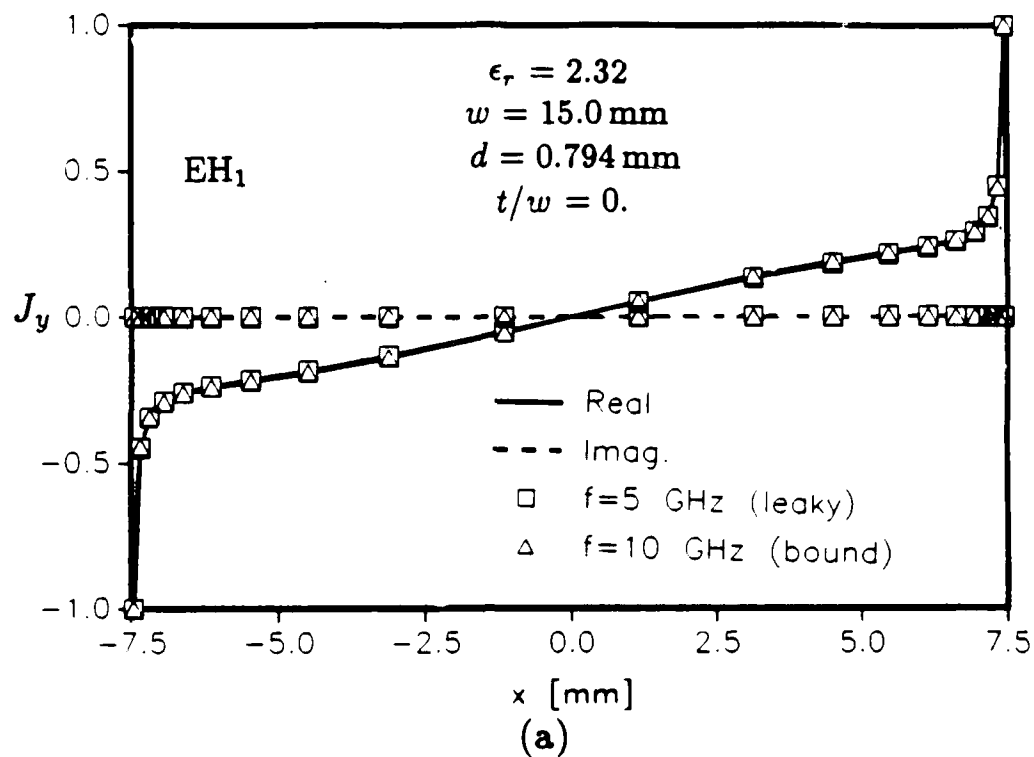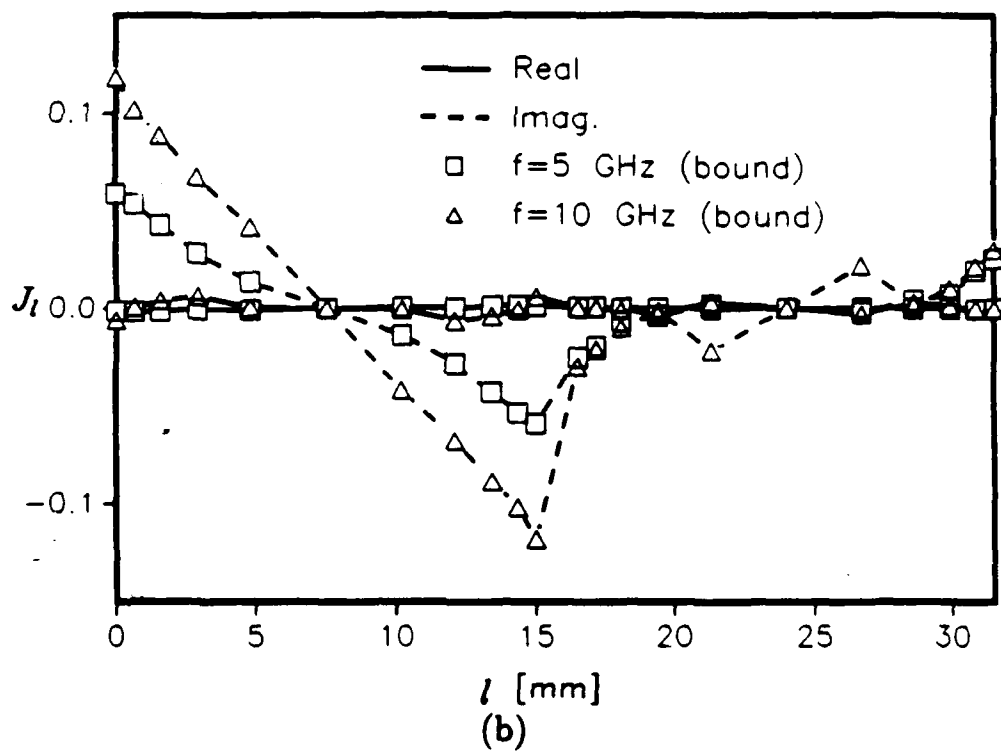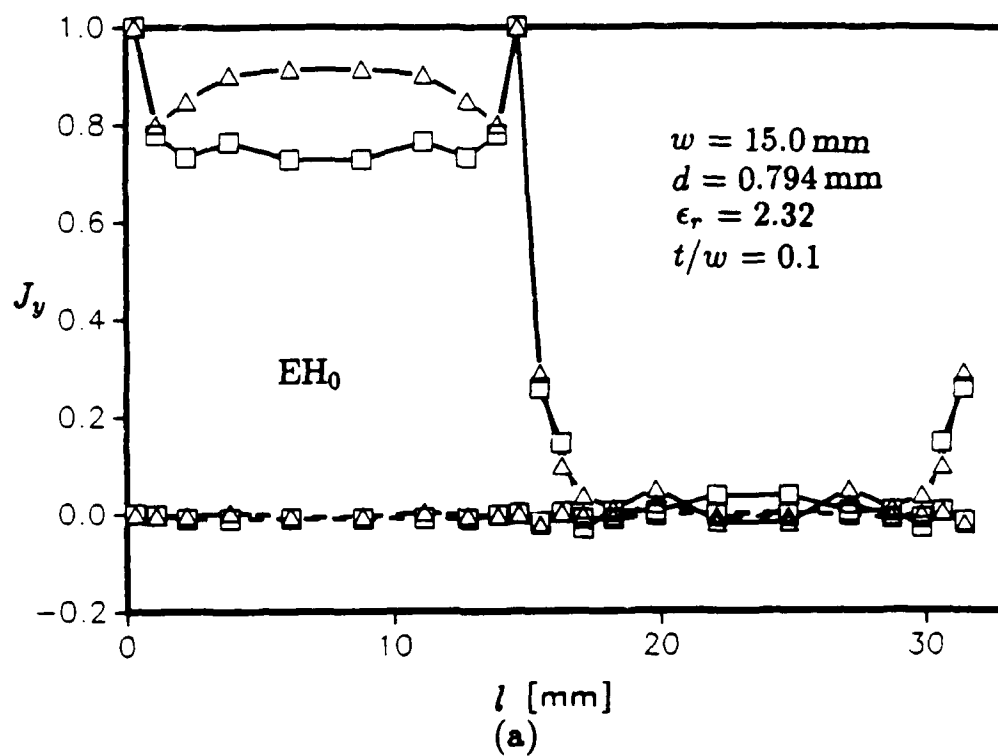
Figure 7.26: (a) Longitudinal and (b) transverse current distributions of the EH_1 mode at $f = 5\,\text{GHz}$ (leaky regime *iii*) and $f = 10\,\text{GHz}$ (bound regime *i*) for a microstrip transmission line of finite thickness.
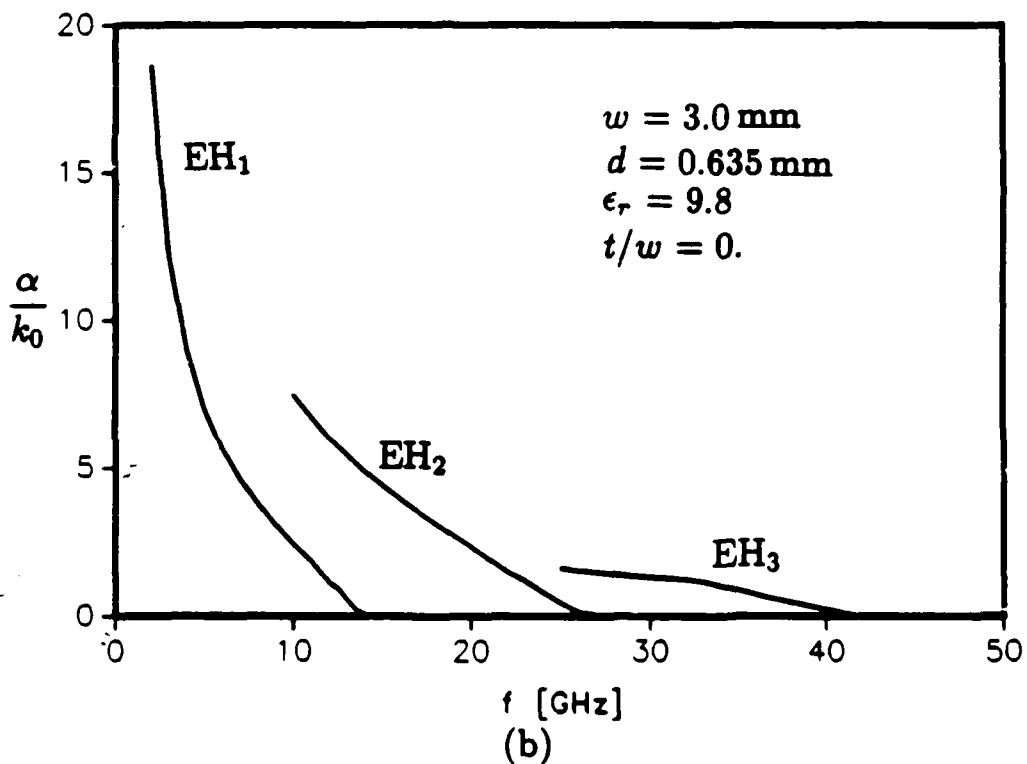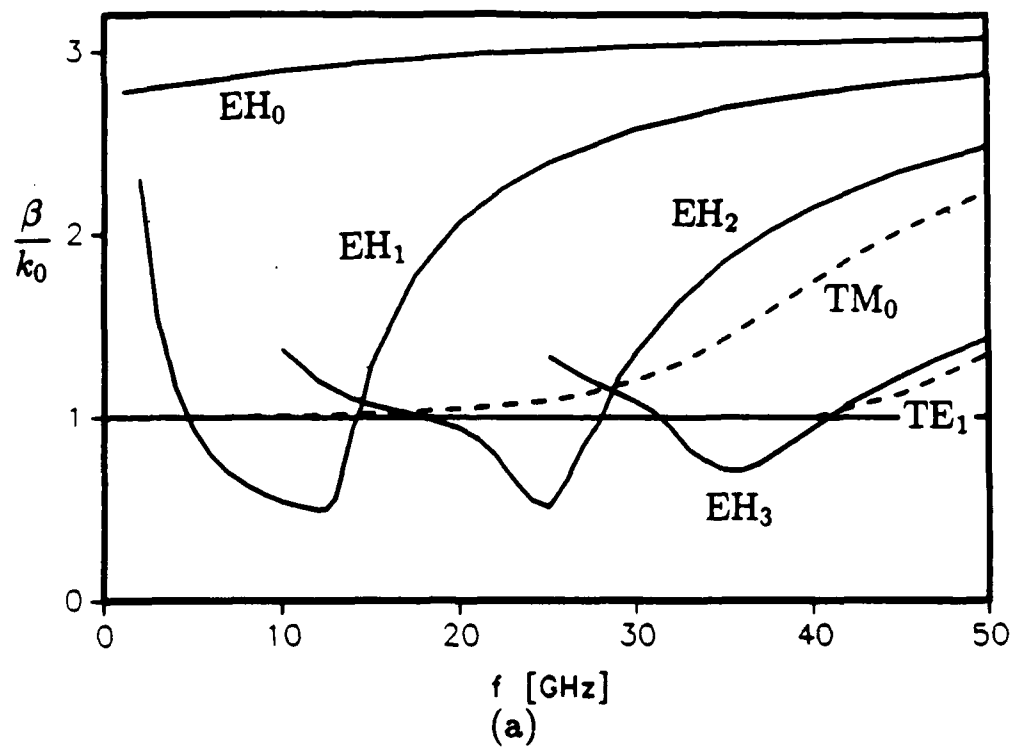
Figure 7.27: Variation with frequency (a) of the normalized phase constant for the lowest mode (EH_0) and the first three higher modes (EH_1, EH_2, EH_3), and (b) of the normalized attenuation constants for the $EH_1, EH_2,$ and EH_3 modes of an infinitely thin microstrip transmission line.

115
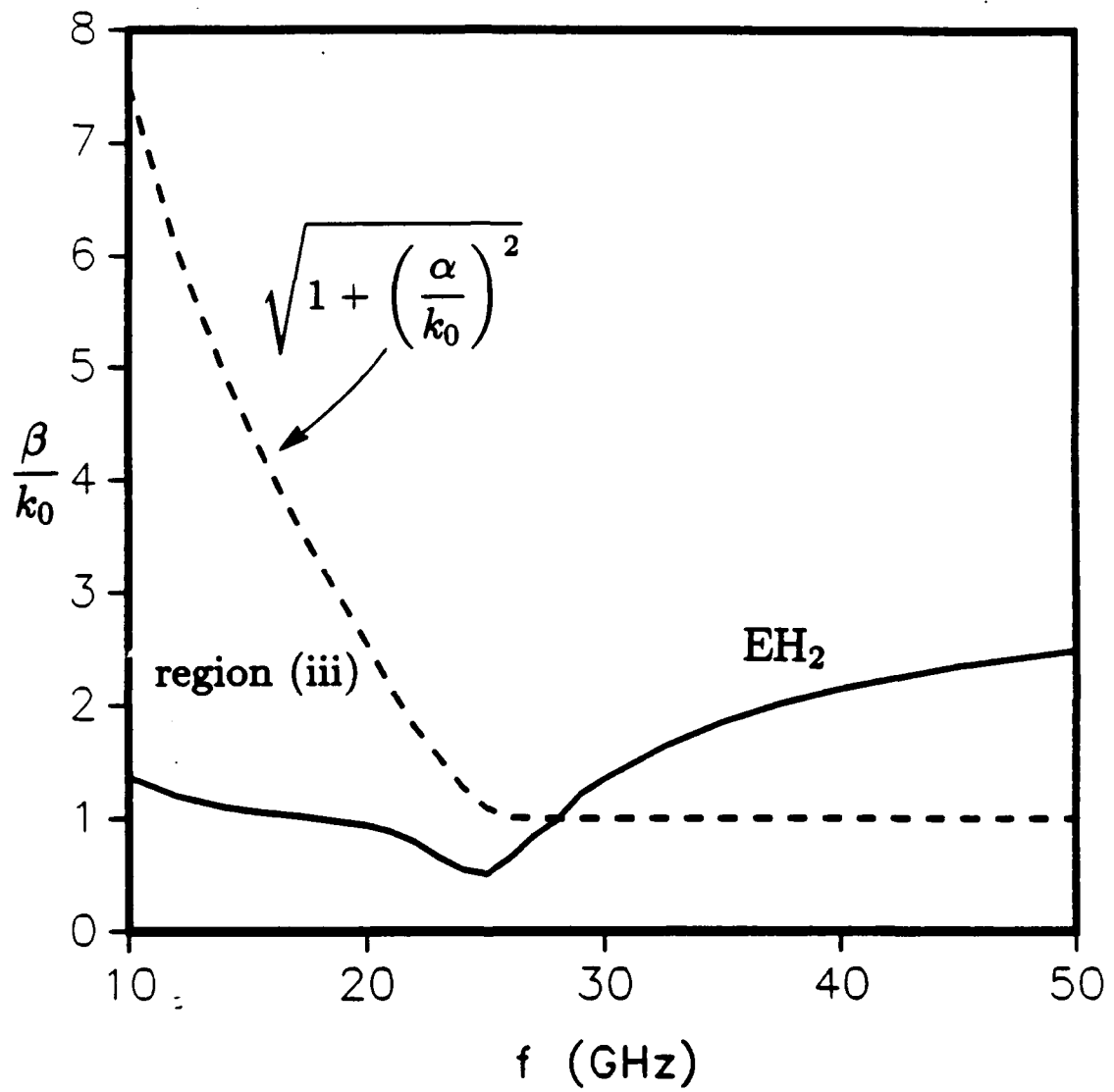
Figure 7.28: Normalized phase constant of the EH_2 mode and the boundary of region iii corresponding to this mode.
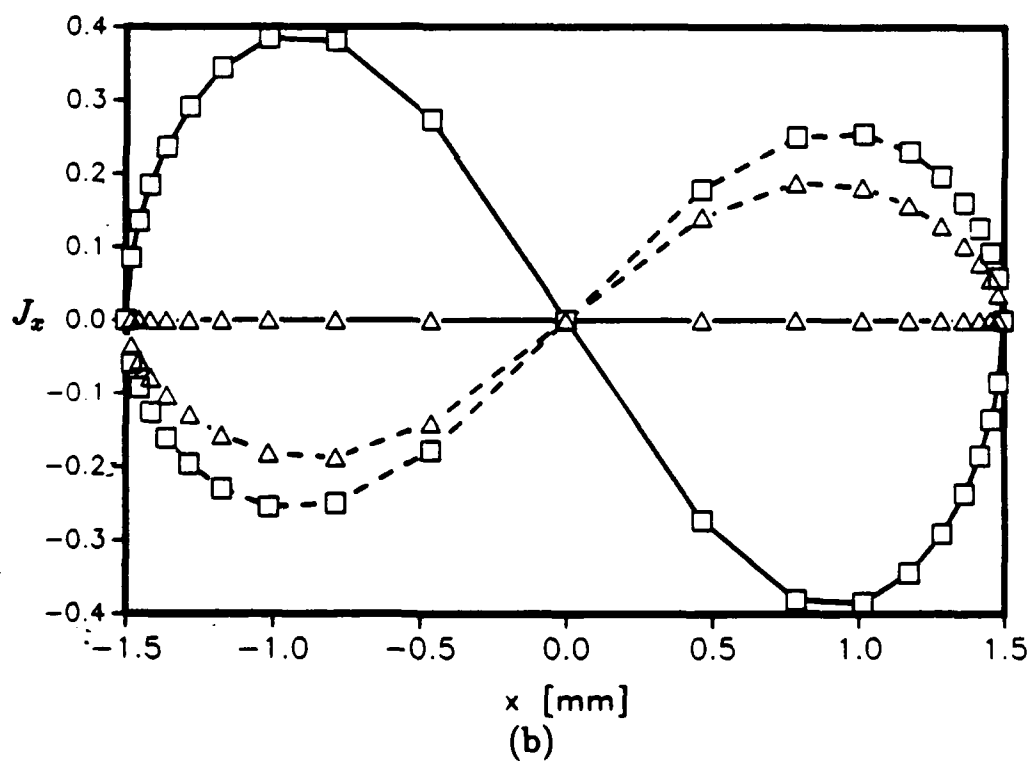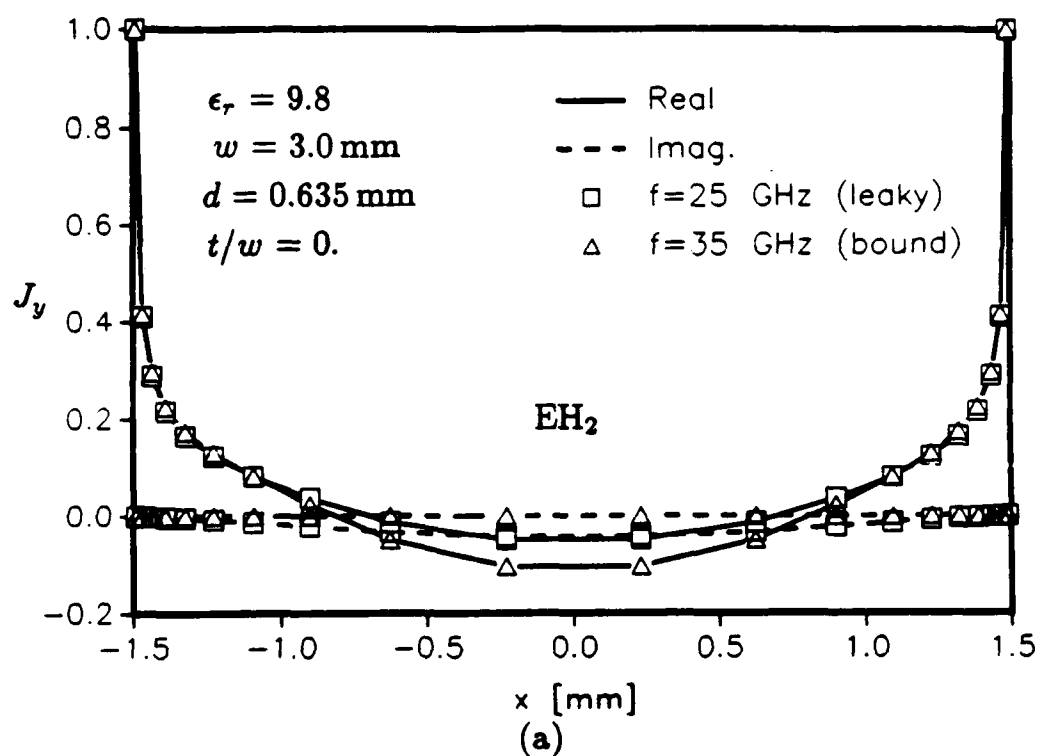
Figure 7.29: (a) Longitudinal and (b) transverse current distributions of the EH_2 mode at $f = 25\,\text{GHz}$ (leaky regime *iii*) and $f = 35\,\text{GHz}$ (bound regime *i*) for an infinitely thin microstrip line.
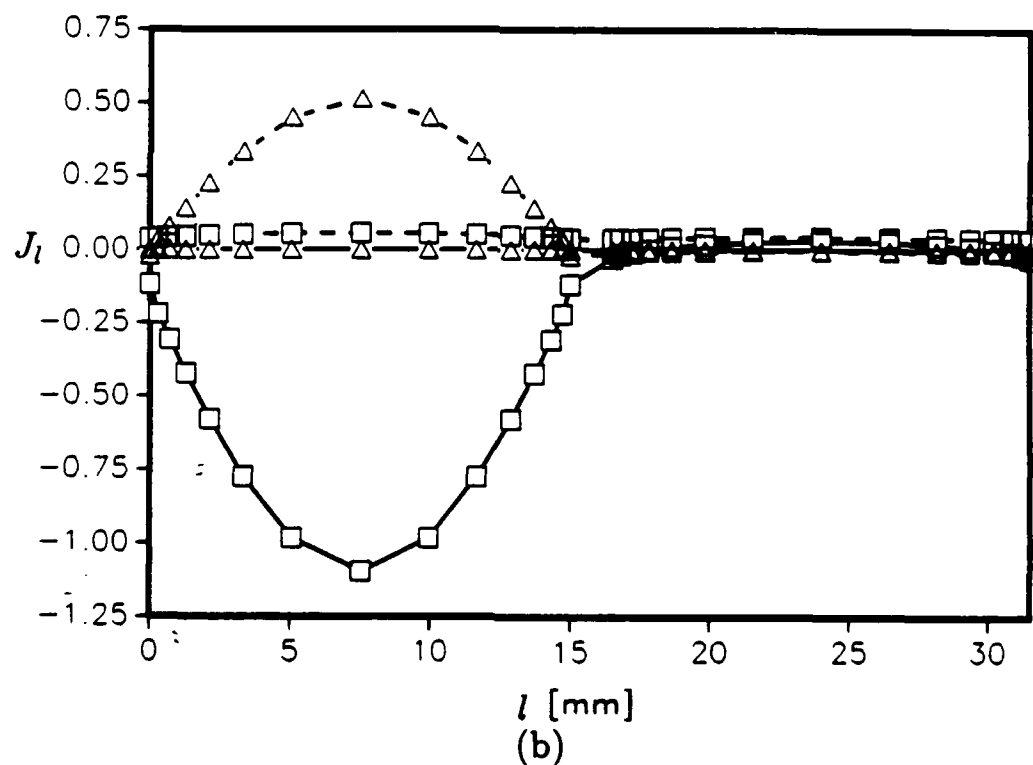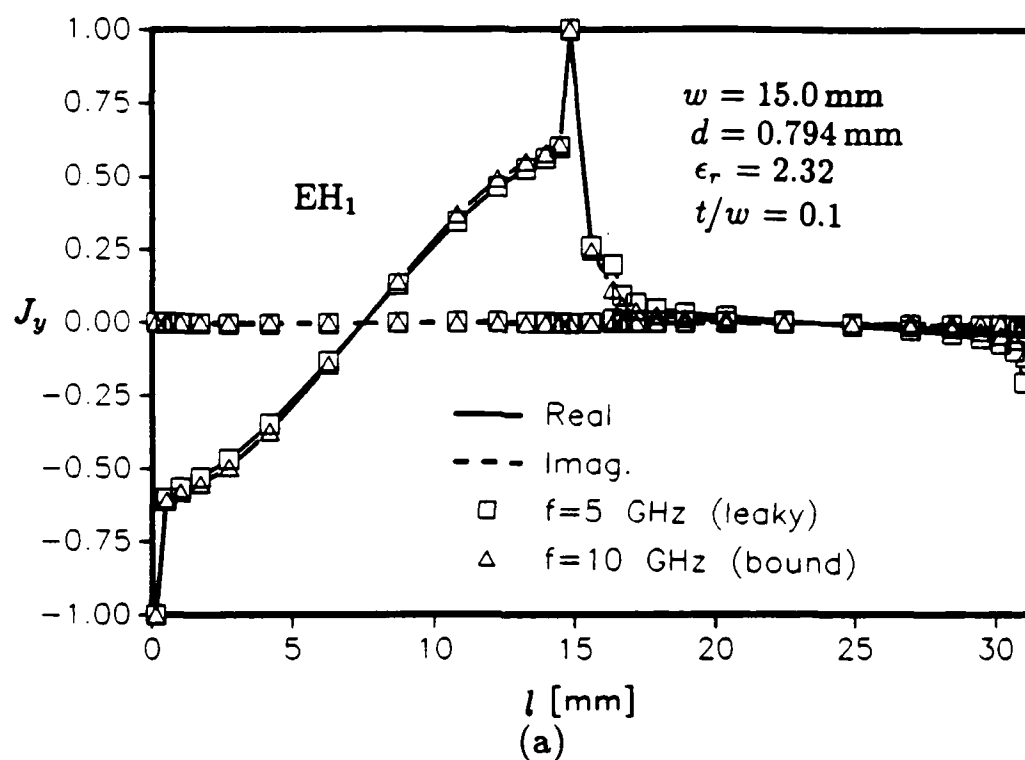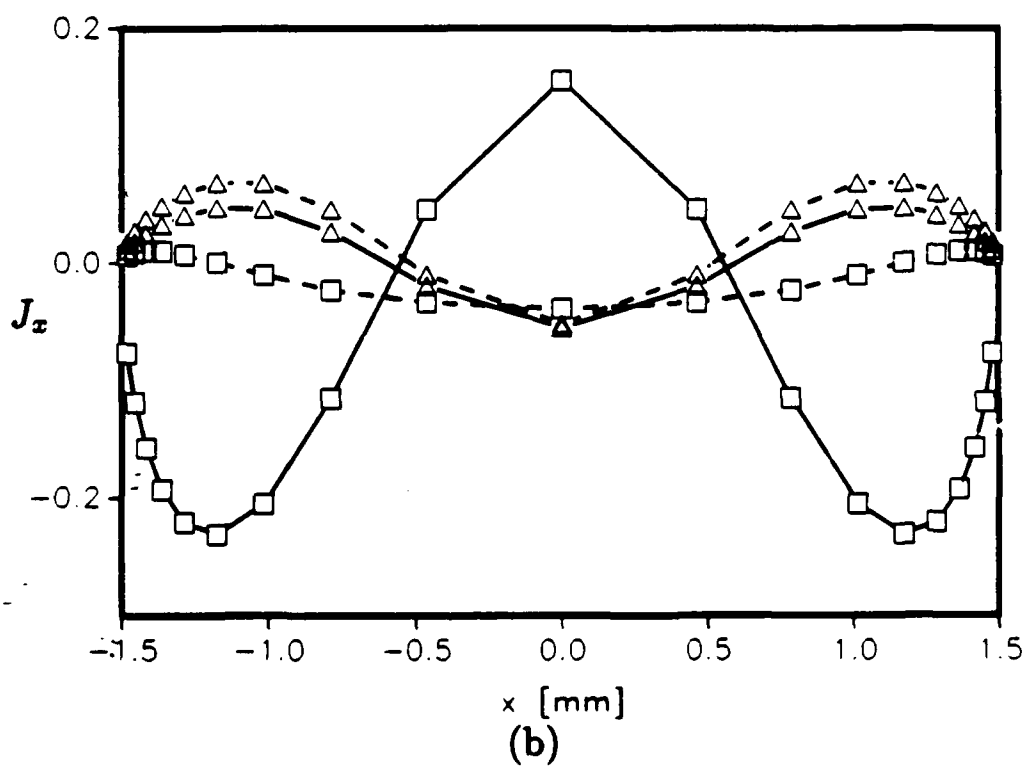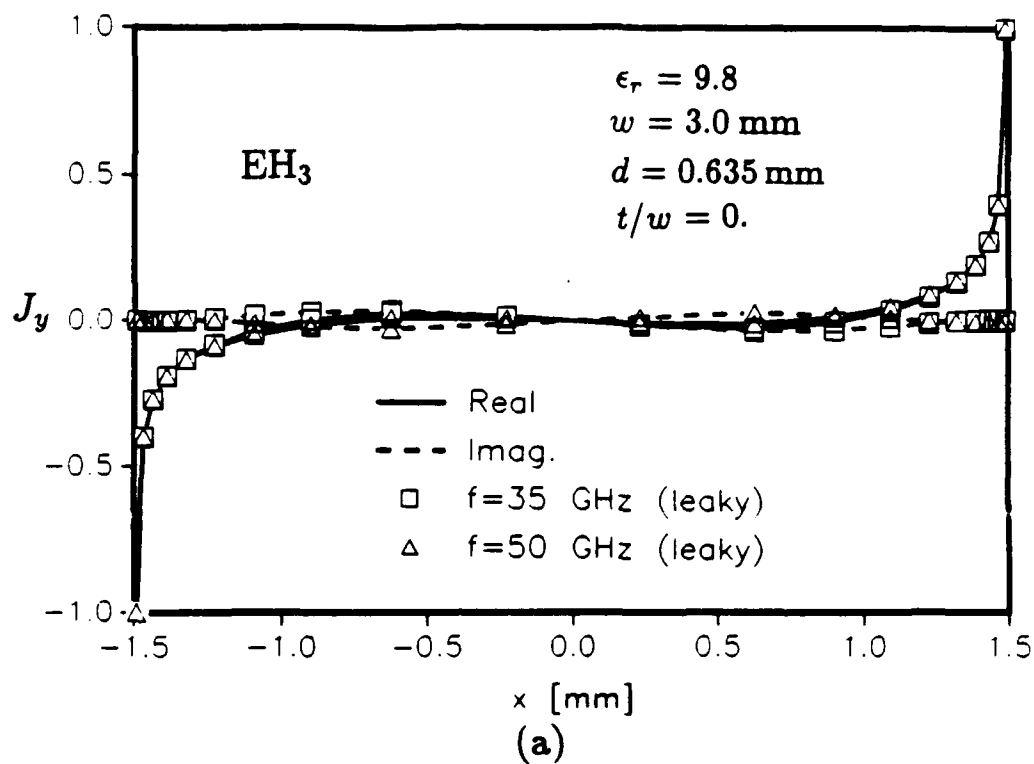
Figure 7.30: (a) Longitudinal and (b) transverse current distributions of the EH_3 mode at $f = 35\,\text{GHz}$ (leaky regime *iii*) and $f = 50\,\text{GHz}$ (leaky regime *ii*) for an infinitely thin microstrip line.
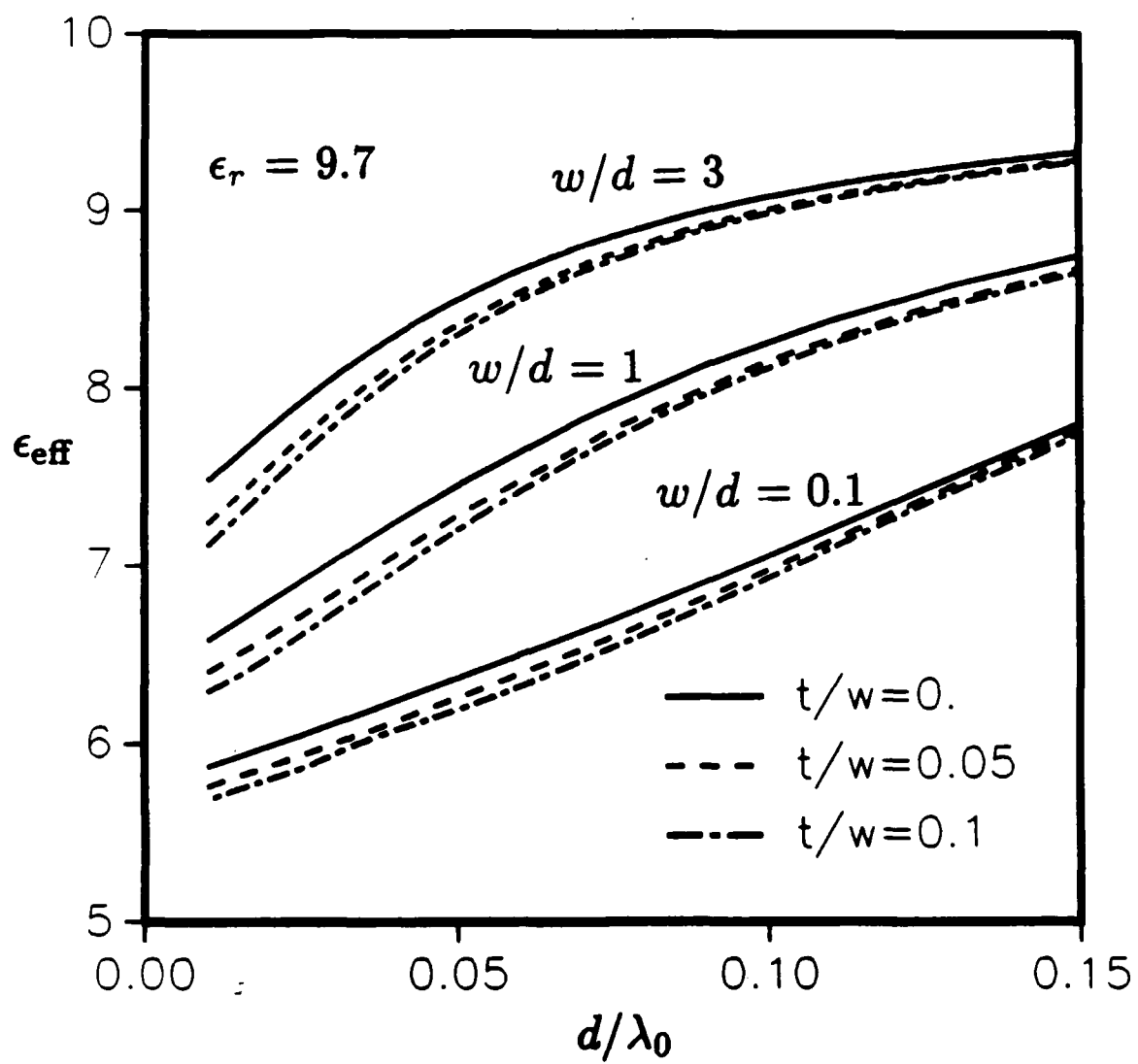
Figure 7.31: Effective dielectric constants of the lowest mode (EH_0) for microstrip lines of different widths and thicknesses.
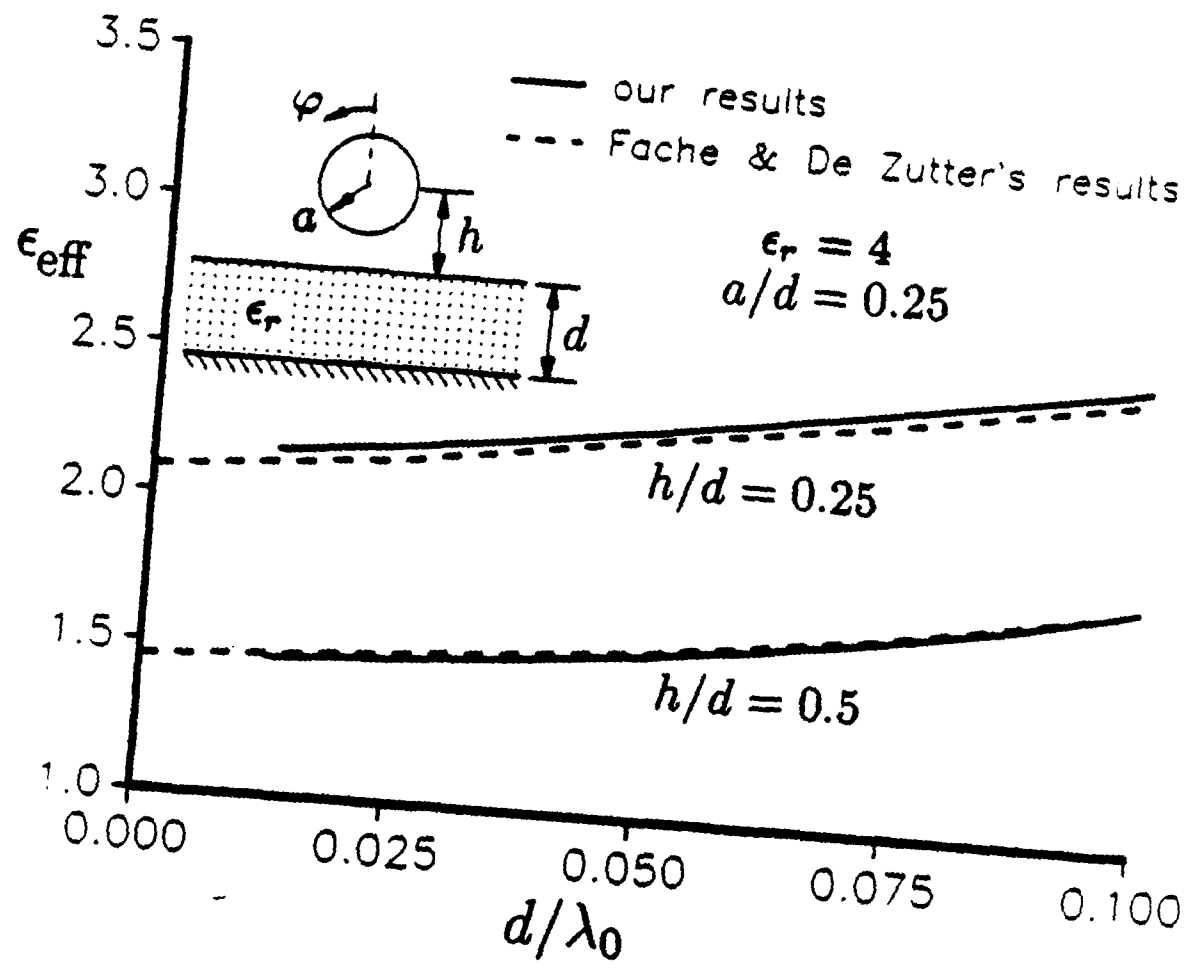
Figure 7.32: Fundamental mode effective dielectric constants for a circular-wire transmission line.
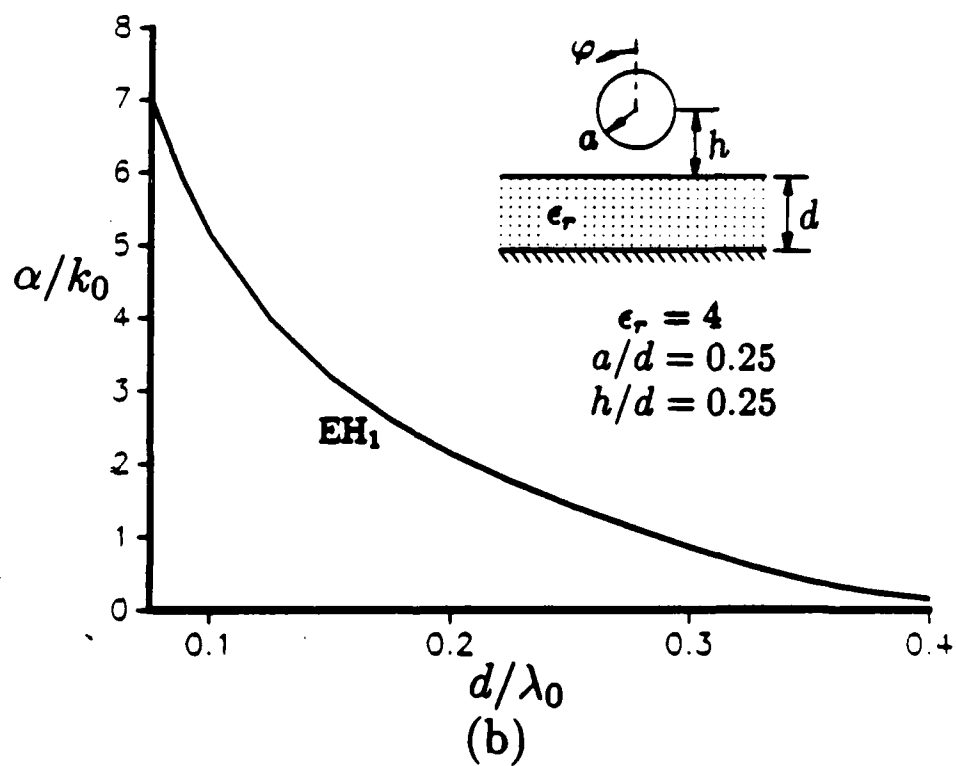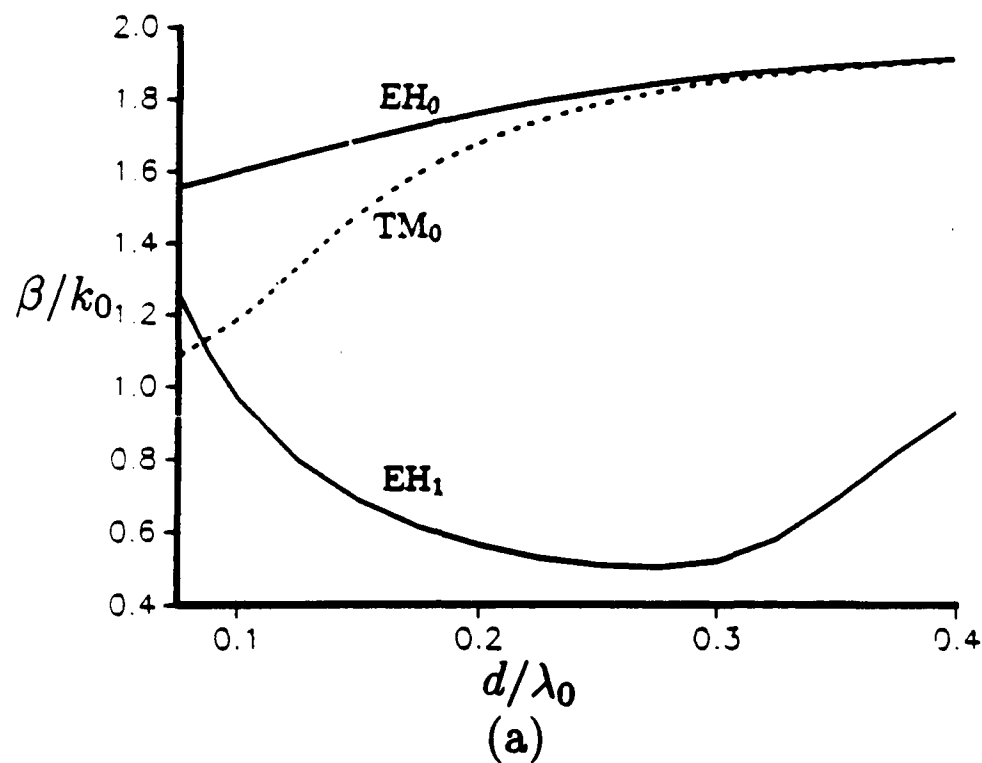
Figure 7.33: Dispersion curves of the fundamental mode and the first higher mode for a circular-wire transmission line. (a) Phase constants. (b) Attenuation (leakage) constant for the higher mode.
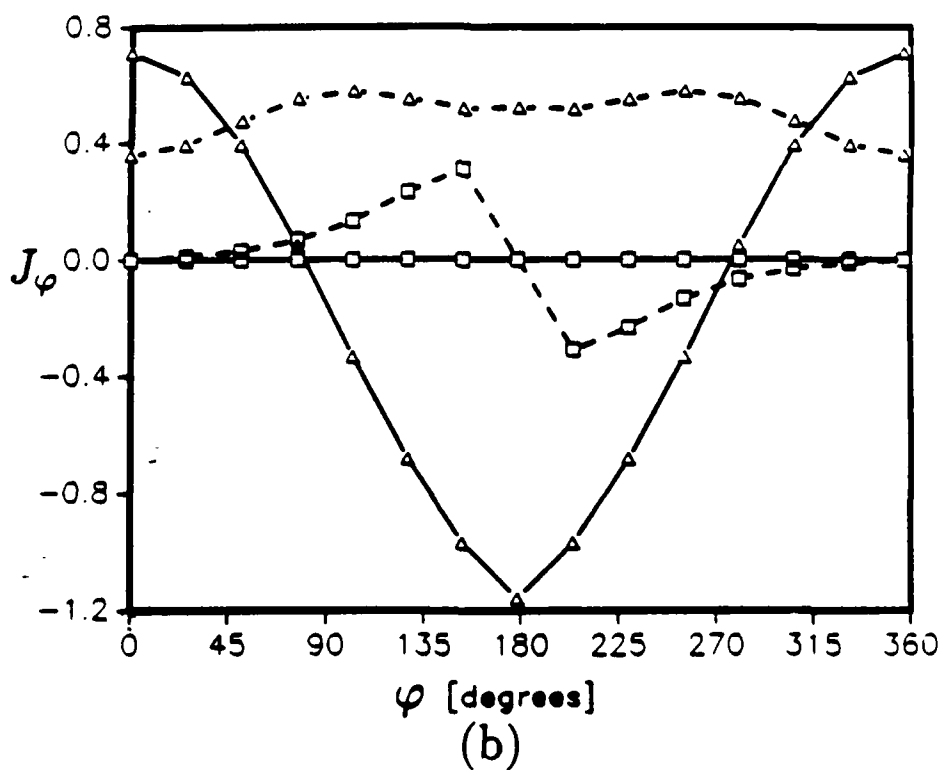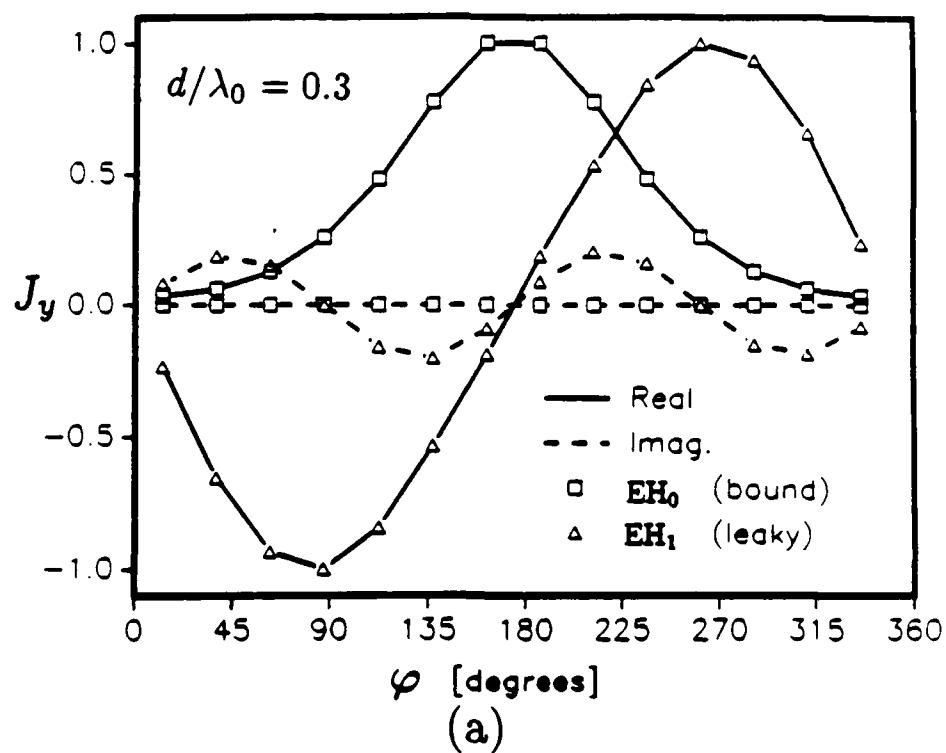
Figure 7.34: (a) Longitudinal and (b) transverse current distributions of the fundamental mode and the first higher mode on a circular–wire transmission line.

Chapter 8

Conclusions

In this work, a rigorous and general procedure has been developed for the analysis of radiation, scattering, and guidance of electromagnetic fields by conducting objects of arbitrary shape embedded in a medium consisting of an arbitrary number of planar, dielectric layers. The key step in this procedure is the transformation of the electric field integral equation into a mixed–potential form, which is amenable to the well–established numerical solution techniques originally developed for arbitrarily–shaped objects in free space. Three particularly useful mixed–potential integral equations (MPIEs) are derived and their properties discussed. One of the three MPIEs, called Formulation C, which is found to be especially well suited for the application of the moment method, is implemented to analyze arbitrarily–shaped, open or closed, conducting surfaces, which penetrate the interface between contiguous dielectric half–spaces. Thin–wire structures are treated as special cases. Formulation C is also specialized to the case of an open transmission line consisting of an infinite conductor of arbitrary cross–section partially embedded in a grounded dielectric slab.

Since at this writing the capability of analyzing the problems of electromagnetic radiation and scattering by three–dimensional PEC surfaces of arbitrary shape in layered media does not exist, the task of validating our results was a difficult one. Data for comparison were only available for thin-wire antennas, the ground stake antenna, and for microstrip patch antennas of several simple shapes. In other cases, we had to rely on the results of two-dimensional analyses. With a few exceptions, our results presented in Chapter 7 compare favorably with the few available measured and numerical results, thus demonstrating—we believe—the validity of the approach advanced here.

Although open microstrip lines have been analyzed by both spectral–domain [83, 84] and space–domain [85, 86] integral equation methods, to our knowledge no results have been published for microstrips of finite thickness. Even for infinitely thin strips, results are only

available for the bound modes. This is possibly due to the fact that the integration paths of the spectral–plane integrals that constitute the kernels of the integral equations must be chosen differently for the bound and leaky modes, respectively, as explained in Section 6.2. Hence, a computer code that is successful for bound mode is likely to fail to find a leaky mode, unless special precautions are taken in the program. This prompted some researchers to voice skepticism about the very existence of the leaky modes in a microstrip. We hope that the results presented in Chapter 7 will put to rest the controversy regarding the existence of leaky microstrip modes.

We wish to point out that, at present, matrix fill time, not the available computer memory, is the overriding factor, which puts practical limits on the size of objects that can be analyzed by the technique advanced here. This is due to the fact that the matrix elements comprise improper, Sommerfeld integrals, which must be repeatedly evaluated by numerical quadrature. as is discussed in Chapter 6. Although it is possible, and desirable, to develop analytical approximations for the Sommerfeld integrals–and thus drastically reduce the computational expense–we have opted in this work for rigorous treatment of those integrals, to avoid the uncertainties associated with approximations, whose ranges of applicability are usually not well–defined. In the case of microstrip patch antennas, considerable savings in matrix fill–time can be realized by using an interpolation method for the Sommerfeld integrals (*cf.* Section 5.3).

Although, for simplicity, we have concentrated in Chapter 5 on the analysis for objects embedded in a two–layer medium, we could almost as easily treat the n–layer case ($n > 2$), for which explicit MPIEs are given in Chapter 4. Also, the approach developed here can be used to analyze arbitrary configurations of surfaces and wires. One could, for example, easily adapt the JUNCTION code [7] for that purpose – as is demonstrated in Section 5.3, where the attachment mode used in JUNCTION was employed to solve the problem of a microstrip patch antenna driven by a coaxial cable. This made it possible to rigorously analyze microstrip antennas coax–fed at an edge or vertex of the patch. The approach developed here can also be directly used to calculate resonant frequencies of microstrip antennas of arbitrary–possibly exotic–shapes. One could also extend it to analyze infinite and finite arrays of microstrip patch antennas of arbitrary shape.

Future work in this area might involve dielectric bodies of arbitrary shape in layered media. For homogeneous bodies, one could apply the surface integral formulation in conjunction with the triangle–patch code [6] and for inhomogeneous objects, the volume integral approach in conjunction with the tetrahedral element model [10]. These techniques can also

be specialized to the analysis of dielectric waveguides consisting of infinite dielectric slabs of arbitrary cross-section embedded in layered media.

Finally, as was already mentioned, there is room for improvements in the evaluation of the Sommerfeld integrals, since most of the computational effort is spent on them.

Appendix A

Kernel Elements of Formulation C for Contiguous Half-Spaces and for a Grounded Slab

A.1 Kernel Elements for Contiguous Half-Spaces

The expressions for the elements of the kernels in (5.1)–(5.3) can be written down by specializing the formulas given in Section 4.3 to the two-layer case (Fig. 5.1a). Thus, when the source and observation points are in the ith region ($i = 1, 2$), one obtains

$$K_{xx}^{ii} = \frac{\mu_i}{4\pi} \left\{ g_i\left(|\boldsymbol{r} - \boldsymbol{r}'|\right) + \frac{\mu_p - \mu_i}{\mu_1 + \mu_2} g_i\left(|\boldsymbol{r} - \boldsymbol{r}''|\right) - \frac{2\mu_p}{\mu_1 + \mu_2} I_1^{ii} \right\} \tag{A.1}$$

$$K_{xz}^{ii} = \frac{\operatorname{sgn}(z)}{2\pi} \cos\zeta \, \frac{\mu_i\left(\mu_p \epsilon_p - \mu_i \epsilon_i\right)}{\left(\mu_1 + \mu_2\right)\left(\epsilon_1 + \epsilon_2\right)}$$
$$\cdot \left\{ \frac{1}{\xi} \left[e^{-jk_i|z+z'|} - |z + z'| \, g_i\left(|\boldsymbol{r} - \boldsymbol{r}''|\right) \right] - I_3^{ii} \right\} \tag{A.2}$$

$$K_{zz}^{ii} = \frac{\mu_i}{4\pi} \left\{ g_i\left(|\boldsymbol{r} - \boldsymbol{r}'|\right) + \left(2\frac{\epsilon_p - \epsilon_i}{\epsilon_1 + \epsilon_2} + \frac{\mu_p - \mu_i}{\mu_1 + \mu_2} \right) g_i\left(|\boldsymbol{r} - \boldsymbol{r}''|\right) \right.$$
$$\left. + 2\left[\frac{\epsilon_i\left(\mu_p - \mu_i\right)}{\mu_p\epsilon_i - \mu_i\epsilon_p} - \frac{\mu_p}{\mu_1 + \mu_2} \right] I_1^{ii} - 2\left[\frac{\mu_i\left(\epsilon_p - \epsilon_i\right)}{\mu_p\epsilon_i - \mu_i\epsilon_p} + \frac{2\epsilon_p}{\epsilon_1 + \epsilon_2} \right] I_2^{ii} \right\} \tag{A.3}$$

$$K_{\phi}^{ii} = \frac{1}{4\pi\epsilon_i} \left\{ g_i\left(|\boldsymbol{r} - \boldsymbol{r}'|\right) - \frac{\epsilon_p - \epsilon_i}{\epsilon_1 + \epsilon_2} g_i\left(|\boldsymbol{r} - \boldsymbol{r}''|\right) \right.$$
$$\left. - 2\frac{\epsilon_i\left(\mu_p - \mu_i\right)}{\mu_p\epsilon_i - \mu_i\epsilon_p} I_1^{ii} + 2\left[\frac{\epsilon_p}{\epsilon_1 + \epsilon_2} + \frac{\mu_i\left(\epsilon_p - \epsilon_i\right)}{\mu_p\epsilon_i - \mu_i\epsilon_p} \right] I_2^{ii} \right\} \tag{A.4}$$

with

126

$$K_{zx}^{ii} = -K_{xz}^{ii} \quad \text{and} \quad K_{zy}^{ii} = -K_{yz}^{ii} \tag{A.5}$$

where K_{yz}^{ii} is given by (2.4) with $\cos\zeta$ replaced by $\sin\zeta$. In the above, we have introduced the notation (*cf.* (3.4))

$$I_1^{ii} = S_0 \left\{ \frac{j\mu_i\left(k_{zi} - k_{zp}\right)}{\mu_1 k_{z2} + \mu_2 k_{z1}} \frac{e^{-jk_{zi}|z+z'|}}{k_{zi}} \right\} \tag{A.6}$$

$$I_2^{ii} = S_0 \left\{ \frac{j\epsilon_i\left(k_{zi} - k_{zp}\right)}{\epsilon_1 k_{z2} + \epsilon_2 k_{z1}} \frac{e^{-jk_{zi}|z+z'|}}{k_{zi}} \right\} \tag{A.7}$$

$$I_3^{ii} = S_1 \left\{ \left[\frac{\left(\mu_1 + \mu_2\right)\left(\epsilon_1 + \epsilon_2\right)}{\left(\mu_1 k_{z2} + \mu_2 k_{z1}\right)\left(\epsilon_1 k_{z2} + \epsilon_2 k_{z1}\right)} + \frac{1}{k_\rho^2} \right] e^{-jk_{zi}|z+z'|} \right\} \tag{A.8}$$

$$g_i(r) = \frac{e^{-jk_i r}}{r} \tag{A.9}$$

and $\boldsymbol{r}'' = \boldsymbol{r}' + 2\hat{z}z'$. The index p in (A.1)–(A.8) assumes the values 1 or 2, but not equal to i (*i.e.*, $p = 1, 2$ and $p \neq i$).

When the source point is in region i and the observation point in region $m \neq i$, one obtains

$$K_{xx}^{mi} = \frac{\mu_m}{2\pi} \frac{\mu_i}{\mu_1 + \mu_2} \left\{ g_m\left(|\boldsymbol{r} - \boldsymbol{r}'|\right) - I_1^{mi} \right\} \tag{A.10}$$

$$K_{xz}^{mi} = \frac{\operatorname{sgn}\left(z\right)}{2\pi} \cos\zeta \frac{\mu_i\left(\mu_i\epsilon_i - \mu_m\epsilon_m\right)}{\left(\mu_1 + \mu_2\right)\left(\epsilon_1 + \epsilon_2\right)}$$
$$\cdot \left\{ \frac{1}{\xi} \left[e^{-jk_m|z-z'|} - |z - z'| g_m\left(|\boldsymbol{r} - \boldsymbol{r}'|\right) \right] - I_3^{ii} \right\} \tag{A.11}$$

$$K_{zz}^{mi} = \frac{\mu_m}{2\pi} \left\{ \left[\frac{\mu_i\epsilon_i}{\mu_m\left(\epsilon_1 + \epsilon_2\right)} - \frac{\mu_i\epsilon_i - \mu_m\epsilon_m}{\mu_i\epsilon_m - \mu_m\epsilon_i} \left(\frac{\mu_i}{\mu_1 + \mu_2} - \frac{\epsilon_i}{\epsilon_1 + \epsilon_2} \right) \right] \right.$$
$$g_m\left(|\boldsymbol{r} - \boldsymbol{r}'|\right) + \frac{\mu_i\epsilon_i - \mu_m\epsilon_m}{\mu_i\epsilon_m - \mu_m\epsilon_i} \frac{\mu_i}{\mu_1 + \mu_2} I_1^{mi}$$
$$\left. - \frac{\epsilon_1\epsilon_2}{\epsilon_1 + \epsilon_2} \frac{\mu_i^2 - \mu_m^2}{\mu_m\left(\mu_i\epsilon_m - \mu_m\epsilon_i\right)} I_2^{mi} \right\} \tag{A.12}$$

$$K_\phi^{mi} = \frac{1}{2\pi} \frac{1}{\epsilon_1 + \epsilon_2} \left\{ g_m\left(|\boldsymbol{r} - \boldsymbol{r}'|\right) \right.$$
$$\left. - \frac{\epsilon_1 + \epsilon_2}{\mu_i\epsilon_m - \mu_m\epsilon_i} \left[\left(\mu_i - \mu_m\right) I_1^{mi} - \frac{\mu_i\epsilon_i - \mu_m\epsilon_m}{\epsilon_1 + \epsilon_2} I_2^{mi} \right] \right\} \tag{A.13}$$

with

127

$$K_{zx}^{mi} = -\frac{\mu_m}{\mu_i} K_{xz}^{mi} \quad \text{and} \quad K_{zy}^{mi} = -\frac{\mu_m}{\mu_i} K_{yz}^{mi} \tag{A.14}$$

where K_{yz}^{mi} is given by (A.11) with $\cos\zeta$ replaced by $\sin\zeta$. In these equations, we have introduced the notation

$$I_1^{mi} = S_0 \left\{ \left[\frac{j\,(\mu_1 + \mu_2)}{\mu_1 k_{z2} + \mu_2 k_{z1}} e^{-jk_{z1}|z'|} + \frac{e^{-jk_{zm}|z'|}}{jk_{zm}} \right] e^{-jk_{zm}|z|} \right\} \tag{A.15}$$

$$I_2^{mi} = S_0 \left\{ \left[\frac{j\,(\epsilon_1 + \epsilon_2)}{\epsilon_1 k_{z2} + \epsilon_2 k_{z1}} e^{-jk_{z1}|z'|} + \frac{e^{-jk_{zm}|z'|}}{jk_{zm}} \right] e^{-jk_{zm}|z|} \right\} \tag{A.16}$$

$$I_3^{mi} = S_1 \left\{ \left[\frac{(\mu_1 + \mu_2)\,(\epsilon_1 + \epsilon_2)\,e^{-jk_{z1}|z'|}}{(\mu_1 k_{z2} + \mu_2 k_{z1})\,(\epsilon_1 k_{z2} + \epsilon_2 k_{z1})} + \frac{e^{-jk_{zm}|z'|}}{k_\rho^{\,2}} \right] e^{-jk_{zm}|z|} \right\}. \tag{A.17}$$

Several comments are in order concerning the form of the above expressions, which resulted–after a considerable amount of manipulations–from the corresponding formulas derived in Section 4.3. The chosen forms have the advantage that most of the contribution to the value of a given kernel element comes from the closed form term, thus deemphasizing the importance of the Sommerfeld integral. We also note that for the given r and r', only three distinct Sommerfeld integrals are called for. Another advantage of this particular formulation is that the Sommerfeld integrals are well–behaved, even when $r = r'$ on the interface.

A.2 Kernel Elements for a Grounded Slab

We now specialize the formulas of Section 4.3 to the grounded slab case (see Fig. 5.1b). When the source and observation points are both in region 1, we obtain

$$K_{xx}^{11} = \frac{\mu_1}{4\pi} \left\{ g_1(|\,r - r'\,|) - S_0 \left[\frac{\mu_1 k_{z2} \cot(k_{z2}d) - j\mu_2 k_{z1}}{D^h} \frac{e^{-jk_{z1}(z+z')}}{jk_{z1}} \right] \right\} \tag{A.18}$$

$$K_{zx}^{11} = -\frac{\mu_1}{2\pi}(\mu_1\epsilon_1 - \mu_2\epsilon_2)\cos\zeta\, S_1 \left\{ \frac{e^{-jk_{z1}(z+z')}}{D^e D^h} \right\} \tag{A.19}$$

$$K_{xz}^{11} = -K_{zx}^{11} \tag{A.20}$$

$$K_{zz}^{11} = \frac{\mu_1}{4\pi} \left\{ g_1(r - r') + S_0 \left\{ \left[\frac{j\epsilon_2 k_{z1} + \epsilon_1 k_{z2} \tan(k_{z2}d)}{D^e j k_{z1}} \right. \right.\right.$$
$$\left.\left.\left. +2(\mu_2\epsilon_2 - \mu_1\epsilon_1)\frac{jk_{z1}}{D^e D^h} \right] e^{-jk_{z1}(z+z')} \right\} \right\} \tag{A.21}$$

128

$$K_\phi^{11} = \frac{1}{4\pi\epsilon_1} \left\{ g_1(\boldsymbol{r} - \boldsymbol{r}') - S_0 \left\{ \left[\frac{\mu_1 k_{z2} \cot(k_{z2}d) - j\mu_2 k_{z1}}{D^h j k_{z1}} \right. \right. \right.$$

$$\left. \left. \left. + 2(\mu_2\epsilon_2 - \mu_1\epsilon_1) \frac{jk_{z1}}{D^e D^h} \right] e^{-jk_{z1}(z+z')} \right\} \right\}. \tag{A.22}$$

When the source point is in region 1 and the observation point is in region 2 ($i = 1$, $m = 2$), we obtain

$$K_{xx}^{21} = \frac{\mu_2}{2\pi} S_0 \left\{ \frac{\mu_1}{D^h} \frac{\sin[k_{z2}(z+d)]}{\sin(k_{z2}d)} e^{-jk_{z1}z'} \right\} \tag{A.23}$$

$$K_{xz}^{21} = \frac{\mu_1}{2\pi} (\mu_2\epsilon_2 - \mu_1\epsilon_1) \cos\zeta S_1 \left\{ \frac{1}{D^e D^h} \frac{\sin[k_{z2}(z+d)]}{\sin(k_{z2}d)} e^{-jk_{z1}z'} \right\} \tag{A.24}$$

$$K_{zx}^{21} = -\frac{\mu_2}{2\pi} (\mu_2\epsilon_2 - \mu_1\epsilon_1) \cos\zeta S_1 \left\{ \frac{1}{D^e D^h} \frac{\cos[k_{z2}(z+d)]}{\cos(k_{z2}d)} e^{-jk_{z1}z'} \right\} \tag{A.25}$$

$$K_{zz}^{21} = \frac{1}{2\pi} S_0 \left\{ \left[\frac{\mu_2\epsilon_2}{D^e} - (\mu_2\epsilon_2 - \mu_1\epsilon_1) \frac{\mu_1 k_{z2} \cot(k_{z2}d)}{D^e D^h} \right] \frac{\cos[k_{z2}(z+d)]}{\cos(k_{z2}d)} e^{-jk_{z1}z'} \right\} \tag{A.26}$$

$$K_\phi^{21} = \frac{1}{2\pi} S_0 \left\{ \frac{j\mu_1 k_{z1} - \mu_2 k_{z2} \tan(k_{z2}d)}{D^e D^h} \frac{\sin[k_{z2}(z+d)]}{\sin(k_{z2}d)} e^{-jk_{z1}z'} \right\}. \tag{A.27}$$

When the source point is in region 2 and the observation point is in region 1 ($i = 2$, $m = 1$), we obtain

$$K_{xx}^{12} = \frac{\mu_1}{2\pi} S_0 \left\{ \frac{\mu_2}{D^h} \frac{\sin[k_{z2}(z'+d)]}{\sin(k_{z2}d)} e^{-jk_{z1}z} \right\} \tag{A.28}$$

$$K_{xz}^{12} = -\frac{\mu_1}{2\pi} (\mu_1\epsilon_1 - \mu_2\epsilon_2) \cos\zeta S_1 \left\{ \frac{1}{D^e D^h} \frac{\cos[k_{z2}(z'+d)]}{\cos(k_{z2}d)} e^{-jk_{z1}z} \right\} \tag{A.29}$$

$$K_{zx}^{12} = \frac{\mu_1}{2\pi} (\mu_1\epsilon_1 - \mu_2\epsilon_2) \cos\zeta S_1 \left\{ \frac{1}{D^e D^h} \frac{\sin[k_{z2}(z'+d)]}{\sin(k_{z2}d)} e^{-jk_{z1}z} \right\} \tag{A.30}$$

$$K_{zz}^{12} = \frac{1}{2\pi} S_0 \left\{ \left[\frac{\mu_1\epsilon_1}{D^e} - (\mu_1\epsilon_1 - \mu_2\epsilon_2) \frac{jk_{z1}}{D^e D^h} \right] \frac{\cos[k_{z2}(z'+d)]}{\cos(k_{z2}d)} e^{-jk_{z1}z} \right\} \tag{A.31}$$

$$K_\phi^{12} = \frac{1}{2\pi} S_0 \left\{ \frac{j\mu_1 k_{z1} - \mu_2 k_{z2} \tan(k_{z2}d)}{D^e D^h} \frac{\sin[k_{z2}(z'+d)]}{\sin(k_{z2}d)} e^{-jk_{z1}z} \right\}. \tag{A.32}$$

Finally, when the source and observation points are in region 2 ($i = 2$, $m = 2$), we obtain

129

$$K_{xx}^{22} = \frac{\mu_2}{2\pi} S_0 \left\{ \frac{-j\mu_2 k_{z1} + \mu_1 k_{z2} \cot(k_{z2} z_>)}{D^h} \frac{\sin(k_{z2} z_>) \sin[k_{z2}(z_< + d)]}{k_{z2} \sin(k_{z2} d)} \right\} \tag{A.33}$$

$$K_{xz}^{22} = \frac{\mu_2}{2\pi} (\mu_2 \epsilon_2 - \mu_1 \epsilon_1) \cos \zeta \, S_1 \left\{ \frac{1}{D^h D^e} \frac{\sin[k_{z2}(z + d)]}{\sin(k_{z2} d)} \frac{\cos[k_{z2}(z' + d)]}{\cos(k_{z2} d)} \right\} \tag{A.34}$$

$$K_{zx}^{22} = -\frac{\mu_2}{2\pi} (\mu_2 \epsilon_2 - \mu_1 \epsilon_1) \cos \zeta \, S_1 \left\{ \frac{1}{D^h D^e} \frac{\sin[k_{z2}(z' + d)]}{\sin(k_{z2} d)} \frac{\cos[k_{z2}(z + d)]}{\cos(k_{z2} d)} \right\} \tag{A.35}$$

$$K_{zz}^{22} = \frac{\mu_2}{2\pi} S_0 \left\{ \frac{-j\epsilon_2 k_{z1} + \epsilon_1 k_{z2} \cot(k_{z2} z_>)}{D^e} \frac{\sin(k_{z2} z_>)}{k_{z2}} \frac{\cos[k_{z2}(z_< + d)]}{\cos(k_{z2} d)} \right.$$
$$\left. -(\mu_2 \epsilon_2 - \mu_1 \epsilon_1) \frac{k_{z2}}{D^h D^e} \frac{\cos[k_{z2}(z + d)] \cos[k_{z2}(z' + d)]}{\sin(k_{z2} d) \cos(k_{z2} d)} \right\} \tag{A.36}$$

$$K_{\phi}^{22} = \frac{1}{2\pi \epsilon_2} S_0 \left\{ \frac{-j\mu_2 k_{z1} + \mu_1 k_{z2} \cot(k_{z2} z_>)}{D^h} \frac{\sin(k_{z2} z_>)}{k_{z2}} \frac{\sin[k_{z2}(z_< + d)]}{\sin(k_{z2} d)} \right.$$
$$\left. -(\mu_2 \epsilon_2 - \mu_1 \epsilon_1) \frac{k_{z2}}{D^h D^e} \frac{\sin[k_{z2}(z + d)] \sin[k_{z2}(z' + d)]}{\cos(k_{z2} d) \sin(k_{z2} d)} \right\} \tag{A.37}$$

where $z_<$ and $z_>$ denote, respectively, the lesser and the greater of z and z'. K_{yz}^{mi} and K_{zy}^{mi} ($m = 1, 2$, $i = 1, 2$) are given by K_{xz}^{mi} and K_{zx}^{mi}, respectively, with $\cos \zeta$ replaced by $\sin \zeta$. In the above equations, we have introduced the notation

$$D^h = j\mu_2 k_{z1} + \mu_1 k_{z2} \cot(k_{z2} d) \tag{A.38}$$

$$D^e = j\epsilon_2 k_{z1} - \epsilon_1 k_{z2} \tan(k_{z2} d). \tag{A.39}$$

Acknowledgments

Bibliography

[1] R. F. Harrington, *Field Computation by Moment Methods*. New York: Macmillan, 1968.

[2] A. W. Glisson, *On the development of numerical techniques for treating arbitrarily-shaped surfaces*. PhD thesis, Dept. Elec. Eng., Univ. Mississippi, 1978.

[3] D. R. Wilton, "Wire problems," in *Numerical and Asymptotic Techniques for Electromagnetics and Antennas* (R. F. Harrington and R. Mittra, eds.), Syracuse Univ. and Univ. Illinois, 1979.

[4] A. W. Glisson and D. R. Wilton, "Simple and efficient numerical methods for problems of electromagnetic radiation and scattering from surfaces," *IEEE Trans. Antennas Propagat.*, vol. AP-28, pp. 593–603, Sept. 1980.

[5] S. M. Rao, D. R. Wilton, and A. W. Glisson, "Electromagnetic scattering by surfaces of arbitrary shape," *IEEE Trans. Antennas Propagat.*, vol. AP-30, pp. 409–418, May 1982.

[6] K. Umashankar, A. Taflove, and S. M. Rao, "Electromagnetic scattering by arbitrary shaped three-dimensional homogeneous lossy dielectric objects," *IEEE Trans. Antennas Propagat.*, vol. AP-34, pp. 758–766, June 1986.

[7] S. U. Hwu and D. R. Wilton, "Electromagnetic scattering and radiation by arbitrary configurations of conducting bodies and wires," Tech. Rep. 87-17, Applied Electromagnetics Lab., Dept. of Electrical Engr., Univ. of Houston, May 1988.

[8] J. J. H. Wang, "Numerical analysis of three-dimensional arbitrarily-shaped conducting scatterers by trilatiral surface cell modelling," *Radio Sci.*, vol. 13, pp. 947–952, Nov.-Dec. 1978.

[9] A. J. Poggio and E. K. Miller, "Integral equation solutions of three-dimensional scattering problems," in *Computer Techniques for Electromagnetics* (R. Mittra, ed.), pp. 159–264, New York: Pergamon Press, 1973.

[10] D. H. Schaubert, D. R. Wilton, and A. W. Glisson, "A tetrahedral modeling method for electromagnetic scattering by arbitrarily shaped inhomogeneous dielectric bodies," *IEEE Trans. Antennas Propagat.*, vol. AP-32, pp. 77–85, Jan. 1984.

[11] W. A. Johnson, D. R. Wilton, and R. M. Sharpe, *PATCH CODE User's Manual.* Sandia National Laboratories, Albuquerque, N. M., 1988.

[12] J. W. Rockway, J. C. Logan, D. W. S. Tam, and S. T. Li, *The MININEC System: Microcomputer Analysis of Wire Antennas.* Boston: Artech House, 1988.

[13] J. C. Logan and J. W. Rockway, "The new MININEC (version 3): A mini-numerical electromagnetic code," Tech. Rep. 938, Naval Ocean Systems Center, San Diego, CA, Sept. 1986.

[14] A. Erteza and B. K. Park, "Nonuniqueness of resolution of Hertz vector in presence of a boundary, and a horizontal dipole problem," *IEEE Trans. Antennas Propagat.*, vol. AP-17, pp. 376–378, May 1969.

[15] K. A. Michalski, "On the scalar potential of a point charge associated with a time-harmonic dipole in a layered medium," *IEEE Trans. Antennas Propagat.*, vol. AP-35, pp. 1299–1301, Nov. 1987.

[16] A. Sommerfeld, *Partial Differential Equations.* New York: Academic Press, 1949.

[17] J. R. Mosig and F. E. Gardiol, "A dynamical radiation model for microstrip structures," in *Advances in Electronics and Electron Physics* (P. W. Hawkes, ed.), vol. 59, pp. 139–237, New York: Academic Press, 1982.

[18] J. R. Mosig and F. E. Gardiol, "General integral equation formulation for microstrip antennas and scatterers," *IEE Proc.*, vol. 132, Pt. H, pp. 424–432, Dec. 1985.

[19] W. A. Johnson, "Analysis of a vertical, tubular cylinder which penetrates an air-dielectric interface and which is excited by an azimuthally symmetric source," *Radio Sci.*, vol. 18, pp. 1273–1281, Nov.-Dec. 1983.

[20] D. R. Wilton and S. Singh, "Analysis of an infinite periodic array of slots with dielectric loading," *1985 AP-S Int. Symp.*, Vancouver, Canada, pp. 229–232, 1985.

[21] K. A. Michalski, C. E. Smith, and C. M. Butler, "Analysis of a horizontal two-element antenna array above a dielectric halfspace," *IEE Proc.*, vol. 132, Pt. H, pp. 335–338, Aug. 1985.

[22] K. A. Michalski and C. E. Smith, "Analysis of parallel monopole antennas residing in contiguous media," *Nat'l Radio Sci. Meeting Digest*, p. 230, Boulder, CO, Jan. 13-16, 1986.

[23] K. A. Michalski, "On the dyadic Green's function for a grounded dielectric slab," *Nat'l Radio Sci. Meeting Digest*, p. 93, Boston, MA, June 25-29, 1984.

[24] K. A. Michalski, "The mixed-potential electric field integral equation for objects in layered media," *Arch. Elek. Übertragung.*, vol. 39, pp. 317–322, Sept.-Oct. 1985.

[25] K. A. Michalski and D. Zheng, "Analysis of wire antennas of arbitrary shape residing in contiguous half-spaces," *5th Int. Conf. Antennas Propagat. (ICAP 87)*, York, UK, pp. 507–511, 1987.

[26] X. B. Xu, *Analysis of TM- and TE- excited cylinders in a region comprising two semi-infinite half-spaces separated by a planar interface*. PhD thesis, Dept. Elec. Eng., Univ. Mississippi, 1985.

[27] G. J. Burke and E. K. Miller, "Modeling antennas near to and penetrating a lossy interface," *IEEE Trans. Antennas Propagat.*, vol. AP-32, pp. 1040–1049, Oct. 1984.

[28] G. J. Burke, "The numerical electromagnetics code (NEC)," in *Applications of the Method of Moments to Electromagnetic Fields* (B. J. Strait, ed.), pp. 449–469, St. Cloud, Florida: The SCEEE Press, 1980.

[29] G. W. Hohmann, "Three-dimensional EM modeling," *Geophys. Surv.*, vol. 6, pp. 27–53, 1983.

[30] P. E. Wannamaker, G. W. Hohmann, and W. A. SanFilipo, "Electromagnetic modeling of three-dimensional bodies in layered earths using integral equations," *Geophysics*, vol. 49, pp. 60–74, Jan. 1984.

133

[31] A. Karlsson and G. Kristensson, "Electromagnetic scattering from subterranean obstacles in a stratified ground," *Radio Sci.*, vol. 18, pp. 345–356, May-June 1983.

[32] R. F. Harrington, *Time-Harmonic Electromagnetic Fields*. New York: McGraw-Hill, 1961.

[33] A. Banos, *Dipole Radiation in the Presence of a Conducting Half-Space*. New York: Pergamon Press, 1966.

[34] B. D. Popovic, M. B. Dragovic, and A. R. Djordjevic, *Analysis and Synthesis of Wire Antennas*. Chichester: Research Studies Press, 1982.

[35] M. Chiba, "Singularities of Green's function in surface integral equations," *Electronics and Communications in Japan*, vol. 66-B, no. 11, pp. 85–93, 1983.

[36] O. D. Kellogg, *Foundations of Potential Theory*. New York: Dover, 1953.

[37] J. G. Fikioris, "Electromagnetic field inside a current-carrying region," *J. Math. Phys.*, vol. 6, pp. 1617–1620, Nov. 1965.

[38] J. Van Bladel, *Electromagnetic Fields*. Washington: Hemisphere, 1985.

[39] M. Marcuvitz and J. Schwinger, "On the representation of the electric and magnetic field produced by currents and discontinuities in wave guides," *J. Appl. Phys.*, vol. 22, pp. 806–819, June 1951.

[40] L. B. Felsen and N. Marcuvitz, *Radiation and Scattering of Waves*. Englewood Cliffs, N.J.: Prentice Hall, 1973.

[41] D. R. Wilton, S. M. Rao, A. W. Glisson, D. H. Schaubert, O. M. Al-Bundak, and C. M. Butler, "Potential integrals for uniform and linear source distributions on polygonal and polyhedral domains," *IEEE Trans. Antennas Propagat.*, vol. AP-32, pp. 276–281, Mar. 1984.

[42] M. F. Costa and R. F. Harrington, "Minimization of radiation from computer systems," *Proc. Int'l Electrical Electronics Conference and Exposition*, pp. 660–665, Toronto, Canada, Sept. 1983.

[43] P. Pichon, J. Mosig, and A. Papiernik, "Input impedance of arbitrarily shaped microstrip antennas," *Electron Lett.*, vol. 24, pp. 1214–1215, 1988.

[44] L. Beyne and D. D. Zutter, "Power deposition of a microstrip applicator radiating into a layered biological structure," *IEEE Trans. Microwave Theory Techn.*, vol. MTT-36, pp. 126–131, Jan. 1988.

[45] J. T. Aberle and D. M. Pozar, "Analysis of infinite arrays of probe-fed rectangular microstrip patches using a rigorous feed model," *IEE Proc.*, vol. 136, Pt. H, pp. 110–119, Apr. 1989.

[46] R. C. Hall and J. R. Mosig, "The calculation of mutual coupling between microstrip antennas with thick substrates," *Digest IEEE AP-S Int'l Symp.*, pp. 442–445, San Jose, CA, June 1989.

[47] C. M. Butler and L. L. Tsai, "An alternate frill field formulation," *IEEE Trans. Antennas Propagat.*, vol. AP-21, pp. 115–116, Jan. 1973.

[48] C. L. Chi and N. G. Alexopoulos, "Radiation by a probe through a substrate," *IEEE Trans. Antennas Propagat.*, vol. AP-34, pp. 1080–1091, Sept. 1986.

[49] R. C. Hall and J. R. Mosig, "Vertical monopoles embedded in a dielectric substrate," *IEE Proc.*, Pt. H, submitted.

[50] G. J. Burke, E. K. Miller, J. N. Brittingham, D. L. Lager, R. J. Lytle, and J. T. Okada, "Computer modeling of antennas near the ground," *Electromagn.*, vol. 1, pp. 29–49, Jan.-Mar. 1981.

[51] E. H. Newman and P. Tulyathan, "Analysis of microstrip antennas using moment methods," *IEEE Trans. Antennas Propagat.*, vol. AP-29, pp. 47–53, Jan. 1981.

[52] M. D. Deshpande and M. C. Bailey, "Input impedance of microstrip antennas," *IEEE Trans. Antennas Propagat.*, vol. AP-30, pp. 645–650, July 1982.

[53] D. M. Pozar, "Input impedance and mutual coupling of rectangular microstrip antennas," *IEEE Trans. Antennas Propagat.*, vol. AP-30, pp. 1191–1196, Nov. 1982.

[54] J. R. Mosig and R. C. Hall, "Numerical analysis of microstrip patch antennas," in *The Handbook of Microstrip Antennas* (J. R. James and P. S. Hall, eds.), Stevenage, UK: Peter Peregrinus, 1989.

[55] A. Hessel, "General characteristics of traveling-wave antennas," in *Antenna Theory Part II* (R. E. Collin and J. Zucker, eds.), pp. 151–258, New York: McGraw-Hill, 1969.

[56] M. Siegel and R. W. P. King, "Electromagnetic fields in a dissipative half-space—a numerical approach," *J. Appl. Phys.*, vol. 41, pp. 245-2423, May 1970.

[57] W. C. Kuo and K. K. Mei, "Numerical approximations of the Sommerfeld integrals for fast convergence," *Radio Sci.*, vol. 13, pp. 407-415, May-June 1978.

[58] C. C. Lin and K. K. Mei, "Radiation and scattering from partially buried vertical wires," *Electromagn.*, vol. 2, pp. 309-334, Oct.-Dec. 1982.

[59] P. B. Katehi and N. G. Alexopoulos, "Real axis integration of Sommerfeld integrals with applications to printed circuit antennas," *J. Math. Phys.*, vol. 24, pp. 527-533, Mar. 1983.

[60] W. A. Johnson and D. G. Dudley, "Real axis integration of Sommerfeld integrals: Source and observation points in air," *Radio Sci.*, vol. 18, pp. 175-186, Mar.-Apr. 1983.

[61] J. R. Mosig and F. E. Gardiol, "Analytic and numerical techniques in the Green's function treatment of microstrip antenna and scatterers," *IEE Proc.*, vol. 130, Pt. H, pp. 175-182, Mar. 1983.

[62] E. K. Miller, A. J. Poggio, and E. S. Selden, "Analysis of wire antennas in the presence of a conducting half-space. Part I: The vertical antenna in free space," *Can. J. Phys.*, vol. 50, pp. 879-888, 1972.

[63] T. K. Sarkar, "Analysis of arbitrarily oriented thin wire antennas over a plane imperfect ground," *Arch. Elek. Übertragung.*, vol. 31, pp. 449-457, 1977.

[64] K. A. Michalski and C. M. Butler, "Evaluation of Sommerfeld integrals arising in the ground stake antenna problem," *IEE Proc.*, vol. 134, Pt. H, pp. 93-97, Feb. 1987.

[65] J. A. Fuller and J. R. Wait, "A pulsed dipole in the earth," in *Transient Electromagnetic Fields* (L. B. Felsen, ed.), pp. 237-269, New York: Springer, 1976.

[66] J. A. Kong, L. C. Shen, and L. Tsang, "Field of an antenna submerged in a dissipative dielectric medium," *IEEE Trans. Antennas Propagat.*, vol. AP-25, pp. 887-889, Nov. 1977.

[67] V. Hansen, "Approximate equations for the nearfield of a horizontal electric dipole on a grounded dielectric slab," *IEE Proc.*, vol. 129, Pt. H, pp. 29-31, Feb. 1982.

[68] L. Grun and Y. Rahmat-Samii, "Polynomial approximations of Bessel, Neumann and Hankel functions for complex arguments," Tech. Rep. 77-15, Electromagnetics Lab., Dept. Elec. Eng., Univ. Illinois, July 1977.

[69] M. Abramowitz and I. A. Stegun, eds., *Handbook of Mathematical Functions.* New York: Dover, 1965.

[70] H. Hurwitz and P. F. Zweifel, "Numerical quadrature of Fourier transform integrals," *Math. Tables Aids Comput.*, vol. 10, pp. 140–149, 1956.

[71] L. M. Brekhovskikh, *Waves in Layered Media.* New York: Academic Press, 1980.

[72] H. Ermert, "Guiding and radiation characteristics of planar waveguides," *IEE Microwave, Optics and Acoustics*, vol. 3, pp. 59–62, Mar. 1979.

[73] A. A. Oliner, "Leakage from higher modes on microstrip line with application to antennas," *Proc. URSI Int. Symp. Electromagn. Theory*, pp. 25–27, Budapest, Hungary, Aug. 1986.

[74] A. A. Oliner and K. S. Lee, "The nature of the leakage from higher modes on microstrip line," *IEEE MTT-S Digest*, pp. 57–60, 1986.

[75] T. T. Wu, "Theory of the microstrip," *J. Appl. Phys.*, vol. 28, pp. 299–302, Mar. 1957.

[76] C. M. Butler, "The equivalent radius of a narrow conducting strip," *IEEE Trans. Antennas Propagat.*, vol. AP-30, pp. 755–758, July 1982.

[77] C. M. Butler and K. A. Michalski, "Analysis of a cylindrical antenna residing in two contiguous half spaces." Nat'l Radio Sci. Meeting, Boulder, CO, January 5-7, 1983.

[78] C. E. Smith, C. M. Butler, C. A. Harrison, and K. A. Michalski, "An experimental investigation of antenna configurations which are near to or pass through an air-water interface." Final Report to the Naval Ocean Systems Center, San Diego, CA, Dept. Elec. Eng., Univ. Mississippi, June 1984.

[79] A. A. Oliner and K. S. Lee, "Microstrip leaky wave strip antennas," *Digest of the AP-S Int'l Symp.*, pp. 443–446, Philadelphia, PA, Aug. 1986.

[80] D. C. Chang and E. F. Kuester, "Total and partial reflection from the end of a parallel-plate waveguide with an extended dielectric slab," *Radio Sci.*, vol. 16, pp. 1–13, Jan.-Feb. 1981.

[81] G. Kowalski and R. Pregla, "Dispersion characteristics of shielded microstrips with finite thickness," *Arch. Elek. Übertragung.*, vol. 25, pp. 193–196, Apr. 1971.

[82] N. Faché and D. De Zutter, "Full-wave analysis of a perfectly conducting wire transmission line in a double-layered conductor-backed medium," *IEEE Trans. Microwave Theory Techn.*, vol. MTT-37, pp. 512–518, Mar. 1989.

[83] T. Itoh and R. Mittra, "Spectral domain approach for calculating the dispersion characteristics of microstrip lines," *IEEE Trans. Microwave Theory Techn.*, vol. MTT-21, pp. 496–499, July 1973.

[84] M. Kobayashi and F. Ando, "Dispersion characteristics of open microstrip lines," *IEEE Trans. Microwave Theory Techn.*, vol. MTT-35, pp. 101–105, Feb. 1987.

[85] J. M. Grimm and J. S. Bagby, "Alternative integral formulation for analysis of microstrip transmission lines," *Nat'l Radio Sci. Meeting Digest*, p. 113, Boulder, CO, Jan. 1988.

[86] N. Fachè and D. D. Zutter, "Rigorous full-wave space-domain solution for dispersive microstrip lines," *IEEE Trans. Microwave Theory Techn.*, vol. MTT-36, pp. 731–737, Apr. 1988.